Nanostructured Interphases for Improved Interfacial Adhesion in Structural and Ballistic Composites

by

Jalal Nasser

A dissertation submitted in partial fulfillment
of the requirements for the degree of
Doctor of Philosophy
(Aerospace Engineering)
in The University of Michigan
2021

Doctoral Committee:

Professor Henry A. Sodano, Chair
Professor Daniel J. Inman
Professor Veera Sundararaghavan
Professor Alan I. Taub

Jalal Nasser
jalaln@umich.edu
ORCID id: 0000-0002-0898-3801

ACKNOWLEDGEMENTS

I would like to thank my advisor Dr. Henry Sodano for providing me with the opportunity to be part of his research group. His exceptional guidance and assistance throughout my PhD journey were instrumental and important for me to complete this dissertation. His willingness to let me solve my own research problems and explore beyond my expertise have also allowed me to build the necessary skill set and confidence to become an independent researcher. Being able to explore various scientific fields through an interdisciplinary approach under his mentoring has been a unique experience that I will reap its benefits for the rest of professional career. I am also sincerely grateful to my dissertation committee members: Prof. Inman, Prof. Sundararaghavan, and Prof. Taub for their generous feedback and support.

I would also like to express my sincere gratitude to Dr. Hyun Sik-Hwang and Dr. Jiajun Lin for their valuable suggestions and advices which allowed me to quickly step into the right track of my PhD journey. I want to thank my past lab mates, Dr. Mohammad Malakooti, Dr. Alireza Nafari, Dr. Lisha Zhang, and Dr. LoriAnne Groo as well as my current colleagues, Mrs. Kelsey Steinke, Mr. Jaehyun Jung, Mr. Ruowen Tu for their unwavering support, generous assistance and warm companionship. I learned tremendously from each one of them, and truly enjoyed our time spent together, both inside and outside the lab.

Finally, I would like to thank my parents, whose love and support drive me through everything I pursue, and all the challenges and obstacles that come with it. It is through their encouragement and sacrifices that I was able to find the motivation and perseverance to complete my PhD.

TABLE OF CONTENTS

LIST OF FIGURES

LIST OF TABLES

ABSTRACT

Fiber reinforced polymer matrix composites are a class of structural materials that have gained high desirability in a wide range of applications over the past few decades. Due to their high specific strength and toughness, low density, and design flexibility, fiber reinforced composites have been preferred over traditional homogenous materials, such as ceramics and metals, in structures and components within the military, aerospace, automotive and marine industries. The two constituents of these composite materials are typically the rigid fibers and compliant polymer resin, acting as reinforcement and matrix phases, respectively. Yet unlike biological multicomponent materials, such as bones, teeth, and bamboo, composites are heterogeneous materials suffering from failure-prone, discontinuous, and discrete fiber-matrix interfaces that limit them from achieving their ideal theoretical mechanical properties. Therefore, improving interfacial adhesion and the load transfer mechanism between the fiber and the matrix, while simultaneously maintaining the structural integrity and light weight of composite structures, is of great importance for the fabrication of high performance composites and has been a long-lasting challenge in the field of composite materials.

This dissertation is an effort to experimentally investigate hierarchical and multifunctional fiber reinforced polymer matrix composites with improved interfacial and interlaminar adhesion through the integration of nanoscale interphases and interlayers. As nanotechnology regularly introduces new functional building blocks, many promising and lightweight nano-reinforcement approaches are continuously emerging and integrated into composite materials. Here, the potential and role of chemical interactions between nanomaterials (aramid nanofibers (ANFs) and nanofibrils, zinc oxide nanowires (ZnO NWs), laser induced graphene (LIG)) and fiber surfaces (aramid, carbon, glass), along with their impact on the morphology and adhesion quality of the resulting interphases and interlayers are initially investigated. As a result, it is demonstrated that well-adhered nanostructured interphases and interlayers can be achieved in various fiber reinforced composites through a number of chemical processes, which include fibrilization, physical and electrostatic adsorption, surface functionalization, hydrothermal growth, and laser-induced graphitization, as well as other mechanical approaches, such as transfer printing and spray-coating.

Further research is then performed to thoroughly investigate and optimize the effect of the introduced nanostructured interphases and interlayers on the interfacial and interlaminar properties of both fabrics and composites under quasi-static and dynamic loading conditions, all while maintaining their structural integrity, light weight, and flexibility.

The obtained results conclusively indicate that aramid nanostructured interphases are capable of enhancing the interfacial shear strength (IFSS) and interlaminar properties of quasi-statically loaded aramid and glass fiber reinforced composites, while also improving the impact response and stab resistance of ballistic protection aramid fabrics. Moreover, ceramic zinc oxide interphases are studied using a novel experimental setup and are shown to allow for the tailoring of composite interfacial properties as a function of the applied strain rate. Finally, ANF and LIG nanostructured interlayers are demonstrated to suppress delamination and improve interlaminar fracture toughness in both aramid and carbon fiber reinforced polymer matrix composites. The nanomaterial reinforced interlaminar regions exhibit improved toughening mechanisms that increase energy absorption, and thus delay catastrophic failure due to delamination in composite structures. The research presented in this dissertation provides a multitude of scalable and efficient approaches for the grafting of nanostructured interphases and interlayers capable of yielding hierarchical and multifunctional fiber reinforced polymer matrix composites with improved mechanical performance and maintained light weight and flexibility.

CHAPTER 1. Introduction

1.1. Motivation

The motivation for this study lies in the development of hierarchal and multifunctional composites, along with the increasing demand for high strength and lightweight structural and ballistic materials. Fiber reinforced polymer matrix composites have attracted significant attention from a number of industries due to their superior specific strength and stiffness, lightweight, and design flexibility, relative to conventional materials, such as metals [1]. For example, aircraft wings fabricated using composite materials can yield considerable fuel consumption savings due to the significant decrease in the weight of the structure, in comparison to traditional metal wings [2]. Moreover, composite materials opened the door for new concepts in the aerospace industry, such as aero-elastic tailoring, which can be used to design aircrafts capable of overcoming or delaying aero-elastic phenomena, e.g. wing divergence and flow separation [3]. The described advantages of composite materials have led to their integration in a large number of applications ranging from the aerospace, automotive, marine, and renewable energy sectors to daily consumer goods and electronics [1]. These composite materials can be classified based on matrix material (ceramic, metal, polymer), reinforcement geometry or aspect ratio (continuous fiber, short fiber, particulate), and structural hierarchy (laminate, honeycomb, sandwich panel) [4]. Many structural and ballistic applications rely on continuous fiber reinforced polymer matrix composites to provide exceptional mechanical properties, while achieving a reduction in weight and an increase in system flexibility. Typically, such composites are constituted of continuous reinforcement in the form of aramid, glass, or carbon fibers that are bonded together using a lightweight polymer matrix, which allows for the support and transfer of mechanical loads within the heterogeneous material[5]. As a result of the increasing demand and use of fiber reinforced composites, industry analysts expect the global market for fiber reinforced polymer composites to grow to up to $37.2 billion by 2022 (Figure 1.1.) [6]. Currently, carbon fiber reinforced composites are being used in the fabrication of commercial aircrafts such as the Boeing 787 and Airbus A380 [7]. Specifically, the airframe of the Boeing 787 Dreamliner is composed of 50% carbon fiber reinforced composites, allowing for an approximately 20% improvement in fuel efficiency compared to its predecessor, the Boeing

767. Such statistics demonstrate the role composite materials are expected to play in the future of large-scale industries.

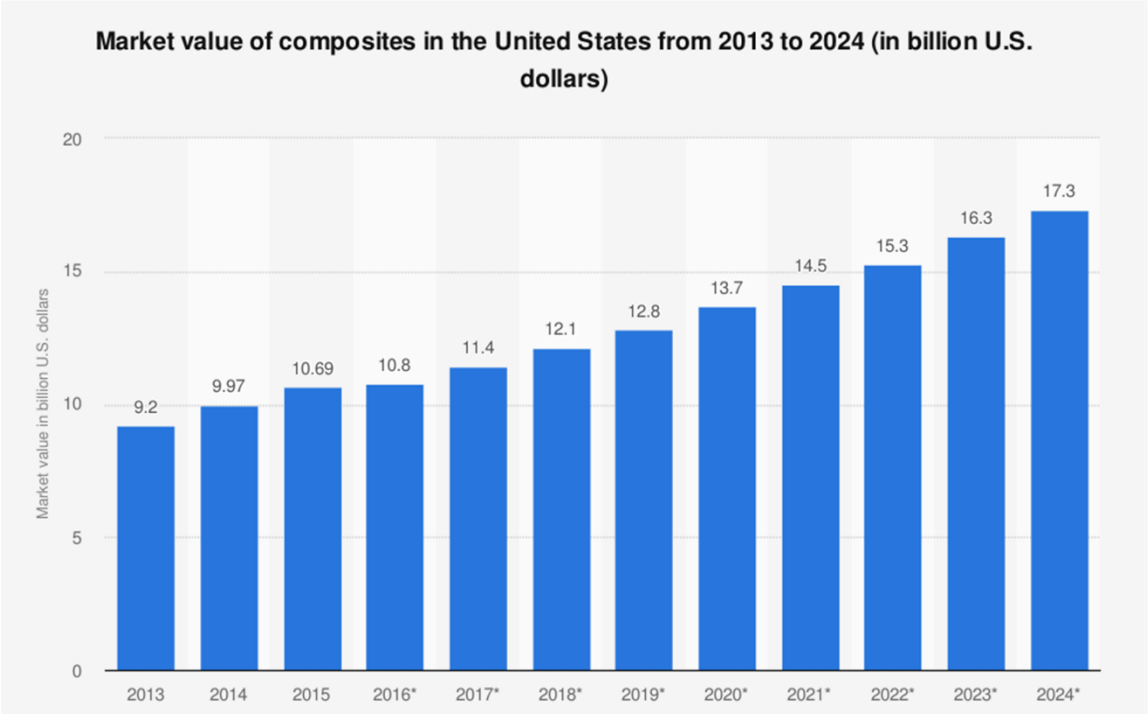

Figure 1.1. Current and projected market value of composites in the United States from 2013 to 2024 (in billion U.S. dollars) [6].

Despite their advantages, continuous fiber reinforced composites fall short of achieving their theoretically expected properties, as their performance is ultimately dictated by the quality of the fiber-matrix interface. The large mismatch in stiffness between the fiber and the matrix, along with weak adhesion, result in poor load transfer between both interfacial constituents and induce delamination due to interlaminar stress concentrations [8]. The discrete fiber-matrix interface is in contrast to that found in natural functional materials, where biologically heterogeneous systems are typically assembled through hierarchically structured interfaces. These natural and functionally graded interfaces are able to bridge between soft and stiff components, providing the necessary load transfer mechanisms for simultaneously high strength and high stiffness materials, such as bones, teeth and cellular materials (Figure 1.2.) [9]. For example, the collagen fibrils in human bones are bonded through nanostructured hydroxyapatite crystals oriented along the fiber axis (Figure 1.2A) [10]. Elsewhere, the strong, yet brittle enamel found in human teeth is bonded to

the tough and soft dentin through a multi-level micro-scalloped junction (Figure 1.2B) [11]. These naturally nanostructured interphases between adjacent components provide natural materials with a combination of strength and toughness which is difficult to replicate in man-made heterogeneous materials. However, with the recent developments in the field of nanotechnology, the concept of assembling nanostructured interphases along the interfacial region of fiber reinforced composites with the goal of improving fiber-matrix adhesion has considerably grown in potential.

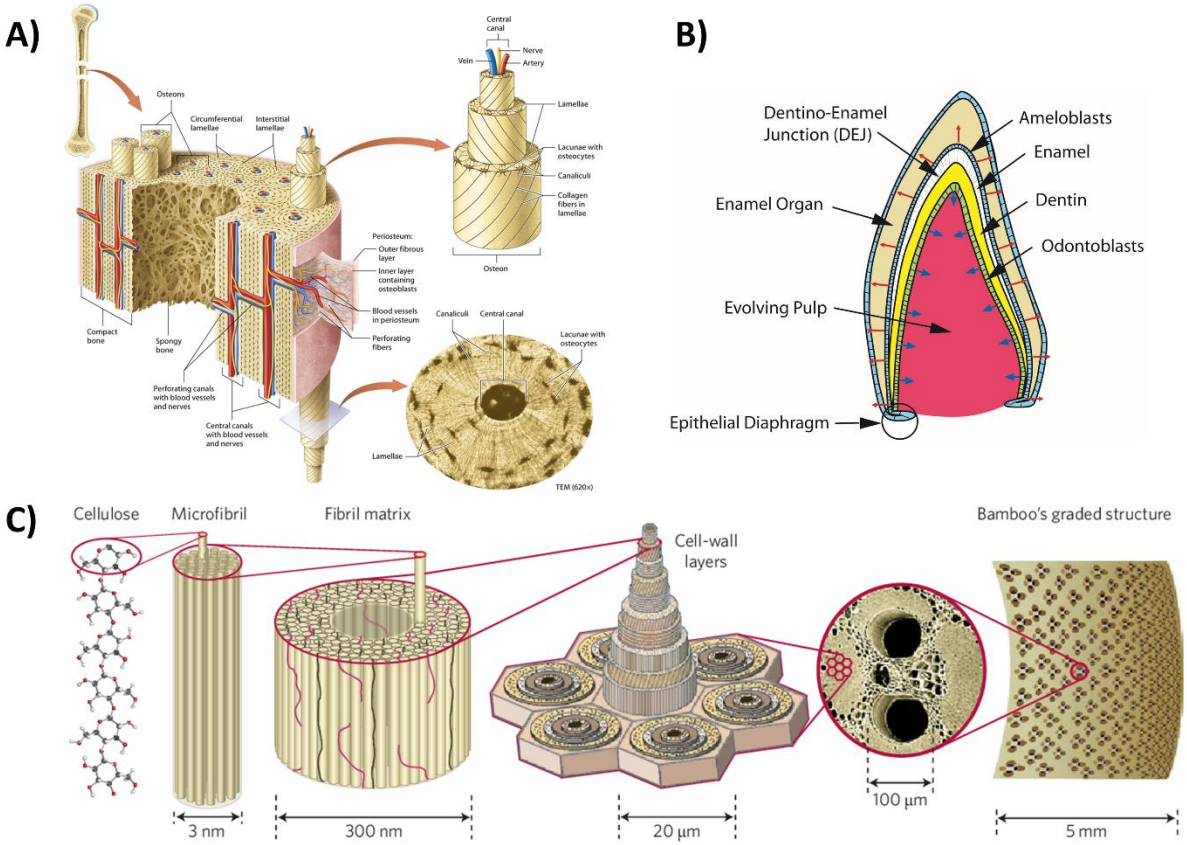

Figure 1.2. Hierarchical structure of bone, teeth, and bamboo. A) Schematic representation of nanometer and micrometer scale hierarchical structure in human compact/cortical bone. B) Schematic representation of the dentino-enamel junction combining and bridging the hard enamel and soft dentin of a human teeth. C) The functionally graded structure of bamboo composed of cellulose fibers embedded in complex structures. The radial density gradient of the parallel fibers enables high load transfer and increased flexural rigidity [10,11].

In this research, the interfacial and interlaminar properties of fiber reinforced polymer matrix composites are improved using a number of nanomaterial-based modification approaches and techniques. Aramid, zinc oxide, and graphene nanomaterials are integrated into aramid, glass, and carbon fiber reinforced composites in order to improve structural and ballistic properties, such

as interfacial shear strength, Mode I & Mode II fracture toughness, short beam shear strength, and ballistic limit. The various nanomaterial-fiber surface and nanomaterial-polymer matrix interactions were both chemically and mechanically characterized and optimized in order to maximize the mechanical performance of the hierarchical composites, all while ensuring the conservation of in-plane or tensile properties. Finally, the modified failure modes as a result of the introduction of such interphases and interlayers are studied and investigated for greater understanding of their reinforcement mechanism and their contribution to the improved interfacial adhesion. Below is a brief review of the history of composites and their structural and non-structural applications, followed by a literature review of the various reported methods and techniques that aim to enhance interfacial and interlaminar properties in fiber reinforced polymer composites. The purpose of the following review is to demonstrate the advantages of a benignly introduced and functionally graded nanostructured interphase or interlayer over a traditional fiber-matrix interface and other interfacial reinforcement approaches that result in composite performance trade-offs.

1.2. History of composite materials

The use of composites by humans can be traced back to early civilizations, as archeological evidence indicates that Mesopotamian and Egyptians settlers (1500 B.C.) used a combination of straw and mud to build strong building structures, boats, and pottery products [12]. Later, around 1200 AD, the Mongols were able to establish military dominance due to their invention of archery composite bows [12]. These bows were formed by bonding wood and bones using protein colloid adhesives derived from animals. However, it was not until the emergence of synthetic resins during the late 1800s that the modern era of composites was made possible. Plastic materials, such as vinyl, polyester, and phenolic, that outperform nature-derived resins were finally obtainable through a relatively simple polymerization process that induces crosslinking between its molecules [13]. After the introduction of fiberglass by Owen Corning in 1935, fiber reinforced polymer matrix composites began to slowly find use in marine and aerospace applications [12]. Following the start of World War (WW) II, the increasing need for lightweight and high strength military structures further accelerated the growth of the composites industry as it is estimated that over seven million pounds of fiberglass composites were used for military applications during the war, primarily in boats, airplanes, and electronic radar equipment sheltering [1]. Post WW II,

composites continued to gain popularity in a number of new fields, as novel manufacturing processes and techniques consistently emerged. This allowed for the integration of fiber reinforced composites into medical, marine, automotive, oil production, and consumer goods industries [5]. With the emergence of aramid and carbon fibers during the 1970s, composites began to find use in ballistic and infrastructural applications [1]. The high energy absorption of aramid fibers made them ideal for ballistic applications, such as body armor, while the exceptionally high specific strength of carbon fibers allowed them to replace steel in a number of structural components [14]. With that, the first ever all-composite-superstructure vehicular bridge was installed in Russell Kansas in 1996, and numerous other all-composite-superstructures followed over the next two decades [15]. Recently, as composite demand continues to grow (Figure 1.3.), research centers around the world are focused on developing new fabrication techniques, such as 3D printing and tow steering, along with incorporating new functionalities into them for various structural and non-structural applications [16,17]. Below is a brief review of the various structural and non-structural functions that are currently expected to be improved or integrated into fiber reinforced polymer matrix composites.

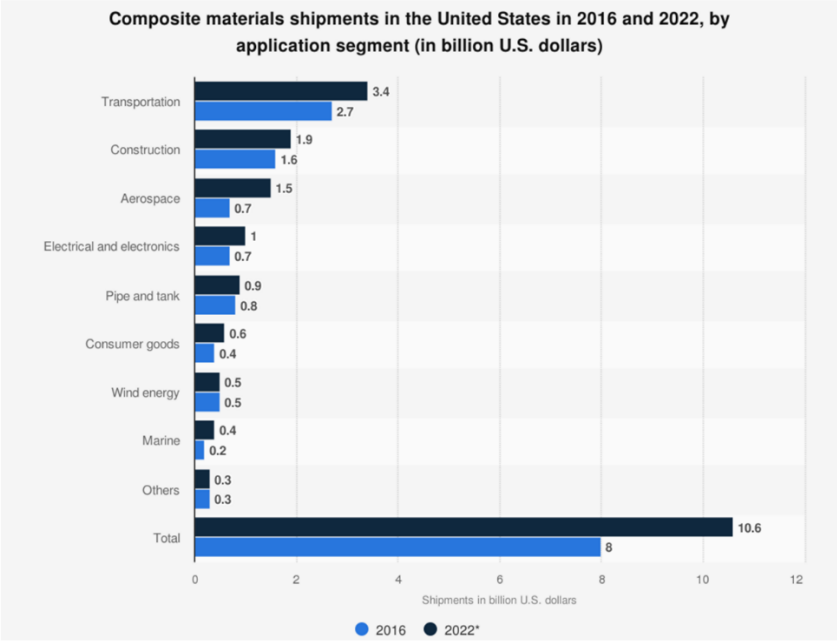

Figure 1.3. Composite materials shipments in the United States in 2016 and 2022, by application segment (in billion U.S. dollars) [6].

1.2.1. Structural functions in composites

Composite materials used in structural and ballistic applications are continuously expected to be improved and display enhanced load bearing capacities. While various forms of reinforcement phases can be used (Figure 1.4.), continuous fiber reinforced composites remain the most popular choice in many structural and ballistic applications [5]. A desirable feature in fiber reinforced polymer matrix composites is the achievement of a simultaneously high strength and toughness performance [1]. While carbon and fiberglass reinforced composites have been shown to possess high specific strength and stiffness, their brittle nature and tendency to delaminate cause them to lack the necessary toughness required in many structural and ballistic applications [18,19]. In contrast, aramid fiber reinforced composites are known for their high fracture toughness and energy absorption ability, as manifested through their impressive ballistic limit, damping, and fatigue performance [20]. Yet due to poor interfacial adhesion, aramid composites display considerably inferior in-plane properties relative to their carbon and glass counterparts. This has resulted in the need to use composites in conjunction with other conventional materials, such as metals and ceramics, in order to satisfy the targeted strength and toughness application requirements [21]. Originally, the development of advanced and multifunctional structural composites aimed to enhance a combination of two or more of these properties. This has been primarily achieved using a variety of techniques that exclusively focus on either the fabric or the resin matrix [5]. These optimizable parameters include the elastic and viscoelastic properties of the matrix, fabric architecture and areal density, the number of plies used, and ply stacking sequence [22]. A popular approach is hybridization, whether through the weaving of tough polymer and stiff ceramic tows together into one fabric, or through the stacking of polymer and ceramic fabrics within one laminate [23,24]. Similarly, the choice of resin can be optimized to suit application requirements, as matrix compliancy and toughness heavily contribute to the overall performance of the composite [25]. While, strong and stiff matrices are ideal for structural applications, more compliant and tougher matrices are capable of absorbing a higher degree of impact energy [26]. However, the mutual exclusivity of strength and toughness in high performance thermoplastic and thermoset resins remains a limiting factor when aiming to simultaneously satisfy two or more structural requirements.

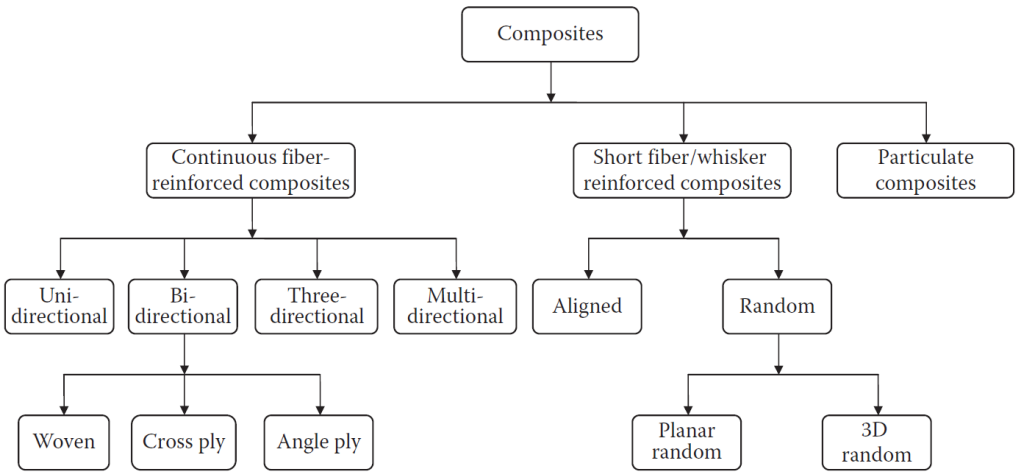

Figure 1.4. Classification of composites based on dispersed phase and adopted configuration [5].

Recently, a large portion of published work in the area of composites has focused on achieving these structural tasks through the introduction of a third, typically micro- or nanoscale phase capable of providing additional reinforcement [17,27]. Such a phase usually consists of fibers, wires, or particles that are directly introduced to the matrix, the fiber surface, or at the level of the interlaminar region with the goal of improving a number of mechanical properties within the composite [28]. Given the importance of load transfer between the fiber and the matrix, reinforcing the interface can be considered a key to designing multipurpose structural composites [25]. In later sections, a review of physical matrix and fiber surface modification techniques will be presented, and their influence on the structural properties of the bulk composite will be discussed. Additionally, given the increasing weight restrictions and higher flexibility demands, the introduction of non-structural functions into fiber reinforced polymer matrix composites to further expand their multifunctionality is another prominent area of research, of which a brief review will be presented below.

1.2.2. Non-structural functions in composites

With the goal of reducing the overall weight, cost, and complexity of composite structures, many researchers have focused on integrating non-structural functions into fiber reinforced composites. This allows for the partial or complete elimination of components that are typically necessary, as the composite structures is moved toward a more self-sufficient performance. Therefore, in addition to their load-bearing functions, these types of composites can be expected

to possess one or multiple non-structural functions such as energy harvesting and storage [29–31], structural health monitoring [32–35], sensing and actuation [36–38], self-healing [39–42], thermal and electrical conductivity [43,44], electromagnetic shielding [45], or biodegradability and recyclability [46,47].

The listed non-structural functions are integrated into composites using a variety of techniques and approaches. For example, by introducing the ability to harness wasted kinetic energy from mechanical vibrations in aerospace and automotive applications, subcomponents, such as batteries, can be eliminated from the host composite structure. This can be achieved through the embedding of thin energy cells or supercapacitors within a composite laminate, allowing for a charge/discharge behavior that can harvest surrounding energy and power certain electrical components [48,49]. Such multifunctional structural composites have been fabricated by Quian et al. by utilizing aerogel-modified carbon fabrics as large surface area electrodes and fiberglass membranes as separators, all embedded within a polymer electrolyte [50]. Another prominent approach is the use of piezoelectric materials, as their ability to easily convert mechanical vibration into a potential difference allows for easy and remarkable energy harvesting performance [29,31]. Early on, Lin et al. demonstrated the ability to integrate sensing, actuation and energy harvesting into fiber reinforced composites through the integration of barium titanate ($BaTiO_3$) coated silicon carbide fibers [51,52]. The $BaTiO_3$, a high dielectric piezoelectric material, is first embedded into a polymer before using it to form a shell around the structural fiber. More recently, Malakooti et al. reported the potential of piezoelectric ZnO NW interfaces to harvest surrounding energy (Figure 1.5.) [53]. The hydrothermally grown piezoelectric interphase is capable of generating up to 0.4 Volts peak-to-peak. The embedding of such functionality into composite materials at a nanoscale level opens the door for the fabrication of high strength materials with embedded energy harvesting capabilities.

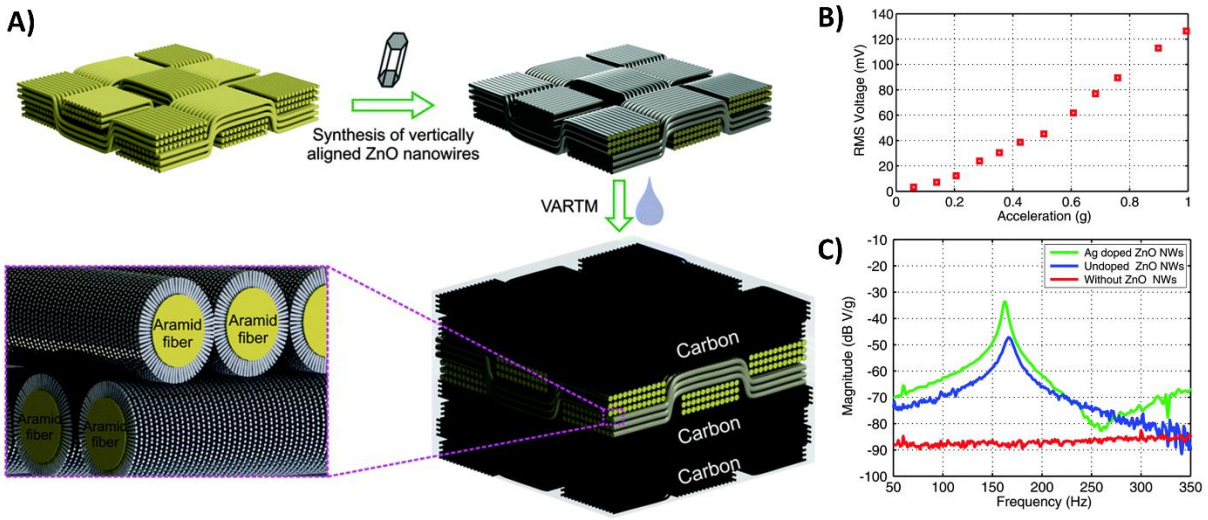

Figure 1.5 High strength multifunctional composites with embedded energy harvesting through ZnO NWs. A) Schematic illustration of the hybrid composite energy harvester fabrication process. B) The dependence of the root mean square (RMS) voltage response on the RMS base acceleration when hybrid composite energy harvester is excited using a sine wave. C) Electromechanical frequency response function characterization of the hybrid energy harvesting composites with silver (Ag) doped and un-doped ZnO NWs compared to a base composite without a ZnO NW interface [53].

Sensing and actuation are other important functionalities that have attracted considerable interest in the field of multifunctional composites. As structural health monitoring continues to gain research traction, many nanomaterial-based techniques have been developed [54]. Whether through piezoresistive or piezoelectric nanomaterials, damage and strain has been successfully monitored in fiber reinforced polymer matrix composites by several researchers. Thostenson et al. demonstrated the ability of piezoresistive carbon nanotube (CNT) networks to detect structural damage in composite materials [55]. Elsewhere, Sharama et al. demonstrated damage detection ability in aramid fiber reinforced composites through the integration of a CNT buckypaper [56]. Recently, Groo et al. introduced similar functionality to both aramid and fiberglass reinforced composites using laser induced graphene (LIG) [57,58]. The piezoresistive nanostructured interphases are capable of detecting both damage and strain, displaying a fast, stable, and sensitive response. Other non-structural functionalities that piezoresistive nanomaterials have been shown capable of providing in fiber reinforced composites include out-of-autoclave curing [59,60] and joule heating [61,62]. Piezoelectric materials, such as ZnO [63], lead zirconate titanate (PZT) [51,64], and polyvinylide fluoride (PVDF) [64], have also been shown to be capable of detecting

damage in fiber reinforced polymer matrix composites. While early work focused on the introduction of piezoelectric, hollow, and active micro-fibers into composite materials [65], more recently reported techniques focus on using nanostructured interphases. Groo et al. demonstrated that a hydrothermally grown ZnO nanowire interphase sandwiched between two carbon electrodes is able to detect multiple damage modes through passive voltage measurements (Figure 1.6.) [63].

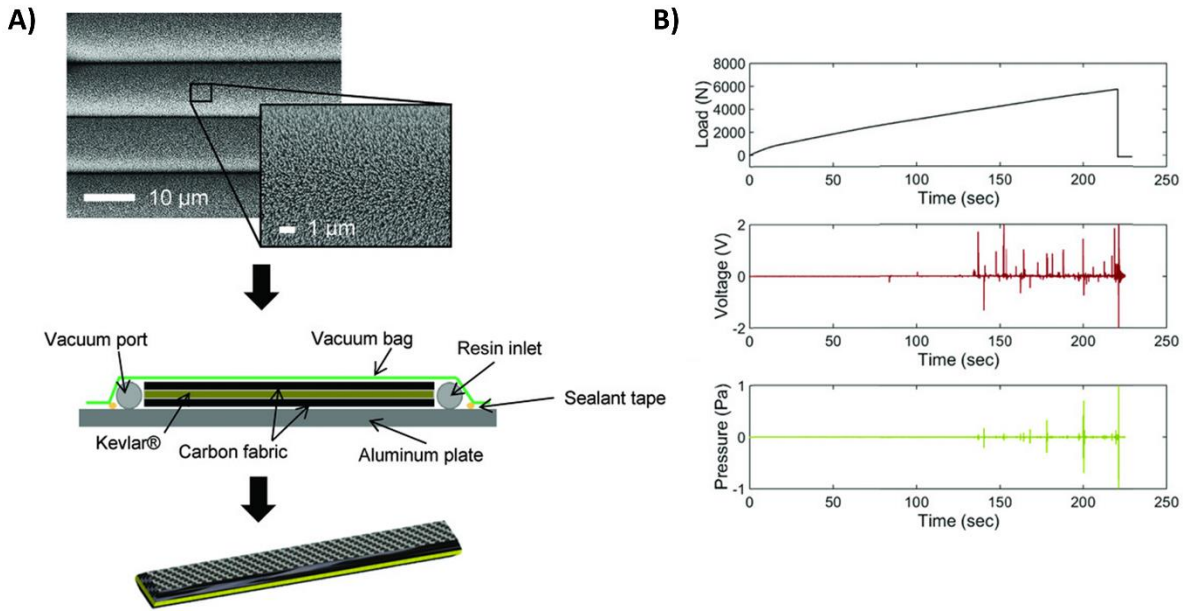

Figure 1.6. In situ damage detection in fiber reinforced composites using integrated ZnO nanowires. A) Vacuum assisted resin transfer molding (VARTM) fabricated hybrid composite test specimen containing ZnO NWs. B) Measured load, voltage across specimen, and microphone pressure readings during tensile testing of specimen containing ZnO NWs [63].

Complimentary to damage detection, damage repair is another highly coveted non-structural function in fiber reinforced composites [40,66]. Inspired by biological systems, composite structures are ideally desired to be capable of sensing, toughening and, ultimately, healing in the presence of damage, and without the need for an external stimulus [10]. Self-healing research efforts have been primarily centered around repairing the matrix through three approaches: capsule based [67], vascular based [68,69], and intrinsic [66,70] (Figure 1.7.). Although microencapsulation is a convenient approach, it only allows for one polymer healing cycle, as the entirety of the healing agents are exhausted during the initial release. Moreover, the empty capsules and vascular channels can act as defect sites that negatively affect the mechanical

performance of the composite structure. In contrast, intrinsic self-healing relies on reversible molecular interactions with the polymer matrix when subjected to a stimulus such as heat, light, or pressure [66]. Many of the intrinsic self-healing approaches have been based on polymerization-depolymerization equilibrium, such as a Diels-Alders reaction [71]. Zhang et al. recently reported a comprehensive study that discusses a novel and highly thermally stable self-healing chemistry that allows for repeatable and efficient recovery of both polymer matrix and composite strengths [39,72]. The developed isocyanurate-oxazolidone (ISOX) polymers rely on the isocyanurate to oxazolidone transformation to achieve healing once a crack is propagated within the composite [73].

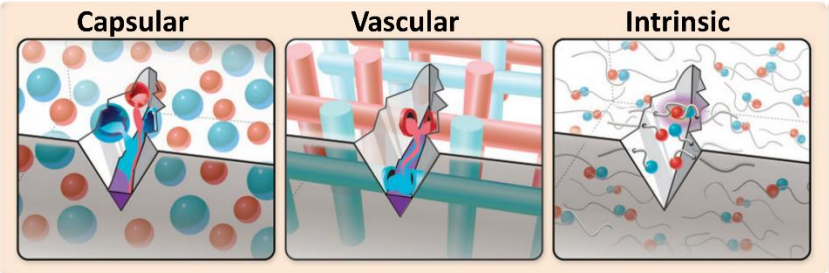

Figure 1.7. Schematic of extrinsic and intrinsic healing mechanisms [66].

In brief, this section summarized primary and secondary functionalities of fiber reinforced composites. Through the presented review, it is evidently clear that nanotechnology is expected to play a prominent role in the development of multifunctional fiber reinforced polymer matrix composites. Nonetheless, structural functions remain critical to the integration of composites in a wider range of applications, as they aim to continue replacing metals and ceramics where possible. The purpose of the following review is to illustrate the various methods and techniques currently developed in order to mechanically reinforce and improve the performance of fiber reinforced polymer matrix composites for structural and ballistic applications.

1.3 Polymer reinforcement

Nanomaterials have been incorporated in polymer matrices with the goal of introducing new properties and improving their overall performance. The resulting class of materials, known as nanocomposites, can be designed, synthesized, and tailored for use in a wide range of structural and non-structural applications [74,75]. Given that the properties of the matrix heavily influence those of the composite, any improvement to the properties of the former is expected to yield similar

results in the latter. With that, the resulting nanocomposites are typically desired to exhibit superior thermal stability, chemical resistance, and mechanical properties, relative to those of the pristine matrix [76]. The improved thermoplastic and thermoset polymers are then usually integrated into multifunctional fiber reinforced composites. Yet, achieving a simultaneous improvement to both strength and toughness in these polymers remains a challenging task due to problems such as poor nanofiller dispersion, weak interfacial interactions, and chemical incompatibility, resulting in tradeoffs between these mutually exclusive mechanical properties [74]. Below is a review of currently reported methods and techniques that use micro- and nanomaterials in order to improve the mechanical properties of polymer matrices, and subsequently fiber reinforced polymer matrix composites.

1.3.1. Polymer nanocomposites

When introducing a second phase into a host polymer material, it is important that the required modifications are performed in a benign, effective, and time-efficient manner that maximizes the structural performance of the nanocomposite. Many nanomaterials have been successfully employed as nanofillers within polymers and yielded considerable improvement to their mechanical properties. In comparison to reinforcements of larger scale, nano-reinforcements are able to produce a considerably larger interaction area within the matrix, thus allowing for more effective transfer of mechanical stresses between both constituents of the composite. Nonetheless, micro-reinforcements have also been extensively used to improve the mechanical properties of polymer matrices. For example, Tjong et al. reported a 125.5% and 27% increase in the Young's modulus and tensile strength, respectively, of short glass fiber reinforced polyamide 6,6 (PA66) composites [77], while Zhao et al. demonstrated an improved wear performance when short glass fibers are introduced into polyimide (PI) [78]. Karsli et al. also observed 50% and 125% improvements to the modulus and yield strength of short carbon fiber reinforced polyamide 6 (PA6), respectively [79]. However, these improvements are typically achieved using high micro-inclusion weight fractions (wt%) that reach up to 30%, and are usually accompanied with severe reductions in the ductility and toughness of the matrix [80].In contrast, many nanofillers, specifically those with larger aspect ratio, are able to produce similar reinforcing performances at considerably lower weight fractions [74]. Nanoclay, a commercially successful nano-reinforcement material, is an inorganic nanofiller that is capable of simultaneously improving the

strength and toughness of certain polymer nanocomposites using a weight fraction of less than 2 wt% [81,82]. This advantage has led to its use in many cyclic loading and ballistic applications such as body armor [83] and military helmets [84]. However, the inorganic material is typically inert and requires specific and extensive surface treatments to both increase its reactivity and compatibility with the polymer matrix, and enable exfoliation [85,86]. Moreover, the simultaneous improvement of strength and toughness was limited to epoxy nanocomposites, as it was not applicable to other polymers such as PA6 [75], polypropylene (PP) [87], and high density polyethylene (HDPE) [88]. Other inorganic nanomaterials that have been exploited for mechanical reinforcement functions in polymers include silicon oxide (SiO_2) [89], titanium dioxide (TiO_2) [90], and nanodiamonds (ND) [91].

Alternatively, CNTs are nanomaterials that have attracted considerable interest due to their multifunctional properties and high aspect ratio. Given their unique characteristics, CNTs can serve multiple roles within polymer matrices by improving both their electrical and thermal properties, while also enhancing mechanical performance [92]. Using only 1 wt% of single-walled carbon nanotubes (SWCNTs), Gao et al. observed 107.5% and 153% increase in the tensile strength and Young's modulus of electrospun PA-6 nanocomposites, respectively [93]. Similarly, Zhang et al. also reported 122% and 115% improvements in the tensile strength and elastic modulus, respectively, of 1 wt% CNT reinforced PA6 nanocomposites that were fabricated using melt-compounding, a more suitable approach for large scale industries [94]. Other CNT reinforced polymers that exhibited enhanced strength and stiffness include epoxy [95], PP [96], HDPE [97], polycarbonate [98], polystyrene (PS) [99], and poly(vinyl) alcohol (PVA) [100,101]. These improvements are attributed to the exceptional mechanical properties and high aspect ratio of CNTs, along with their ability to establish electrostatic and Van der Waals interactions with the polymer matrix [102]. The load transfer mechanism in CNT reinforced nanocomposites can be further enhanced using functionalization techniques, such as nitric acid oxidation, which populates CNTs with polar moieties that allow for greater chemical interaction with the polymer matrix (Figure 1.8.) [95,103]. Moreover, these improved mechanical properties of the nanocomposites are achieved with minimal decrease in their strain to failure, in comparison to that of short fiber reinforced polymers, thus largely maintaining the ductility of the polymers [104]. However, a preserved polymer toughness is not always guaranteed, as 1 wt% SWCNT reinforced PI fibers prepared using melt processing were found to suffer from an 85.7% decrease in strain to failure,

despite a 34% improvement to their tensile strength [105]. Due to their hydrophobic nature and tendency to aggregate, stable and uniform dispersion of CNTs in a liquid polymer reins are difficult to obtain [106]. This poor CNT dispersion in polymers leads to the formation of defects and agglomerations within the fabricated nanocomposites, causing for poor stress distribution and reducing their mechanical performance, especially at higher CNT weight fractions. Furthermore, as previously mentioned, the chemically inert surface of CNTs requires extensive chemical pre-processing and functionalization in order to establish sufficient and viable interfacial interactions within the nanocomposites [95,107]. It is therefore desired to introduce high aspect ratio nanofillers with a readily available capacity to chemically interact with polymer matrices, and that are capable of improving the mechanical performance of polymer-based nanocomposites.

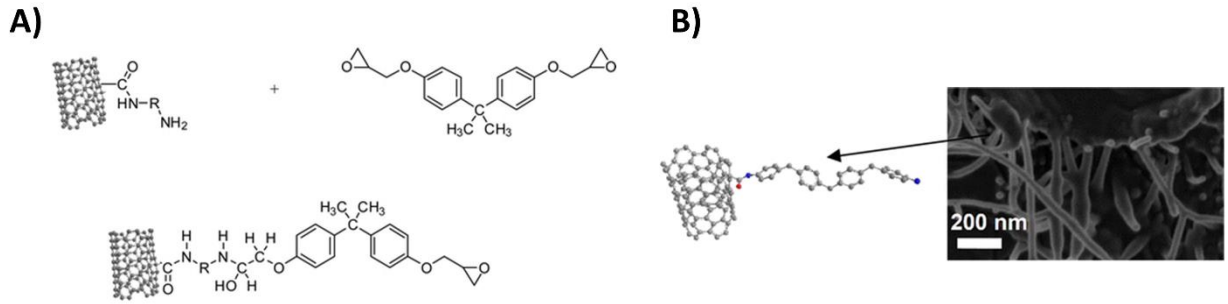

Figure 1.8. Dispersion of functionalized CNTs in epoxy resin. A) Reaction of amine functionalized CNT with bisphenol A diglycidyl ether (DGEBA). B) High-resolution SEM image of CNT/epoxy fracture surfaces [95].

Aramid nanofibers (ANFs) are surface-reactive polymer nanofibers that have been recently shown to provide mechanical reinforcement in both stiff and soft polymers. These nanofibers are obtained through a dissolution and deprotonation process that preserves their original chemical structure and increases the surface reactivity of the original fiber [108]. Xu et al. demonstrated that water-rich soft ANF-PVA composites fabricated using supercritical CO_2 drying are capable of replicating the performance of structural biomaterial systems such as collagen-proteoglycan (Figure 1.9A) [109]. Guan et al. also reported that solution cast 6.5 wt% ANF reinforced PVA nanocomposites exhibit 79.2% and 148.8 % increase in tensile strength and toughness, respectively [100]. Elsewhere, Lin et al. successfully isolated ANFs from a dimethyl sulfoxide (DMSO) solution using a simple, scalable, and low-cost dissolution approach (Figure 1.9B) [110]. When

1.5 wt% of the collected ANF powder was dispersed in epoxy, the nanocomposites displayed 28% and 22% increase in elastic stiffness and toughness, respectively. Such results are promising, as simultaneous improvements to both the strength and toughness of the matrix are rarely using other types of nanofillers. The theorized reinforcement mechanism in ANF reinforced nanocomposites is the improved stress transfer at the level of the nanofiller-matrix interface due to hydrogen bonding and π-π stacking between the reactive ANFs and the polymer matrix material [100,110–112]. Such interactions are similar to the amide-amide hydrogen bonding found in macroscale aramids, and are believed to be responsible for the strong intermolecular bonding between the crystalline sheets of aramid materials [113,114]. While many of the developed nanocomposites can be used independently in a number of applications, many of them are incorporated into fiber reinforced polymer matrix composites for various goals, as detailed below.

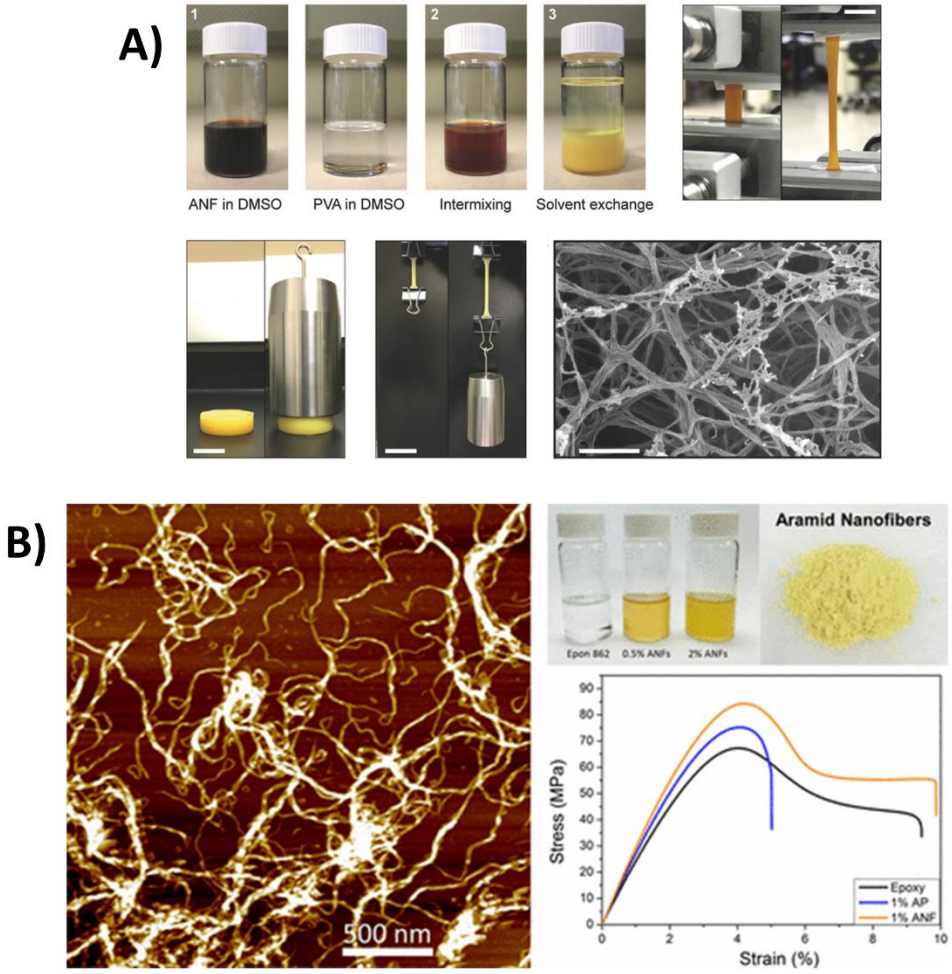

Figure 1.9. ANFs as nanofillers in soft and stiff polymer nanocomposites. A) Water-rich Kevlar® based biomimetic nanocomposites. ANFs and PVA are dispersed in DMSO to form a hydrogel before freeze drying the mixture to yield an aerogel. The soft material exhibits exceptional load-bearing and energy dissipation abilities that mimics cartilages found in humans and animals. B) ANF reinforced epoxy resin. The nanofibers are isolated from a suspension in the form of a powder, and re-dispersed in epoxy resin. The resulting ANF/epoxy nanocomposites are found to exhibit simultaneous improvements in strength, stiffness, and toughness [109,110].

1.3.2. Fiber reinforced polymer matrix composites

A number of the previously discussed nanofillers have also been used to mechanically strengthen fiber reinforced polymer matrix composites through resin mixing. CNTs have been a popular nanofiller choice due to their multifunctional performance, allowing for the introduction of both structural and non-structural functions into composites [115]. Godara et al. reported an 83% increase in the Mode I fracture toughness (G_{IC}) of carbon fiber composites when 1 wt% of CNTs is dispersed in the resin bath prior to prepreg fabrication [116]. Such an approach was used in order to circumvent the well-known difficulties of dispersing CNTs in most polymers, yet CNT agglomerations still resulted in a 20% decrease in the tensile strength of the carbon fiber composites. The challenge of adequately dispersing CNTs within resin are further exacerbated when vacuum assisted resin transfer molding (VARTM) is used, as the G_{IC} of the composites was reported to only increase by a maximum of 20% [117]. Dynamically, multi-walled CNTs and NH_2-CNTs have been shown to improve both the impact strength and ballistic limit of fiberglass reinforced composites, respectively [118,119]. A number of other organic and inorganic nanomaterials have also been shown to yield improvements to the structural and ballistic fiberglass composite properties through a resin mixing approach, as detailed in Table 1.1.

Table 1.1. l Resin-mixed nanofillers in fiberglass reinforced composites.

Nanofiller	Specimen	Strain-rate	Mechanical properties	Improvement	Ref
SiC/SiO_2	SF	Quasi-static	Interfacial shear strength	23%	[120]
ZrO_2	Laminate	Quasi-static	Flexural strength	22 %	[121]
GO	Laminate	Quasi-static	Flexural strength	21%	[122]
GnPs	Laminate	Quasi-static	Flexural modulus	26.3%	[123]
Nanoclay	Laminate	Quasi-static	Flexural modulus	25%	[124]
Nanoclay	Laminate	Dynamic	Impact energy	5%	[125]
NH_2-CNTs	Laminate	Dynamic	Impact strength	56%	[126]
MWCNTs	Laminate	Dynamic	Ballistic limit	6.5 %	[127]
GnPs	Laminate	Dynamic	Projectile exit velocity	89%	[128]

An alternative approach is to rely on soft, polymer based nanofillers in order to toughen stiff, yet brittle polymer matrices. For example, Ozdermir et al. used a dispersion of rubber nanoparticles in an epoxy matrix to yield a 250% improvement in the G_{IC} of carbon fiber reinforced composites [129]. Uddin et al. also showed that the introduction of silica nanoparticles into the epoxy matrix phase can considerably improve both the longitudinal compression and transverse tensile strength of unidirectional fiber reinforced composites [130]. As previously indicated, large aspect ratio nanofillers are favored due to their ability to yield a considerably larger interaction area between the nano-reinforcement and the matrix. Nanomaterials such as such as nanocellulose fibers [131,132] and nanorods [133] have been previously dispersed at low concentrations within the liquid resin, and were shown to be able of improving the overall performance of the composite. Polymeric ANFs have also been introduced using various approaches in fiber reinforced composites with the aim of enhancing their mechanical performance [134,135]. Patterson et al. reported maximum improvements of 40%, 42% and 17% in interfacial shear strength (IFSS), short beam shear strength (SBS) and G_{IC}, respectively, when ANFs were dispersed in epoxy matrix and then infused into aramid fabric to fabricate composite laminates (Figure 1.10.) [136]. The enhanced interfacial and interlaminar performance was attributed to the stronger and tougher epoxy matrix, along with the chemical compatibility and hydrogen bonding between the ANFs and both the matrix and macroscale aramid surfaces, respectively. Despite the improved matrix performance yielding enhanced composite properties, the problem of poor and weak adhesion between the fiber and the matrix remains unaddressed. Therefore, as detailed in the next section, great effort has

been allocated to developing interfacial reinforcement techniques that can improve interfacial adhesion and provide the desired structural and ballistic composite performance.

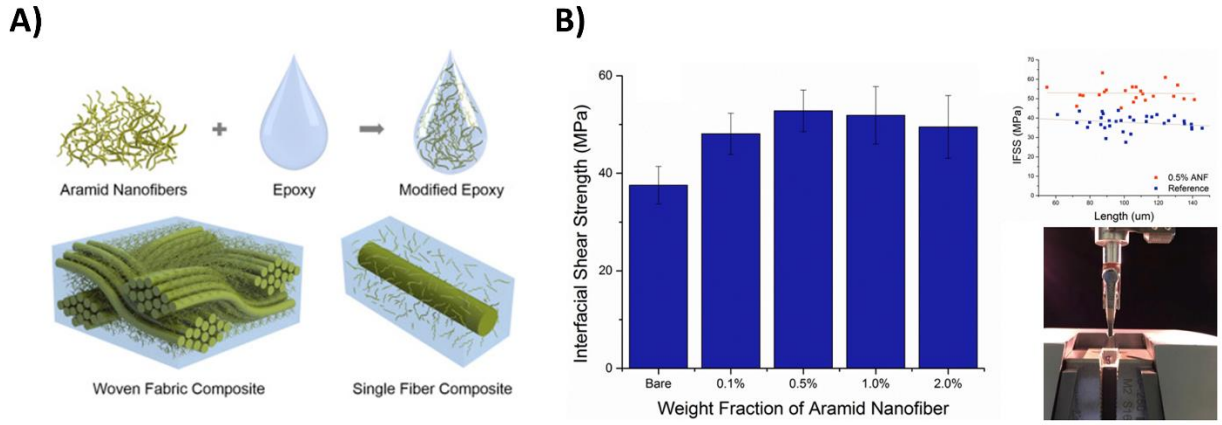

Figure 1.10. ANF reinforced aramid fiber epoxy matrix composites. A) Schematic of matrix modified fiber reinforced polymer composite and the incorporation of ANFs. B) Single fiber pullout test for ANF reinforced aramid composites [136].

1.4. Interfacial reinforcement

The fiber-matrix interface represents the interaction area between the reinforcement and matrix phases of a composite material. Typically, the weak interface is a site for stress concentrations due the dissimilar nature of the composite constituents. Given the large mismatch in elastic stiffness between the fiber and the matrix, composite materials are usually unable to achieve their targeted properties, and are prone to quick failure under out-of-plane, transverse shear, and compression loading conditions [137]. It is thus necessary to understand the mechanics driving interfacial behavior during quasi-static or dynamic loading. These interfacial properties can be isolated and studied in depth through mechanical tests such as single fiber segmentation and pullout testing [138]. Given the size of the embedded fiber length during pullout testing, which will be discussed later, interfacial interactions can be described using the shear lag theory [8,139–141]. While primarily used for short and discontinuous fiber reinforced composites, the shear lag theory offers insights into the interfacial load transfer mechanism. Assuming axial force equilibrium on a small element of the composite (Figure 1.11A) and around the fiber-matrix interface, the axial stress (σ_f) and shear stress (τ_i) are related through the following relationship:

$$\frac{d\sigma_f}{dx} = -\frac{2\tau_i(x)}{r_0} \tag{1.1.}$$

where r_0 is the fiber diameter. Assuming that the fiber and the matrix exhibit perfect adhesion, the interfacial shear stress can be expressed as:

$$\tau_i(x) = \frac{G_m(u_m(x,R) - u_m(x,r_i))}{r_0 \ln(\frac{R}{r_0})} \tag{1.2.}$$

where G_m is the shear modulus of the matrix, and $u_m(x, R)$ and $u_m(x, r_i)$ are the matrix displacement at r=R and r=r_0, respectively. R is then chosen to be at a remote location from the fiber, where the matrix strain is uniform. It should be noted that the described relationship holds when assuming that the matrix solely carries shear stress, and thus any radial displacement is insignificant. Assuming isotropy, and combining the previous two equations, the differential axial stress can be expressed as:

$$\frac{d\sigma_f}{dx} = \frac{E_m(u_R - u_{r_0})}{(1+\nu_m) r_0^2 \ln(\frac{R}{r_0})} \tag{1.3.}$$

where E_m and ν_m are the elastic modulus and Poisson ratio of the matrix, respectively. The short notations u_R and u_{r0} are used to indicate $u_m(x, R)$ and $u_m(x, r_i)$, respectively. Differentiating equation 1.3., a second order ordinary differential equation is obtained, whose solution is found to be:

$$\sigma_f = E_f \varepsilon_m + B sinh\left(\frac{nx}{r_0}\right) + D cosh(\frac{nx}{r_0}) \tag{1.4.}$$

where:

$$n = \frac{E_m}{(1+\nu_m) E_f \ln(\frac{R}{r_0})} \tag{1.5.}$$

$$\frac{du_r}{dx} \cong \varepsilon_m \tag{1.6.}$$

When applying the boundary conditions of zero axial stress at fiber extremities, the resulting axial stress solution is of the form:

$$\sigma_f = E_f \varepsilon_m \left(1 - \cosh\left(\frac{nx}{r_0}\right) \operatorname{sech}(n\frac{L}{r})\right) \tag{1.7}$$

where L is the fiber half-length. Using equation 1.1, the interfacial shear stress can be expressed as the following:

$$\tau_i = \frac{n}{2} E_f \varepsilon_m \sinh\left(\frac{nx}{r_0}\right) \operatorname{sech}(n\frac{L}{r})) \tag{1.8}$$

Given that during interfacial testing, such as single fiber pullout (Figure 1.11B), interfacial shear stresses are induced along a short embedded fiber length through axial loading of the free length

of the fiber, shear lag theory represents a relatively accurate representation of the stress transfer mechanism at the fiber-matrix interface. Nonetheless, the assumed interfacial adhesion remains dependent on chemical and mechanical interactions between the fiber and the matrix, both of which can be improved using a variety of techniques. The following sections will detail the currently developed surface modification techniques to improve interfacial adhesion in fiber reinforced polymer matrix composites for both structural and ballistic applications.

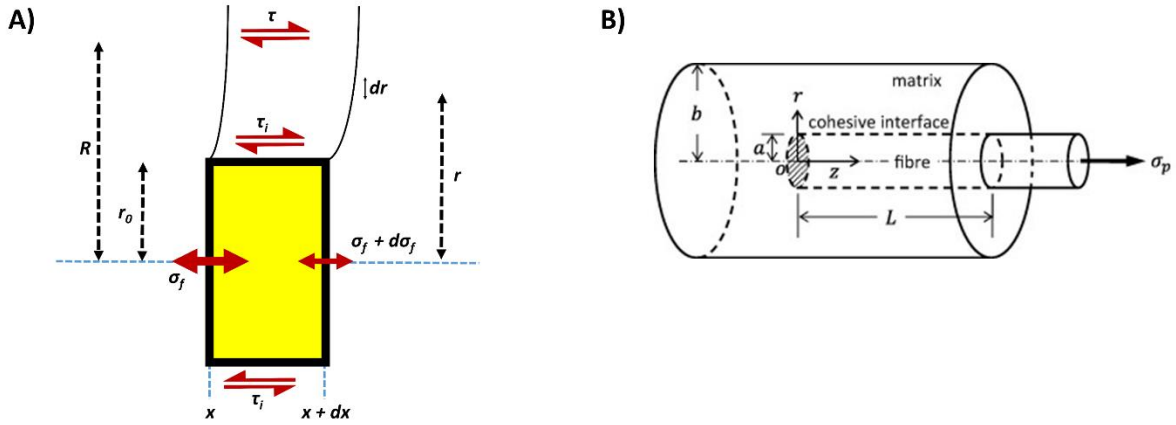

Figure 1.11. Load transfer at fiber-matrix interface. A) Shear lag model diagram for axial and shear stresses at fiber-matrix interface. B) Schematic of single fiber pullout specimen testing [141].

1.4.1. Structural applications

A strong and well-adhered fiber-matrix interface is necessary to maximize the performance of fiber reinforced polymer matrix composites used in structural applications. Such an interface can help increase delamination resistance, which is the primary failure mode of composites during service. The quality of the fiber-matrix interface is typically dependent on the degree of chemical interaction, mechanical interlocking, and the size of the interaction surface area between the fiber and matrix [8]. The literature review presented in this section is primarily dedicated to the various modification techniques pertaining to the chemistry and morphology of the fiber surface, and their resulting effects on the overall mechanical properties of composites, with particular emphasis on the interfacial properties.

1.4.1.1. Chemical treatments

A popular interfacial reinforcement approach relies on the introduction of functional groups onto the fiber surface in order to enhance chemical interaction between the fiber and matrix. As a result, various surface treatments have been investigated with the goal of changing the roughness and chemistry of the fiber surface to improve both the chemical interaction and mechanical interlocking with the polymeric matrix. Through chemical treatments such as gas plasma, acid [142–144] and base hydrolysis [142], and ultra-sonication [142–144], the surface roughness and density of polar functional groups on the surface of the fiber can be effectively increased. In particular, the treatment of aramid fibers using acids such as H_3PO_4 [142] and diluted H_2SO_4 solutions [145] have been reported in the literature. Tarantili et al. reported an aramid fiber treatment method that employs a methacryloyl chloride and carbon tetrachloride solution [146]. The treatment is found to increase the flexural strength of the aramid reinforced composites by enhancing the surface energy and improving the fiber-matrix interaction, primarily due to the addition of methacrylic functional groups to the surface of the fiber. However, a severe decrease of approximately 50% in the tensile strength of the treated aramid fiber reinforced composites was reported and was attributed to the excessive etching suffered by the fibers. Yue et al. also proposed an acetic anhydride treatment followed by methanol washing for aramid fibers, and reported a 60% increase in IFSS [147]. It is claimed that the increase in IFSS is caused by the undulation of the fiber surface, thus improving mechanical interlocking. The surface was also found to be rich with oxygen functional groups, allowed for enhanced chemical interaction between fiber and matrix [142]. However, prolonged acid treatments were detrimental to the core of the fiber, resulting in a 41% decrease in IFSS compared with that of bare fibers, as the harsh treatment condition severely damage the fiber surface and exposes its core. Another method used to introduce functional groups to fiber surfaces is plasma treatment (Figure 1.12) [148]. Li et al. reported the use of a polymer-forming plasma treatment to deposit a polymer film containing active functional groups on fiber surfaces [149]. The allylamine plasma treatment leads to a dramatic increase in IFSS of ultra-high strength polyethylene (UHMWPE) fibers. However, it was also found that the tensile strength of the fibers decreased due to plasma etching. The combination of both plasma treatment and chemical treatment have also been prominent, as reported by Han et al. [150]. Carbon fibers were first plasma-treated and then immersed in an acidic solution containing silane coupling agents. An interlaminar shear strength (ILSS) improvement of 48% was observed; however, the tensile

strength of the carbon fibers was also decreased by 16% after an argon gas plasma treatment of only 3 minutes. Other plasma treatments, such as nitration-reduction [151], follow similar trends to what is discussed above, and any resulting improvements in the ILSS and IFSS of the composites come at the expense of the tensile properties of the fibers.

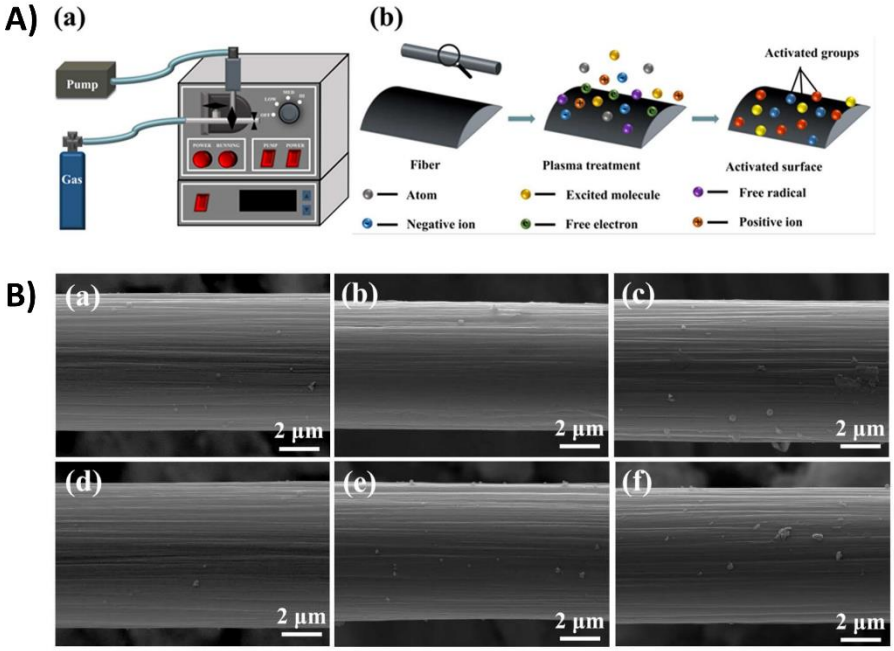

Figure 1.12. Plasma treated carbon fibers. A) Diagram of plasma treatment equipment and their effect on the carbon fiber surface. B) SEM images of carbon fibers at different plasma treatment severity ranging from 30 seconds to 5 minutes [148].

A series of chemical treatments and modification techniques, known as sizing, which are primarily used with fiberglass, have also been developed in order to increase reactivity between the fiber surface and the matrix [152–155]. Some benefits of surface sizing include overcoming frictional and electrostatic effects, or increasing the tensile strength of the fibers through the reduction of surface defects post-manufacturing [156]. However, the main role of sizing is to improve interfacial adhesion using chemical coupling agents that can interact with both the fiber and the matrix [157]. The treatment of fiberglass with silane coupling agents for composite applications has been extensively studied over the past several decades due to their ability to provide functional groups capable of bonding to both the inorganic glass surface and the organic polymer matrix. Korjakin et al. compared the performance of fiberglass composites with a

polyethylene surface treatment to that of silane, and found up to a 147% increase in Mode II fracture toughness (G_{IIC}) when a silane coupling agent (SCA) combined with an epoxy modifying agent was used [158]. This is primarily attributed to the improved chemical bonding between the fiber and matrix, which results in an enhanced interfacial adhesion and improved stress distribution in fiberglass composites. Gao et al. also reported more than a 100% increase in IFSS and up to 94 times higher debonding energy absorption when colloidal silica particles were introduced on the surface of fiber glass in combination with a commercial SCA [159]. In addition to the improved chemical interaction, the silica particles increase the surface roughness by up to 310%, creating a larger interaction surface area and providing anchoring sites for the fiber surface inside the resin matrix. However, many silane treatments are specific to the choice of resin, while multi-compatible silane treatments typically result in up to a 10% reduction in the in-plane performance of the composite [8]. Moreover, silanization of fiberglass can create a soft interphase which reduces both the composites stiffness and toughness [160], while also decreasing the glass transition temperature [161]. This can both limit the use of fiberglass composites in extreme temperature environments and complicate the design process of the composites and the prediction of the properties, given that nanoscale chemical interactions are mostly neglected in many practical engineering models of composite structures.

Therefore, it can clearly be seen that the majority of chemical treatments lead to a trade-off between different mechanical properties of fiber reinforced composites. With that, the focus of recent research has shifted to investigating the potential of nanostructured interphases in yielding both improved mechanical and chemical interactions between the fiber and the matrix. Below is a review of some of the more promising interphase design techniques reported in literature.

1.4.1.2. Nanostructured interphases

Interphase design is a prominent technique when it comes to interfacial reinforcement in fiber reinforced composites. Typically, the interphase is grown or adhered to the fiber surface, resulting in a larger interaction surface area and increased roughness. Some of the most recently discussed interphase design materials in the literature include CNTs [115], ZnO nanoparticles [162], TiO_2 nanoparticles [163], and aramid nanofibers [110]. The high aspect ratio and tunable surface chemistry of CNTs have led to their introduction into fiber reinforced composites through a variety of methods aiming to improve the interfacial adhesion and overall performance of the

composite [164,165]. The growth of CNTs on ceramic fiber surfaces, such as carbon and glass, is typically achieved using chemical vapor deposition (CVD) (Figure 1.13.) [166]. Qian et al. reported that the grafting of CNTs on the surface of silica fibers yields a 150% increase in IFSS of their composites [167], however, the tensile strength of the silica fibers decreases significantly due to a combination of catalyst etching and high-temperature processing (600 °C). Elsewhere, Downs et al. showed a more than 400% increase in IFSS of carbon fiber composites containing a hierarchical CNT interphase under quasi-static loading conditions, yet at the expense of the tensile strength of the fibers [168]. Therefore, CNT grafting using CVD is expected to severely damage organic fibers such as carbon. As a solution, Anthony et al. recommended the application of a potential difference during synthesis to preserve the tensile strength of carbon fibers. However, the resulting interfacial shear strength (IFSS) of the CNT coated carbon fibers was at best similar to that of commercially sized fibers [165]. Moreover, the high operating temperatures used for CVD is incompatible with polymer fibers, such as aramids and polyethylene, as they risk melting. Nonetheless, the lower reactivity of inorganic fiberglass allows for the optimization of CVD conditions in order avoid the degradation of the strength and tensile properties of the fibers [169]. However, CVD remains an energy intensive method that allows for minimal control over the adhesion between the CNTs and the fiber surface, while the high processing temperatures also risk burning off existing sizing that was introduced during fiber manufacturing [169]. Alternatively, Godara et al. used a benign drawing technique to coat fiberglass with CNTs, and observed more than a 90% increase in IFSS [170]. Another relatively harmless technique is electrophoretic deposition (EPD), which was used by An et al. to yield up to 50% increase in the IFSS of E-glass fibers [171]. EPD overcomes the electrically insulating nature of fiberglass by applying intimate contact between the fabric and a cathode [169,172], however, the method is shown to result in CNT coatings of non-uniform thickness which negatively affects resin wetting. Similar techniques have been used to strengthen the fiber-matrix interface using graphene-based nanomaterials; yet they face similar challenges to those employing CNTs [173–179].

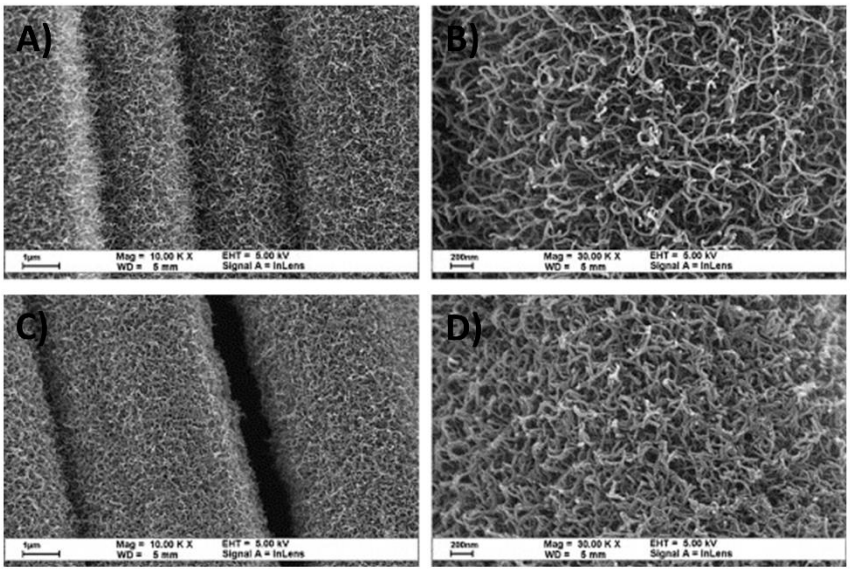

Figure 1.13. CNT coated carbon fibers. SEM images of as-grown and acid treated CNTs on activated carbon fiber fabrics using a low concentration of catalyst impregnation solution (0.1 M) [166].

Hydrothermal reactions are another viable technique for the synthesis of multifunctional nanostructured interphases on the surface of organic fibers without deteriorating the mechanical properties of the fiber [53,63]. Recently, ZnO NWs have been shown to be a promising, multifunctional whiskerization material when vertically synthesized on the surface of reinforcing fibers (Figure 1.14.) [144,180,181]. The surfaces of the fibers can be whiskerized with arrays of ZnO NWs using hydrothermal (<90 °C) aqueous solution-based processes that entirely preserve the strength of the fiber. The NWs result in a considerably increased interaction surface area, providing an interlocking tool between the fiber and matrix. Galan et al. reported a 228% improvement in the IFSS of carbon fiber reinforced polymer matrix composites during quasi-static loading when ZnO NWs with an optimized aspect ratio were introduced onto the surface of the carbon fibers [182]. It was observed that IFSS increased approximately linearly with both increasing NW length and diameter. Swaminathan et al. also reported a 430% increase in the IFSS of ZnO NW coated fiberglass using a similar hydrothermal method [183]. The benign hydrothermal method is similarly applicable to polymer fibers, as shown by Ehlert et al. who showed that using a functionalization and ion exchange procedure, the aramid fiber surface can populated with carboxylic acid prior to NW growth, thus improving adhesion between the fiber and the ZnO NWs and resulting in a 51% increase in IFSS [184]. In fiber reinforced composites,

the introduced ZnO NWs are able to provide out-of-plane reinforcement under quasi-static loading, creating a functional gradient between the dissimilar fiber and matrix materials, and reducing stress concentrations.

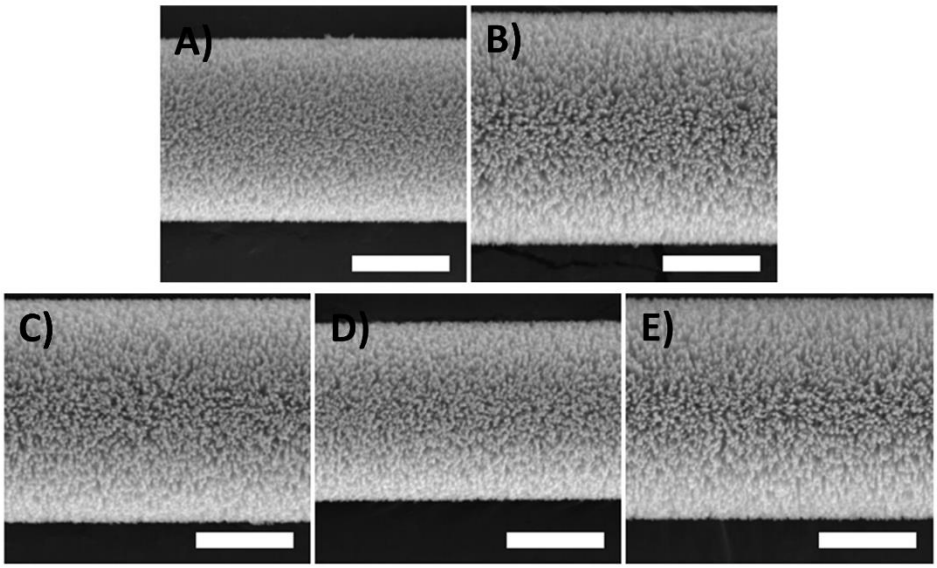

Figure 1.14. ZnO coated IM8 carbon fibers for improved interfacial shear strength (scale bars are 5 μm) [181].

Polymer nano-reinforcements have also been used to realize nanostructured interphases on fiber surfaces. Lee et al. successfully coated carbon fibers with ANFs, aiming to improve the interactions between carbon fibers and the epoxy matrix [134]. The ANF coating is created using anodic EPD approach, taking advantage of the negative charge and high electrical mobility of the ANFs in the colloidal solution. With ANF coating concentrations as low as 0.025 wt% on the carbon fiber, surface free energy and IFSS were found to increase by 39.7% and 34.9%, respectively. However, as the wt% of the ANFs was increased, SBS improvement was limited by poor resin infiltration and reduced surface roughness due to excessive coating. Park et al. also employed a graphene oxide (GO) functionalization to the surface of the non-conductive fiberglass, before performing layer-by-layer (LbL) assembly of ANF coatings in a diluted (0.04 wt%) ANF suspension [135].However, the time-consuming functionalization and assembly process resulted in only 23% and 39% improvements to the fiberglass surface free energy and IFSS, respectively. The smooth ANF coatings induced insignificant changes to the surface roughness and yielded near

identical mechanical testing results in comparison to those when using only a GO layer. Therefore, while promising, the potential of ANFs to both improve mechanical interlocking between the fiber and the matrix and enlarge the interaction surface area has not been fully realized.

In summary, the fiber-matrix interface can be reinforced using a number of techniques that yield improved composite structural performance. However, in the case of ballistic applications, a different set of interfacial properties is required. This presents significant obstacles when trying to design a fiber-matrix interface capable of simultaneously satisfying structural and ballistic application requirements. In the following section, a review of the developed methods and techniques to improve the ballistic properties of both woven fabric and fiber reinforced polymer composites will be presented.

1.4.2. Ballistic applications

Armors used for ballistic protection can be qualified as either soft body armor or hard body armor. Due to their lightweight nature, composite materials are growing in use for ballistic applications, whether in the form of fabric or fiber reinforced composites. In the case of soft body armor, polymeric fabrics, such as Kevlar® and Spectra®, have been used to protect soldiers and law enforcement personnel ever since their invention in the 1960s [185,186]. However, despite their advantages, current soft body armor requires thick layers (~ 50 layers), and are only able to protect against low energy projectile, such as handgun munitions and low speed debris [187,188]. Given that the performance of these fabrics is heavily dependent on interyarn friction, the improvement of fiber-fiber interactions can heavily enhance the impact response of the fabric. Elsewhere, hard body armor is required to provide ballistic protection in helmets, shields, combat vehicles, and military shelters [189–191]. These structures typically require a simultaneously high structural and ballistic performance. However, while structural applications require strong interfacial adhesion, a weaker fiber-matrix interface allows for higher energy absorption when composites are subjected to a ballistic impact [192]. The described contrast in optimal interfacial properties results in considerable design challenges, clearly highlighting the necessity of composites capable of meeting such performance duality. In the upcoming sections, a review of currently reported methods and techniques found in the literature to improve the ballistic performance of fabrics and fiber reinforced composites are reported.

1.4.2.1. Fabrics

Due to their superior energy absorption abilities, polymer fabrics are a popular choice in soft body armor applications. This has spurred considerable research aiming to improve the ballistic performance of dry woven polymer fabrics through techniques ranging from numerical analysis and modeling, to experimental studies and mechanical testing [193]. The effects of multiple fabric and environmental parameters on impact response have been investigated, including the number of fabric plies used and their stacking sequence, fabric architecture, interyarn friction, operating temperatures, and projectile characteristics [193]. By accounting for the contact between adjacent plies of a target, the numerical model proposed by Ting et al. demonstrated an improved ballistic performance with increased friction slippage at yarn crossing points [194]. Such results indicate the importance of interyarn friction as an energy dissipation mechanism of impact-loaded woven fabrics. Experimentally, the energy absorption of polymer fabrics was found to be roughly proportional to the areal density, but not to the mesh density or weave tightness [195]. Hybrid fabrics composed of a combination of aramid (Kevlar®) and carbon fibers were also found to exhibit superior ballistic performance [196], while the difference in the performance of the plied versus spaced configuration was concluded to be dependent on the geometry and velocity of the impacting projectile [197,198]. Other studies focused on the effects of fiber twist and yarn crimp on the ballistic performance of the fabric. Rao et al. optimized the tensile strength of fibers through a twist angle of 7° [199], while Chitrangad et al. reported an improvement in the limit velocity required for a projectile to penetrate target fabrics, known as the V_{50} speed, when hybridized weaves were designed for simultaneous failure of weft and warp yarns [196]. By replacing the original weft yarns with ones possessing larger elongation, the effect of yarn crimp was mitigated, and yarn undulation was reduced. Moreover, low-temperature operating conditions were also found to be ideal for the energy absorption performance of fabrics such as Dyneema® and Kevlar 29®, as increasing temperatures led to a decrease in the elastic modulus of the fiber [200]. Finally, projectile properties, such as geometry and mass [195], angle of incidence [201], and point of impact [202] were also found to have significant impact on the ballistic performance and energy dissipation mechanisms of woven fabric.

As previously stated, a significant energy dissipation mechanism during the impact response of woven fabrics is interyarn friction, as the mobility and friction between fabric yarns during impact is directly correlated to the fiber–fiber interfacial properties of the fabric. Recently,

many fiber surface modification techniques, such as lubrication [203,204], coatings [205–207], and interphase design [162,167], have been proposed to improve the impact response of fabrics through increasing interyarn friction. Dischler et al. reported a superior distribution of ballistic energy and improved interyarn friction in aramid fabrics when a 2 μm pyrrole thick coating was applied to the aramid fibers [208]. Moreover, Chitrangad et al. developed a fluorinated finish for aramid fibers that increases interyarn friction [209], however, the finishing was found to be incompatible with water-repellant agents, leading to increased slippage of the bullet between yarns and lower interyarn friction in wet fabrics [210,211]. Impregnating Kevlar® fabric with colloidal shear thickening fluids was also reported as an applicable method to enhance ballistic performance through a reduced yarn mobility. Lee et al. reported an improved impact resistance at higher strain rates with no loss of fabric flexibility when using colloidal shear thickening fluids [188]. The improved properties at high strain rates were attributed to the transfer of the loading concentration from the primary yarns to the entirety of the aramid fabric. However, shear thickening fluids fail to provide any impact protection at lower strain rates or against stabbing attacks [212]. The use of ethylene/methyl acrylate copolymer coatings to improve the interyarn friction of aramid fabrics was also studied by Gawandi et al. It was reported that by hot pressing the polymer-coated fabric, transverse infiltration of the polymer coating into the yarn crossing sections can be achieved, and a 124% increase in tow pullout peak load was observed [213]. The improved fabric ballistic performance o obtained using the discussed surface modification techniques confirms the important role of interfacial properties to the impact response and behavior of aramid fabrics.

Recently, interphase design has also found its way into the reinforcement of woven fabrics for ballistic applications. By grafting nanomaterials onto the surface of the fiber, sliding friction between yarns can be increased, as the mobility of both the fiber and tows is decreased [162,167]. Obradović et al. demonstrated improved ballistic performance in aramid composites through the addition of silica nanoparticles to the fiber surfaces [214]. Labarre et al. also showed a 230% increase in the yarn pullout peak load by coating MWCNTs onto the surface of aramid fibers using an ultra-sonication treatment [206]. However, other more effective CNT grafting methods, such as CVD, require high operating temperatures that are incompatible with polymer aramid fibers. As previously discussed, the development of novel ZnO NWs hydrothermal growth methods has enabled the benign grafting of nanomaterials on aramid fiber surfaces without any degradation of the fibers [180,215]. Hwang et al. showed the ability to tailor the interyarn friction of ZnO NW

coated aramid fabrics by controlling the nanowire morphology, and observed up to 22.7 times higher energy absorption in comparison to an untreated fabric [216,217]. The increase in interyarn friction when a ZnO interphase is added limits yarn mobility within the fabric and results in an improved ballistic performance. Moreover, as seen in Figure 1.15., Malakooti et al. reported a 66% increase in the impact resistance of ZnO NW coated aramid fabrics, compared to that of untreated fabric, when subjected to intermediate velocity impact tests [218]. These improvements to the impact response of the fabric were explained to be a result of the increase in mechanical interlocking and contact area between neighboring aramid fibers and tows [137,219].

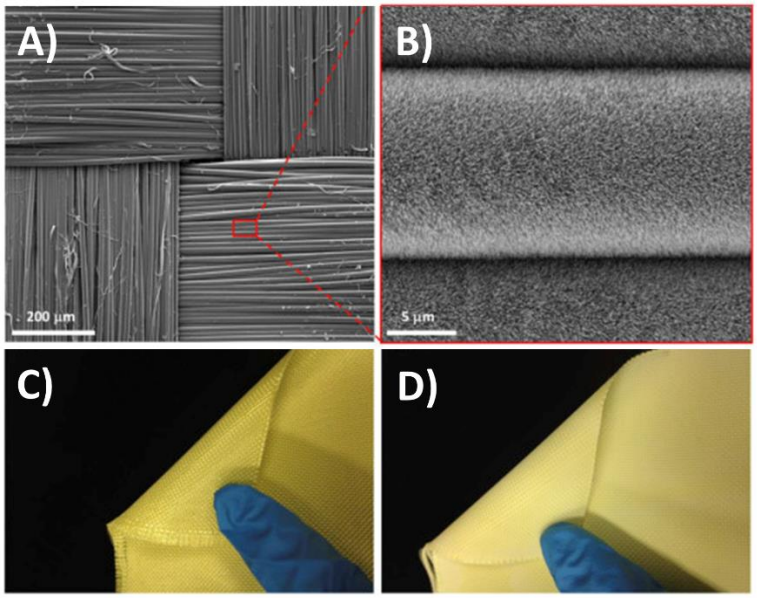

Figure 1.15. ZnO nanowires coated aramid fabrics for improved impact response. A) & B) SEM images of the ZnO coated aramid fabric and its new morphology. C) & D) The flexibility of the fabric is found to be maintained post-growth, with only a slight color change [218].

While dry fabrics can be useful for ballistic protection in soft body armor, they are not a viable option when load-bearing abilities are also required. Therefore, many applications necessitate the use of fiber reinforced composites, where the structure should be able to simultaneously withstand both quasi-static and dynamic loading scenarios. In the following section, a review of methods and approaches that have been adopted to achieve these requirements is presented.

1.4.2.2. Fiber reinforced polymer matrix composites

Numerous techniques and methods have emerged to produce composite systems with simultaneously high ballistic and structural performances. In the mid-1990s, Fink et al. presented a multi-layer structural laminate for ground combat vehicle protection [220,221]. The proposed composite integral armor (CIA) included ceramic alumina tiles for ballistic protection and a thick composite plate to act as structural backing. However, the CIA possessed a low mass efficiency that fell considerably short of the requirements for military applications. Other methods aim to reduce the weight of the system through the use of polymer fiber reinforced polymer matrix composite laminates for ballistic reinforcement. This is evident in the design of U.S. military helmets, where carbon fiber shells are over-molded with layers of high-molecular-weight polypropylene in order to simultaneously provide structural integrity and ballistic protection [222–224]. Alternatively, Harach et al. developed metallic–intermetallic laminates (MIL) as a new class of synthetic multifunctional materials [225]. Inspired by the multifunctionality of biological systems, titanium and aluminum foils are processed to produce metallic laminates with hierarchal microstructures that result in good structural and ballistic performance, in addition to their impressive electrical and thermal properties. While such composites achieve multifunctionality without the need for multiple components, the high areal density and rigidity of MIL limits its use in applications where flexibility and light weight are of high importance [226]. Another approach to improve the ballistic performance of fiber reinforced composites is through modifying the choice of matrix resin. Vieille et al. conducted a comparative study on thermoplastic- and thermosetting-based carbon fiber laminates and found that the former exhibited less delamination and better blast impact performance [227]. Yet weak fiber–matrix interfaces and low melting points have restricted thermoplastic resins to consumer goods and products.

Considerable interest has been recently shown in modifying carbon fiber and fiberglass reinforced polymer matrix composites for high structural and ballistic performance using various techniques [228–230]. As previously mentioned, carbon fiber and fiberglass reinforced composites possess properties such as high specific tensile strength and stiffness, and considerably low strain to failure, making them suitable for structural applications but not ideal for most ballistic ones [231]. This is primarily due to the localization of failure at the point of impact when these composites are struck by a projectile [232]. One way to improve the impact response of these composites is through the design of a fiber–matrix interface that improves structural performance

at low strain rate loading conditions, while maximizing its energy absorption at high strain rates. A weaker interface would enable the tough fiber of absorbing impact energy, whereas a strong interface would increase the resistance to delamination and matrix cracking of the composite under static loading. This dual structural performance would eliminate the need for multi-component protection systems, while satisfying weight, flexibility, and cost requirements. Many sizing techniques [205,233], and chemical and plasma treatments [234,235] have been reported for carbon fibers and fiberglass with the goal of tailoring the fiber–matrix interface for structural functionality and high and low strain rates. However, most of these methods result in fiber core damage and surface etching, leading to a considerable reduction in the tensile strength of the fibers, and thus sacrificing the structural performance of the composites for an improvement in their ballistic properties.

As previously discussed, under quasi-static loading conditions, a hierarchical CNT interphase is capable of considerably improving interfacial adhesion in fiber reinforced composites. However, similar IFSS measurements under dynamic loading conditions are unavailable in literature due to the difficulty of replicating the necessary experimental conditions and high dimensional accuracy using dynamic actuators. This has led to greater focus on studying the bulk properties dynamically loaded carbon fiber reinforced composites containing CNTs. Sharma et al. reported a 48% increase in impact strength of CNT coated carbon fiber reinforced composites when tested using a drop tower impact system [236]. This improvement in impact strength is attributed to the ability of CNTs to bridge micro-cracks near the fiber matrix. However, as discussed, CNT synthesis is achieved through high temperature CVD processes that require the use of catalysts, resulting in significant degradation of the fiber strength. Thus, any interfacial improvement gained under static and dynamic loading conditions comes at the expense of in-plane properties. Recently, Groo et al. demonstrated that piezoelectric interphases provide larger improvement to the damping behavior of carbon fiber composites, relative to non-piezoelectric ones of similar morphology [237]. Such behavior is attributed to the ability of piezoelectric material to convert vibrational energy to electrical energy that can be easily dissipated through the conductive fibers. While there has been no research on the impact response of ZnO coated fiber reinforced composites, many studies have shown that a ZnO interphase possess the potential of improving the ballistic performance of composites. Malakooti et al. demonstrated that the addition of a ZnO NW interphase to hybrid carbon fiber composites leads to a remarkable increase in

damping properties and flexural rigidity (Figure 1.16). Specifically, when ZnO NWs are added, a 200% increase in loss factor was observed over a neat composite, while the energy absorption of the composite was also improved [215]. Therefore, previous studies have shown that a ZnO NW interphase can increase the IFSS of composites under quasi-static loading conditions, while showing great promise for being a suitable interphase in ballistic applications. Nonetheless, understanding the behavior of a ZnO interphase within a fiber reinforced composite and its influence on the mechanical performance and interfacial properties of the composite under intermediate and high strain rate loading conditions is necessary and important before its integration into ballistic applications. Yet as previously mentioned, this remains to be studied, characterized, or reported in the literature.

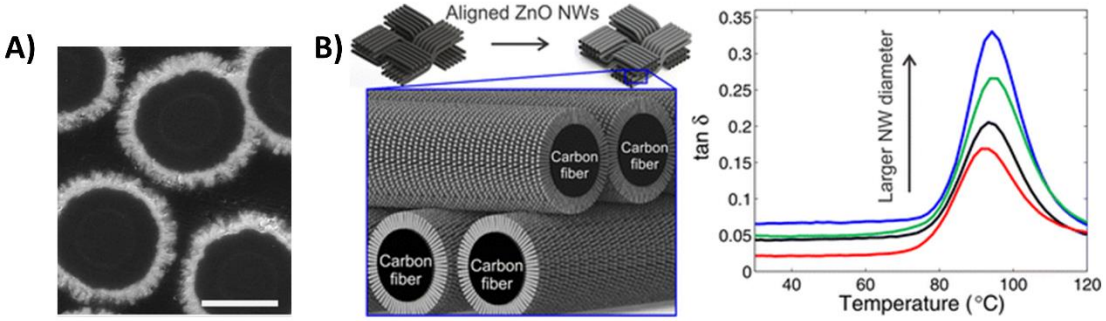

Figure 1.16. ZnO NW arrays for hybrid composites with high damping. A) SEM cross-sectional images of carbon fiber composites containing ZnO NWs. B) Schematic illustration of the ZnO modification to carbon fabric for hybrid composites. The damping of the hybrid composites is found to be improved with increasing nanowires diameter as shown by an increases in tan δ [215].

The interfacial reinforcement techniques detailed in this section have great potential to introduce a new generation of hierarchical fiber reinforced composite materials with improved properties and multifunctionality. However, an alternative approach aims to suppress delamination in composite materials by specifically addressing the weaknesses of the interlaminar region. The nature of these developed interlaminar reinforcements are investigated in the next section.

1.5. Interlaminar reinforcement

Delamination in fiber reinforced composites typically occurs due to the propagation of cracks within the interlaminar region. This region consists of the zone between adjacent plies of a composite laminate, and is primarily composed of matrix, while being bounded by fiber matrix

interfaces [238]. As a result, the mechanical performance of the interlaminar region relies on properties such as matrix toughness and interfacial adhesion [239]. Therefore, by redesigning the interlaminar region to push crack initiation and propagation away from the weakly adhered interfaces and into the tougher matrix, delamination can be partially or completely suppressed in fiber reinforced composites.

Previously developed interlaminar reinforcement techniques have primarily focused on modifying the structure of the fabric, the fiber-matrix interface, or the polymer matrix, all with the goal of improving the fracture toughness of fiber reinforced composite. Reported methods such as 3D weaving [240,241], braiding [242,243], and tufting [244] have each been shown to provide through-thickness reinforcement and lead to increased resistance to delamination in composite materials. Unfortunately, these techniques are limited to textile laminates that are fabricated using resin transfer molding techniques, and thus cannot be applied to prepreg laminates. However, this can be overcome using z-pinning, a method that aims to provide higher resistance to delamination using metal or fiber reinforced composite nails that mechanically bind plies together [245,246]. This extensively studied technique for out-of-plane reinforcement has shown that the addition of a 4% volume fraction of z-pins can improve the out-of-plane strength of prepreg laminates by more than 20% [245]. Yet this improvement typically comes at the expense of the composite's in-plane properties, as the introduced z-pins are shown to reduce tensile properties by up to 10% due to fiber damage and the formation of in-plane defects. Other research has focused on the replacement of the brittle epoxy matrix used to bind the plies with a more ductile thermoplastic matrix [247–249]. Freiderich et al. found that a polyether ether ketone (PEEK) matrix resulted in G_{IC} and G_{IIC} values that were up to 10 times higher than those of epoxy based carbon fiber composites [250]. However, high toughness thermoplastic matrices present significant challenges in the form of their high processing temperatures and increased cost, thus limiting their use in large scale industries.

Given the increasing interest in the introduction of nanomaterials into composite materials, considerable research has been allocated to understanding their ability to toughen fiber reinforced composites. Wang et al. reported an improvement of up to 20% in both the G_{IC} and G_{IIC} of carbon fiber composites when silicon carbide (SiC) whiskers were dispersed along the surface of the prepregs before the layup process. This has been attributed to the ability of the whiskers to bridge any crack forming between plies and resist its propagation. Similarly, interleaving is a technique that aims to interrupt crack propagation in fiber reinforced composites through the introduction of

an inter-ply nanostructured layer [251,252]. These interleaves are typically required to be lightweight, thin, and porous to avoid any penalties to the weight, in-plane properties, or resin impregnability of the composite. This is can be achieved through the electrospinning of thermoplastic nanofibers on the surface of prepregs and fabrics, which is a method that has shown great promise in strengthening the interlaminar region of composites [253–256]. Hamer et al. reported a maximum improvement of 300% in the G_{IC} of carbon fiber reinforced composites through the electrospinning of Nylon 66 nano-fibril mats [257], while Magniez et al. achieved a 57% increase in G_{IIC} when polyvinylidene fluoride (PVDF) nanofibrous membranes were electrospun onto carbon fabrics [258]. However, the PVDF interleave also resulted in a 20% reduction in G_{IC}, leading to a tradeoff between the interlaminar response of the composite under different loading conditions. Zhang et al. reported a 32% improvement in the G_{IC} of carbon fiber composites when polyetherketone cardo (PEK-C) nanofibers are electrospun on the surface of the carbon fiber fabric (Figure 1.17.) [256], however, the PEK-C nanofibers also resulted in an 18% decrease in flexural strength. Li et al. observed a 281% increase in the G_{IC} of carbon fiber reinforced composites containing electrospun polysulfone membranes, along with a slight improvement in the flexural properties [259]. Other polymer nanofibers that have also been shown to improve the interlaminar properties of carbon fiber composites include polycaprolatone [260], polystyrene [255], Polybenzimidazole [261], and Polyamide-66 [252,257]. Despite these improvements, the time-consuming nature and complexity of the electrospinning process limits it from being incorporated into the fabrication of large composite structures. Therefore, it is necessary to develop simple, efficient, yet also effective interlaminar nano-reinforcement solutions that can sustain the various loading requirements to which composites are subjected.

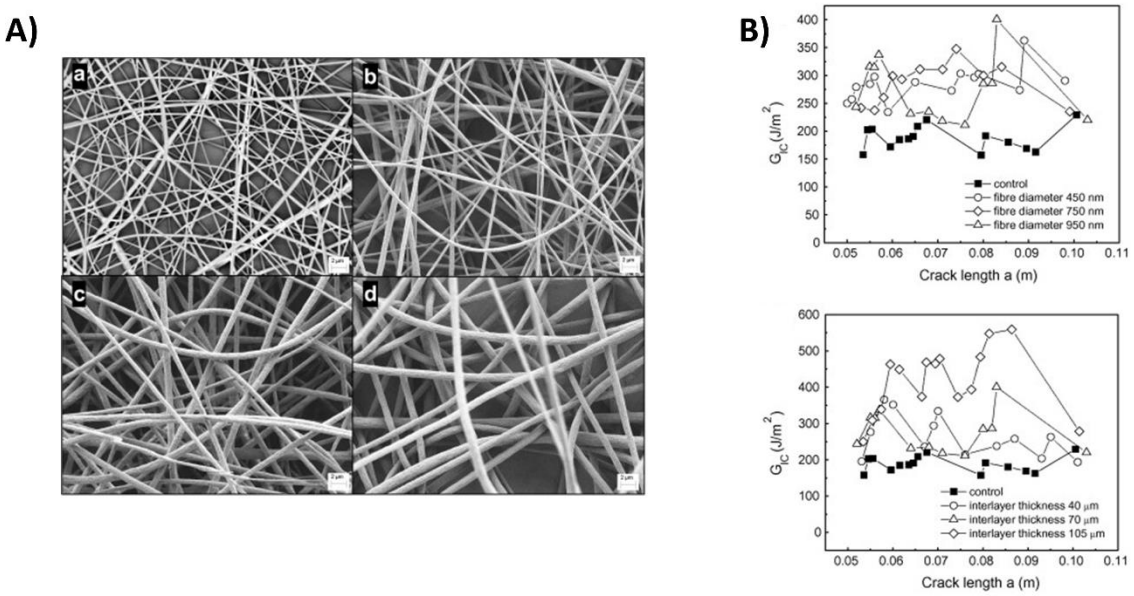

Figure 1.17. Polyetherketone-cardo (PEK-C) nanofiber toughened carbon fiber reinforced polymer matrix composites. A) SEM images of electrospun PEK-C nanofibers with various diameters. B) Delamination fracture toughness of carbon fiber composites containing PEK-C interlayer. The performance of the interlayer is found to be dependent on its thickness and the diameter of the nanofibers [256].

In addition to the previously described techniques, CNTs can be introduced into fabrics and prepregs through spraying [262,263], array transferring [264], and interleaving[265–267] prior to composite curing and fabrication. Given the difficulties in effectively realizing good CNT dispersion in resins, interleaving through a number of approaches such as veiling [268] and buckypapers [265] have recently gained popularity. Lee et al. demonstrated up to 350% and 246% increase in G_{IC} and G_{IIC}, respectively, when a CNT coated nano-woven tissue was introduced in carbon fiber composites [266]. Ou et al. also showed that multi-walled CNT veils can increase the G_{IC} of carbon fiber composites by 20%, while CNT buckypapers allowed for a 31% and 104% in the ILSS and G_{IIC} of the composites, respectively [268]. These improvements were attributed to the ability of the interlayer to stop crack propagation and induce sufficient fiber bridging in order to delay interlaminar failure. Similarly, other techniques rely on GO interleaves and interlayers to toughen carbon fiber reinforced composites [269,270]. Ning *et al.* reported a 170.8% increase in G_{IC} when GO sheets are introduced in the form of an interleave in carbon fiber composites [271]. In a series of studies, Liu *et al.* reported 102.3 % and 154.47% improvements in the G_{IC} and G_{IIC} of carbon fiber composites reinforced using a multilayers graphene/CNT spray-coated interlayer

[272,273]. Jia et al. also developed a 3D network graphene interlayer capable of realizing 70% and 206% increases in G_{IC} and G_{IIC} of carbon fiber reinforced composites [274]. Yet, the described process requires CVD growth of the 3D graphene network and considerable pre-processing prior to introduction in composites, thus reducing its time, cost and energy-efficiency. Finally, the transfer of vertically aligned CNT forests from a substrate onto the surface of carbon fiber prepregs has also been shown to toughen carbon fiber composites. The thin interlayer allows for the maintenance of the in-plane properties of the composites, while yielding 100% and 200% higher G_{IC} and G_{IIC}, respectively, by acting as "nanostitches" that join plies together (Figure 1.18) [275]. The original results from the technique reported considerable performance enhancement, however the CNT length could not be consistently processed to a length below 100 μm due to the rapid growth rate, leading to an increase in the interlaminar spacing by approximately 50 times the original value, and thus significantly reducing fiber volume fraction and in-plane strength. More recent studies that have used reduced length nanotubes have reported only marginal improvements to the fracture toughness and ILSS of a composite. For instance, Lewis et al. reported only a 6% improvement in the ILSS of IM7/8552 carbon fiber composites reinforced with CNTs, and a slight decrease in ILSS when using Toho Tenax HTS40/Q-1112 prepreg system [276]. Ni et al. reported their latest G_{IC} results at the 2019 AIAA SciTech Conference and showed a 6% decrease in the G_{IC} of CNT reinforced AS4/8552 prepreg, along with an unchanged G_{IIC} [277]. Furthermore, these methods are challenged by the high cost of CNT synthesis, which remains an obstacle to their integration in industrial composite structures.

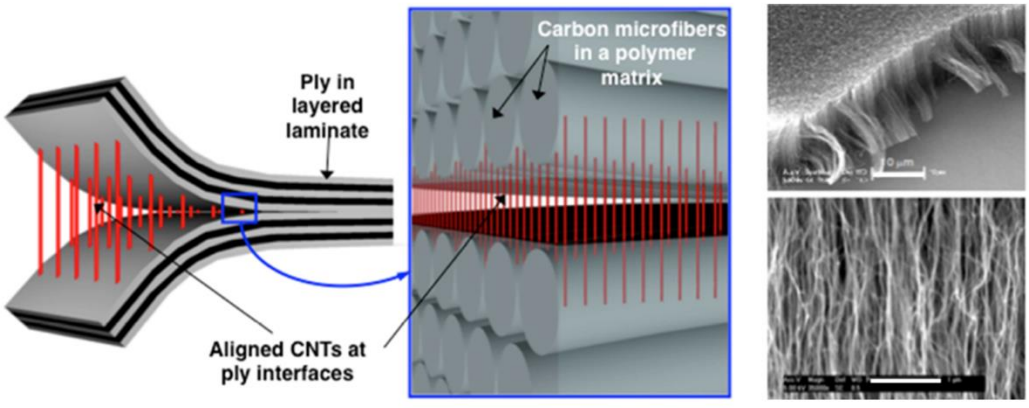

Figure 1.18. Use of vertically aligned CNTs to join prepreg composite interfaces. The illustrated mechanism shows vertically aligned CNTs bridging the crack between two plies, along with SEM images of the CVD synthesized CNT forests [275].

The presented review clearly shows that the use of nanomaterials to modify structural and non-structural properties of fiber reinforced composites has been a rapidly growing research field. With the continuous development of new nanomaterials, their role and contribution to the improved performance of composite materials is ever evolving. This dissertation focuses on three novel nanomaterials and their potential in achieving various structural functionalities in composite materials, as will be discussed below.

1.6. Choice of nanomaterials

While there are a number of nanomaterials that can be used improve the structural performance of fiber reinforced composites, this dissertation focuses on three novel ones: aramid nanofibers and nanofibrils, ZnO NWs, and laser induced graphene (LIG). Each of these materials possess its own advantages and disadvantages, as well as various potential applications or uses which are discussed in detail in the following sections.

1.6.1. Aramid nanofibers (ANFs) and nanofibrils

Until recently, polymeric nanofibers could primarily only be obtained through electrospinning or polymerization induced self-assembly techniques [278]. In 2011, ANFs were proposed by Yang et al. as a polymeric nanoscale building block that could be exploited in a large number of applications [108]. The unprecedented ANF polymeric dispersions are obtained through the dissolution of macroscale aramid fibers in a basic DMSO solution that abstracts mobile hydrogen bonds from the amide functional groups, and considerably weakens hydrogen bonding between polymer chains. The increased electrostatic repulsion within the aramid structure leads to the dissolution of the macroscale fiber into nanofibers of identical chemical structure. The resulting large aspect ratio nanofibers presumably maintain the aromatic polyamide backbone, excellent mechanical properties, and thermal and chemical resistance of macroscale aramid fibers. However, the originally inert aramid surface is also enriched with polar functional groups that increase their reactivity, such as carboxylic acids, carbonyls, and hydroxyls [136]. Moreover, ANFs have been found to exhibit excellent water repellency, while also being capable of providing high ultra-violet (UV) radiation protection [278]. Given the availability of the nanofibers in the form of a suspension, 2D and 3D nanoscale ANF-based structures such as films, coatings, particles, and

aerogels are easily attainable (Figure 1.19.). Due to the high strength and flexibility of the ANFs, the polyamide-based nanomaterial has also been shown to be capable of functioning as a networked matrix material for nanofillers such as CNTs [112,279], graphene [111], gold nanoparticles [280], and polyhedral oligomeric silsesquioxane (POSS) nanoparticles [281]. In addition, ANFs have been used to fabricate nanocomposite buckypapers [108,282] and membranes [281] for applications such as battery separators[283], electromagnetic shielding devices [284], electronic insulation [285], infrared protection [286], and biomimetic devices [109]. ANFs have also acted as interphases [134] and nanofillers [110] that provide mechanical reinforcement in certain fiber reinforced polymer composites [135,136]. Recent work reported by Yang et al. suggests a modified version of the traditional deprotonation technique that is 41 times more time-efficient than the original process [287]. Such advances facilitate the production of ANFs and accelerate their integration into large-scale production processes.

In addition to ANFs, the dissolution and deprotonation process can be exploited to develop a new aramid fiber surface treatment. By treating aramid fibers in a similar basic solution at room temperature, and for considerably shorter treatment periods, aramid nanofibrils can be directly generated along the aramid fiber surface. This work will be discussed more fully in later chapters, and for the first time, the potential of these nanofibrils in improving the adhesion of aramid fiber-matrix interfaces will be investigated.

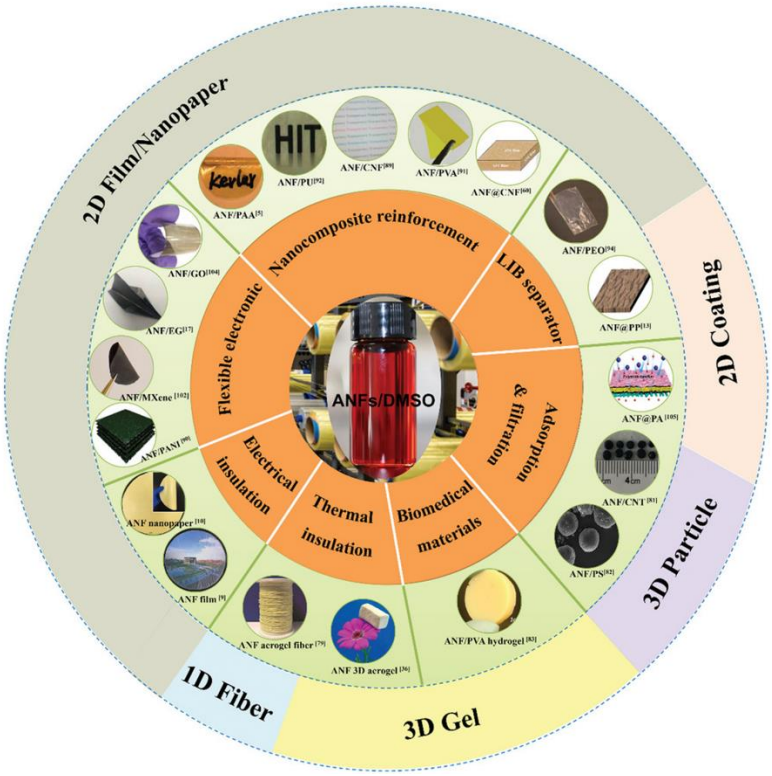

Figure 1.19. Macroscopic morphologies of advanced ANF-based materials and their potential application fields [278].

1.6.2. Zinc oxide (ZnO) nanowires (NWs)

ZnO is one of the first piezoelectric materials to be studied due to its attractive piezoelectric, semiconducting, and optical properties [288]. ZnO NWs are ceramic nanomaterials of wurtzite crystal structure and controllable morphology, often synthesized using CVD and hydrothermal reactions [289]. CVD is primarily used to synthesize ZnO NWs on non-organic substrates for a variety of applications such as energy harvesting [290], photocatalysis [291], field emission devices [292], UV detection [293], biosensing [294], and dye-sensitized solar cells [295]. However, given the high processing temperature inside a CVD chamber, organic fibers are severely damaged when adopting such a ZnO growth approach [296]. Yet using hydrothermal reactions, ZnO NWs can be grown on carbon, glass, and aramid fibers in aqueous solutions and at low temperatures, all while maintaining the original strength of the fibers [297]. Since Lin et al. demonstrated the first benign growth of ZnO NW arrays on carbon fiber surface in 2009 [180], ZnO nanowires have been integrated into fiber reinforced polymer composites to improve quasi-static and dynamic mechanical properties, or to introduce new functionalities such as energy

harvesting and damage detection. Nonetheless, the functionality of ZnO in composite materials is yet to be completely explored.

1.6.3. Laser induced graphene (LIG)

Carbon based nanomaterials, such as CNTs, GO, and carbon nanoparticles are heavily studied due to their exceptional mechanical, electrical, thermal, and chemical properties [298]. However, with the discovery of graphene during the mid-2000s, a one atomic layer thick material with unique properties, great research interest has been invested in understanding its behavior and improving the efficiency of its fabrication process [299]. Furthermore, the exceptional electrical properties of graphene are expected to revolutionize the electronic and energy storage industry, and its unmatched mechanical strength and surface area size promises an unprecedented structural performance. Nonetheless, the fabrication of graphene remains an extremely challenging process [300]. While high quality graphene can be produced using CVD-based processes, the extremely high production costs hinders its commercial use. In contrast, large volumes graphene flakes can be produced using chemical oxidation techniques, yet this comes at the expense of the severe deterioration of graphene properties [301]. Therefore, with high purity graphene monolayers remains being very costly [53,54], cheaper alternatives such as GO has been extensively studied and adopted in a variety of structural and non-structural applications [302].

In 2014, Lin et al. reported a process for the induction of 3D porous graphene, referred to as laser induced graphene (LIG), on commercial PI films under ambient conditions using a CO_2 infrared laser [303]. The laser irradiation of the polyimide substrate results in the photo-thermal conversion of sp^3 carbon atoms into sp^2 carbon atoms [303]. The results were further confirmed through high resolution transmission electron microscopy (TEM) images showing an abundance of pentagon-heptagon pairs, thus demonstrating the ultra-crystalline feature of the LIG. Additionally, X-ray photoelectron spectroscopy (XPS) of the LIG primarily showed a C1s peak, with greatly reduced C–N, C–O, and CO peaks which are typically found in polyimide. The morphology and microstructure of the LIG is controllable through the laser induction parameters such as speed, power, and pulsing density (Figure 1.20A) [304]. Due to its multifunctionality and ease of fabrication, LIG has been integrated into many novel technologies, including microfluidic devices, acoustic and strain sensors, soft electronics, micro-supercapacitors, surface wetting, joule heating, anti-biofouling, and memory devices (Figure 1.20B.) [305–307]. Recently, Chyan et al.

reported an expanded list of substrates on which the LIG could be directly generated which included a number of thermoplastics and thermosets, one of which is poly (paraphenylene terephthalamide), commercially known as Kevlar® [308]. While LIG has been primarily used to fabricate sensors and devices [305,306], its unique properties remain unexploited in the field of fiber reinforced composites.

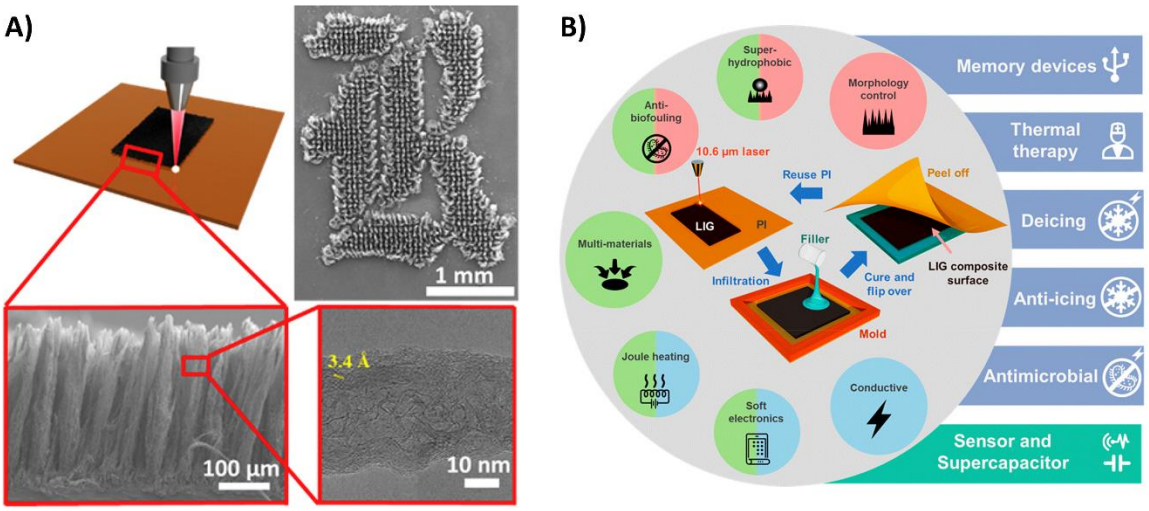

Figure 1.20. LIG on polyimide substrate. A) Control of LIG morphology through varying the pulsing density to generate more fiber-like microstructures. B) Schematic of the fabrication of LIG polymer composites. The resultant LIG composites possess multifunctional properties that are potentially useful in several applications [304,305].

1.7 Dissertation overview

In the following section, a detailed description of the research performed in each of the upcoming chapters is provided:

Chapter 2 investigates the effect and role of chemical interactions between the three discussed nanomaterials and fiber surfaces using a series of characterization techniques. The chapter begins with a brief overview of the various chemical bonds that can be achieved in a nanomaterial-fiber system. The role of amide-amide hydrogen bonding in achieving excellent chemical interaction between both ANFs and aramid nanofibrils, and the typically inert macroscale aramid fibers is investigated for the first time through chemical and mechanical characterization approaches. The results provide a quantitative explanation for the relatively easy formation of well-adhered ANF interphases on the surface of aramid fibers without the need for prior functionalization. Due to the

absence of such interactions in fiberglass, high charge density cationic polymer coatings, such as Polydiallyldimethylammonium chloride (PDDA), are demonstrated as a potential alternative for inducing the formation of well-adhered ANF interphases on fiberglass surfaces. In the case of ZnO NWs, it is shown that the quality and adhesion of the ZnO interphase on carbon fiber and fiberglass surfaces can be improved through surface oxidation techniques, such as nitric and piranha acid treatments, respectively. In addition, the chemical interaction between LIG and the aramid fabric on which it is induced is characterized, while also being shown to be easily transferable from polymer substrates to tacky carbon fiber prepreg surfaces. The findings in this chapter are instrumental in ensuring optimal chemical and mechanical interactions in every nanomaterial-fiber system considered in this work in order to maximize the performance of the resulting fiber reinforced composites.

Building on the findings of the previous chapter, Chapter 3 focuses on characterizing the performance of some of the discussed nanostructured interphases under quasi-static loading conditions. In this chapter, it is shown that ANF interphases are capable of reinforcing the fiber-matrix interface through a combination of chemical interaction and mechanical interlocking. The chapter begins by reviewing the single fiber testing methods used to measure the interfacial properties of fiber reinforced composites. Using single fiber pullout (SFP), the ANF coated aramid and fiberglass composites are found to exhibit a 70.27% and 83.2% increase in IFSS, respectively. Similarly, surface fibrilized aramid composites are observed to yield a 128% improvement in IFSS under quasi-static loading conditions. The chemistry, morphology, and roughness of the ANF coated and fibrilized fiber surfaces are investigated and studied in order to optimize treatment conditions. The treated surfaces display an increase in roughness and polar functional group content, both of which are desirable features when aiming to improve fiber-matrix interactions. In addition, the benign nature of these treatments is confirmed through single fiber tensile testing. The performance of these interphases in bulk composites is also studied using SBS testing. The findings of this chapter contribute to understanding the influence of nanostructured interphases on fiber-matrix adhesion, and present new approaches that are applicable to the large-scale manufacturing of improved composite materials for structural applications.

Given that ballistic applications require different interfacial conditions than structural applications, Chapter 4 focuses on characterizing the performance of another set of nanostructured interphases under dynamic loading conditions. The dynamic response of both aramid fabric and

ceramic fiber reinforced composites is studied post-interfacial modification. It is shown that aramid fabric fibrilization can be optimized to induce 550%, 12%, 230% improvements to the interyan friction, ballistic limit and stab resistance of the fabric, respectively, all while maintaining its tensile strength. The improved performance of the aramid fabric is found to be due to the enhanced interyarn friction and fiber-fiber interactions as a result of the generated fibrils. Additionally, carbon and fiberglass composites are investigated, and it is demonstrated that ZnO interphases can realize the desired multifunctional performance of a simultaneously optimal interfacial behavior under both quasi-static and dynamic loading conditions. Using a novel, in-house experimental setup, ZnO coated carbon fiber and fiberglass reinforced composites are found to display a maximum improvement in IFSS of 83% at quasi-static loading rates, and a maximum decrease in IFSS of 56% at high loading rates, all relative to untreated fibers. As shown through the inspection of the fractured fiber surfaces post-pullout, the ceramic nature of the ZnO nanowires causes them to be prone to brittle interfacial failure, thus allowing for easier release of the fibers from the matrix. The described behavior permits the tougher fibers to primarily absorb blast energy in the case of an impact. The findings of this chapter result in an improved ballistic performance of woven aramid fabrics and introduce the tailoring of interfacial properties in carbon fiber and fiberglass reinforced composites for an optimal response under both quasi-static and dynamic loading conditions, simultaneously.

Chapter 5 of this dissertation develops two different nanoscale interlayers for the toughening of aramid and carbon fiber reinforced composites and improving their interlaminar properties. The first interlayer is comprised of ANFs that are directly spray-coated onto the surface of carbon fabric. The ANF interlayered woven carbon fiber composites display a 34% and 82% increase in their SBS and initiation G_{IC}, respectively, all while maintaining their tensile strength. Additionally, the ANF interlayer is found to induce a more cohesive interlaminar failure within the carbon fiber composites. The second approach uses LIG interlayers to toughen aramid and carbon fiber reinforced composites. Two different methods are used to incorporate the LIG within the two sets of composites: the LIG is directly induced on the surface of the aramid fabric using a direct laser writing treatment, while, in contrast, the LIG is transfer printed onto carbon fiber prepregs prior to curing the composite. The interlayer morphology is optimized for both composite sets, and, as a result, the LIG coated aramid composites experience a 70% and 20% increase in SBS and initiation G_{IC}, respectively, while the carbon fiber based composites display a 41% and 69%

improvement in initiation G_{IC} and pre-cracked G_{IIC}, respectively. Furthermore, the thin LIG interlayers are successfully integrated within each composite set while maintaining the original elastic and viscoelastic properties of the composites. It can also be noted that the exceptional mechanical, thermal, and electrical properties of LIG allows it to potentially play a multifunctional role in both aramid and carbon fiber reinforced composites. The findings of this chapter present new solutions for the toughening of fiber reinforced composites using multifunctional and ultra-thin interlayers without sacrificing the in-plane properties.

The final chapter of this dissertation begins with a brief overview of the detailed findings and outcomes discussed throughout the dissertation. Following an overview, the contributions of this dissertation and their possible influence on future research investigating the development of hierarchical and multifunctional fiber reinforced polymer matrix composites with improved interfacial adhesion are discussed. Finally, the last section of this chapter discusses potential future work and how to expand on the obtained and reported findings.

CHAPTER 2. Study of Interphase-Fiber and Interlayer-Fabric Chemical Interactions

2.1. Chapter introduction

This chapter focuses on the chemical interactions at the level of the interphase-fiber interface to maximize the performance of these nanostructured interphases in fiber reinforced composites. The replacement of a traditional fiber-matrix interface with a functionally graded one results in the formation of two additional interfaces, the interphase-matrix and fiber-interphase interfaces. For the interphase to be effective, these two interfaces are required to be stronger than the original fiber-matrix interface. While the interphase-matrix interface benefits from a large degree of mechanical interlocking, the fiber-interphase interface is heavily reliant on chemical adhesion between the nanomaterial and fiber surface. Therefore, to assess and optimize the interactions between the various types of nanomaterials and fiber surfaces considered in this dissertation, a series of characterization techniques were used. The existing chemical interactions were studied and improved where possible to enhance the performance of these interphases and interlayers in fiber-reinforced composites.

In the first part of the chapter, the interactions between aramid nanofiber (ANF) interphases and aramid/glass fiber surfaces are studied and improved. The excellent compatibility between ANFs and macroscale aramids is demonstrated through a detailed study that highlights the potential of amide-amide hydrogen bonding between ANFs and polyamide 6 molecules. In the absence of such interactions in glass fibers, a cationic coating is proposed to electrostatically attract ANFs onto the glass surface. Moreover, the potential of an aramid fiber surface fibrilization technique is discussed as a method to generate a nanostructured interphase directly on aramid fiber surfaces. In the second part of the chapter, the importance of surface functionalization for adhesion between zinc oxide (ZnO) interphases and fiber surfaces is discussed, and surface oxidization treatments for both carbon and glass fibers are proposed and studied. Finally, the potential of introducing laser-induced graphene (LIG) interlayers onto the surfaces of aramid and carbon fibers is considered. The LIG is directly induced on the aramid fiber surface, causing it to be inherently bonded to the surface through mechanical and chemical interactions. As for carbon fiber prepreg

surfaces, the LIG interlayer is mechanically transferred to its surfaces and firmly stuck to its tacky surface, despite the absence of noticeable chemical interactions. The understanding of these nanomaterial-fiber interactions allows for the maximization of the performance of these interphases and interlayers in later chapters.

2.2. A review of the various types of chemical bonds

In a typical fiber-matrix interface, chemical adhesion is usually achieved through covalent bonds, hydrogen bonding, or van der Waals interactions [309]. When introducing an interphase, it is expected to potentially realize such chemical bonds with the matrix, in addition to an improved level of mechanical interlocking. However, the interphase is also required to exhibit a sufficient degree of chemical bonding to the fiber surfaces. These intermolecular bonds can be ionic bonds, hydrogen bonds, or Van der Waals interactions [310] (Figure 2.1.). Covalent bonds are typical intramolecular interactions formed through the sharing of electrons between two neighboring atoms and are considered to be the strongest form of chemical bonds [309]. The polarity of covalent bonds depends on the electronegativity of the atoms involved, as similar electronegativity results in non-polar bonds, while a difference in electronegativity yields polar ones. Ionic bonds are also a genre of strong chemical bonding that can be either intermolecular or intramolecular, and is achievable through the transfer of electrons between atoms [310]. However, in the case of fiber surfaces, especially inert ones such as aramids, these interactions necessitate chemical treatments and the introduction of additional functional groups to induce them [114]. Another form of interactions is hydrogen bonding, which is usually formed between hydrogen atoms attached to electronegative atoms and other atoms, most notably oxygen, nitrogen, and fluorine [311]. While hydrogen bonds are considerably weaker than covalent and ionic bonds, they can still be found in numerous organic and inorganic systems such as polymers [312], solvents [313], proteins [314], and deoxyribonucleic acid (DNA) [315]. On a molecular level, Van der Waals bonds are also possible through electrostatic interaction between two participating atoms or molecules [316] (Figure 2.2.). This establishes weak interactions between the opposite charges of two molecules in proximity of each other, aligning positive ends to negative ones. Such interactions are common in applications such as polymers, condensed matters, and structural biology [317]. For example, graphite is a well-known for being a crystalline material consisting of two-dimensional sheets stacked parallel to one another, and held together through Van der Waals forces [316]. Similarly,

amide-amide hydrogen-bonded aramid sheets are stacked radially using Van der Waals forces around the axis of the fiber [185]. Therefore, given their relative simplicity, hydrogen bonding and Van der Waals interactions are viable forms of intermolecular bonds that can be potentially exploited when trying to improve fiber-interphase adhesion.

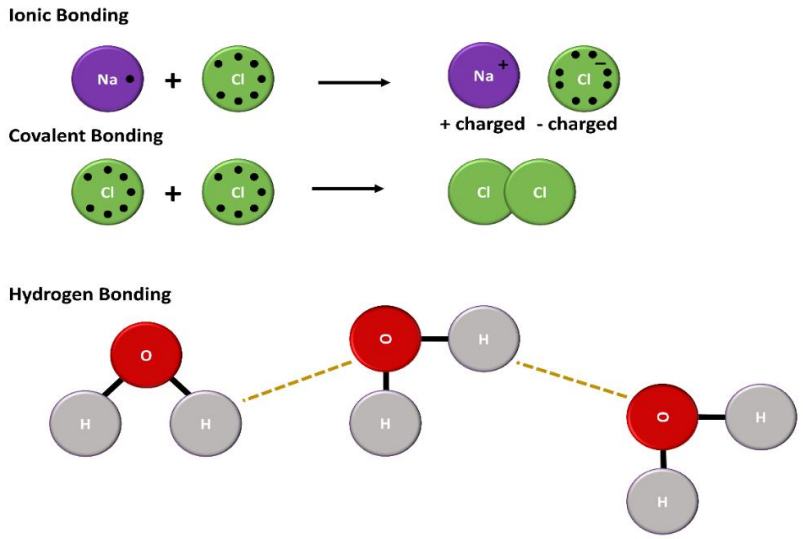

Figure 2.1. Examples of chemical bonds.

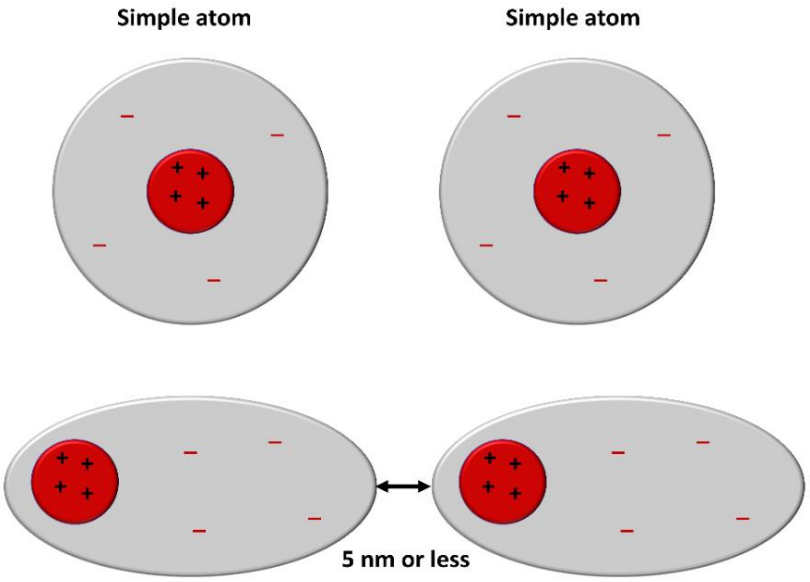

Figure 2.2. Van der Waals interactions.

The weak intermolecular interactions detailed above have been shown to be a promising

approach to self-assemble nanoscale polymer monolayers on fiber surfaces. Such self-assembly can be induced through electrostatic interactions, hydrogen bonding, Van der Waals forces, and π-π stacking [318]. With the growing interest in interphase design, the development of methods and approach to assemble nanomaterials on fiber surfaces with sufficiently strong adhesion is necessary. In the following section, the chemical interactions between ANFs and fiber surfaces of similar composition, such as macroscale aramid, or a different one, such as glass, will be studied and assessed.

2.3. Assembly of ANFs on aramid and glass fiber surfaces

2.3.1. ANF synthesis and properties

The overall excellent performance of aramid fibers can be partially attributed to the strong molecular interactions between its crystalline sheets [185]. However, while the chemical and thermal resistance of aramid fibers is highly advantageous in certain applications, it also hinders their solution processability or melting when aiming to scale them down to a nanofiber size [278]. With the goal of preparing aramid nanomaterials, two main strategies emerged: a bottom-up approach that relies on polymerization-induced self-assembly techniques [319], and a top-down approach that includes electrospinning [320], mechanical disintegration [321], and deprotonation [108]. Bottom-up approaches are found to be unable to produce aramid nanofiber diameters of less than 50 nm [319]. Similarly, electrospinning is limited to a nanofiber diameter of 500 nm, while also presenting equipment corrosion problems due to the use of sulfuric acid as a solvent [320]. Although mechanical disintegration can yield nanofibers with diameters as small as 10 nm, it is still an energy-intensive method with low yield, and a damaging one to the fiber's mechanical properties [321]. In 2011, Yang et al. revisited an old p-phenylene terephthalamides (PPTA) deprotonation approach and was able to form a stable suspension of ANFs with diameters ranging between 3-30 nm and a length of up to 10 μm [108]. Macroscale aramid fibers are stirred in a potassium hydroxide (KOH)/dimethyl sulfoxide (DMSO) solution for 7 days to realize a uniform dispersion of ANFs. The basic solution induces the deprotonation of the macroscale aramid fibers through abstracting the hydrogen bond from the amide group and generating negatively charged polyanions (Figure 2.3.). The growing electrostatic repulsion with continued deprotonation splits macroscopic PPTA into microfibrils and continues to do such until reaching the targeted nanofiber size. The resulting ANFs are well-dispersed within the solution due to a balance between

electrostatic repulsion, Van der Waals forces, and π-π stacking.

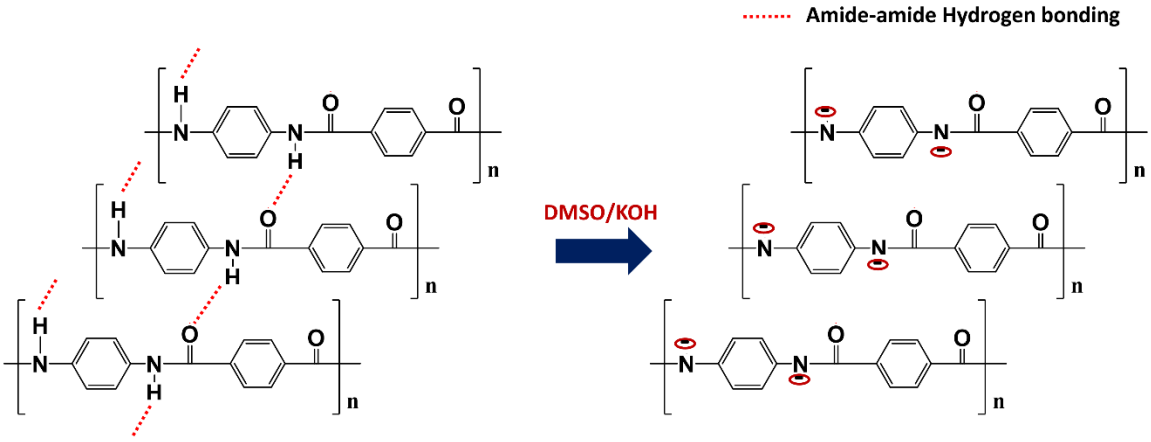

Figure 2.3. Deprotonation of macroscale PPTA fiber in DMSO/KOH solution.

The ANFs obtained using such a process are of a high aspect ratio (Figure 2.4 A & B) and are expected to maintain a similar chemical structure and mechanical strength to that of their macroscopic counterparts. From Figure 2.4C & D, it can be seen that the high thermal stability of ANFs is preserved, as thermal decomposition does not start until 536 °C, and no melting point is detected up to 300 °C, making it ideal for use in the fabrication of both thermoset and thermoplastic matrix composites. In addition, when comparing their FTIR spectrum to that of macroscale aramid fibers, it can be clearly seen that the ANFs maintain their chemical structure after deprotonation (Figure 2.4E). The ANFs can be either kept dispersed in the DMSO solution, washed, re-protonated and re-dispersed in a different solvent, such as acetone, or completely isolated in powder form (Figure 2.4F). The ability of ANFs to establish hydrogen bonds has been reasoned to be behind its excellent performance as a nanofiller in various ANF reinforced polymer nanocomposites [110,287,322–324]. Specifically, the inherent ability of ANFs to establish amide-amide hydrogen bonds allows them to assemble and create ANF films like buckypapers using methods such as layer-by-layer assembly and vacuum filtration. In the following section, these amide-amide interactions will be studied and compared to conventional hydrogen bonding through chemical and mechanical characterization techniques. The results will allow for a greater understanding of the potential of assembling ANF interphases on aramid fiber surfaces. Furthermore, approaches for the assembly of ANFs onto glass and carbon fiber surfaces will be presented, while an aramid fiber fibrilization process will also be discussed.

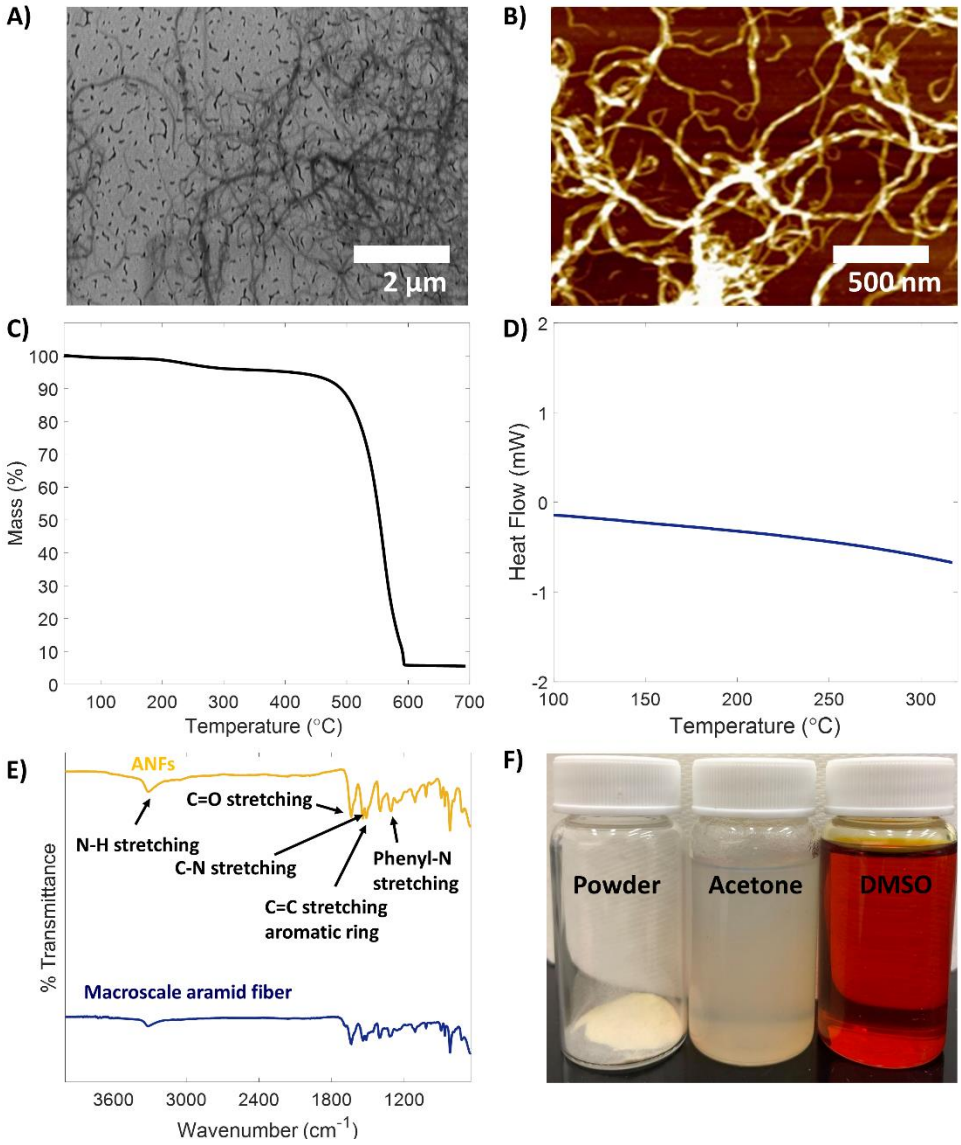

Figure 2.4. ANF characterization. A) SEM image of ANFs spin-coated on a silicon wafer. B) Atomic force microscopy (AFM) images of ANFs. C) Thermogravimetric analysis (TGA) curve of ANFs. D) Dynamic scanning calorimetry (DSC) curve of ANFs. E) FTIR spectra of ANFs and macroscale aramid fibers. F) Solution dispersed and isolated ANFs.

2.3.2. Study of amide-amide hydrogen bonding interactions

As previously mentioned, amide-amide interactions in ANFs have been restricted to the self-assembly of films and buckypapers and remain unexploited with regards to ANFs acting as nanofillers or interphases. In this section, the role of amide-amide hydrogen bonding in ANF-reinforced PA6, polyamide-imide (PAI), and PI nanocomposites is investigated using a series of chemical characterization and mechanical testing techniques. By comparing the performance of

ANFs in these polymers, a greater understanding of the effect of amide-amide hydrogen bonding on interfacial properties and the load transfer mechanism between ANFs and amide-based polymers can be obtained. The performance of ANFs in polyamide 6 (PA6), where amide-amide interaction opportunities are available, is compared to its performance in polyimide (PI), where such interactions are absent. The importance of amide-amide interactions for an improved ANF performance are further confirmed through investigating its performance in polyamide-imide (PAI), which contains both an amide and imide backbone (Figure 2.5). While ANFs are able of establishing amide-amide hydrogen bonding with polymers containing imide backbones, its effect on the mechanical and chemical performances of these polymers, relative to amide-amide interactions, will be demonstrated to be considerably inferior.

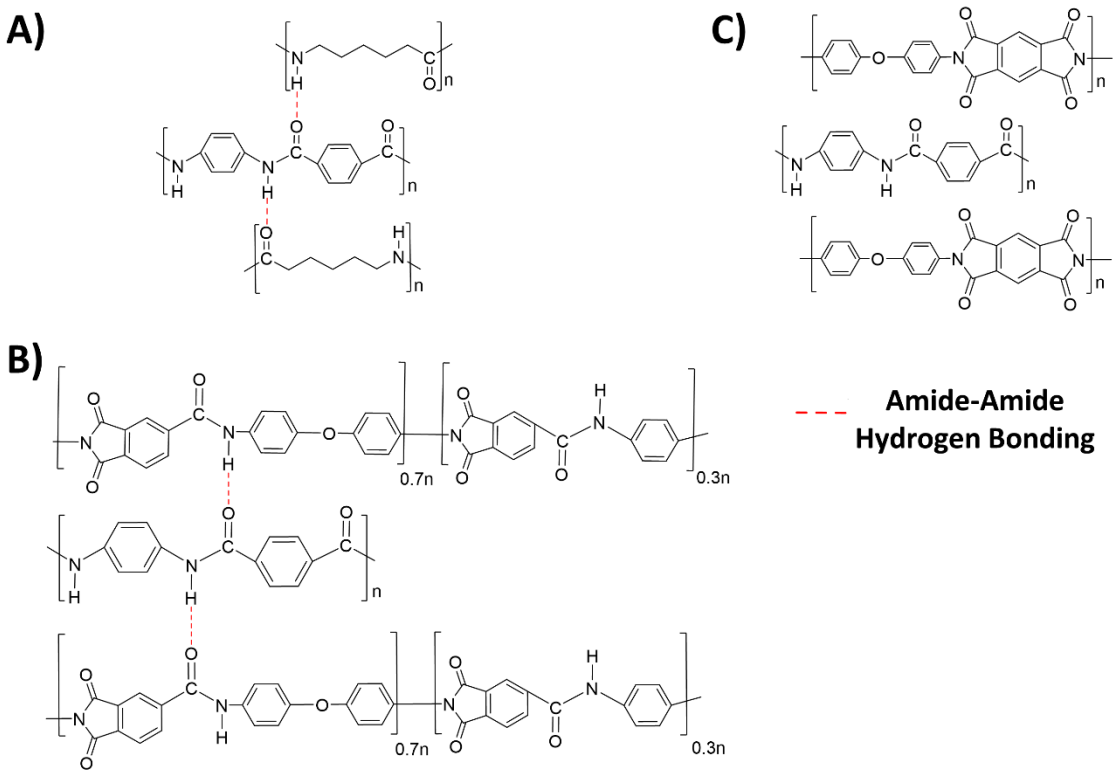

Figure 2.5. Amide-amide interactions. A) Amide-amide (C=O ··· NH) hydrogen bonding between PA6 and ANFs. B) Amide-amide (C=O ··· NH) hydrogen bonding between PAI and ANFs. C) Absence of amide-amide hydrogen bonding between PI and ANFs.

Here, ANF reinforced nanocomposites are prepared using a solution casting method, where ANFs are dispersed in polymer solutions at various weight fractions, cast onto glass plates, and dried appropriately in a convection oven. In the case of polyimide nanocomposites, a multiple step-

wise heat imidization process is used, where ANFs are originally dispersed in polyamic acid, prior to heat treatment [325]. The extent of amide-amide hydrogen bonding between the ANFs and the polymer matrices is first investigated and confirmed using FTIR. Generally, such a characterization approach has been shown to be highly sensitive to the strength and extent of intermolecular hydrogen bonding, as it manifests in shifts to the wavenumbers of characteristic absorption under FTIR [326–328]. Due to the commonality of their polymer backbone structure, the FTIR spectra of PA6 and ANFs share many identical absorption peaks (Figure 2.6A). The primary difference between both compounds is ANFs possessing aromatic repeating units, while PA6 having aliphatic ones (Figure 2.5A). Both spectra display peaks corresponding to N-H stretching vibrations (3290 cm^{-1}), amide I C=O stretching vibrations (1649 cm^{-1}), and mixed vibrations of amide II N-H bending and C-N stretching (1546 cm^{-1}), while that of C=C stretching vibration of aromatic (1516 cm^{-1}) ring is unique to ANFs. As seen in Figure 2.6B, the FTIR spectrum of the ANF reinforced PA6 nanocomposites is largely similar to that of neat PA6 due to the minuscule amount (< 3 wt%) of ANFs used to reinforce the polymer films. Nonetheless, the introduced ANFs result in a considerable blue shift to the wavenumber position corresponding to the N-H stretching mode, indicating the existence of amide-amide hydrogen bonding between ANFs and PA6 (Figure 2.6C). When ANF concentration in the PA6 nanocomposites is increased from 0 to 2.5 wt%, a maximum shift of 4.635 cm^{-1} in the N-H band position is observed (Table 2.1.). Despite the following changes being small in magnitude, the observed blue shift is a clear indicator of intermolecular hydrogen bonding between ANFs and PA6. Given that the blue shift occurs in the range of 3250 cm^{-1} to 3370 cm^{-1}, these intermolecular interactions are possibly the result of hydrogen-bonded amide-amide functional groups (Figure 2.5A) [326]. This mimics the strong intermolecular hydrogen bonding of adjacent polymer chains in PPTA, a primary factor in the excellent mechanical properties of aramid (Kevlar®) fibers [114]. Therefore, the detected amide-amide molecular interactions between the nanofiller and the polymer matrix are achieved without the need for prior functionalization or processing and can potentially help improve the interfacial properties within these nanocomposites. Similar to PA6, PAI possesses the ability to establish amide-amide hydrogen bonding with the ANFs nanofillers. The imide chain of the PAI chemical structure is represented through symmetrical (1706 cm^{-1}) and asymmetrical (1780 cm^{-1}) C=O peaks, along with the C-O-C bond peak (1084 cm^{-1}) under FTIR (Figure 2.6D). Concurrently, polyamide corresponding peaks such as N-H stretching (3306 cm^{-1}) and amide C=O stretching

(1650 cm^{-1}) are also easily detectable in the FTIR spectrum of PAI. In comparison to PA6, the N-H stretching band is of considerably weaker intensity. Yet when examining the FTIR spectra of ANF reinforced PAI nanocomposites, a blue shift to the N-H stretching band can also be observed (Figure 2.6E & F). When the ANF concentration in the nanocomposites is increased from 0 to 2.5 wt%, a maximum increase of 1.57 cm^{-1} in the N-H band position is found (Table 2.1.). This indicates the presence of intermolecular amide–amide hydrogen bonding between ANFs and the PAI matrix (Figure 2.5B). Therefore, the ANF reinforced PAI nanocomposites are expected to benefit from these chemical interactions in the form of improved interfacial properties and stress transfer between the nanofiller and the matrix. In the case of PI nanocomposites, the opportunity for amide-amide hydrogen bonding between the ANFs and the matrix does not exist. Polyimide, here specifically poly 4-4'oxydipgenylene Pyromellitimide (PMDA-ODA), is a linear polymer comprised of heterocyclic rings that are linked together through one or multiple covalent bonds [105]. In comparison to ANFs, the FTIR spectra of polyimide contain many unique characteristic peaks, such as C=O bending (717 cm^{-1}), C-O-C stretching (1086 cm^{-1}), C=O symmetrical stretching (1702 cm^{-1}), and C=O asymmetrical stretching (1783 cm^{-1}) (Figure 2.6G). Furthermore, when inspecting 3200 cm^{-1} - 3400 cm^{-1} range of the nanocomposites FTIR spectra, it is found to be negligibly affected by the addition of ANFs to the PI polymer. Such an observation is indicative of the absence of any amide-amide hydrogen bonding between the nanofiller and the imide-based matrix. Given that amide groups are not found in polyimide, the absence of such chemical interactions is expected (Figure 2.5C). It should be noted that amide-imide hydrogen bonding remains possible through the C=O of the PI and the N-H of the ANFs, yet negligible shift is detected to the C=O band position under the FTIR (Table 2.1.). Therefore, given the lack of amide-amide hydrogen bonding in these nanocomposites, the influence of these bonds on the mechanical performance of nanocomposites can be properly isolated, assessed, and then compared to that of the previously discussed ANF reinforced PA6 and PAI nanocomposites.

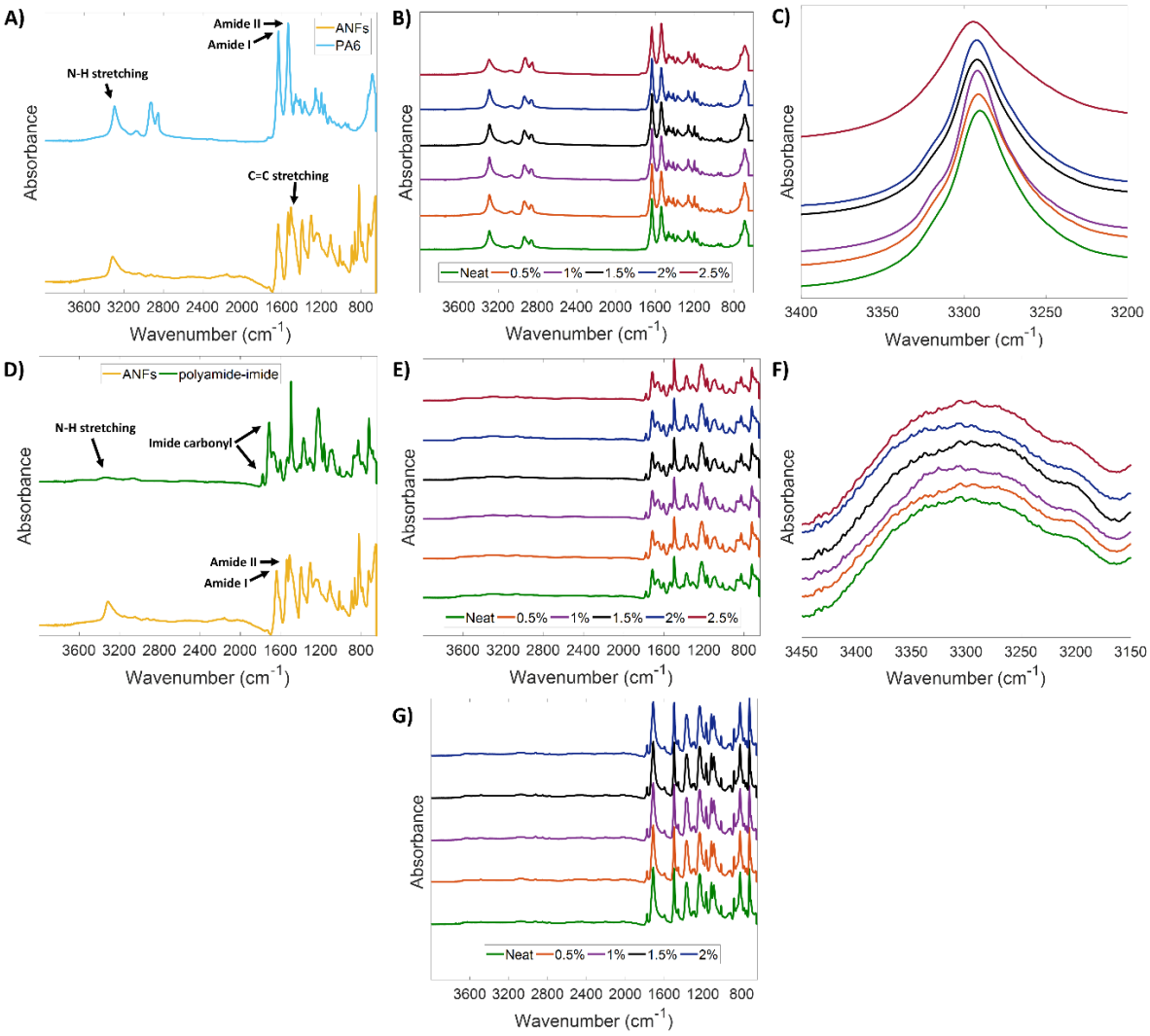

Figure 2.6. FTIR analysis of amide-amide hydrogen in ANF reinforced polymer nanocomposites. The FTIR spectra of: A) isolated ANFs and PA6. B) Neat and ANF reinforced PA6 nanocomposites. C) Neat and ANF reinforced PA6 nanocomposites in the range of 3200-3400 cm^{-1}. D) PAI and isolated ANFs. E) Neat and ANF reinforced PAI nanocomposites. F) Neat and ANF reinforced PAI nanocomposites in the range of 3150-3450 cm^{-1}. G) ANF reinforced PI nanocomposites.

Table 2.1. FTIR observed maxima of N-H stretching vibration and C=O symmetrical bands in neat and ANF reinforced PA6, PAI and PI nanocomposites, respectively.

ANFs concentration (wt%)	PA6 N-H Stretching Wavenumber (cm^{-1})	PAI N-H Stretching Wavenumber (cm^{-1})	PI C=O symmetrical Wavenumber (cm^{-1})
Neat	3290.06	3305.05	1706.3
0.5	3291.4	3305.5	1706.3
1	3291.9	3305.7	1706.5
1.5	3292.1	3305.9	1706.4
2	3292.3	3306.4	1706.5
2.5	3294.7	3306.5	1707.3

Furthermore, the thermal stability of the ANF reinforced nanocomposites is investigated using TGA (Figure. 2.7.). The decomposition temperature of the PA6 matrix (440 °C) is found to be slightly improved by a maximum of 4.3 °C when adding 2.5 wt% ANFs. The thermal stability of PAI (575 °C) is also increased by a maximum of 14.6 °C due to the addition of 2.5 wt% ANFs. The observed trend in Figure 2.7. is expected due to the high thermal stability of both polymeric polyamide-based nanofillers and matrices. Nonetheless, the high thermal stability of PI nanocomposites is found to be minimally affected by the introduction of ANFs, as no noticeable increase in decomposition temperature is observed (Figure 2.7C). Therefore, given the high thermal stability of ANFs (Figure 2.4.), the nanocomposites are expected to maintain their original thermal stability or exhibit improved ones due to chemical compatibility between the nanofibers and the matrix.

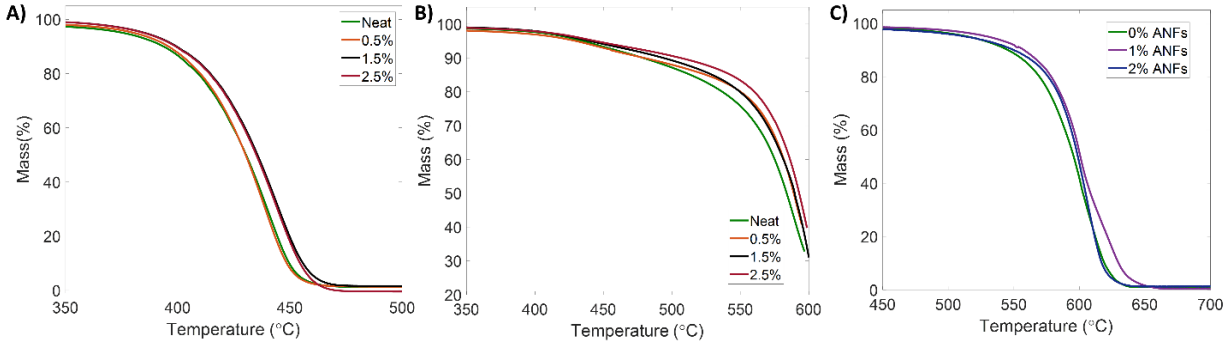

Figure 2.7. Thermal stability of ANF reinforced nanocomposites. The TGA curves of A) PA6. B) PAI. C) PI.

The effect of ANFs on the mechanical properties of the polymer nanocomposites is investigated through tensile testing according to ASTM D638 [329]. The amide-amide interactions are expected to enhance the ANF nanofiller performance. As shown in Figure 2.8A & B, both the tensile strength and elastic modulus of PA6 display an initial increase when introducing a low weight fraction of ANFs, and continue to exhibit improvements with increasing nanofiller concentration, before reaching saturation. In comparison to neat PA6 (72.4 MPa), a maximum increase in the tensile strength of ANF reinforced PA6 nanocomposites of 117.34 MPa is measured at a 1.75 wt% nanofiller concentration, yielding an improvement of 62.07% (Figure 2.8A). Similarly, the elastic modulus of PA6 nanocomposites is also found to increase to a maximum of 4.79 GPa at an ANF concentration of 1.5 wt%, a 27.05% increase relative to that of the neat PA6 (3.77 MPa). These results highlight the capacity of the nanoscale reinforcement to improve the mechanical strength and stiffness of PA6 considerably. The inherent chemical interactions between ANFs and PA6 through amide-amide hydrogen bonding help reduce stress concentrations and enhance load transfer between the nanofiller and the matrix, resulting in an overall improvement to the mechanical performance of the nanocomposites. The enhanced interfacial properties provide more effective loading energy dissipation mechanisms within these nanocomposites that prevent crack growth and delay tensile failure. While the tensile strength and elastic modulus are decreased for ANF weight fractions greater than 1.75 wt%, both the strength and stiffness of the PA6 nanocomposites remain higher than that of neat PA6. Therefore, ANFs can strengthen the elastic properties of PA6 as a result of the high chemical compatibility between the nanofiller and the matrix, courtesy of amide-amide hydrogen bonding.

ANF reinforced PAI nanocomposites also exhibit improved mechanical properties at low ANFs weight fractions. In comparison to neat PAI (152 MPa), a maximum increase in the tensile strength of ANF reinforced PAI nanocomposites of 193 MPa is observed using a 1 wt% nanofiller concentration, leading to an improvement of 25.4% (Figure 2.8C). Similarly, the elastic modulus of PA6 nanocomposites is also found to increase to a maximum of 5.96 GPa at an ANF concentration of 1.5 wt%, a 40.56% increase relative to that of the neat PAI (4.24 MPa) (Figure 2.8D). With amide-amide hydrogen bonding being accessible to the dispersed ANFs and the PAI matrix, the nanocomposites are presented with good interfacial properties that maximize the capacity of nanofillers to strengthen and the reinforce the polymer matrix. The improved mechanical response highlights the efficient load transfer mechanism between the ANFs and PAI,

along with the reduction in interfacial stress concentrations through a combination of increased surface area and amide-amide hydrogen bonding. Similar to PA6, when the weight fraction of ANFs is increased from 1.5 wt% up to 2.5 wt%, both the tensile strength and elastic modulus of the nanocomposite are decreased by a maximum of 20% and 45%, respectively. Nonetheless, the mechanical properties of the 2.5 wt% reinforced nanocomposites remain considerably improved relative to that neat PAI. Thus, ANF reinforced PAI nanocomposites exhibit a simultaneously stronger tensile response, highlighting the advantages of ANFs as nanofillers in matrices of polymer backbones of similar chemical structures.

Elsewhere, the addition of ANFs into a PI matrix yields minimal improvements to the elastic properties of the nanocomposites. As seen in Figure 2.8E & F, the tensile strength and elastic stiffness of the ANF reinforced PI nanocomposites are observed to only increase by a maximum of 3% and 7%, respectively, relative to neat PI. Despite their good dispersion, ANFs are incapable of providing substantial improvement to the mechanical properties of the PI nanocomposites. Given the absence of an amide structure in PI, the ANFs are unable to establish amide-amide hydrogen bonds with the PI matrix and are restricted to amide-amide hydrogen bonds. This reduces the strength of interfacial properties within the PI nanocomposites and limits the efficiency of load transfer between the ANF and surrounding matrix material, in comparison to PA6 and PAI. While hydrogen bonding remains possible between PI and ANFs, the absence of amide-amide interactions limits the contributing factors to the improvement of strength and stiffness in these nanocomposites to mainly mechanical effects, such as an increase in surface area. It should be noted that the strain-to-failure of all three polymer nanocomposites is maintained, indicating the ability of ANFs in preserving these polymers' ductility.

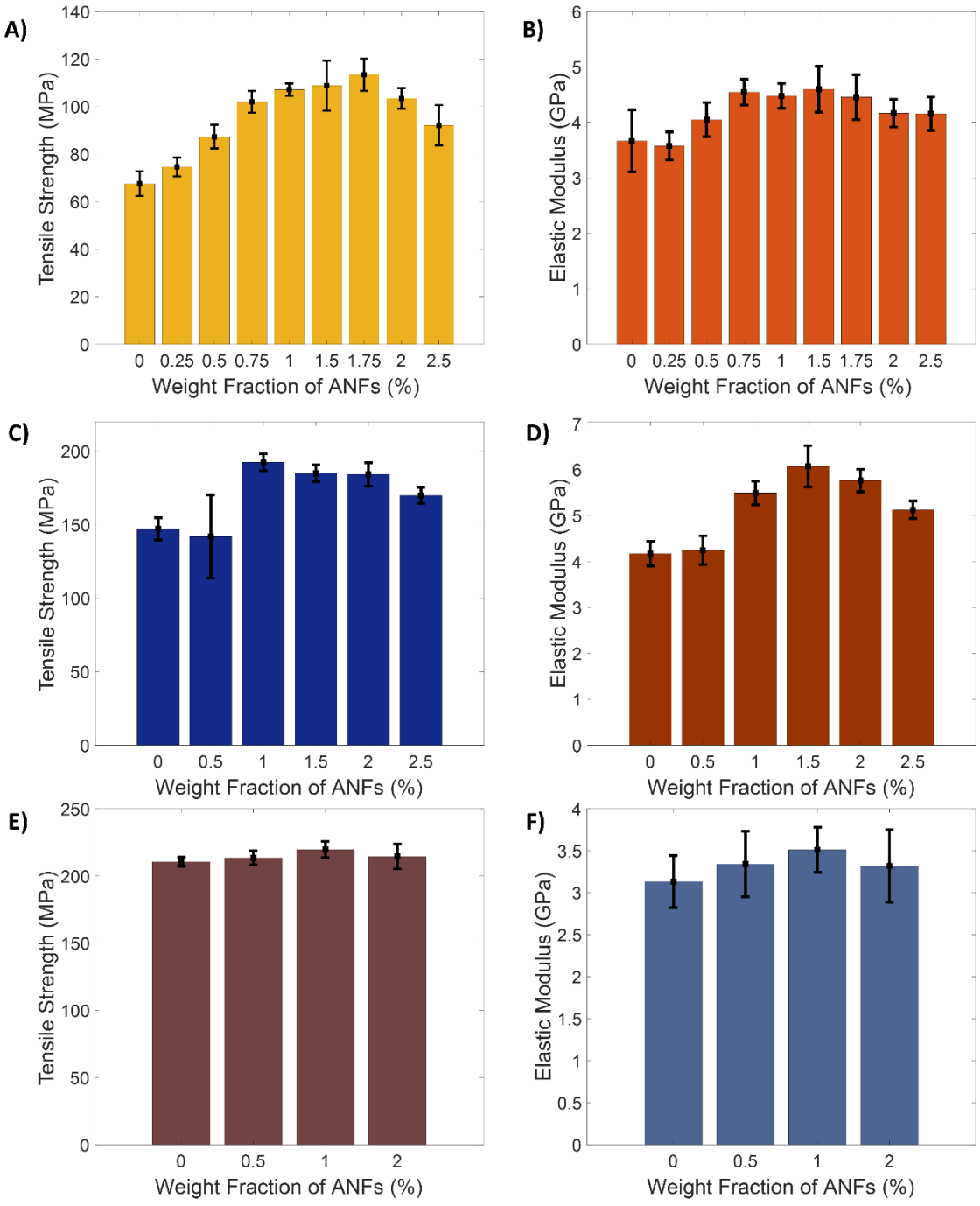

Figure 2.8. Mechanical properties of ANF reinforced polymer nanocomposites. A) Tensile strength of PA6. B) Elastic modulus of PA6. C) Tensile strength of PAI. D) Elastic modulus of PAI. E) Tensile strength of PI. F) Elastic modulus of PI.

The observed correlation between the reinforcing performance of ANFs and amide-amide

hydrogen bonding opportunities highlights the significant role of these interactions to the overall properties of the nanocomposites, and its superior performance relative to general forms of hydrogen bonding, such as amide-imide in this case [185]. The effect of such interactions on the mechanical performance of ANF reinforced PA6, PAI, and PI polymer nanocomposites can be clearly seen in Figure 2.9. The innate ability to form such bonds between ANFs and amide-based polymers provides a significant improvement to the mechanical performance of the resulting amide-based nanocomposites. While other nanomaterials such as carbon nanotubes (CNTs) and graphene require surface functionalization to significantly improve both the strength and toughness of similar nanocomposites [44], ANFs are inherently capable of establishing strong chemical interaction with PA6 and PAI, through amide-amide hydrogen bonding. Another polymer of a similar amide-based structure is aramid fibers, as PPTA is comprised of a polyamide backbone [185]. Due to their near-exact chemical structure, the results presented here indicate the potential of strong ANF-aramid fiber interaction through amide-amide hydrogen bonding, allowing for the formation of a high-performance, well-adhered ANF interphase along the aramid fiber surfaces. The details of realizing such interphase and its performance in aramid fiber-reinforced composites will be further explained in the next chapter.

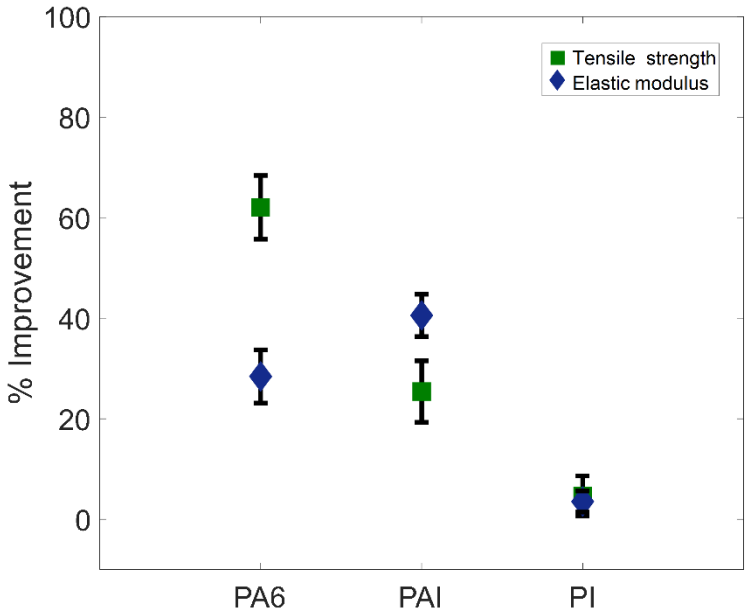

Figure 2.9. Maximum improvement to the tensile strength and elastic modulus of ANF reinforced nanocomposites relative to neat ones.

2.3.3. Potential of ANF-PDDA electrostatic interactions

The previously discussed amide-amide interactions can be exploited to form well-adhered interphases on the surfaces of aramid fibers. However, such chemical bonding opportunities are not available in the case of other fibers such as carbon and glass. Previous work relied on energy-intensive approaches, such as electrophoretic deposition in order to adhere ANFs to conductive carbon fiber surfaces [134]. Yet a similar approach cannot be applied to electrically insulating fibers, such as E-glass. Past studies have relied on a surface functionalization that coats the fibers with a positively charged graphene oxide layer in order to attract negatively charged ANFs dispersed in a suspension [135]. However, the resulting ANF coatings are of high smoothness and contribute minimal improvements to the interfacial properties of glass fiber composites, relative to just a graphene oxide coating. Another cationic coating that has been previously used to attract and assemble ANFs is polydiallyldimethylammonium chloride (PDDA), as it served as an initial layer during a layer-by-layer assembly approach for forming ANF films on glass slides [108]. Typically, the high charge density cationic polymer is applied to a surface using a simple and fast dip-coating process that forms a nanoscale coating in order to initiate flocculation or nanomaterial self-assembly [330]. Similarly, here, a PDDA coating can be applied to the surface of glass fibers in order to electrostatically attract negatively charged ANFs present in the solution and form a well-adhered nanostructured interphase (Figure 2.11). In addition, an ANF interlayer can be deposited onto carbon fiber surfaces using a simple spray-coating process that avoids any agglomeration problem through resin mixing. These ANF interphases and interlayer are expected to exhibit a sufficient degree of adhesion to the fiber and fabric surface, which will potentially allow them to significantly improve the interfacial and interlaminar properties of fiber reinforced composites. The performance of these interphases and interlayers will be studied and investigated in later chapters.

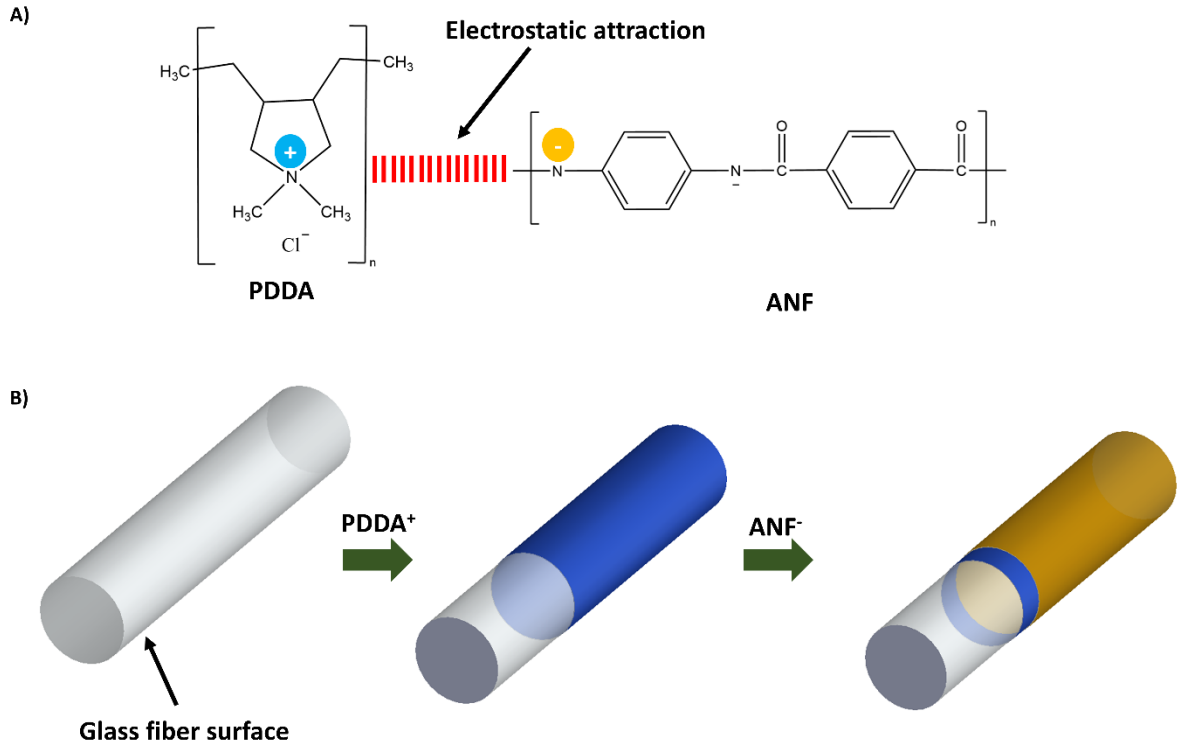

Figure 2.10. PDDA/ANF coating. A) Electrostatic attraction between cationic PDDA and anionic ANFs. B) Schematic of glass fiber surface sizing using a PDDA/ANF coating.

2.3.4. Fibrilization of aramid fibers

The fibrilization of aramid fibers has always been a topic of interest for the generation of aramid micro- or nanofibers. PPTA fibers possess strong covalent bonds along the axial direction and weak intermolecular ones along the radial direction, allowing for easy exfoliation along the fiber axis under mechanical or chemical stimulus [278]. Earlier techniques used either Hollander beaters or pulp refiners to mechanically disintegrate the fibers and split them into microfibrils of considerably smaller diameters [287,331]. Later, hydrolysis treatments coupled with multiple cycles of high-pressure water jet atomization were used to disintegrate aramid fabric into nanofibers [321]. Yet all these techniques are primarily concerned with transitioning the macroscale aramid fibers to a nanoscale level. Moreover, these energy-intensive techniques are extremely damaging to the performance of the macroscale aramid fibers and the resulting aramid fibrils, pulp, or nanofibers, leading to the degradation of the mechanical properties of aramid products.

In this work, the dissolution and deprotonation process developed by Yang et al. [108] will

be used to generate nanofibrils along the macroscale aramid fiber surfaces, while maintaining their mechanical properties. Typically, the deprotonation process splits the PPTA fiber into microfibrils over a lengthy period of 7 days, until ANFs are obtained. By considerably reducing the treatment period and avoiding vigorous mechanical stirring, aramid fibers surfaces can be fibrilized while potentially avoiding the deterioration of their mechanical properties. The DMSO/KOH solution is stirred for 30 mins prior to the introduction of the aramid fabric, which is soaked in the solution for periods ranging between 1 and 10 hours (Figure 2.11.). While certain fibrils are to separate from the macroscale aramid fibers, a large amount of them can be expected to remain attached to the aramid fabric through their inherent amide-amide hydrogen bonds. These intermolecular interactions can guarantee sufficient adhesion between the nanofibrils and the macroscale aramid fiber surfaces. Furthermore, the fibrilization period can be optimized to generate a considerable fibrils density while maintaining fiber tensile properties. The performance of such a fibrilized interphase will be assessed in later chapters, both in structural composite materials and soft body armor ballistic protection. In the following section, the adhesion between a different set of nanomaterials, ZnO nanowires, and the surfaces of carbon and glass fibers will be discussed.

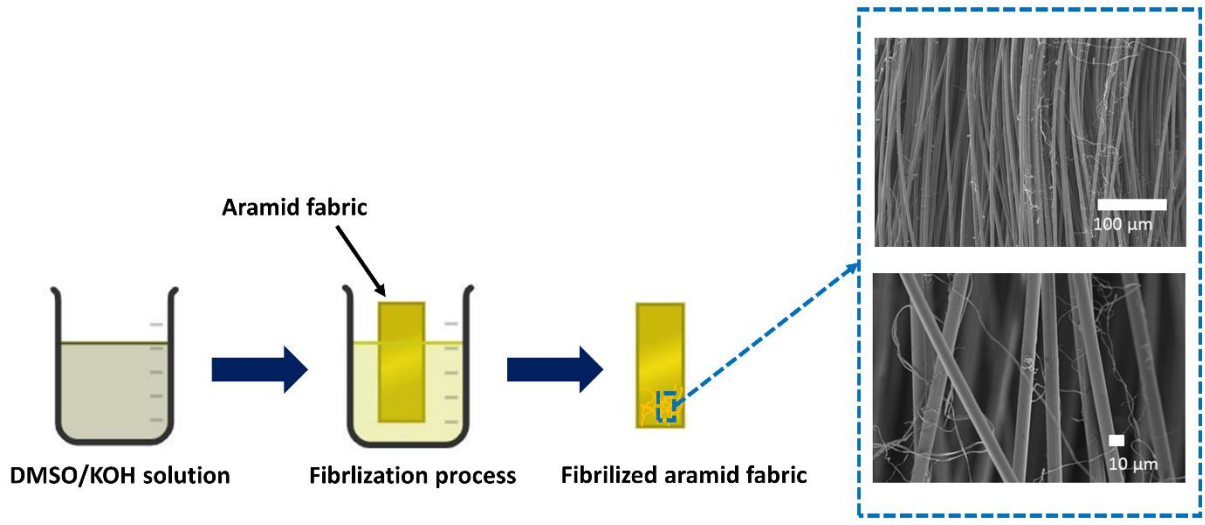

Figure 2.11. Aramid fabric fibrilization process.

2.4. ZnO NWs on carbon and glass surfaces

Whiskerization has been a popular approach for interphase design in fiber-reinforced composites, as long aspect ratio nanomaterials can provide a great opportunity for mechanical interlocking between the fiber and the matrix. ZnO nanowire is a commonly used whiskerization

material that has been demonstrated to improve interfacial properties of fiber reinforced composites. In the following section, the chemical adhesion between these ZnO fibers and fiber surfaces will be discussed and improved.

2.4.1. ZnO nanomaterial growth and structure

Given the sensitivity of fibers to the high-temperature conditions necessary to grow ZnO using chemical vapor deposition (CVD), hydrothermal reactions have been determined to be a more suitable approach for fiber surface whiskerization due to their mild reaction conditions [180,332]. Initially, the fiber surfaces are coated with a polycrystalline ZnO nanoparticles seed layer, before introducing them in a growth solution that contains ZnO salts and bases. Once heated, heterogeneous nucleation induces the growth of nanowires on the facets of the pre-deposited ZnO seeds. When using Hexamethylenetetramine (HMTA) as a weak base, the hydrothermal reaction undergoes the following steps as per Wang et al. [332]:

$$(CH_2)_6N_4 + 6H_2O \leftrightarrow 4NH_3 + 6HCHO \quad (2.1.)$$

$$NH_3 + H_2O \leftrightarrow NH_3 \cdot H_2O \quad (2.2.)$$

$$NH_3 \cdot H_2O \leftrightarrow NH_4^+ + OH^- \quad (2.3.)$$

$$Zn^{2+} + 2OH^- \leftrightarrow Zn(OH)_2 \quad (2.4.)$$

$$Zn(OH)_2 \overset{\Delta}{\leftrightarrow} ZnO + H_2O \quad (2.5.)$$

Similar to other hydrothermal reactions in aqueous solutions, the growth of the ZnO nanostructure is driven by the minimization of the Gibbs free energy, where the balance between surface energy and phase transformation energy dictates the final nanowire size (Figure 2.12A) [333,334]. As previously reported in the literature, a homogenously precipitated ZnO interphase possesses an inferior performance in fiber reinforced composites [335]. Therefore, it is necessary to force heterogeneous nucleation in order to allow the ZnO crystals to grow solely from the exposed seed layer. This can be ensured through the addition of buffers or inhibitors, such as ammonium hydroxide and polyethylenimine (PEI), in the growth solution [182]. Typically, hydrothermally grown ZnO nanowires possess a wurtzite structure consisting of alternative packing of Zn^{2+} and O^{2-} [297,332]. This results in negatively charged crystal top (0001), and positively charged crystal bottom surfaces (Figure 2.12B). Therefore, ZnO nanowires grow along the non-polar faces of {0110} and {2110}, with their morphology largely being largely dependent on the growth process

[336]. Usually, the morphology of ZnO nanowires can be tailored by controlling the concentration of PEI in the growth solution, as it adsorbs these non-polar surfaces, thus decreasing nanowire diameter and increasing its aspect ratio. This approach has been previously demonstrated to generate ZnO interphases of various morphologies on carbon fiber surfaces [182]. Similar growth conditions will be used in this work, as further detailed in chapter 4. Efforts to characterize the mechanical properties of free-standing ZnO nanowires have shown that it possess a brittle response to tensile loading, which is expected in the case of such ceramic nanomaterials [337–339]. The measured tensile strengths were found to be within a 3-10 GPa range, while modulus measurements were found to vary widely, depending on the testing technique [340,341]. Moreover, the elastic properties of these nanowires were found to be dependent on their length, diameter and growth process. Nonetheless, all reported experiments indicate that these nanowires tend to fail in a brittle manner, and at fracture strains less than 7.5%. In the following section, the adhesion between ZnO nanowires and fiber surfaces will be discussed.

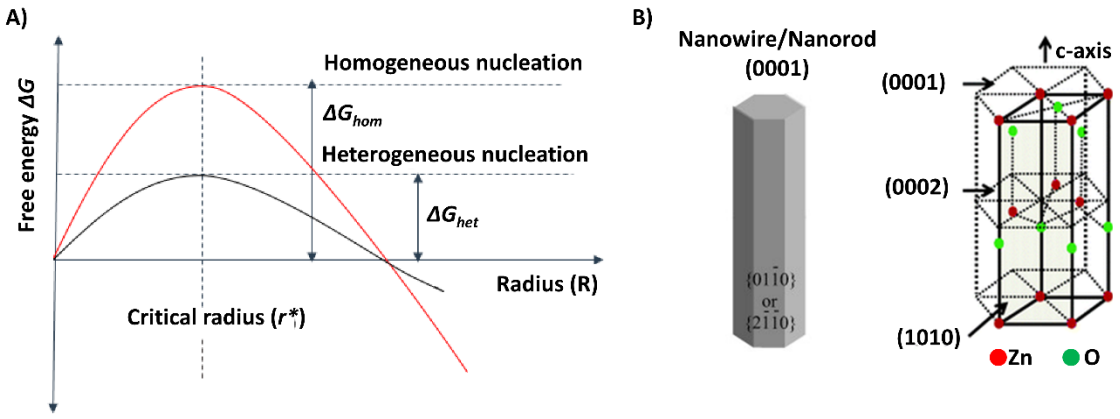

Figure 2.12. ZnO NWs hydrothermal growth. A) The overall excess free energy for heterogeneous and homogeneous nucleation, as function of cluster size [342]. B) Wurtzite structure of ZnO, showing polar surface such as negatively charged (0001) or (0002) plane [332,343].

2.4.2 The role of surface chemistry in adhesion of ZnO to fiber surfaces

As previously mentioned, when introducing an interphase, two interfaces are created to replace the original one. For a superior interphase performance, both the fiber-interphase and interphase-matrix interfaces are required to be stronger than a traditional fiber-matrix interface [8]. While the interphase-matrix interface benefits from the ability of the whisker-like nanomaterials to strongly interlock and embed inside the matrix, fiber-interphase interactions are primarily reliant

on chemical adhesion between them. Despite the fact that the hydrothermal growth of ZnO nanowires on fiber surfaces does not require prior surface treatments and is achievable under conditions that are benign to the fiber, the quality and performance of the resulting interphases are heavily dependent on its adhesion to the fiber surface. Previous studies have shown that quasi-static interfacial failure in ZnO-coated carbon fiber reinforced composites is initiated through the debonding of the nanowires from the fiber surface [180]. In 2013, Ehlert et al. demonstrated that adhesion between carbon fiber surfaces and ZnO nanowires is improved in the presence of oxygen surface functional groups [344]. When comparing the effect of various surface treatments, such as hydrazine reduction, selective oxidation, or defect grafting, nitric acid oxidation treatment was determined to be the most effective in improving interfacial adhesion between ZnO nanowires and IM8 carbon fibers. The interfacial shear strength (IFSS) was found to directly correlate to the relative fraction of surface oxygen-containing functional groups, where an increase in these surface groups yielded higher IFSS. Due to their high polarity, ketones are observed to have the strongest interactions with Zn ions within the ZnO crystals. This is due to them possessing accessible lone pairs that are not sterically hindered by hydrogen atoms like those on hydroxyl and carboxylic acid functional groups [344]. Therefore, in order to achieve optimal ZnO performance under quasi-static loading conditions, the surface of carbon fibers used in this work is to be oxidized using a similar process. By further populating the carbon fiber surface with oxygen-containing functional groups, the ZnO interphase is expected to exhibit a stronger adhesion to the carbon surface. Thus, nitric acid oxidation can be performed through first refluxing AS-4 carbon fiber tows in 100 mL of 70% nitric acid (70%, ACS certified: Fisher Scientific) for 4 hours. Soxhlet extraction is then performed for 8 hours to wash the fibers with deionized water, before drying them at 100 °C overnight. Characterization of the nitric acid functionalization is performed using XPS, and the C1s spectra for each sample are displayed in Figure 2.13A. The spectra clearly show an increase in oxygen functional groups post-nitric acid functionalization. While the concentration of hydroxyl groups remains relatively unchanged, the concentration of ketones and carboxyl is 65% and 78% increased, respectively. Therefore, the newly produced oxygen-containing functional groups enable strong binding between the ZnO NWs and the carbon fiber surface, which can improve load transferring and mechanical interlocking between both constituents of the fiber-matrix interface.

The adhesion of the ZnO interphase to the glass fiber surface is also heavily dependent on the chemical composition of the glass surface, and the interaction between its

functional groups and the wurtzite ZnO. As mentioned, a strong glass fiber-ZnO interface is of great importance to maximize the interfacial performance of the interphase at low strain rates. While surface functionalization prior to ZnO growth on carbon and aramid fiber surfaces have been previously reported [184,344], there remains a need to develop such a treatment for glass fibers. In addition to the nitric acid carbon fiber functionalization previously discussed, a functionalization and ion-exchange procedure to populate aramid fiber with carboxylic acid functional groups was also developed to ensure good adhesion between the ZnO interphase and the aramid surface [184]. As for glass fibers, they are primarily composed of oxides, such as silica (SiO_2) and alumina (Al_2O_3). Nonetheless, the glass fiber surface still contains oxygen functional groups such as silanol (Si-O-H), which can offer limited chemical bonding capacity with ZnO through their hydroxyl end [345]. Therefore, it is necessary to increase the oxygen surface content through oxidative treatments. Here, a piranha solution oxidization treatment is performed for 10 minutes inside a 20 mL solution consisting of a 3:1 volumetric mixture of sulfuric acid (95.0−98%, ACS reagent, Sigma-Aldrich) and hydrogen peroxide acid (30%, ACS reagent, Sigma-Aldrich), respectively. The pH of the fiber surface is then neutralized through washing with ammonium hydroxide (28−30%, ACROS Organics) and water, successively, until a slightly basic pH is achieved. The effect of the oxidization process on the glass fiber surface chemistry is characterized using XPS (Figure 2.13C). It should be noted that according to TGA, any existing surface sizing or coating on the fiber surface is partially removed by post-cleaning and acetone/ethanol washing, and completely removed by post-piranha treatment (Figure 2.13B). An increase in oxygen surface content is clearly observed post-functionalization, going from 62% up to 76% after a 10-minute treatment in a piranha solution. This is highlighted by the considerable broadening of the oxygen peak pertaining to the silica at the glass fiber surface. The piranha solution is a strong oxidizer that will hydroxylate the glass fiber surface and increase its silanol content [345]. Therefore, the oxidizing solution helps eliminate any remaining organic contaminants off the ceramic fiber surface while enriching it with oxygen. The new surface chemical composition promotes better adhesion between the ZnO NWs and the glass fiber surface, thus potentially further strengthening interfacial properties of glass fiber reinforced composites. Interestingly, the increase in surface oxygen content can also enhance the performance of a traditional fiber-matrix interface in glass fiber reinforced composites, as it can offer more reaction sites for bonding with epoxy functional groups [346]. This can be confirmed through average IFSS measurement, as further discussed in

the following sections. In addition, the preserved bulk chemical structure of the functionalized glass fibers is confirmed using FTIR, due to its large interaction volume. The IR spectra of both untreated and functionalized glass fibers are shown in Figure 2.13D. Any form of carbon impurities on the glass fiber surface is removed using the previously described solvent and piranha wash, eliminating any absorbance peaks associated with organic contaminants. After functionalization, the IR spectrum of the glass fibers is found to be unchanged relative to that of untreated fibers. The characteristic bands of glass fibers are located at 1093 cm^{-1}, 993 cm^{-1}, and 791 cm^{-1} corresponding to Si-O and Si-OH vibrational stretching, and Si-O bending, respectively [347]. Given that no changes to the peak intensities nor shifting to their respective wavenumbers are observed, it can be implied that the effect of the piranha solution treatment is limited to surface functionalization and avoids causing harmful and permanent modifications to the glass fiber's bulk chemical structure. In conclusion, carbon and glass fiber can be functionalized using previously and newly developed techniques in order to maximize the potential for chemical adhesion between the ZnO nanowires and their surfaces. These treatments are expected to not affect the tensile properties of the fibers and improve IFSS in quasi-statically loaded composites, as will be shown in later chapters.

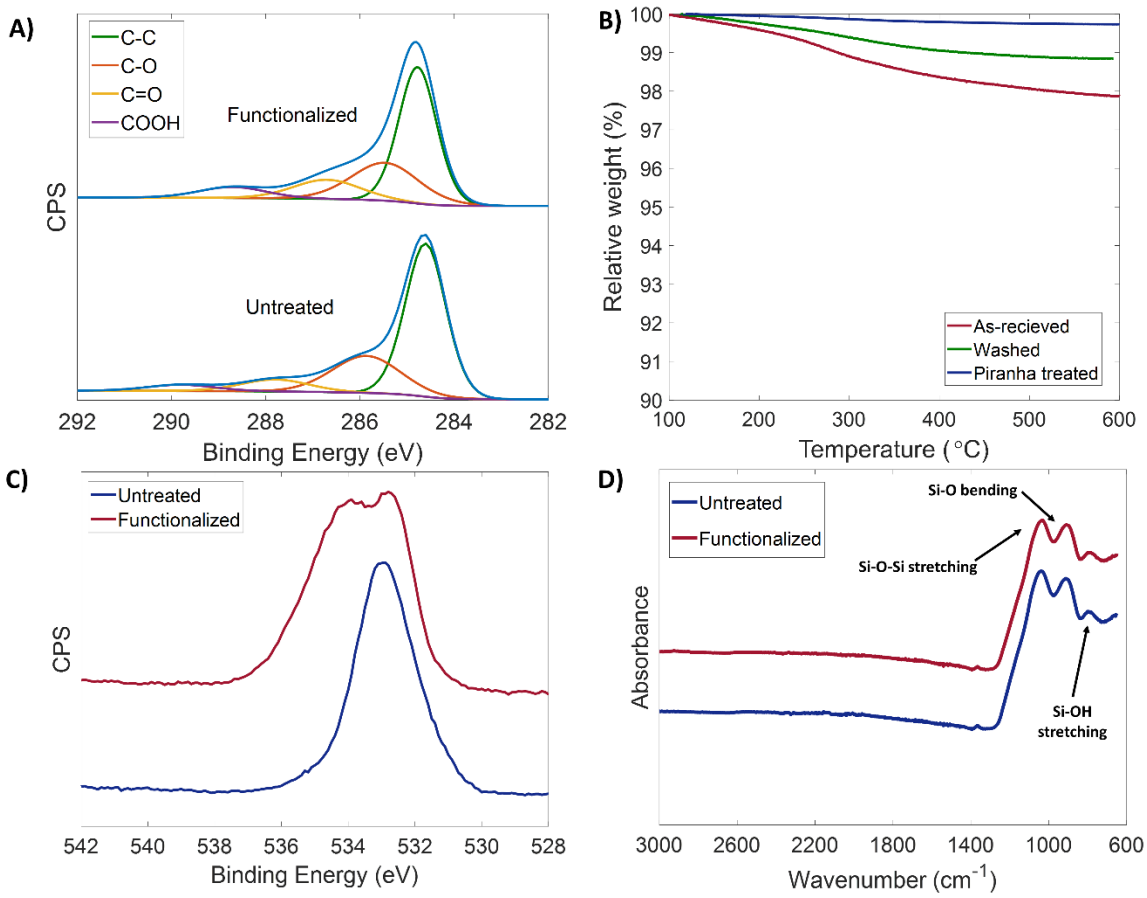

Figure 2.13. Carbon and glass fiber surface Functionalization prior to ZnO growth. A) Deconvoluted and normalized C 1s XPS spectra of untreated and functionalized carbon fibers. B) TGA curves of as-received, washed, and piranha treated glass fibers prior to ZnO growth. C) Normalized O 1s XPS spectra of untreated and functionalized glass fiber. D) FTIR spectra of untreated and functionalized glass fibers.

2.5. LIG on aramid and carbon surfaces

Carbon-based nanomaterials have been widely used to improve the multifunctionality of fiber-reinforced composites, whether through interphase design, resin mixing, or interleaving [115]. A novel carbon-based nanomaterial that is yet to be exploited for such applications is LIG. In the following section, the ability to adhere LIG interlayers onto aramid fabric and carbon prepreg surfaces will be discussed and demonstrated.

2.5.1. LIG synthesis and chemical structure

Early methods for generating graphene, such as high-temperature CVD and hydrothermal hot water reduction, suffered from problems such as high costs, poor geometrical control, and complicated synthesis routes [348]. However, these challenges can be overcome through the recently developed laser-induction process proposed by Lin et al., allowing for synthesis of graphene in a fast, cost-effective, and controlled manner [303]. As can be seen in Figure 2.14, the process involves firing a 40W focused CO_2 infrared laser beam onto a polyimide substrate, which induces the liquefaction and carbonization of polyimide, generating 3D porous graphene. The use of different substrates on which the LIG can be generated will be later discussed. It is reported that a minimum fluence of 5.5 J/cm^2 is required for the initiation of fluid fragmentation in the polyimide substrate using such a CO_2 laser system [304]. This can be achieved by adjusting and tuning various laser parameters until carbonization is observed.

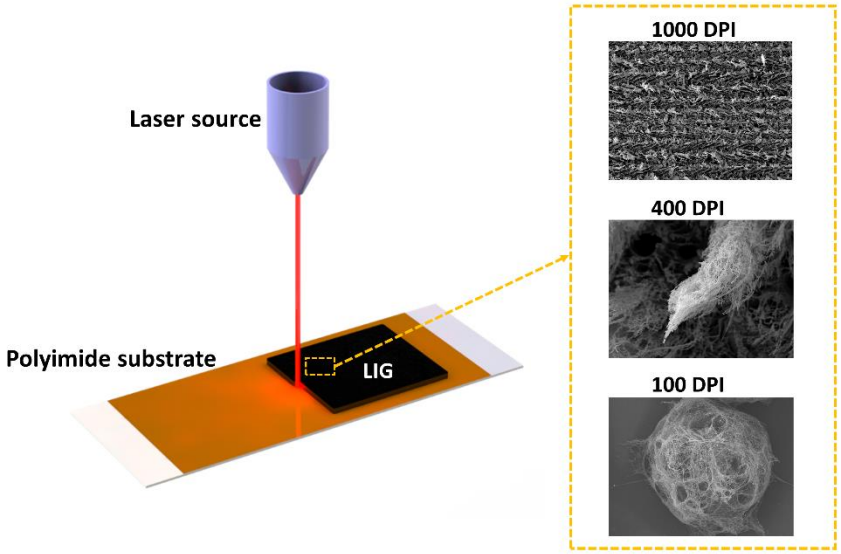

Figure 2.14. Scheme of LIG synthesis process.

While the fluence of the induction process is heavily dependent on parameters such as focusing distance and laser output power, the morphology of the resulting LIG is primarily controllable through the laser's pulsing density. As observed using SEM imaging, varying the pulsing density of the laser produces LIG hierarchical microstructures of different morphologies (Figure 2.15). At 1,000 dots per inch (DPI) and 7.2 W (12%), the LIG possesses a thin sheet-like structure (Figure 2.15A), while forests of LIG pillars of similar density are formed at 500 DPI and a similar output power (Figure 2.15B). The observed transition in morphology is due to the

decrease in pulse overlapping and fluence intensity during the successive polyimide liquefaction and carbonization process [304]. As overlapping between successive laser pulses is decreased, individual and distinctly tall graphene pillars of different end geometries are induced. Figure 2.15C shows pillars possessing sharp, pin-like ends that are formed at 400 DPI, whereas those at 200 DPI display blunter ends (Figure 2.15D). The height of these pillars is usually dependent on the laser's fluence, growing taller with increasing output power [304]. At 100 DPI, arrays of evenly spaced, porous graphene micro-hemispheres are generated (Figure 2.15E & F). These individual microstructures possess a diameter of approximately 110 µm and are 10-45 µm apart, where each represents an individual laser impulse at its focused spot size. Each of these various, high aspect ratio, and fuzzy LIG morphologies potentially possess unique characteristics that can result in different interlayer behavior when introduced within the interlaminar region of fiber-reinforced composites.

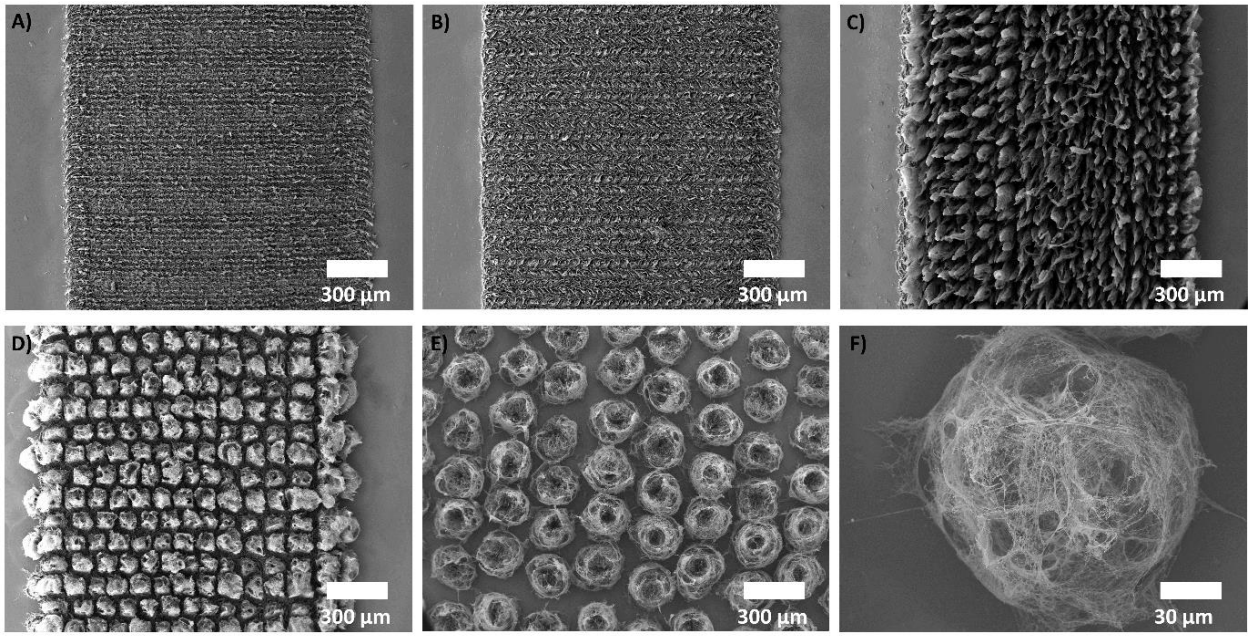

Figure 2.15. Surface morphology of LIG at varying pulsing densities. A) 1000 DPI. B) 500 DPI. C) 400 DPI. D) 200 DPI. E) & F) 100 DPI.

In order to confirm that the laser induction process generates graphene, and not amorphous carbon, several chemical characterizations are performed. Lin et al. were first to discuss the photo-thermal conversion of sp^3-carbon atoms into sp^2-carbon atoms through laser irradiation [303]. They confirmed it through high-resolution transmission electron microscopy (TEM) images

showing an abundance of pentagon-heptagon pairs and demonstrating the ultra-crystalline feature of the LIG. The TEM images were found to display the characteristic 3.37Å d-spacing of graphene. X-ray photoelectron spectroscopy on the LIG also showed a C-C C1s peak primarily, with C-N, C-O, and C=O peaks originally found in polyimide being greatly reduced. The atomic percentage of the carbonized surface is determined to be dependent on the induction power, displaying a maximum of 97% C1s, while O1s and N1s constituted the remaining 3%. Moreover, Duy et al. were the first to confirm that the chemical structure of the LIG is maintained when modifying rastering pulsing density to obtain different LIG morphologies [304]. Here, the various LIG surfaces are first characterized using Raman spectroscopy (Figure 2.16A). Irrespective of the pulsing density, the graphitic structure of the laser-induced graphene is confirmed through the presence of typical D-band, G-band, and 2D-band peaks at approximately 1355 cm^{-1}, 1585 cm^{-1}, and 2700 cm^{-1}, respectively. While the D and G peaks indicate the carbonization of the polyimide substrate, the 2D peak suggests graphitization and graphene formation, as it represents the second-order zone boundary phonons [349]. Such a peak signals the presence of a few-layer graphene structure [350]. As expected, the ratio of integrated G and D peak intensities (I_G/I_D) is found to decrease from 2.24 to 1.04 when decreasing pulsing density from 1000 DPI to 100 DPI. This is the result of the decrease in fluence intensity with decreasing pulsing density, as the polyimide substrate is exposed to a reduced degree of laser irradiation [304]. Nonetheless, the quality of the LIG can be further optimized independent of morphology through other parameters, such as output power and rastering speed. The described results confirm the graphitic nature of the LIG and agree with other reported studies that chemically characterize LIG [303–306]. Furthermore, the chemical compositions of the various LIG surfaces are studied using XPS (Figure 2.16B). When the pulsing density is decreased from 1000 DPI to 200 DPI, the surface oxygen content (O 1s) is found to decrease from 5.29 % to 1.57% (Table 2.2). The observed trend indicates that the LIG obtained at lower pulsing densities possess a reduced oxygen content [351]. However, the LIG generated at 100 DPI is observed to display a chemical composition closer to that of polyimide, showing an unexpected 7.96 % increase in O 1s content, relative to that at 200 DPI. Moreover, unlike LIG generated at higher pulsing densities, both polyimide and 100 DPI LIG display residual nitrogen (N 1s) and silicon (Si 2p). This can be attributed to the relatively low spatial density of the 100 DPI LIG (Figure 2.15E), which results in the X-ray source simultaneously detecting both the intact polyimide surface and the graphitic surface. It should be noted that the detected silicon residual is

due to the adhesive layer that covers the polyimide films used in this work. For more accurate dimensional control over the studied area, the elemental composition of the various LIG surfaces is also obtained using EDS (Figure 2.16C). Given the availability of SEM imaging, EDS allows for high accuracy elemental composition analysis of a single LIG pillar generated at 100 DPI independent of the surrounding polyimide substrate. As the pulsing density is gradually decreased from 1000 DPI to 100 DPI, the LIG oxygen concentration is found to similarly decrease from 4.5% to 1.4 %, confirming that the reduction in pulsing density from 200 DPI to 100 DPI reduces the LIG oxygen content. This is also in agreement with the XPS oxygen content trend for LIG generated at pulsing densities ranging between 1000 DPI and 200 DPI. In conclusion, decreasing the induction pulsing density while maintaining a constant output power reduces the LIG oxygen content. Nonetheless, the remaining oxygen is primarily in the form of carbonyl groups that are capable of chemically interacting with the matrix, allowing for stronger bonding at the level of the interlayer-matrix interface [351]. These results confirm the graphene nature of the laser induction's product; and therefore, it is expected to possess excellent mechanical, electrical, and thermal properties.

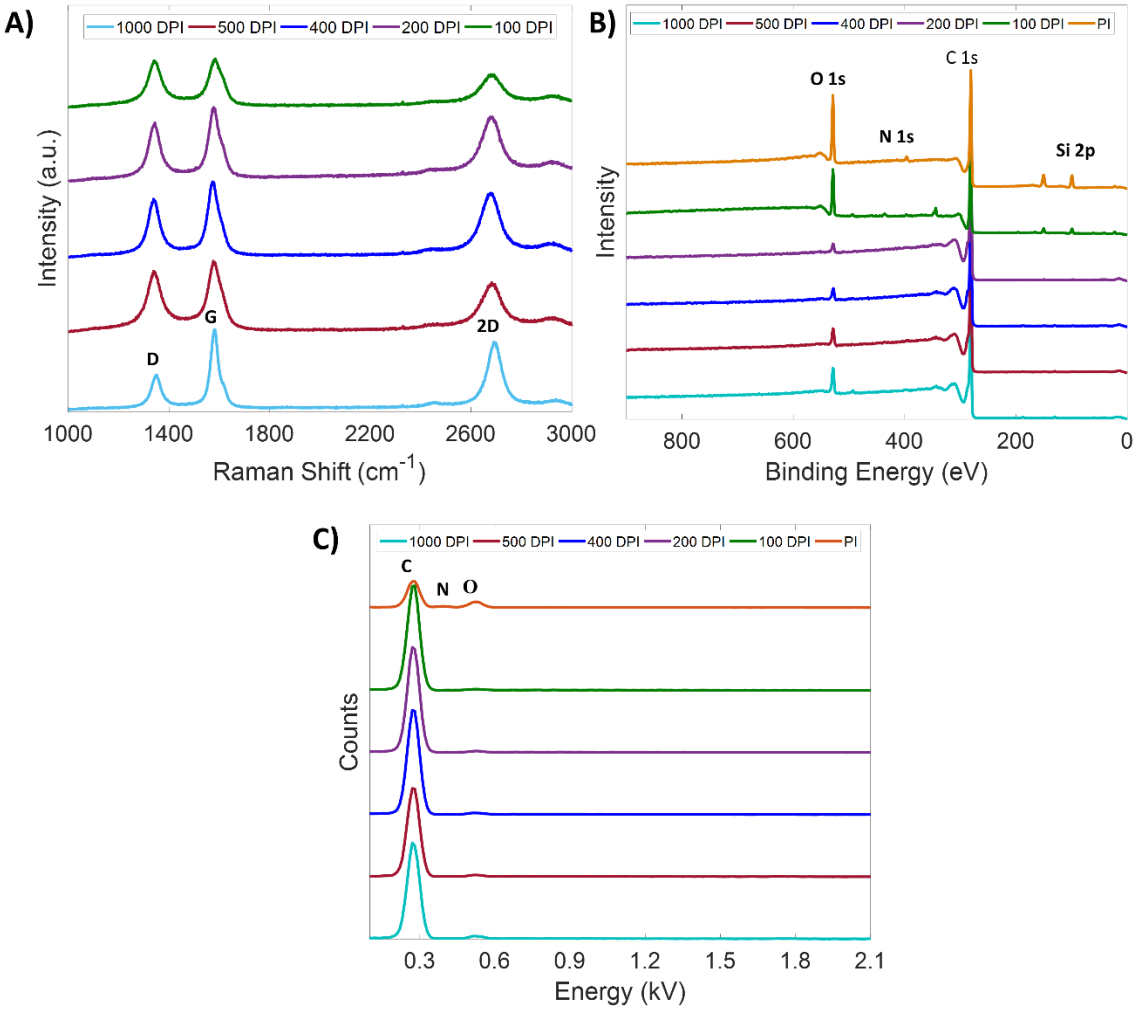

Figure 2.16. Chemical characterization of LIG. A) Raman spectra of LIG at a 16% output power and varying pulsing densities. B) XPS spectra of polyimide and LIG at a 16% output power and varying pulsing densities. C) EDS spectra of polyimide and LIG at a 16% output power and varying pulsing densities.

Table 2.2. Oxygen and carbon contents of LIG at a 16% output power and varying pulsing densities using XPS and EDS elemental composition analysis techniques.

	XPS		EDS	
	% C 1s (284.7 eV)	**% O 1s (532 eV)**	**% C (277 eV)**	**%O (525 eV)**
PI	80.99	11.97	71.1	23.7
100 DPI	86.34	9.53	98.6	1.4
200 DPI	98.43	1.57	98.1	1.9
400 DPI	97.57	2.43	97.6	2.4
500 DPI	96.74	3.26	97	3
1000 DPI	94.91	5.29	95.5	4.5

2.5.2. LIG-aramid interface

While earlier work only reported successful LIG synthesis on polyimide and polyetherimide, later studies expanded the list of possible substrates [303]. Through defocusing the laser, the conversion of high-temperature resistant polymers into graphene can be achieved at lower fluences, thus protecting the substrates from the ablation and considerable thermal damage, which would otherwise diminish its performance [47]. The list includes thermosets, natural polymers, and thermoplastics such as polyamide-imide, polyether ether ketone, and aramid. As seen in Figure 2.17A, the 0.3 mm defocused laser ablation of aramid Kevlar fabric yields a darker color with increasing laser output power, indicating the occurrence of carbonization. The original Raman spectra of the untreated aramid fabric show the characteristic peaks for PPTA, with the peaks at 1517 cm^{-1} and 1608.5 cm^{-1} corresponding to the C=C ring axial vibration mode, while those positioned at 1569 cm^{-1} and 1647 cm^{-1} belong to the radial vibration mode originating at amide II and amide I, respectively (Figure 2.17B). These aramid fibers are known to be highly crystalline, primarily due to the exact disposition of its monomers along both the axial and radial directions, and the high regularity of its polymer chains [185]. Figure 2.17C shows the Raman spectra of an LIG coated aramid fabric induced at 20%, displaying typical peaks of a graphitic structure D-band, G-band, and 2D-band at 1354 cm^{-1}, 1580 cm^{-1}, and 2699 cm^{-1}, respectively. As expected, the degree of aramid fabric graphitization increases with an increasing power output of

the induction (Figure 2.18A-D) [303]. Here, the speed, defocusing distance, and pulsing density of the induction process are maintained constant, and therefore only the laser output power of is to affect the degree of graphitization. Typically, there exist a critical output power at which carbonization is initiated, while the quality of the LIG is expected to improve with increasing power until it starts degrading due to oxidation in the air [303]. At a lower output power of 8 % and 10%, the Raman spectra are considerably noisy, and a low I_G/I_D ratio is observed (Figure 2.18A & B). This is the result of the non-uniformity of the aramid surface chemistry due to the limited graphitization process. As power increases up to 16 %, the aramid fabric surface is further graphitized, as reflected by the appearance of distinct G and D peaks (Figure 2.18C & D). However, their 2D peak is considerably weaker than that obtained at an output power of 20 %. These results indicate that an induction power of 20% is ideal for the graphitization of the aramid fabric. The observed strong D peak in Figure 2.17C is the result of defects and broken symmetry sites, indicating a low LIG quality with an I_G/I_D ratio of 1.29. While the quality of the induced graphene on the aramid substrate is considerably lower than that observed on other substrates, such as polyimide and polyether ether ketone (PEEK), it is in agreement with other reported studies of LIG treated Kevlar fabric [308,352]. Nonetheless, the LIG can introduce multifunctionality to the aramid fabric in the form of a graphitized surface and can be further optimized depending on the choice of application.

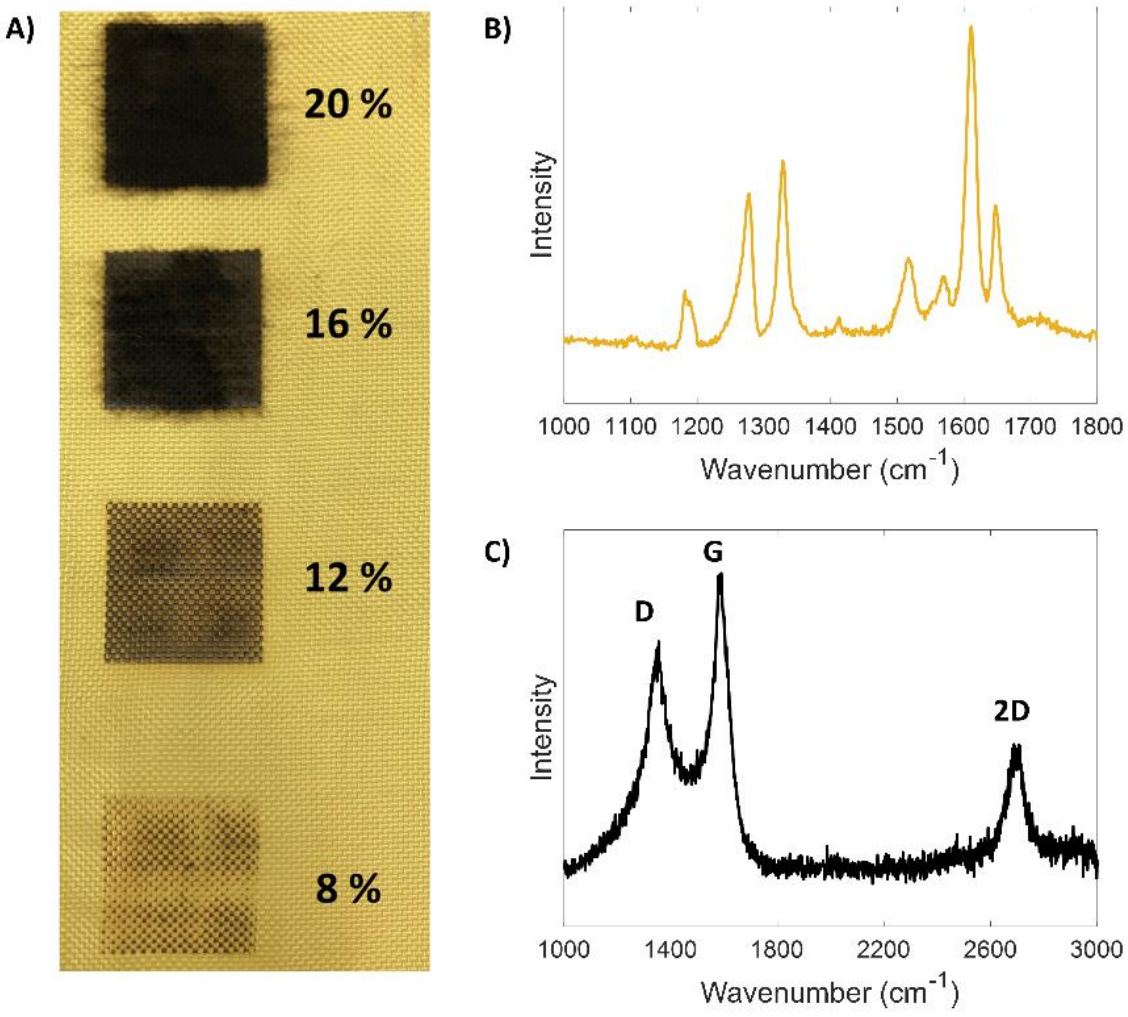

Figure 2.17. LIG on aramid fabric. A) Aramid fiber surface after laser induction at various power outputs. B) Raman spectrum of untreated aramid fabric. C) Raman spectrum of LIG coated aramid fabric at an induction power of 20%.

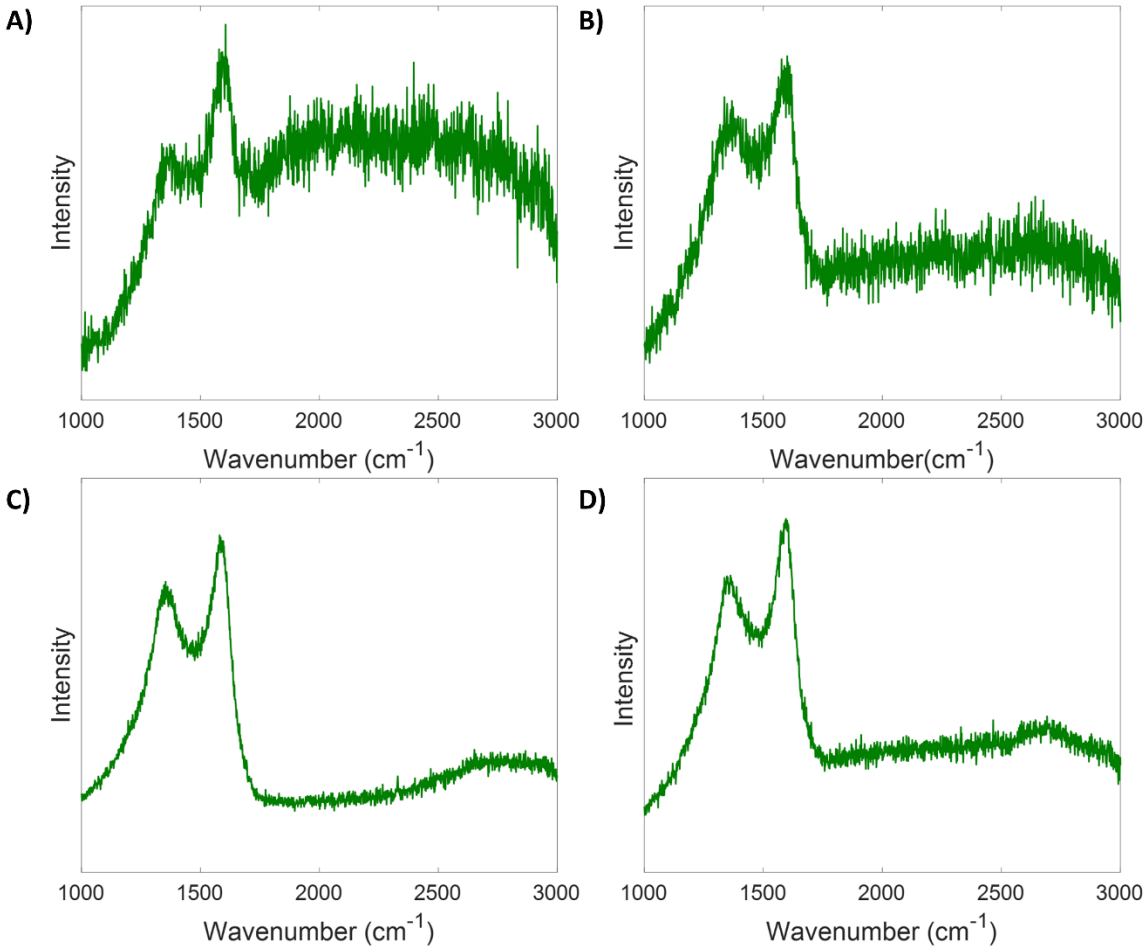

Figure 2.18. Raman spectra of LIG coated aramid fabric at various induction powers. A) 8%; B) 10%; C) 12%; D) 16%.

The LIG coating of the aramid surfaces is further characterized using XPS analysis of C 1s spectrum, as seen in Figure 2.19. While the XPS spectra of the untreated aramid fabric can be deconvoluted into three bonding state peaks corresponding to C-C, C-N, and C=O at 284.7 eV, 285.9 eV, and 287.8 eV, respectively, the bonding state peak of the LIG coated aramid fabric is exclusively dominated by that of C-C. During laser ablation, ketone and amine bonds are broken and removed in the form of gaseous products while the carbon atoms are rearranged to form graphene [352]. Therefore, the carbon content in LIG coated aramid fabric is increased, while that of other components, such as nitrogen and oxygen, is decreased. Therefore, the LIG is successfully adhered to the aramid surface through a direct laser writing method. Given that the LIG is part of the fabric, it is expected to be both inherently chemically and mechanically bonded to the aramid

surface. The various LIG morphologies on aramid fabric and their mechanical performance will be further discussed in later sections

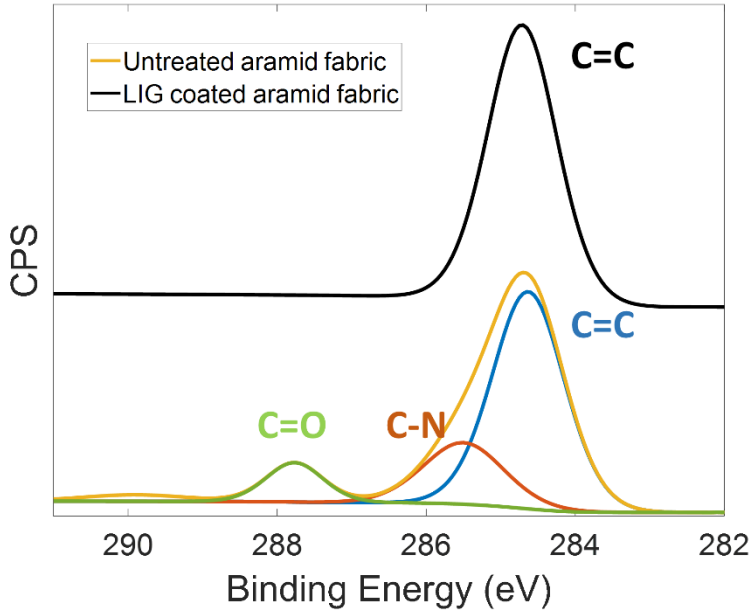

Figure 2.19. C 1s XPS spectra of untreated and LIG coated aramid fabric.

2.5.3. LIG-carbon interface

Unlike aramids, carbon fabric is not a substrate on which LIG can be directly generated. Despite their electrical and thermal conductivity, carbon fiber reinforced composites still lack the hierarchical mechanical functionality that the LIG provides in order to overcome interlaminar stress concentrations and delay delamination. Nonetheless, due to their tackiness, carbon fiber prepregs provide an opportunity to mechanically transfer the LIG from a polyimide substrate onto a carbon fiber prepreg. Prior work has shown that vertically aligned CVD-grown CNTs can be transfer-printed from a silicon wafer onto a carbon fiber prepregs and act as interlaminar reinforcement [275]. By adjusting the applied pressure, the CNTs forest were transferred from the silicon substrate onto the tacky prepreg while maintaining their alignment, forming an interlayer that can toughen carbon fiber composites. Similarly, here, the LIG is transplanted from polyimide substrates on tacky carbon fiber prepregs while maintaining their alignment. As seen in Figure 2.20, the transfer process allows for complete and uniform transfer of the vertically aligned LIG forest. The efficiency of the process is vastly improved by slightly heating the substrates to increase

the tackiness of the prepreg during transfer. Moreover, LIG generated at lower pulsing densities of 500 DPI or less is found easier to transfer than those induced at 1000 DPI due to their more individual microstructures. While in such case, the LIG-carbon interface is not a conventional one and may potentially lack considerable chemical interactions, the LIG is expected to act as an interlayer that is firmly imbedded inside the matrix once the prepregs are cured. The vertically aligned LIG can populate the interlaminar region, mechanically joining two adjacent layers. Further characterization of the interlayer and its performance will be performed in the following section. Therefore, it can be concluded that the LIG can be firmly attached to aramid and carbon fiber surfaces through direct laser writing and transfer printing, respectively, and adhered to them through inherent chemical and mechanical interactions.

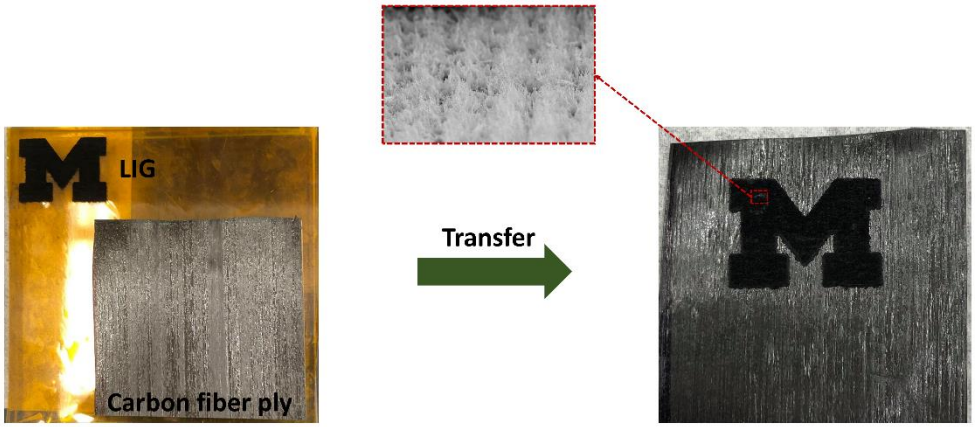

Figure 2.20. Transfer printing of LIG onto unidirectional carbon fiber prepreg ply.

2.6. Chapter summary

In this chapter, fiber-interphase interactions between different nanomaterials and fiber surfaces were investigated and assessed to maximize the performance of interphases in fiber-reinforced composites. The potential of amide-amide hydrogen bonding for the self-assembly of ANFs onto aramid fiber surfaces is studied in polyamide-based matrices and demonstrated to be advantageous over other forms of hydrogen bonding. An electrostatic adhesion approach using a cationic polymer coating is also discussed as a method to induce sufficient adhesion between ANFs and glass fiber surfaces. Furthermore, a novel aramid fiber surface fibrilization technique is presented as a potential approach to directly introduce an aramid nanostructured interphase onto

macroscale fabric or fiber surfaces.

In addition, the importance of high surface oxygen content to the adhesion of ZnO to fibers surfaces is discussed, and functionalization approaches are developed. For carbon fibers, a previously developed nitric acid functionalization technique is used to increase oxygen-containing functional groups on the surface, specifically ketones, by 5.05%. For glass fibers, a new piranha solution oxidization method is developed and used to increase surface oxygen content by 14%. The oxidized surfaces present improved chemical adhesion with the ZnO nanowires, resulting in better interphase performance when incorporated into composite materials. Furthermore, the LIG is demonstrated to be directly inducible on aramid fabric, as well as transfer-printable onto carbon fiber prepregs. Through direct laser writing, the graphitic nanomaterial is generated directly on aramid fabric and therefore is inherently mechanically and chemically adhered to the surface. As for carbon fiber prepregs, their tackiness allows for the transplantation of the LIG from the polyimide substrate through a manual pressure process that maintains their alignment. The LIG is therefore adhesively attached to the prepregs, forming a well-adhered and uniform interlayer. Overall, this chapter focused on understanding fiber-interphase interactions and improving them for optimal adhesion. The following chapters will investigate the performance of these interphases and interlayers as interfacial and interlaminar reinforcements in a variety of fiber-reinforced composites.

CHAPTER 3. Development and Optimization of Nanostructured Interphases for Structural Composites

3.1. Chapter Introduction

The following chapter focuses on the introduction of aramid-based nanostructured interphases onto the surfaces of aramid and glass fibers to maximize the interfacial properties of their corresponding composites for structural applications. In order to assess the quality and potential use of these interphases, the resulting surface morphology and chemistry is characterized through a series of techniques such as SEM, AFM, FTIR, and XPS. Single fiber tensile tests are used to investigate the effect of the treatment conditions on the tensile properties of the fibers, while interfacial properties are measured using quasi-static single fiber pullout (SFP) testing. The SFP tests are designed to induce catastrophic interfacial failure and avoid friction effects that can yield inaccurate results. Finally, the performances of these interphases in bulk composites is examined through short beam shear testing which evaluates the interlaminar properties.

In the first part of the chapter, aramid nanofiber (ANF) interphases that were adsorbed on aramid and glass fiber surfaces are investigated. Through SEM and AFM imaging, the surfaces of the fibers are found to have increased roughness, which is desirable to improve mechanical interlocking between the fiber and the matrix. Moreover, through XPS and FTIR the fiber surfaces are found to be enriched with polar functional groups that can enhance chemical bonding between the fiber and epoxy matrix. Through quasi-static SFP and short beam shear testing, the introduced ANF interphases are found to exhibit improved interfacial and interlaminar properties, signaling enhanced interfacial interactions and a stronger fiber-matrix interface. The quality and performance of these interphases is optimized through varying the treatment periods. In the second part of his chapter, the dissolution and deprotonation process is modified in order to fibrilize aramid fibers. The short period fibrilization process yields improved aramid surface reactivity and generates nanofibrils capable of mechanically interlocking with the matrix. The improved surface chemistry and morphology is then demonstrated to result in enhanced interfacial and interlaminar properties under quasi-static loading conditions. Finally, the tensile properties of both ANF coated and fibrilized fibers is confirmed to be maintained, highlighting the benign nature of these

treatments and their suitability for industrial composite applications.

3.2. Review of quasi-static interfacial testing techniques

It is generally accepted that single fiber composite specimens are the most suitable approach for the direct evaluation of interfacial behavior of composite materials, specifically the interfacial shear strength (IFSS), given that it eliminates many of the material interactions that can skew the results [318]. The four most commonly used methods for the measurement of a single fiber composites' IFSS under quasi static loading are single fiber pushout [353], single fiber fragmentation [184], micro-droplet [354–356] and single fiber pullout [162] (Figure 3.1.). The single fiber fragmentation (SFF) test is the most widely employed within the composites community [357]. In the SFF test, a single fiber is embedded into a polymer matrix, before subjecting it to tensile loading until the fiber reaches its tensile strength (σ_f) leading to fiber fracture inside the matrix due to the high surface area relative to cross-sectional area (Figure 3.1A). The loading of the fiber is continued until the fragments saturate [358]. Based on the assumption that stress is transferred only through the interface, shear lag theory can be applied to identify IFSS. However, the SFF approach is not suitable for high strain to failure fibers since the matrix may yield prior to achieving fiber fracture saturation [335,359]. Single fiber pushout is another common IFSS evaluation technique that measures the force required to push an embedded fiber out of a portion of the composite specimen using an indenter (Figure 3.1B) [353,360]. The advantage of this test lies in the clear demonstration of debonding failure. However, the method's minimum deformation requirements are incompatible with polymeric fibers, such as aramids, as the indenter typically damages the polymer fiber during testing rather than achieving the correct pushout behavior [357]. Micro-droplet is also a viable approach in which a single droplet of polymer is applied to the fiber and subsequently sheared using a set of knife edges on a micro-vise (Figure 3.1C). Micro-droplet is an appealing approach due to its simplicity and limited equipment requirements, however the results are highly dependent on the shape of the droplet which dictates loading conditions, leading to high variability and poor statistical significance of the collected data [355]. Parameters that require extreme care during specimen fabrication, such as conus angle and droplet length, can heavily influence the level of stress concentration at the tip of the droplet and lead to inaccurate measurements [354]. Furthermore, the small volume of the droplet changes the cure kinetics, which affects the validity of the data [361].

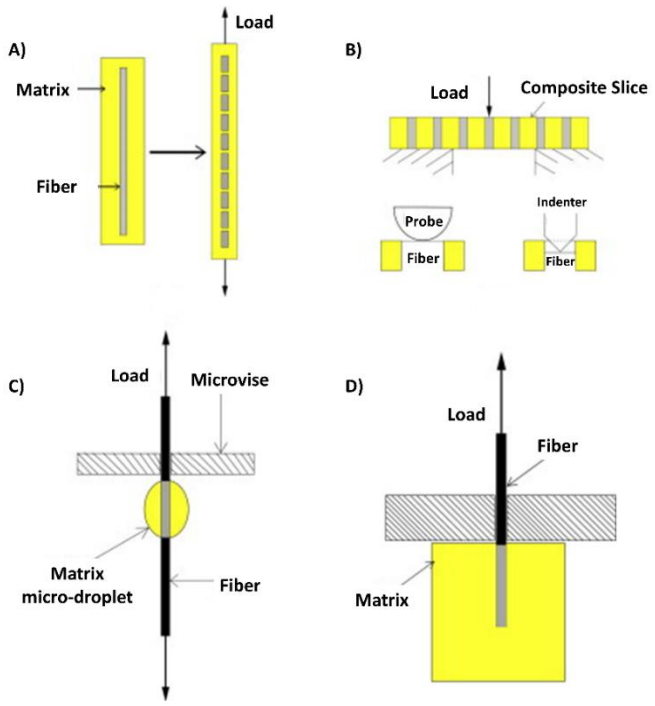

Figure 3.1. Single fiber composite testing for determining the interfacial shear strength of fiber-matrix interfaces. A) Single fiber segmentation, B) single fiber pushout test, C) micro-droplet test, and D) single fiber pullout test [318].

An alternative to each of these tests is single fiber pullout (SFP) (Figure 3.1D & 3.2A). In this test, a fiber is partially embedded in a matrix, which is fixed, and an external force is applied to the free end of the fiber until pullout is achieved [362–364]. The catastrophic nature of the fiber-matrix interface failure makes it a good candidate for the assessment of interfacial properties under both quasi-static and impact loading conditions [365,366]. A critical component of the SFP test is the choice of embedded fiber length, which ensures that interfacial failure will occur prior to tensile failure of the loaded fiber. The interfacial shear strength (τ) (IFSS) of the specimen during SFP can be expressed according to the Tyson and Kelly model [364] as:

$$\tau = \frac{F}{\pi d l} \tag{3.1.}$$

where F is the peak load at which pullout occurs, d is the diameter of the fiber, and l is the embedded length of the fiber. The applied load also results in tensile stress (σ_f) developing within the fiber which can be expressed as:

$$\sigma_f = \frac{F}{\pi r^2} \tag{3.2.}$$

where r is the radius of the fiber. Combining Eqs. 3.1. & 3.2. allows the determination of the maximum possible embedded length of the fiber inside the matrix, where:

$$l = \frac{r\sigma_f}{2\tau} \tag{3.3.}$$

Thus, for an aramid (Kevlar®) or glass fiber having a tensile strength ranging between ~ 2.5- 3.7 GPa, a diameter of ~10-12 μm, and using an IFSS of ~40-50 MPa [367], the maximum calculated allowable embedded length is ~400 μm. However, in long embedded lengths that approach millimeter lengths, the distribution of shear loading is discontinuous and results in friction and crack propagation effects, leading to a more complicated debonding load response, and causing Eqs. 3.1. to be invalid [362]. Therefore, it is necessary for the chosen embedded lengths to be smaller than $l_{maxcatastrophic}$ to ensure catastrophic interfacial failure (Figure 3.2B). In the case where embedded fiber lengths fall between $l_{maxcatastrophic}$ and $l_{maxfriction}$, a considerable amount of frictional energy is dissipated during pullout, causing for the Tyson and Kelly model to be no longer valid. Once $l_{maxfriction}$ is exceeded, fiber pullout becomes independent of embedded length and a steady state crack propagation behavior is expected. Therefore, using a safety factor of 4, the single fiber composites used for IFSS measurements are to have embedded lengths of less than 100 μm. However, embedded lengths of less than 20 μm are also to be avoided in order to eliminate the possibility of cross-sectional effects influencing the accuracy of measurements [362]. Therefore, SFP is an interfacial testing technique that can yield clear debonding failure, is suitable for both polymer and ceramic fibers, and allows for accurate IFSS measurements if designed properly.

While the SFP sample preparation process can be challenging, we have developed a simple and rapid process to enable SFP testing to be performed with high statistical significance (Figure 3.2C) [136,290]. Specimens are fabricated using slit silicon molds that allow for the embedded fiber length to be controlled under an optical microscope. The epoxy matrix consists of an Epon® 862 (Hexion, Inc.) and Epikure® curing agent W (Hexion, Inc.) mixture at a ratio of 100:26.4, which is cured in the silicon molds for 6 hours at 125 °C. The specimens are then removed from the molds and tested using an Instron universal load frame (Model 5982) with a 2530 static 5 N load cell at a cross-head speed of 1 mm/min, until a 40% peak load drop and complete pullout behavior is observed. This SFP technique allows for accurate IFSS assessment in order to understand the effect of chemically treatments, or nanostructured interphases on interfacial adhesion in fiber reinforced composites.

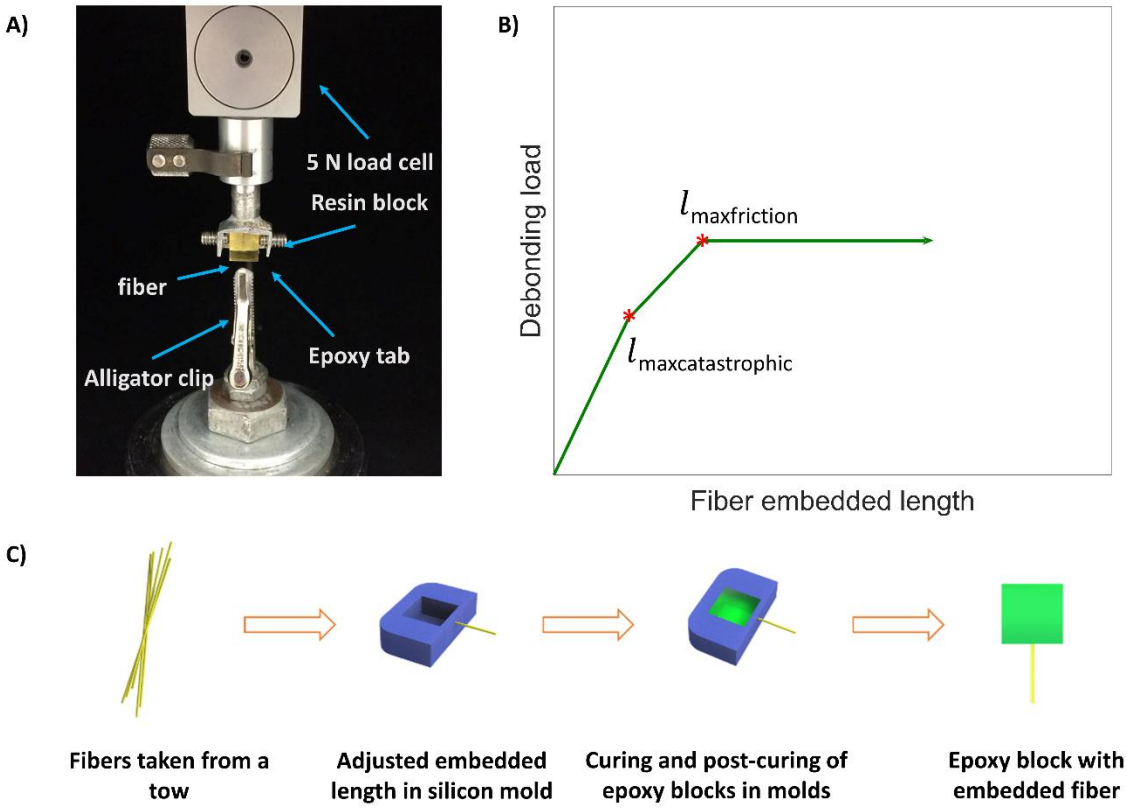

Figure 3.2. Single fiber pullout testing. A) SFP experimental setup. B) Theoretical embedded fiber length versus debonding load. C) Schematic of SFP specimen fabrication process.

3.3. ANF nanostructured interphase

3.3.1. Adsorption of ANFs onto fiber surfaces

The coating of aramid and glass surfaces with ANFs is realized using a simple dip-coating process in an ANF solution. Therefore, 0.2 wt% ANF suspensions are first prepared using the dissolution and deprotonation method described in Yang et al.[108]. A mixture of 1 g of aramid fibers (KM2+, style 790 scoured, CS-800), 1.5 g of finely ground potassium hydroxide (KOH), and 500 ml of dimethyl sulfoxide (DMSO) is prepared in a 1-liter bottle and stirred using a magnetic stirrer at 400 rpm for 7 days. The polymeric dispersion is obtained through the dissolution and deprotonation of the macroscale aramid fibers in the basic solution, where mobile hydrogen bonds are extracted from the amide functional groups, therefore considerably weakening hydrogen bonding between polymer chains. Pieces of aramid fabric are soaked in the solution and then removed successively over the next 10 minutes, after 1, 2, 3, 4, 5 and 10 minutes, respectively.

The aramid fabric pieces are then immediately rinsed in water and ethanol before being dried at 80 ℃ for 12 hours, and under vacuum. Untreated aramid fibers are also cleaned in an equivalent manner for reference. As for glass fibers, plain weave fabric pieces (Fiberglast) are cut into 5 x 5 cm squares and cleaned using successive sonication in acetone (≥ 99.5%, ACS reagent: MilliporeSigma) and ethanol (≥ 99.5%, ACS reagent: Fisher Scientific). The glass fiber surfaces are then positively charged through soaking them in a 1 wt% Polydiallyldimethylammonium chloride (PDDA) solution (MilliporeSigma) for 2 minutes, followed by air drying for 12 hours. The glass fiber pieces are finally dipped in the ANF suspension for 1, 3, and 5 minutes, followed by thorough rinsing using water and ethanol, and then drying at 100 °C for 10 hours under vacuum.

3.3.2. Characterization of surface morphology and chemistry

The modified aramid and glass fiber surface morphology due to the adhered ANFs is evaluated through SEM imaging (Figure 3.3 & 3.4.). Figure 3.3. demonstrates how the nanostructured coating fully covers the initially smooth aramid fiber surfaces (Figure 3.3A). The entangled and agglomerated ANFs are randomly aligned on the aramid surface, building networked structures of much larger scale than the individual nanofibers (Figure 3.3E). When dip-coating a tow, fabric or unidirectional tape of aramid fibers, the assembly of ANFs onto the macroscale surface is achieved by wetting through micro- and meso-channels, leading to the formation of web-like structures capable of bridging neighboring aramid fibers (Figure 3.3E & F). It should be noted that once the solvent is completely evaporated, the coated aramid fibers are thoroughly washed with DI water in order to neutralize the negatively charged ANFs. While these inter-fiber nanofiber structures are expected to further enhance the interfacial properties of aramid reinforced composites by anchoring the ANF interphase firmly into the matrix, an excessive coating can lead to weaker composites through the blockage of resin infiltration during composite fabrication [134,207]. Nonetheless, these morphological changes to the initially smooth aramid surface introduce a desired coarseness and roughness that allows for mechanical interlocking between the aramid fiber and the matrix. Moreover, further enhancement of interfacial properties can be achieved through the increased interfacial surface area induced by the introduction of the ANF interphase. Therefore, the adhered ANF interphase can yield desired morphological features when trying to enhance interfacial adhesion in aramid fiber reinforced composites.

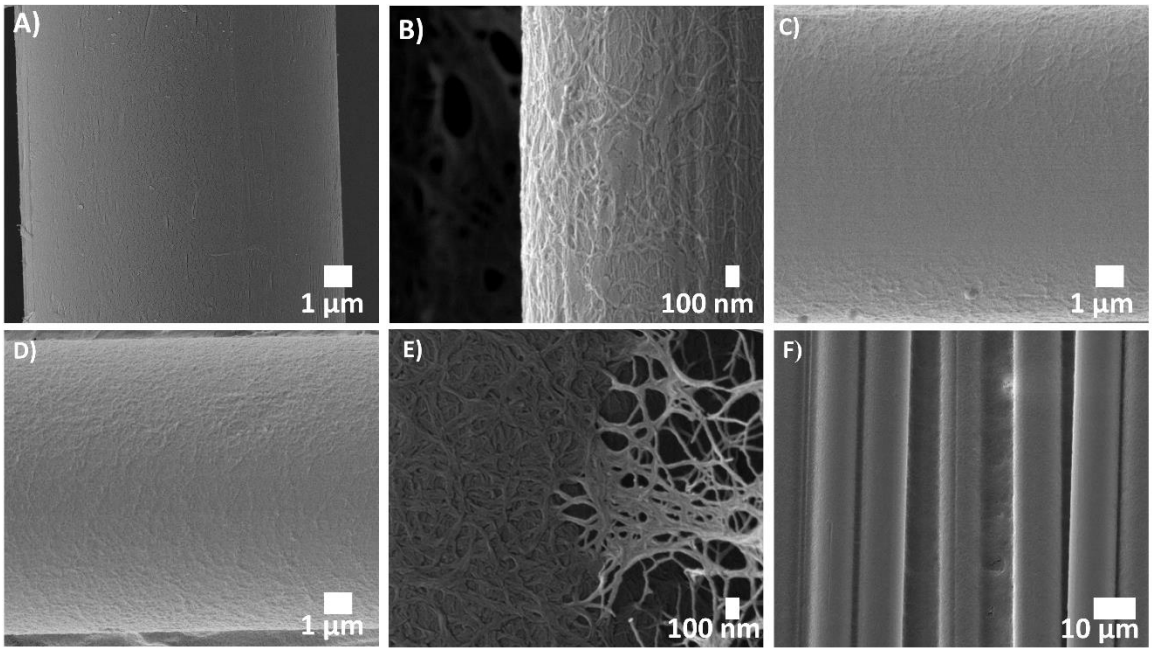

Figure 3.3. Scanning electron microscopy of untreated and ANF coated aramid fibers for surface morphology comparison. A) Untreated aramid surface. B-D) ANF nanostructured interphase on single aramid fiber surface after: B) 1-minute treatment. C) 2-minute treatment. D) 3-minute treatment. E) Agglomeration of ANFs along fiber surface and the formation of web-structures between neighboring fibers. F) ANF coated aramid fabric.

The surface morphology of glass fibers is also considerably modified post PDDA and ANF treatments. Initially, the cleaned and untreated glass fibers display a smooth surface that offers little opportunity for mechanical interlocking with the wetting resin (Figure. 3.4A), leading to interfacial adhesion being primarily dependent on chemical bonding and compatibility between the fiber and the matrix. Once the PDDA coating is applied, the glass fiber surfaces are found to be slightly roughened (Figure. 3.4B). However, the thickness of the polymeric coating is observed to be negligible, as the diameter of the glass fibers remain relatively unchanged. The subsequent soaking of these fibers in the ANF suspension for a treatment period of only 1 minute results in a surface that is covered with networks of entangled ANFs (Figure. 3.4C & D). When the treatment period is further increased to 3 minutes, the ANF interphase completely and uniformly coats the glass surface, forming a continuous and nanostructured interphase of desirable morphology (Figure. 3.4E & F). Given that the thickness of the interphase does not exceed that of a small number of agglomerated nanofibers, the thickness of the ANF coating is expected to be within the range of the nanofiber diameter. This is confirmed through the negligible changes to glass fiber

diameter post-treatment, as typical monolayer ANF coatings are measured to be less than 2 nm thick [108]. In comparison to Park et al. [135], such ANF coatings present a considerably rougher surface morphology, all while maintaining a nanoscale thickness. The ANF induced surface morphology provides the potential to improve interlocking between the fiber and the matrix by allowing the glass surface to be anchored in the matrix. As observed in Figure. 3.4G & H, a prolonged treatment period of 5-minute results in excessive and undesirable ANF agglomerations on the glass surface, producing a porous and non-uniform interphase of increased thickness. Such a morphology can possibly lead to defects and voids within the composite by hindering the liquid resin from properly wetting the glass fiber surface and increasing the preform infusion time. The mechanical performance of these interphases in both aramid and glass composites is quantified in later sections in order to determine optimal ANF treatment periods.

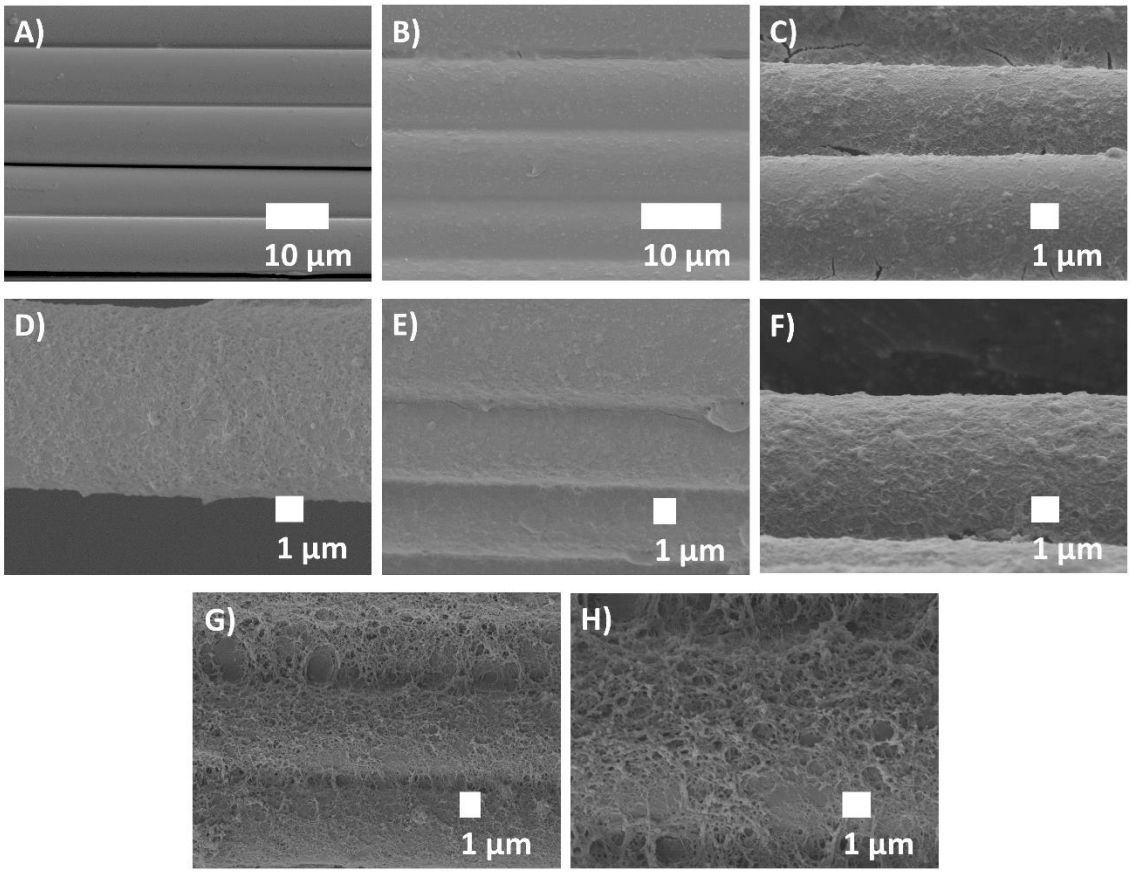

Figure 3.4. SEM imaging of untreated and ANF coated glass fiber surfaces for varying treatment durations. A) Untreated glass fiber surface. B) PDDA coated glass fiber surface. C–H) ANF interphase on glass fiber surface for a treatment duration of: C) & D) 1 minute, E) & F) 3 minutes, G) & H) 5 minutes.

The morphological changes introduced by the ANF interphase to the surface of aramid and glass fibers are then studied using AFM scanning (Figure. 3.5 & 3.6), where a significant increase in surface roughness is found post-treatment. The surface roughness of each fiber is quantified through XEI (PSIA Corporation) analysis software and reported in Table 3.1. Both the root-mean square (RMS) roughness (R_q) and the average roughness (R_a) of ANF coated aramid fibers are increased by more than 88.9% following a 1-minute treatment. A maximum increase in average roughness is obtained in ANF coated aramid fibers after a treatment period of 3 minutes, showing an increase of 100.1%, compared to untreated aramid fiber. Similarly, the glass fiber surface is considerably coarsened due to the assembled ANF interphase, showing a maximum increase in RMS roughness of 45.72% after a 5-minute treatment, relative to untreated glass surfaces. The increase in surface roughness is attributed to the coarser surface geometry created by the adhered ANFs on the surface of the fibers. Rougher aramid and glass surfaces provide an opportunity for increased interlocking between the fiber and the matrix, therefore potentially strengthening interfacial adhesion between the fiber and matrix. However, it is also observed that the increase in roughness does not follow a linear relationship with prolonging treatment period. For both aramid and glass fibers, the increase in surface roughness with increasing treatment periods is minimal, signaling a potential saturation in surface roughness. The observed trend indicates that the rate of ANFs assembly on fiber surfaces is not constant, as will be explained in the following section. It should be noted that error associated with non-contact scanning using an AFM can yield different measurements than the actual surface geometry [162].

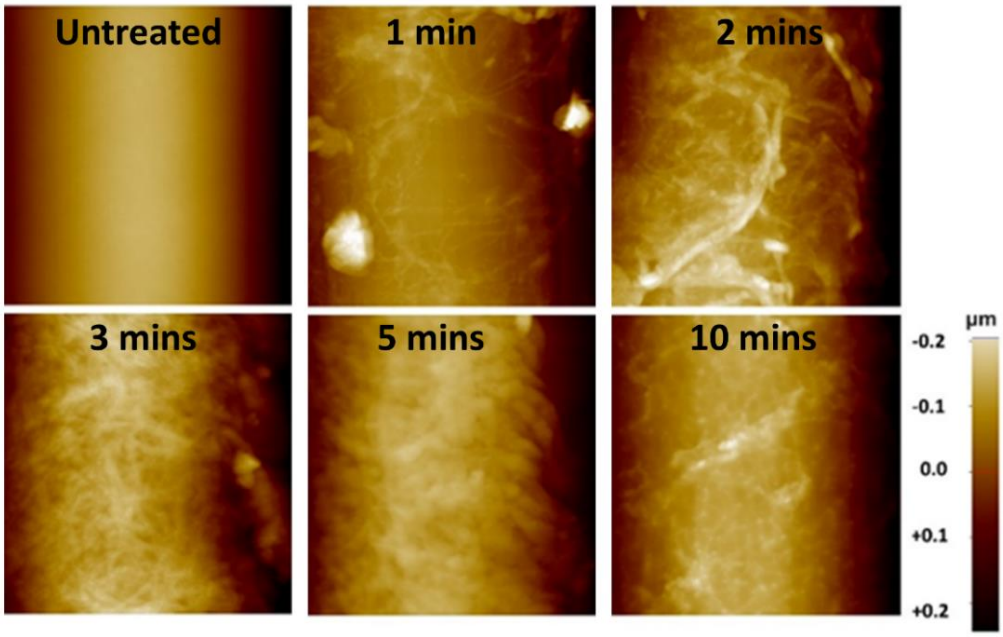

Figure 3.5. AFM surface scans of untreated and ANF coated aramid fibers at various treatment durations.

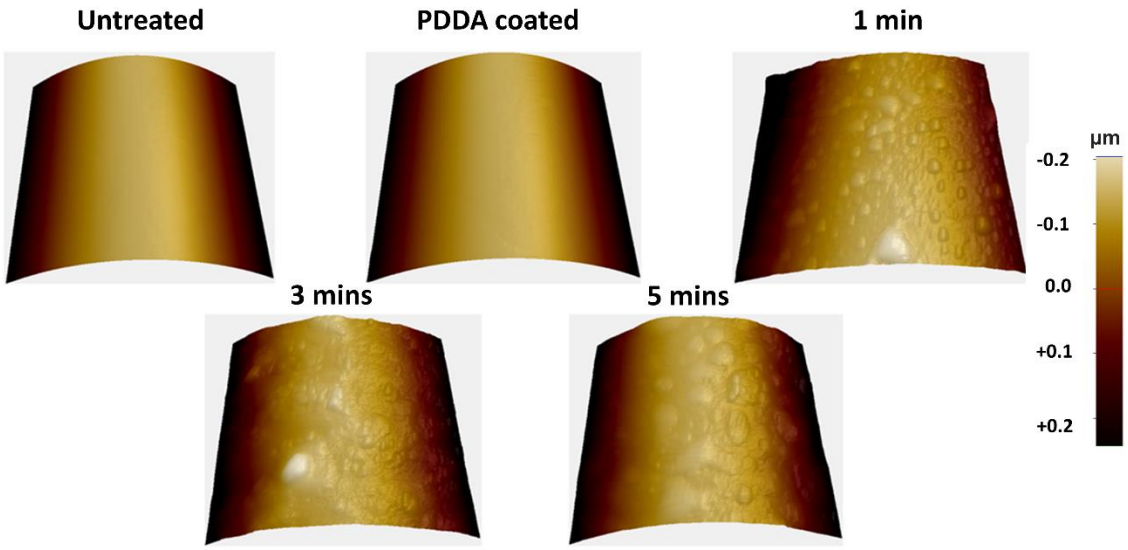

Figure 3.6. AFM surface scans of untreated and ANF coated glass fiber at various treatment durations.

Table 3.1. Measurements of R_q and R_a surface roughness on untreated and ANF coated aramid and glass fibers at various treatment durations.

Treatment	R_q **(nm)**	R_a **(nm)**
Aramid fiber		
Untreated	27.99	24.12
1-minute treatment	51.79	46.92
2-minute treatment	54.39	47.83
3-minute treatment	56.38	49.34
5-minute treatment	56.53	49.09
10-minute treatment	56.13	49.18
Glass fiber		
Untreated	67.1	57.03
PDDA coated	70.64	60.67
1-minute treatment	79.82	68.52
3-minute treatment	89.21	74.57
5-minute treatment	97.78	79.73

The observed non-linear trend and saturation behavior in surface roughness can be justified by examining the ANF surface assembly mechanism (Figure 3.7.). The deprotonated ANFs are initially in a stable dispersion inside the basic solution, as electronic repulsion between neighboring nanofibers keeps them in equilibrium [108]. When a macroscale aramid fiber is introduced, physisorption between ANFs and the macro-aramid fiber surface occurs by means of Van der Waals forces and amide-amide hydrogen bonding, establishing negatively charged ANFs that occupy the aramid surface area and provide a largely increased roughness (Figure 3.7A). Despite minimal evidence of perturbation of electronic states between the adsorbent and adsorbate, adsorption is believed to be primarily established through the previously discussed amide-amide hydrogen bonding, similar to the intermolecular interactions found between aramid crystalline sheets [185]. Such interactions allow for ANFs to sufficiently assemble and strongly adhere to the aramid surface without the need for prior functionalization. Given the absence of such chemical interactions between aramids and ceramic glass, the assembly of ANFs on the glass fiber surfaces is initiated through electrostatic adsorption between the ANFs and PDDA surface coating (Figure

3.7B). The applied PDDA coating positively charges the fiberglass surface, therefore enabling it to attract the negatively charged and dispersed ANFs. Therefore, once the PDDA coated glass fibers are inserted in the ANF suspension, the ANFs begin to assemble on the positively charged fiber surface through electrostatic adsorption. As the adsorption process continues, both aramid and glass fiber surfaces become increasingly negatively charged due the attached ANFs, causing electric repulsion between them and the free ANFs remaining in the dispersion. Additionally, unoccupied fiber surface areas become scarce, making further ANF attachment more difficult. Thus, the observed nonlinear increases in RMS and average surface roughness, and the eventual saturation behavior, are attributed to the decrease in free surface area on the surfaces of the fibers, and the electronic repulsion between attached and free ANFs.

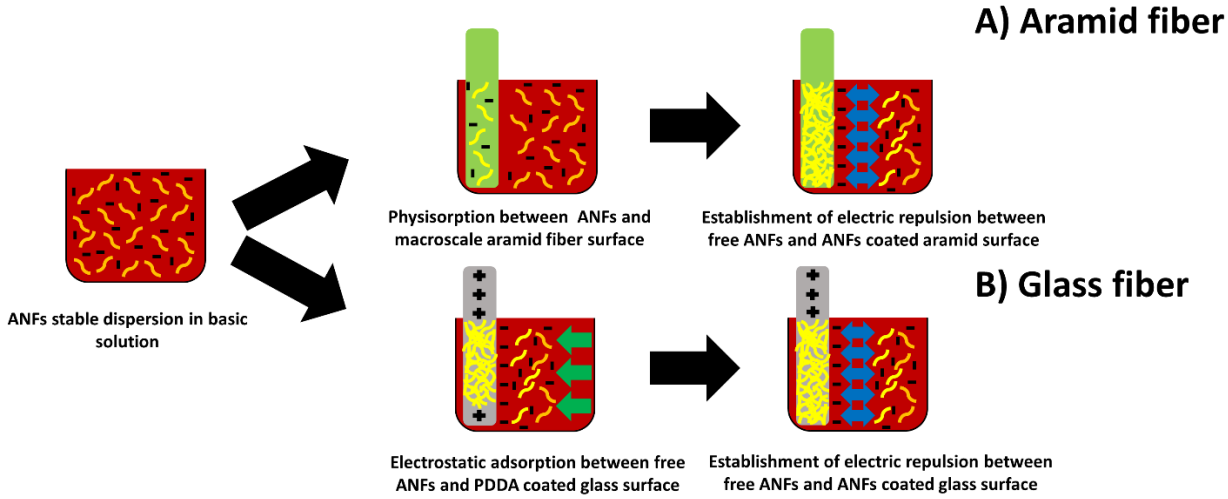

Figure 3.7. Adsorption of ANFs onto aramid and glass fiber surfaces. A) Physisorption of ANFs onto aramid surfaces. B) electrostatic adsorption of ANFs onto PDDA coated glass surfaces.

Given the nanoscale nature of the aramid interphase, its weight quantification is a challenging task. This is particularly difficult in the case of ANFs adsorbed onto aramid fibers, as both the fiber and interphase share similar chemical and thermal properties, causing it to be difficult to distinguish them when using traditional characterization techniques. However, the quantification of electrostatically adsorbed ANF interphases onto glass fibers can be achieved using thermogravimetric analysis (TGA) (Figure 3.8.). This is made possible by the extremely high thermal stability of glass fibers, relative to the polymer interphase [368]. Given that PDDA and ANFs begin to decompose at considerably different temperatures of 315 °C and 536 °C (Figure 3.8A), respectively, TGA analysis of glass fibers at various treatment periods can be used to

quantify the amount of ANFs adsorbed on the surface. Through previous visual inspection of SEM images, the ANF coating on the fiber surfaces is observed to spatially densify with increased treatment periods. In the case of untreated glass fibers, less than a 0.5% decrease in relative weight is observed, which can be possibly attributed to residual organic contamination on the surface. However, ANF coated glass fibers displayed a decreasing trend in relative weight with increasing treatment periods, reaching a maximum decrease of 2.2 % after a 5-minute treatment period (Figure 3.8B). The contributions of both surface coating components to the overall weight of glass fibers can be decoupled through the distinct changes to the slopes of the TGA curves around 250 °C and 500 °C, corresponding to the degradation of PDDA and ANFs, respectively. As observed in Figure 3.8B, the majority of the interphase weight is from the PDDA, as the ANFs consist, at most, less than approximately 0.5% of the overall treated glass fiber relative weight. Given the relatively similar amount of PDDA on fiber surfaces, the observed trend indicates that the quantity of ANFs attached to the fiber surfaces is increased with longer treatment periods, and that electrostatic equilibrium is unattained during a short dip-coating duration of 5 minutes. Moreover, the following measurements confirm the lightweight nature of the adsorbed interphase, therefore avoiding a significant increase to the overall weight of the fibers post-treatment. Finally, given the similarity of interphase density when comparing SEM images of ANF coated aramid and glass fibers, the ANF interphases are also expected to yield similar negligible changes to the weight of macroscale aramid fibers.

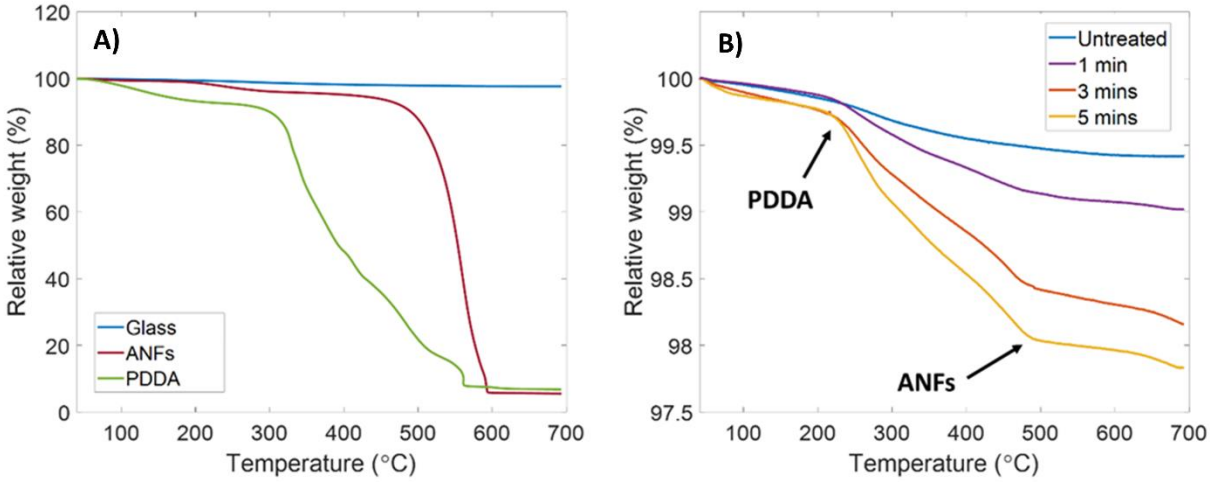

Figure 3.8. Quantification of the ANF interphase. A) TGA of untreated glass fibers, ANFs, and PDDA. B) TGA of untreated and ANF coated glass fibers at varying treatment durations.

Understanding of the adsorption process can be further achieved through investigating the chemical structure of the treated fibers using FTIR. The FTIR spectrum, seen in Figure 3.9A, shows that the ANFs have an essentially unchanged structure in comparison to that of macroscale aramid fibers, with the exception of a significant increase in the peaks corresponding to C=O stretching (1510 cm^{-1}) and Phenyl-N stretching (1309 cm^{-1}). These results indicate that ANFs contain more functional groups such as amines and carboxylic acids, resulting from the deprotonation process. These functional groups have the potential to form covalent and hydrogen bonds with epoxy matrices, therefore strengthening fiber-matrix chemical interactions. Moreover, as shown in Figure 3.9A, the FTIR spectra of ANF coated aramid fibers are similar to that of untreated ones. No significant peak shift or transmittance change are observed, indicating that the short adsorption process does not induce any chemical modification to the macroscale aramid fiber surfaces, and does not risk deteriorating the mechanical properties of the treated aramid fiber. When inspecting the FTIR spectra of untreated and PDDA coated glass fibers, it is found to be mainly dominated by absorbance peaks corresponding to Si-O (1093 cm^{-1}) and Si-OH (993 cm^{-1}) vibrational stretching, and Si-O bending bands (791 cm^{-1}) (Figure 3.9B). This is expected given that glass fibers are primarily composed of silicon oxides and alumina [347,368].Moreover, the PDDA coating is found to yield insignificant changes to the glass fiber FTIR spectrum. However, once treated, the ANF interphase can be detected on the glass surface through the appearance of peaks corresponding to the aramid structure, such as N-H stretching (3326 cm^{-1}), C=O stretching (1645 cm^{-1}), C-N stretching (1541 cm^{-1}), and C=C stretching (1510 cm^{-1}). The detection of these organic bands, despite the volume of ANFs being miniscule relative to that of the bulk material, highlights the potential of the functional groups associated with ANFs to chemically bond with the epoxy resin through covalent and hydrogen bonding. Furthermore. the original Si bands, corresponding to glass fibers, exhibit no shift in their wavenumbers or changes in peak intensities post-treatment, indicating that, similar to aramid fibers, the chemical structure of glass fibers is preserved.

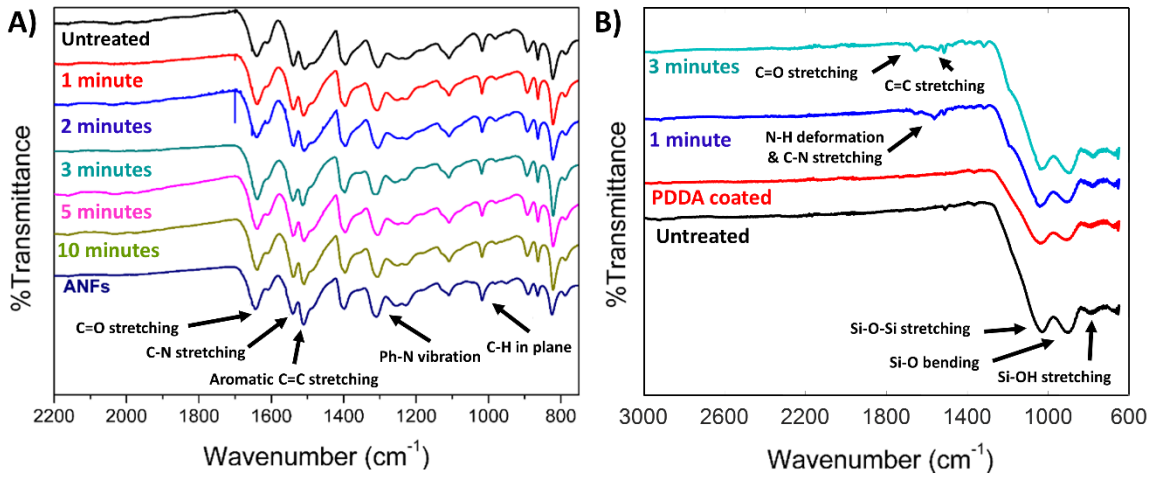

Figure 3.9. FTIR spectra of untreated and ANF coated fibers. A) aramid fibers. B) glass fibers.

Additional insight into the adsorption process is gained by studying the surface chemical composition of the treated fibers. XPS is performed on both untreated and ANF coated fibers, and the results are shown in Figure 3.10. and quantified in Table 3.2. The addition of the ANF interphase to the aramid fiber surfaces results in a significant change to their chemical composition, as the concentration of carboxylic acid (COOH) is increased from 0.0 to 3.14 % after a 3-minute treatment, before saturation. Given the short treatment periods, macroscale aramid fiber hydrolysis can be ruled out and the detected carboxylic acid can be attributed to the introduced ANFs. Previous studies have shown that ANFs gain COOH surface functional groups due to the deprotonation process [136]. The addition of such functional groups to the aramid fiber surface is desired since it increases surface reactivity, and therefore is capable of improving chemical interaction between the fiber and the epoxy matrix. Moreover, the concentration of carboxylic acid can be used to as a mean to quantify the concentration of ANFs adhered to the aramid fiber surface. The saturation in COOH concentration after a 3-minute treatment indicates that the ANF adsorption is halted during longer treatment periods. In addition, the trend between surface COOH concentration and adsorption periods is in good agreement with that of surface roughness reported in Table 3.1. Elsewhere, the surface chemical composition of treated ceramic glass fiber is found to be considerably similar to that of ANFs, displaying the presence of oxygen surface functional groups, such as ketones (~10%) and carboxylic acids (~ 3%), that are initially nonexistent. Thus, the existence of these functional groups on the glass surface confirms the presence of a dense ANF interphase, highlighting the improved surface reactivity and its potential in improving chemical

interaction between the fibers and the matrix.

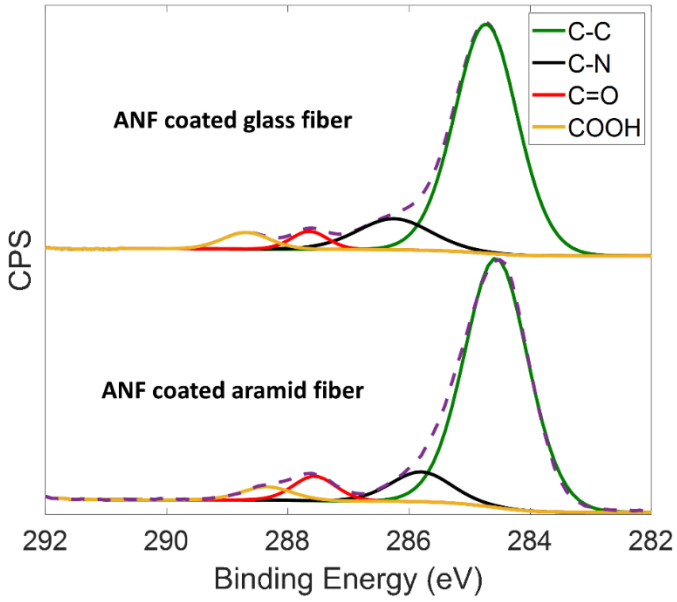

Figure 3.10. Normalized XPS spectra of C1s content of ANF coated aramid and glass fibers, deconvoluted by the existing carbon states.

Table 3.2. Decomposed C1s energy state concentrations and bonding-state peak locations of untreated and ANF coated aramid and glass fibers for various treatment times.

	%C-C (284.7 eV)	%C-N (285.9 eV)	%C=O (287.8 eV)	%COOH (289.3 eV)
Aramid nanofibers	67.46	19.38	8.21	4.95
Aramid Fiber				
Untreated	81.11	10.25	8.64	0.00
1 minute treatment	81.55	9.32	7.5	1.64
2-minute treatment	79.06	11.04	7.75	2.16
3-minute treatment	79.88	11.38	5.6	3.14
5-minute treatment	78.99	12.22	5.35	3.43
10-minute treatment	78.49	12.31	5.79	3.41
Glass fiber				
1-minute treatment	65.32	22.14	10.01	2.43
3-minute treatment	66.47	21.06	9.49	2.97
5-minute treatment	66.84	20.15	10.27	2.74

3.3.3. Measurement of fiber tensile strength

A critical aspect of any interface enhancement method is that its implementation does not degrade the longitudinal properties of the fibers. In order to demonstrate the benign nature of the ANF adsorption process, the tensile strength of single aramid and glass fibers prior to and after various treatments is measured. As discussed in the introduction of this dissertation, many reported surface treatment methods applied to aramid and glass fibers are accompanied with a loss of tensile strength, yielding inferior in-plane properties when integrated into composites. Therefore, the preservation of fiber strength post-treatment is very important to demonstrate the effectiveness of an interface enhancement method. To measure these tensile properties, single fiber tensile testing is performed according to ASTM C-1557 (Figure 3.11A). Fibers of each set are inserted into cardboard frames with 5-minute epoxy (Loctite) at a gauge length of 12.7 mm. The 5-minute epoxy is then cured over at least 8 hours at room temperature. Fiber specimens are tested at an extension rate of 16 μm/s on a 5982 series Instron load frame with a 5 N capacity static load cell, where the

stress-strain curves are calculated in order to obtain corresponding tensile strength measurements. As observed in Figure 3.11B & C, the tensile strength of both aramid and glass fibers are statistically indifferent following PDDA and ANF coating across all treatment periods, which was confirmed using one-way ANOVA analysis (p-value>0.05). This indicates that the proposed dip-coating process is benign and does not weaken the fibers. Such is expected, as the KOH inside the solution is completely consumed during the initial dissolution and deprotonation process that generates the ANFs, resulting in an ANF suspension that is only mildly basic. Moreover, the short treatment periods limit the exposure of the fibers to this basic environment, and therefore ensure that the fiber surface avoids damage. This claim is confirmed by studying the effect of longer treatment durations on the tensile strength of the fibers. Given that aramid fibers are considerably more prone to hydrolysis than glass fibers in such a basic solution, only aramid fibers were considered for this experiment. The tensile strength of aramid fibers soaked for 24 hours in a colloidal ANF/DMSO solution is compared to that of aramid fibers soaked in a KOH/DMSO solution for 24 hours (Figure 3.11D). The fibers treated in the ANF/DMSO solution are observed to retain their original strength, while those dipped in the KOH/DMSO solution display a 12% decrease in tensile strength. The conservation of strength after a long treatment period in an ANF/DMSO solution can be attributed to the absence of KOH, as it is completely consumed during the ANFs deprotonation and dissolution process. In contrast, the considerable decrease in aramid fiber strength post-soaking in a KOH/DMSO solution is attributed to the unreacted KOH inducing aramid hydrolysis, thus leading to the degradation and fibrilization of the aramid fibers. It can be then concluded that the ANF dip-coating process preserves the original tensile properties of the fibers, and that their use in aramid and glass fiber reinforced composites does not risk degrading in-plane properties.

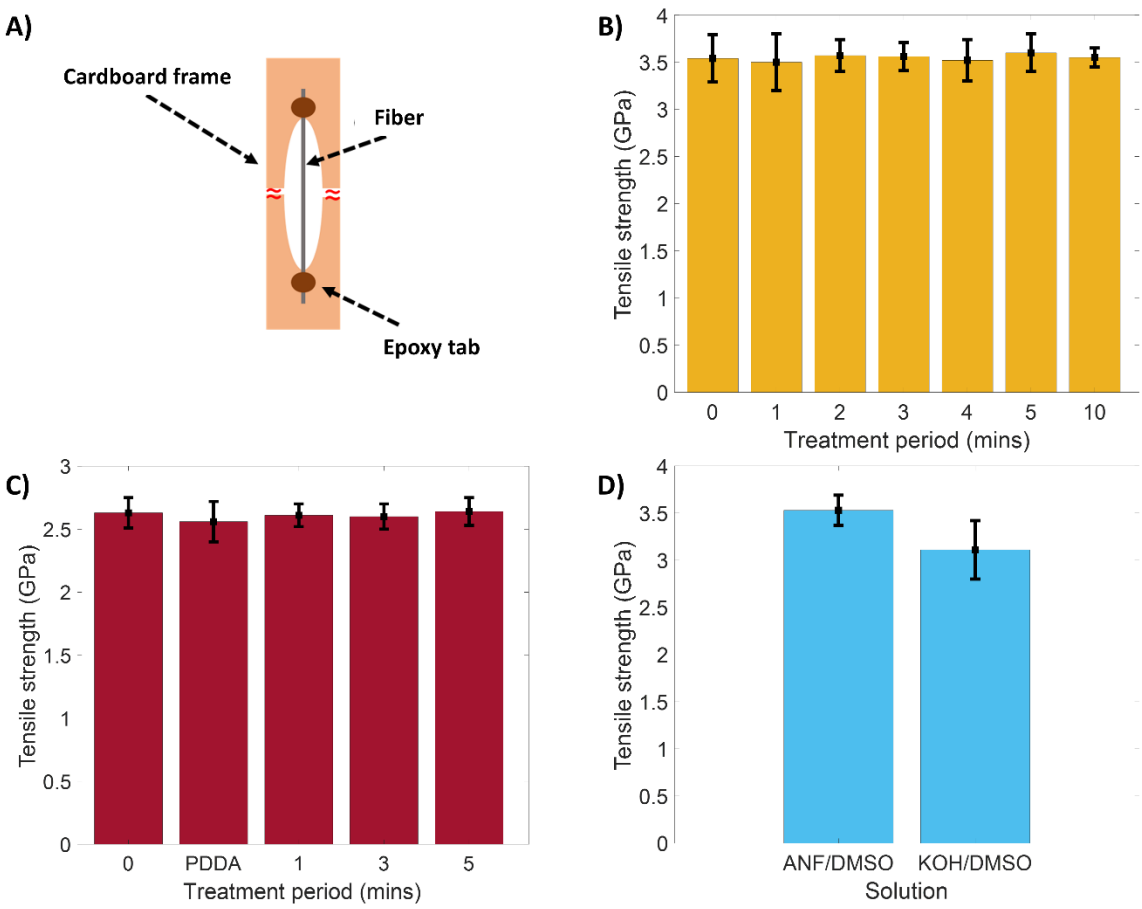

Figure 3.11. Tensile properties of untreated and ANF coated aramid and glass fibers. A) Schematic of single fiber tensile testing specimen. B) Tensile strength of untreated and ANF coated aramid fibers for various treatment durations. C) Tensile strength of untreated and ANF coated glass fiber for various treatment durations. D) Tensile strength of aramid fibers in ANF/DMSO and KOH/DMSO solutions for 24 hours.

3.3.4. Examination of interfacial properties

The addition of an ANF interphase should assist in overcoming the stress discontinuities present in a typical discrete fiber-matrix interface by bridging both its components through a combination of improved mechanical and chemical interactions. To confirm the effectiveness of ANFs as an interfacial reinforcement, IFSS of ANF coated fibers embedded in an epoxy matrix are measured through SFP testing. Single fiber pullout testing is a well-documented method that allows for the measurement of the debonding load between the matrix and embedded fiber [362,364,366]. The nanoscale thickness and uniformity of the ANF interphase along the surface of the fibers, as confirmed through SEM and AFM, ensures that the microscale embedded fiber is an

accurate reflection of the reinforcement mechanism at the macroscale level. Specimens are tested using the setup shown in Figure 3.12A, which allows for loading of the fiber in tension through gripping its free end, at the level of the tab, using a clip, while displacing the epoxy block. This configuration is chosen for testing instead of the more conventional fixed matrix-loaded fiber tab due to the ease of aligning the fiber along the vertical direction by hanging it prior to gripping. Accurate vertical alignment of the fiber is critical for obtaining clean, complete pullout and accurate IFSS measurements. As previously mentioned, the experiment is designed such that debonding of the fiber-matrix interface happens through catastrophic failure by controlling the embedded length to be less than 100 μm (Figure 3.12B). Otherwise, debonding would occur at a constant rate, initiated through an initial crack propagation, while also introducing frictional forces that complicate the determination of IFSS [362]. Given these considerations, and irrespective of the loading configuration [366], the constant shear model developed by Kelly and Tyson is a suitable one for obtaining IFSS [364]. In the case of premature tensile fiber failure during testing, new specimens were retested. The measured IFSS of untreated and ANF coated aramid fibers is shown in Figure 3.12C, while Figure 3.12D demonstrates the independence of the measured IFSS from fiber embedded length. The low data variability also shows uniformity and consistency in the reinforcing capacities of the ANF interphase and its potential on the macroscale level. When compared to the IFSS of untreated aramid fibers (36.5 MPa), a maximum IFSS of 63.83 MPa is observed after a 3-minute treatment, yielding an improvement of 70.27 %. Longer treatment periods of up to 10 minutes shown no significant statistical improvement in IFSS, signaling a saturation in the reinforcing capacities of the ANF interphase. The rate of improvement in IFSS follows a nonlinear trend, as 65% of the maximum IFSS improvement is achieved after only a 1-minute treatment. The displayed saturation of IFSS in lengthier treatments indicate the absence of ANF agglomerations at the fiber-matrix interface. Such agglomerations have been previously show to act as defects and debonding agents along the interface [136]. The observed saturation in IFSS can be attributed to the previously discussed saturation in surface roughness and COOH surface concentration, signaling a limit in the interfacial reinforcing performance of the adsorbed ANF interphase. The direct correlation between aramid fiber surface roughness, the concentration of surface functional groups, and the reinforcement performance of the adsorbed interphases indicate that a combination of mechanical interlocking and chemical interaction are the main reinforcement mechanism. The adsorption and well-adhesion of the nanofiber interphase to the

initially smooth fiber surface through amid-amide hydrogen bonding and coordinated π-π stacking roughens the fiber surface and allows for a higher degree of mechanical interlocking, as the interphase is wetted and diffused into the epoxy matrix. The introduction of such a hierarchical surface structure reduces interfacial stress concentrations and improves load transfer between the rigid fiber and the compliant matrix. Moreover, the carboxylic acid rich ANFs also allow the aramid fibers to overcome their low surface energy [134], providing improved wetting and bonding with the epoxy matrix, while allowing for crosslinking with the epoxy resin during its cure [369,370]. It should be noted that the observed saturation in interfacial properties highlights the brief treatment period required to achieve considerable improvements, indicating that the described process would be compatible with large-scale fiber manufacturing. These results indicate that the ANF physisorption method is a highly effective and efficient technique to improve the interfacial strength in aramid fiber reinforced composites.

In order to assess the influence of electrostatic interactions on the performance of the ANF interphase, interfacial shear strength of the single glass fiber composites is assessed both with and without the presence of a PDDA coating (Figure 3.12E). In the absence of the PDDA coating, a maximum improvement of 52.4% in IFSS is found after a 3-minute treatment (72.9 MPa), relative to that of untreated fibers (47.6 MPa). This is achieved using simple physisorption of ANFs onto the glass surface when inserted in the ANFs suspension. When PDDA is coated onto the glass fiber surface, a new maximum IFSS of 87.21 MPa is reached, corresponding to an 83.2% increase relative to untreated glass fibers. The electrostatic interactions between the positively charged PDDA coated fiber surface and the negatively charged ANFs induces the assembly of a more tightly packed nanostructured interphase, yielding an improved adhesion to the fiber surface. Furthermore, the PDDA coating results in a more uniform ANF interphases for a specific treatment, as the standard deviation in all data sets is observed to be reduced. The uniform positive charge across the fiber surface due to the PDDA reduces inconsistencies during ANF surface assembly, rendering ANF adsorption a more consistent process. As previously discussed, the observed interfacial reinforcement is a result of the coarser fiber surface, which allows for the glass fiber surface to be firmly embedded inside the epoxy matrix, improving the transfer of mechanical stresses between the elastically mismatched constituents of the interface. In addition, the excellent compatibility of the interphase with the epoxy resin, through the addition of polar functional groups, helps improve surface wetting and enables chemical bonding between the matrix and the

previously unreactive fiber surface. When the treatment period is increased to 5 minutes, the IFSS is found to decrease both with and without the use of a PDDA coating by 77% and 49% relative to 3-minute treatments, respectively. The porous and non-uniform ANF networks formed across the fiber surface after a 5-minute treatment (Figure 3.4G & H) increase the density of defects at the interface and disrupts the resin wetting process, forming a discontinuous and defective interfacial region [134]. However, the resulting IFSS remains comparable to that of untreated glass composites. It can be then concluded that similar to an ANF interphase phisisorbed on aramid fibers, an electrostatically adsorbed ANF interphase is capable of reinforcing the glass fiber-epoxy matrix interface.

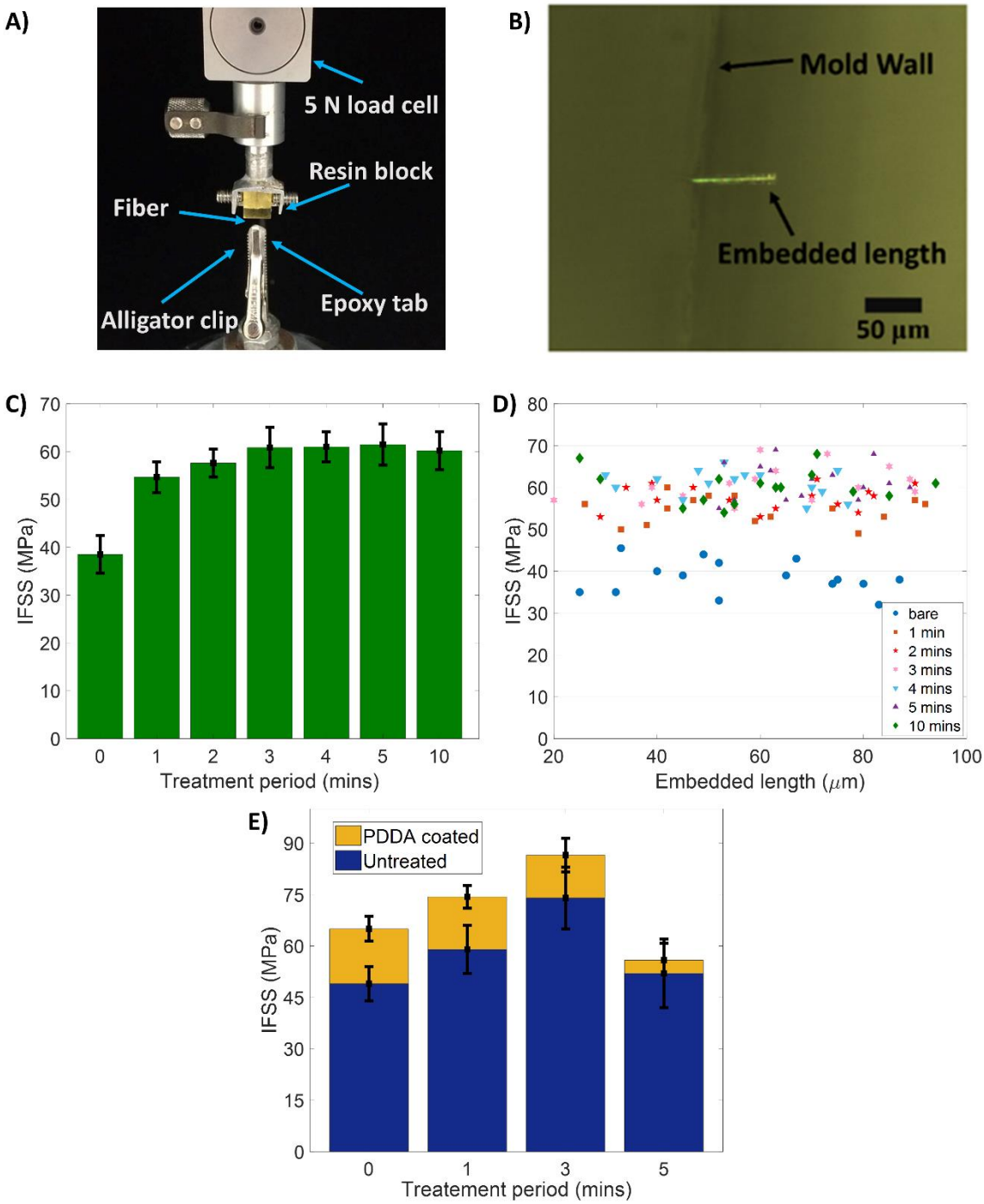

Figure 3.12. Interfacial properties of untreated and ANF coated aramid and glass fibers. A) Single fiber pullout experimental test setup. B) Controlled embedded length of tested specimen. C) Interfacial shear strength of untreated and ANF coated aramid fibers. D) IFSS vs embedded lengths of aramid specimens. D) IFSS of untreated and PDDA coated ANF coated glass fibers.

3.3.5. Examination of interlaminar properties

To demonstrate that the achieved interfacial improvements translate into a laminated composite, the adsorption process is applied to aramid and glass fabrics and short beam shear testing is performed. With interfacial adhesion being a critical aspect to the overall mechanical performance of composites, its enhancement is expected to be reflected in improvements to the bulk properties of the composite. Given that delamination is a major cause of failure in composites, a well adhered fiber-matrix interface is necessary to reinforce the interlaminar region and provide greater resistance to crack initiation and propagation. The short beam strength of a composite is often dependent on interfacial adhesion, as well as the toughness of the matrix, and thus can be used to demonstrate the effects of an ANF interphase on the fiber-matrix interactions in bulk composites. Here, composite plates are fabricated using a vacuum assisted resin transfer molding (VARTM) process. ANF coated aramid and glass fabric preforms are infused with Epon 862/Curing Agent W resin mixture (100:26.4), and then cured at 177 °C for 150 minutes in a hot press (100 psi). Specimens are then cut to dimensions according to ASTM D2344 standard and tested on a 5982 series Instron load frame, using a 3-point bending fixture and a 100 kN load cell at a cross-head speed of 1 mm/min (Figure 3.13A). Short beam strength (SBS) is calculated according to Equation (3.4.):

$$SBS = \frac{3P}{4bt} \tag{3.4.}$$

Where b is the width, t is the thickness in the direction of the applied load and P is the maximum applied load at the center of the specimen. The SBS of untreated aramid reinforced composites is measured to be 17.23 MPa and is found to increase to 20.59 MPa after a one-minute treatment, corresponding to a 19.5% improvement (Figure 3.13B). Further improvement is observed in specimens with treatment periods of 2 and 3 minutes, registering a 24.31% and 25.6% increase compared to untreated specimens, respectively, but only a 4.03% and 5% increase over 1-minute treated specimens, respectively. The considerable improvement in SBS signifies that the ANFs web-like structures seen in Figure 3.3E & 3.3F did not contribute to the formation of voids and defects inside the composites. Moreover, no degradation in SBS is observed for treatment periods longer than 3 minute, as confirmed using one-way ANOVA analysis (p-value > 0.05). The described saturation in SBS agrees well with that previously observed in IFSS. The SBS of the ANF coated glass fiber composites is also found to follow an identical trend to that of its

corresponding IFSS, as it displays a maximum of 57.1 MPa after a 3-minute treatment period, corresponding to a 35.3% improvement in SBS relative to PDDA coated composites (42.2 MPa) (Figure 3.13C). It should be noted that only the SBS of glass composites coated with both PDDA and ANFs is studied, given their superior interfacial reinforcing performance during SFP testing. The SBS of untreated SBS specimens (39.43 MPa) is found to be 6.56% lower than that of PDDA coated specimens (42.2 MPa). Yet in order to isolate the effect of ANFs on the interlaminar properties of glass fiber composites, the performance of PDDA/ANF treated specimens is compared to that of only PDDA coated specimens. The improved SBS highlights the ability of the ANFs to reinforce the interlaminar region of aramid and glass fiber composites, as the introduced interphase reduces shear stress concentration and allows for a higher capacity to withstand mid-span deformation. When the ANF interphase is embedded in the matrix, the discrete interlaminar region becomes hierarchically nanostructured, therefore bridging discontinuities and delaying interlaminar failure through an improved load transfer mechanism between the fiber and the matrix. While short beam shear testing measures the behavior of the bulk material, it is often dictated by the properties of the interface. Therefore, it should be expected that an improved interfacial shear strength translates into an improved interlaminar shear strength. It should be noted that interfacial adhesion is not the only mechanism dictating failure under short beam shear loading, and therefore a lower bulk strength enhancement is expected when compared to IFSS improvements alone. However, ANFs have also been shown to improve the mechanical properties of the epoxy matrix, including its fracture toughness and elastic properties [110]. Therefore, in the case where a small amount of ANFs detach from the surface during the VARTM process, it can locally toughen and strengthen the matrix, providing further means for improving SBS of these composites. For a longer treatment period of 5 minutes, 57% and 25% decrease in SBS of the glass fiber composite is observed relative to that of the 3-minute ANF treated and PDDA coated glass SBS specimens, respectively. The weaker composite performance can be attributed to the accumulation of defects within the interlaminar region due to the poor quality of the fiber-matrix interface and the partial blocking of resin infiltration during VARTM (Figure 3.4G & H). Greater insight into the strengthening mechanism of the ANF interphase on glass fiber composites is obtained through the analysis of stress vs mid-span extension curves obtained during SBS tests (Figure. 3.13D). Glass fiber polymer matrix composites are known to possess short beam strength and stiffness that are relatively higher than that of polymer fiber based ones, such as aramids, yet

they are unable of supporting a similar amount of large mid-span deformations [371]. Therefore, these composites typically fail abruptly at the mid-plane section due to their low ductility and the accumulation of high interlaminar shear stress concentrations in them. This is reflected in the observed brittle response of the untreated glass composite, as highlighted by a sharp drop in stress at failure and its inability to support a steady stress state. However, in the presence of an ANF interphase, the failure mode of the glass fiber composites is hybridized to include certain characteristics that are unique to polymer fiber reinforced composites. The ANF reinforced glass specimens display a smoother transition from a maximum stress to an inferior and residual one, showing the ability to carry up to 75% of the maximum experienced stress, while supporting larger mid-span deformations. Therefore, the improved fiber-matrix interactions due to the introduction of an ANF interphase allows higher resistance to shear stress at both the interface and interlaminar region, providing a method to alleviate the primary failure mechanism in glass fiber reinforced composites. In conclusion, the introduced ANF interphase is able of providing a stronger interlaminar region in aramid and glass fiber reinforced composites.

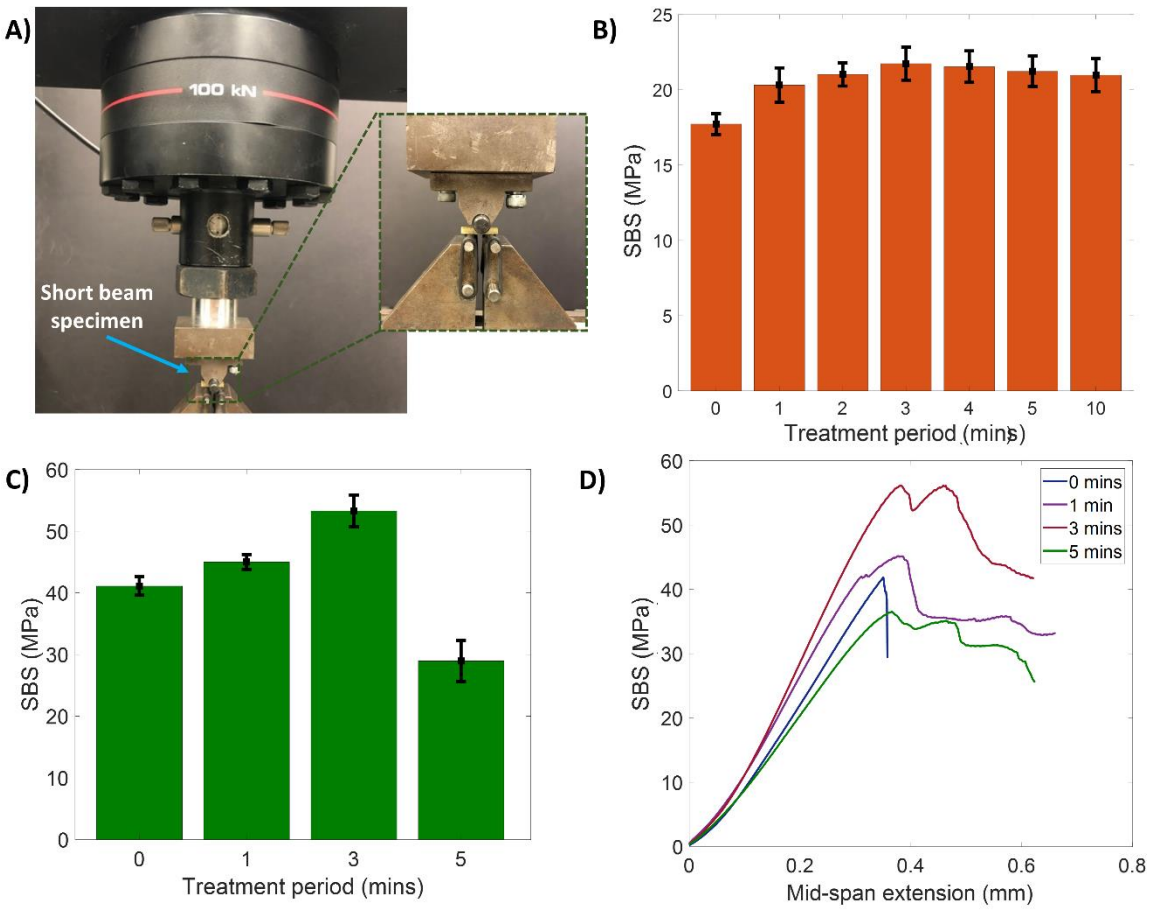

Figure 3.13. Interlaminar properties of untreated and ANF coated aramid and glass fiber reinforced composites. A) Experimental setup for short beam testing. B) SBS of untreated and ANF coated aramid composites. C) SBS of untreated and ANF coated glass fiber composites. D) Stress vs mid-span extension curves of glass fiber composite during short beam testing.

The failure modes of the short beam specimens are studied using post-testing SEM imaging. The inelastic deformation failure mode of the aramid specimens, derived from there high fracture toughness, is preserved and strengthened. Given the non-delaminating failure mode of aramid short beam specimens, the effect of ANFs during aramid delamination is studied through micrographs of manually delaminated 3 minute-treated aramid short beam specimen surfaces (Figure 3.14A-C). The delaminated surfaces are prepared by manually bending the SBS samples post-freezing them in liquid nitrogen to induce brittle failure. The nanostructured interphase is found to be unbundled and dispersed on the lamina surface (Figure 3.14B & C). This indicates the ability of the ANFs to maintain their bonding with the surface of the fiber throughout the resin infusion, curing process and interlaminar failure. SEM imaging of glass SBS fractured surfaces also reveals morphological changes due to the ANF interphase. In the case of PDDA coated SBS specimens, adhesive failure is clearly detected, as uncovered glass fibers and minimal matrix material can be found across the surface (Figure 3.14D & E). Yet in the presence of ANFs, the fractured glass SBS surfaces are found to be considerably covered with matrix residues (Figure 3.14F-J) and ANF networks (Figure 3.14K & L), indicating stronger adhesion between the glass surface and the matrix, and signaling a more cohesive interlaminar failure. The ANF reinforced fiber-matrix interface induces strong inter-ply adhesion and forces-initiated cracks to grow away from the interlaminar boundaries, thus providing the glass fiber composites with improved fracture energy absorption mechanisms. Such findings confirm that the glass SBS specimens exhibit inelastic deformation during failure, in addition to their original failure mode of interlaminar shear. Therefore, an ANF interphase considerably toughens glass fiber composites, while maintaining and reinforcing their unique high strength and stiffness. In conclusion, the adsorbed ANF interphase is capable of simultaneously strengthening and toughening both aramid and glass fiber reinforced composites, while introducing unprecedented and desirable characteristics into their failure modes. In the following section, the dissolution and deprotonation process used to generate ANFs will be considerably shortened in order to act as a macroscale aramid fiber surface treatment. The treatment maintains the structural integrity of the aramid fibers, while generating surface

nanofibrils and polar functional groups that improve its reactivity and mechanical interlocking abilities in a composite. The effect of the proposed fibrilization treatment on the interfacial and interlaminar properties of aramid fiber reinforced composites will be extensively studied and discussed.

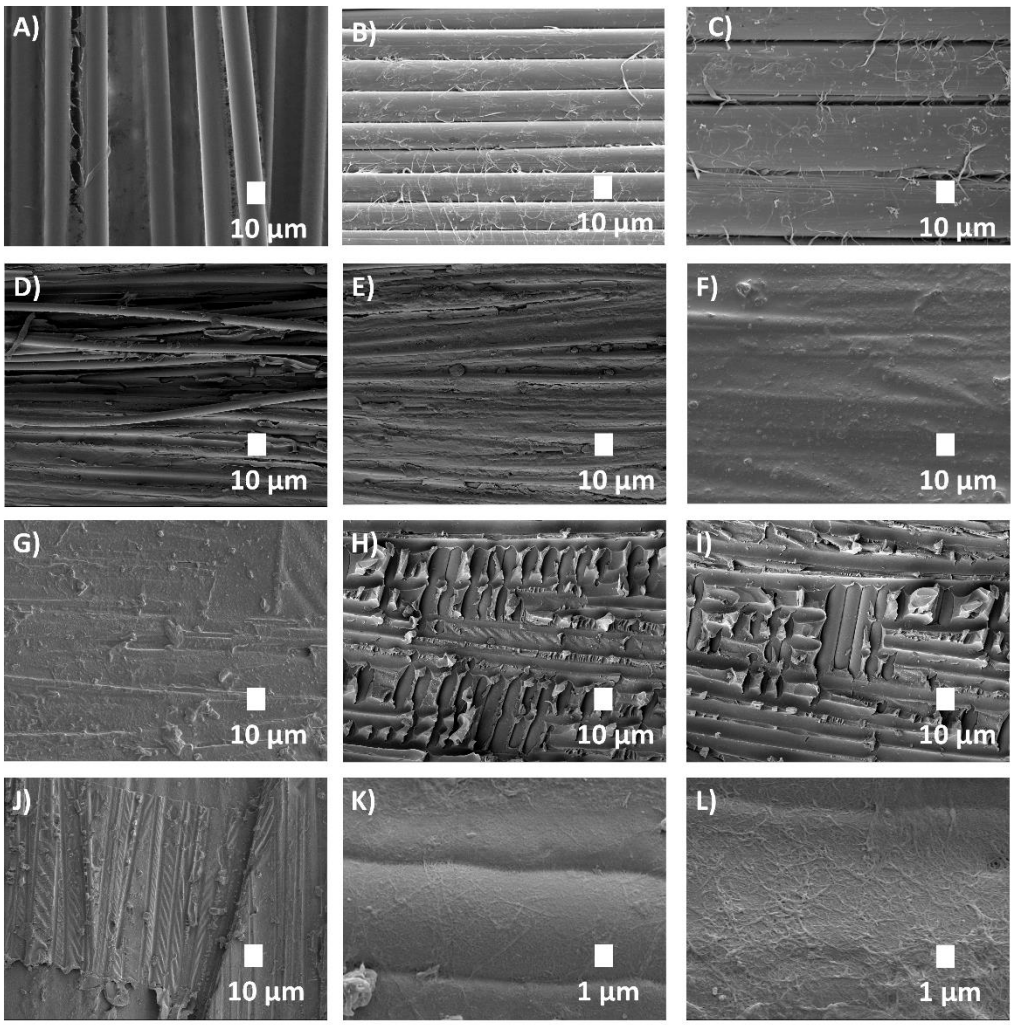

Figure 3.14. Fractured surfaces of untreated and ANF coated aramid and glass fiber composites. A) Surfaces of dip-coated aramid fabric pre-fabrication of laminate. B &C) Delaminated surfaces of an ANF coated aramid reinforced composite. D) & E) PDDA coated glass surface. F) & G) 1-minute PDDA/ANF coated glass surface. H-J) 3-minute PDDA/ANF coated glass surface. K & L) ANFs networked structures at the fracture surfaces of 3-minute PDDA/ANF coated glass short beam specimens.

3.4. Aramid fibrilized interphase

3.4.1. Fibrilization of aramid fabric

In lieu of completely dissolving the aramid fibers into ANFs, it is possible to fibrilize their surfaces using a similar deprotonation process, yet at considerably shorter treatment periods that preserve the aramid fiber structure while populating its surfaces with aramid nanofibrils. Here, fibrilization of the aramid fabric is achieved using the following procedure. Aramid fabric (KM2+, DuPont) is cut into 5 cm × 5 cm squares, successively cleaned using acetone and ethanol, and then dried at 100 ˚C for 12 hours under vacuum. A solution consisting of 1.5 g of KOH (ACS certified, Fisher Scientific) and 500 mL of DMSO (ACS certified, Fisher Scientific) is prepared in a 1-liter glass beaker. The solution is stirred for 30 mins prior to adding the aramid fabric strips to the beaker. The fabric pieces are soaked in the solution and then removed successively over the next 4 hours, at a 1-hour interval (Figure 3.15.). The fibrilized aramid strips are then washed with ethanol and dried at 80 ˚C under vacuum for 12 hours.

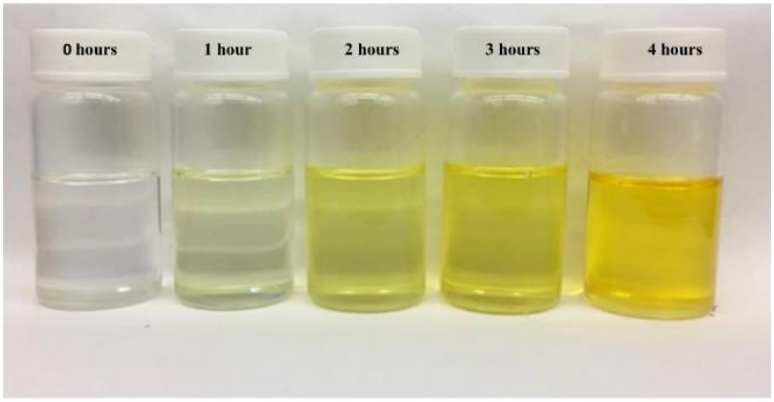

Figure 3.15. Color change of the DMSO/KOH solution as fibrilization process ensues.

3.4.2. Characterization of surface chemistry and morphology

The effect of the fibrilization process on the aramid fiber surface morphology is evaluated through SEM imaging before and after treatment. The resulting changes to the aramid surface can be noted by the densification of fibrils, as shown in Figure 3.16. The diameter of the resulting fibrils ranges from over 2 microns (Figures 3.16B & C) to less than 300 nm (Figures 3.16E & F). The formation the fibrils is attributed to the deprotonation process that macroscale aramid fibers endure in such a basic condition [108]. As inter-chain hydrogen bonds are broken, aramid fibrils

start to disassemble from the macroscale fibers, eventually forming a uniform suspension of aramid nanofibers. The fibrils appear in random orientations and varied sizes. As the fibrilization period is increased, more negatively charged aramid nanofibers are formed and dissolved into the solution, as detected by the change in solution color seen in Figure 3.15. In this study, relatively short treatment periods are investigated in order to avoid any significant damage to the mechanical properties of the macroscale aramid fibers. Moreover, short fibrilization periods ensure that a significant amount of the newly formed fibrils remain connected to the aramid fiber surfaces, since the strength of the fibril-fiber bond is important to the reinforcement performance of the newly introduced interphase. Figure 3.16D displays how formed fibrils can maintain their partial attachment to the fiber. The obtained microstructure can play a key role in enhancing mechanical interlocking at the fiber-matrix interface.

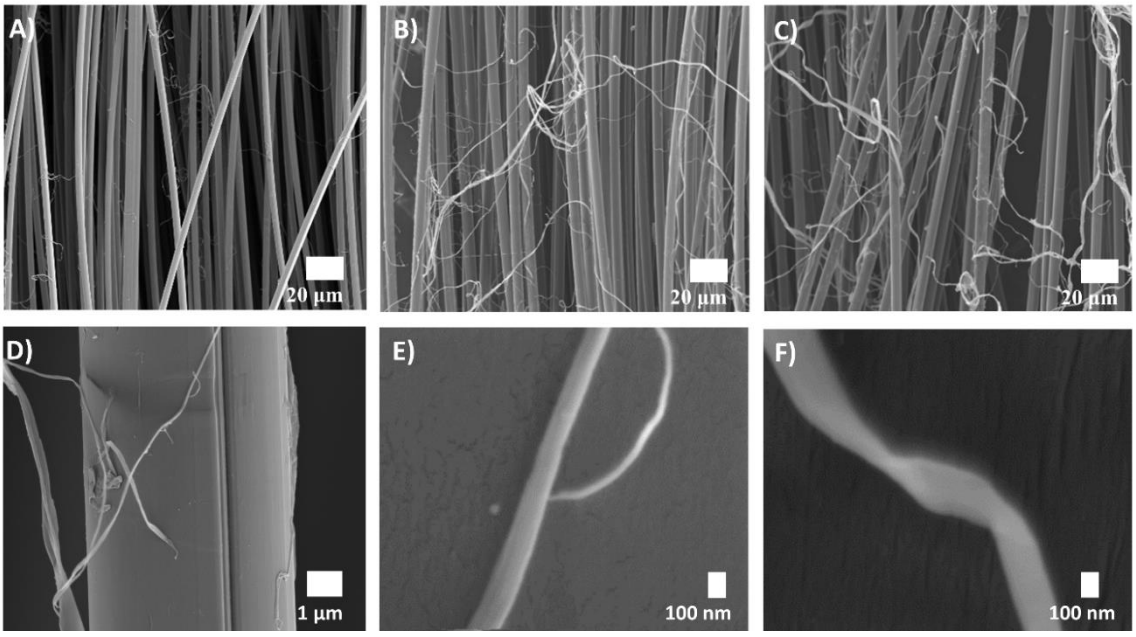

Figure 3.16. Scanning electron microscopy images of untreated and fibrilized aramid fibers. A) Untreated fibers. B) Aramid fibers after a 2-hour fibrilization treatment. C) Aramid fibers after a 3-hour fibrilization treatment. D) Aramid fibrils bonded to macroscale fiber. E) & F) Nanoscale aramid fibrils.

The characterization of the aramid surface chemical composition post-treatment allows for greater understanding of how the fibrilization process effects the chemical reactivity of aramid fibers. XPS is performed on untreated and fibrilized aramid fibers, and the results are shown in Figure 3.17., and quantified in Table 3.3. The XPS spectra show an increasing amount of

carboxylic acid (COOH) formed during the fibrilization process, indicating an ongoing hydrolysis process on the surface of the aramid fibers. The concentration of carboxylic acid on the surface of aramid fibers is observed to increase up to 4.04% as the treatment period reaches 3 hours. Meanwhile, increases in ketone (C=O) bonds and C-N bonds are also observed with increasing treatment periods, due to deprotonation initiated by the basic nature of the treatment solution, which cleaves the amide bond into a primary amine and a carboxylic acid. As previously mentioned, methods of adding polar functional groups to the surface of aramid fibers are always desired since they can increase surface reactivity and improve chemical interaction between the fiber and the epoxy. An increase in oxygen-containing functional groups on the fibrilized aramid fiber surfaces can lead to better wettability to matrix materials, such as epoxy, and therefore improving fiber-matrix interfacial adhesion.

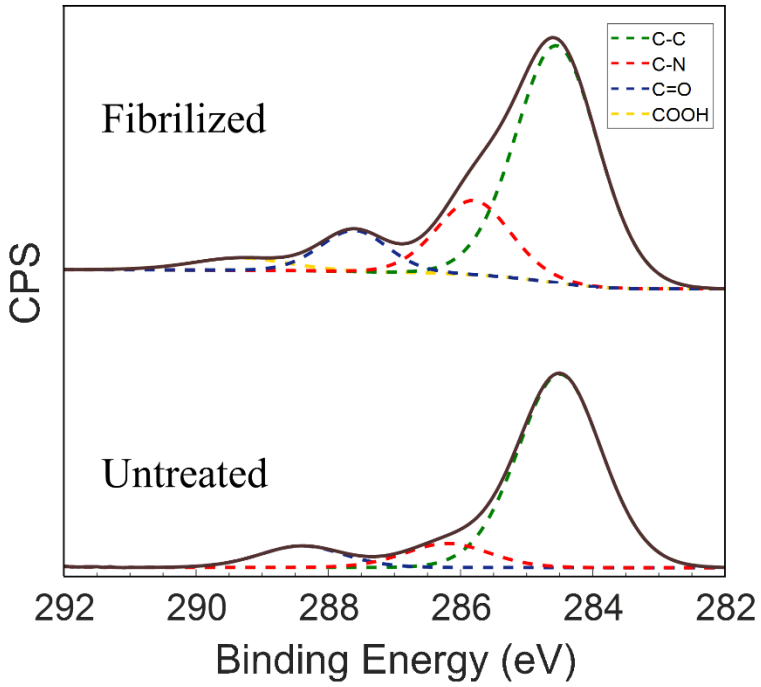

Figure 3.17. Normalized C 1s XPS spectra of untreated and fibrilized aramid fibers. The spectra are deconvoluted by the existing carbon states.

Table 3.3. Experimental bonding-state peak locations and concentrations of the decomposed C 1s energy state of untreated and treated aramid fibers.

	% C-C (284.7 eV)	% C-N (285.9 eV)	% C=O (287.8 eV)	% COOH (289.3 eV)
Aramid fiber				
Untreated	80.97	10.04	8.99	0.00
1-hour treatment	77.54	13.51	8.8	0.25
2-hour treatment	73.54	13.97	9.05	4.44
3-hour treatment	67.49	18.88	9.59	4.04
4-hour treatment	65.1	21.16	10.08	3.67

Further characterization of the fibrilized aramid chemical structure is obtained using FTIR. Figure 3.18A shows that there are no major changes in the IR spectra of the fibrilized aramid fibers when compared to untreated ones, indicating that no significant degradation took place during the fibrilization process. Nonetheless, detailed FTIR spectra in Figure 3.18B shows a relatively increased absorbance of the peak located at 1610 cm^{-1} in fibers fibrilized for 2 or more hours, corresponding to an increase in C=O stretching. This indicates an increase of carboxylic acid groups, which agrees with the XPS results. Furthermore, a peak shift corresponding to aromatic C=C stretching is observed in the spectra of fibers treated for 2 or more hours. The peak shifts from 1507 cm^{-1}, for untreated and 1 hour treated fibers, to 1515 cm^{-1}, for the remaining of treated fibers. The described shift indicates a decrease in the conjugation length of the p-phenylene terephthalamides (PPTA) molecules. This is assumed to be due to the dissolution and deprotonation process during fibrilization, which cleaves the hydrogen and amide bonds within the highly crystalline aramid fibers, forming free ends of amine and carboxylic acid functional groups. The free ends of the functional groups lead to a less stacked molecular structure on the surface of treated aramid fibers. The presence of such functional groups on both the surface of the aramid fiber and fibrils allows for improved adhesion and chemical interaction between the fiber surface and the matrix, while retaining the original chemical structure that gives aramid fibers its unique mechanical properties.

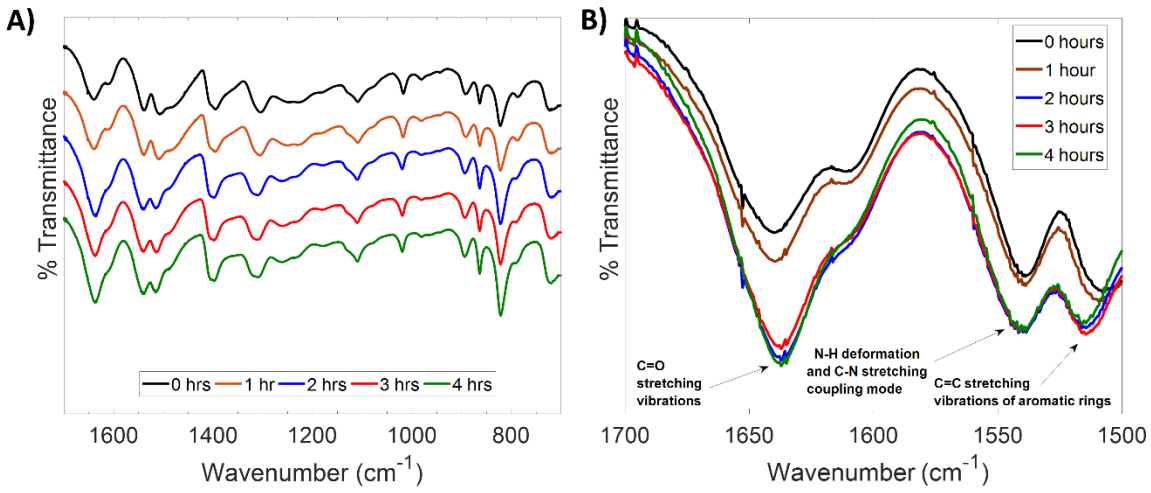

Figure 3.18. FTIR of untreated and fibrilized aramid fibers. A) Normalized FTIR spectra of aramid fibers for different treatment periods. B) Normalized FTIR spectra of different treatment periods showing a reduced transmittance of C = O stretching, which signals an increase in carboxylic acid surface functional groups.

3.4.3. Measurement of fiber tensile strength

As previously mentioned, the enhancement of the fiber-matrix interface should not come at the expense of the strength of the fibers, so it is essential to maintain the critical in-plane properties of the resulting aramid composite. To ensure that the fibrilization process does not significantly degrade the tensile properties of aramid fibers, single fiber tensile testing is performed on untreated and fibrilized aramid fibers using the similar experimental process detailed in section 3.3. Figure 3.19A shows the tensile strength for untreated and treated fibers, while Figure 3.19B shows the linear behavior of the corresponding stress and strain curves. None of the treated fiber sets display any significant statistical decrease in tensile strength when compared to untreated fibers, confirming the benign nature of the fibrilization process used here. However, it should be noted that, as previously shown in Figure 3.11., such a treatment is capable of reducing aramid fiber strength if prolonged, thus justifying the relatively short treatment durations employed here. It can be then concluded that the tensile strength of aramid fibers is fully preserved after the fibrilization process, and that in-plane properties of aramid fiber reinforced composites are not at risk of decreasing.

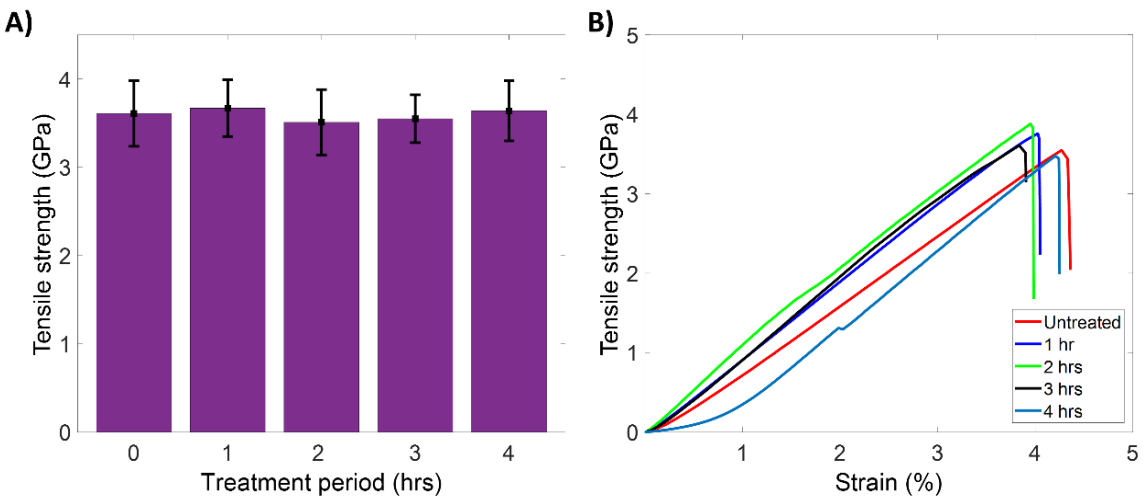

Figure 3.19. Tensile properties of untreated and fibrilized aramid fibers. A) Tensile strength. B) Corresponding stress-strain curves.

3.4.4. Examination of interfacial properties

The interfacial strength of untreated and fibrilized fibers is obtained through quasi-static SFP testing, and the results are shown in Figure 3.20. Initially, IFSS of the single fibrilized aramid fiber composites are observed to improve as the fibrilization period is increased (Figure 3.20A). After a fibrilization period of three hours, a maximum IFSS of 74.3 MPa is obtained, showing approximately a 128% increase from an IFSS of 32.7 MPa for untreated fibers. The increase in IFSS is consistent across varying embedded lengths (Figure 3.20B), implying that the improved IFSS is independent of fiber geometry or the embedded fiber surface area. This low IFSS variability over the full range of embedded lengths allows for the assumption of a consistent and uniform improvement of fiber-matrix interactions all along the interface, and the potential of the fibrilization treatment to improve the reinforcing performance on a macroscale level. The significant improvement in IFSS can be attributed to the increased mechanical interlocking, since the fibrilization process creates a hierarchical structure at the surface that enhances the interaction and load transfer between aramid fibers and matrix. Moreover, the improved surface reactivity due to the introduced surface oxygen functional groups allows for enhanced chemical interaction between the fiber and the matrix. However, it should be noted that the increase in IFSS saturates after a fibrilization period of three hours, before showing a drop. Regardless, the IFSS from fibers after a 4-hour treatment is still 75.2% higher than untreated fibers. A possible reason for the

observed drop in IFSS is that the aramid fibril-fiber interface is weakened as the reaction ensues. With increasing fibrilization periods, fibrils generated at an early stage will detach from the fiber surface, and thus lose their ability to provide mechanical interlocking between the fiber and the matrix. However, the aramid fibers will still retain some of the original fibrils, while new fibrils will continue to be generated during the fibrilization process, resulting in an IFSS higher than that of untreated fibers. Additionally, it should be noted that the fibrilization process is expected to continue in the case where the aramid strips are kept in solution until fibers are completely dissolved, and a stable dispersion of aramid nanofibers is formed, similar to what is reported in Yang et al. [108]. However, as fibrilization period is prolonged, the risk of weakening the tensile strength of the aramid fibers is also considerably increased (Figure 3.11D). Therefore, an optimized fibrilization period of three hours is preferred to achieve the best fiber-matrix reinforcing performance.

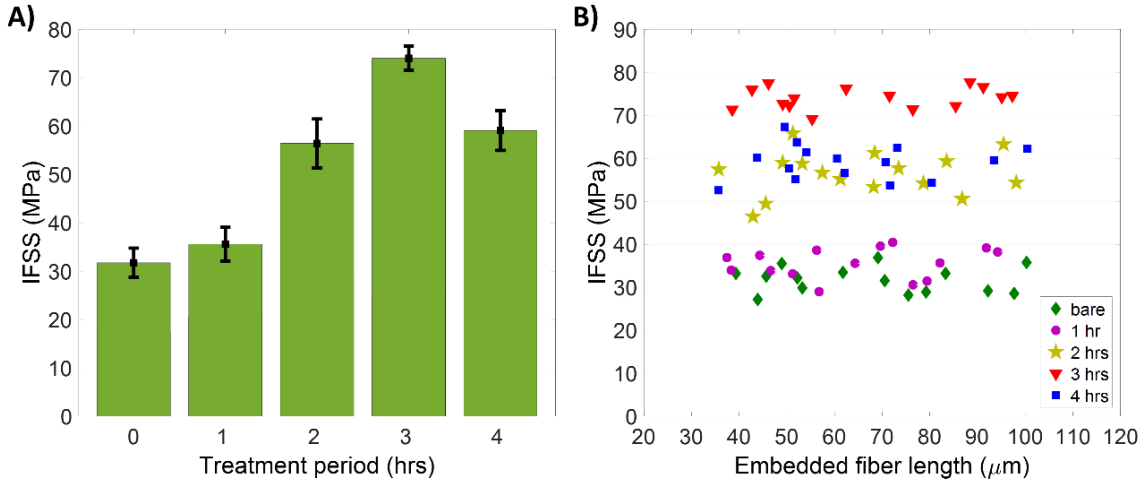

Figure 3.20. Interfacial properties of untreated and fibrilized single fiber aramid composites. A) Interfacial shear strength of aramid fibers at various treatment periods. B) Distribution of interfacial shear strength over the range of embedded lengths for various treatments periods.

3.4.5. Examination of interlaminar properties

The observed increase in IFSS should translate to an improved interlaminar behavior in laminated aramid composites since the quality of the interlaminar region is often dependent on the adhesive shear strength between the fiber and matrix. The untreated and fibrilized aramid laminates were fabricated using a VARTM process and tested according to ASTM D2344. A maximum SBS of 28.3 MPa is observed after a 2-hour treatment, reflecting a 63% improvement relative to

untreated aramid specimens (17.65 MPa) (Figure 3.21A). Although SBS is maximized through a 2-hour treatment, the recorded SBS after 3 and 4 hours of fibrilization still exceeds that of untreated aramid fibers. Similar to IFSS, the drop in SBS can be attributed to the detachment of fibrils from the surface of the aramid fibers. However, the formation of new fibrils ensures the maintenance of a superior SBS, relative to that of untreated aramid specimens. Greater understanding of this toughening mechanism in aramid fiber reinforced composites can be achieved by analyzing the failure modes of the specimens post-testing. Typical short beam failure modes of composite specimens are shown in Figure 3.21C, while Figure 3.21D displays untreated and fibrilized aramid short beam specimens post-testing. The observed failure mode in untreated aramid specimens is inelastic deformation. However, fibrilized specimens are found to fail in a combination of inelastic deformation and interlaminar shear at the mid-thickness of the specimens. Interlaminar shear is a failure mode that is usually attributed to glass and carbon fiber reinforced composites[372], both of which usually possess a considerably higher SBS than that of aramid reinforced composites. This claim can be further proven through examining the stress-displacement curves recorded during short beam shear tests (Figure 3.21B). Untreated aramid specimens do not exhibit a sharp drop in stress at failure and continue to carry almost 80% of the recorded peak load until the end of the test. In contrast, failure in fibrilized samples is attained in the form of a sharp drop in stress to a residual stress that ranges between 75% and 85% of the maximum experienced short beam stress. However, the specimens remain able of carrying a portion of the load until the end of the test, in a similar manner to untreated specimens. The conserved ability to carry short beam load is a characteristic of the inelastic deformation failure mode of tough aramid fiber composites, while the featured sharp drop after reaching peak load usually signals an interlaminar shear failure mode. Therefore, the fibrilization process conserves the high fracture toughness properties of aramids, while also yielding a higher SBS. In conclusion, the fibrilization process can strengthen the interlaminar region of aramid reinforced composites, while maintaining its original and unique failure mode of inelastic deformation.

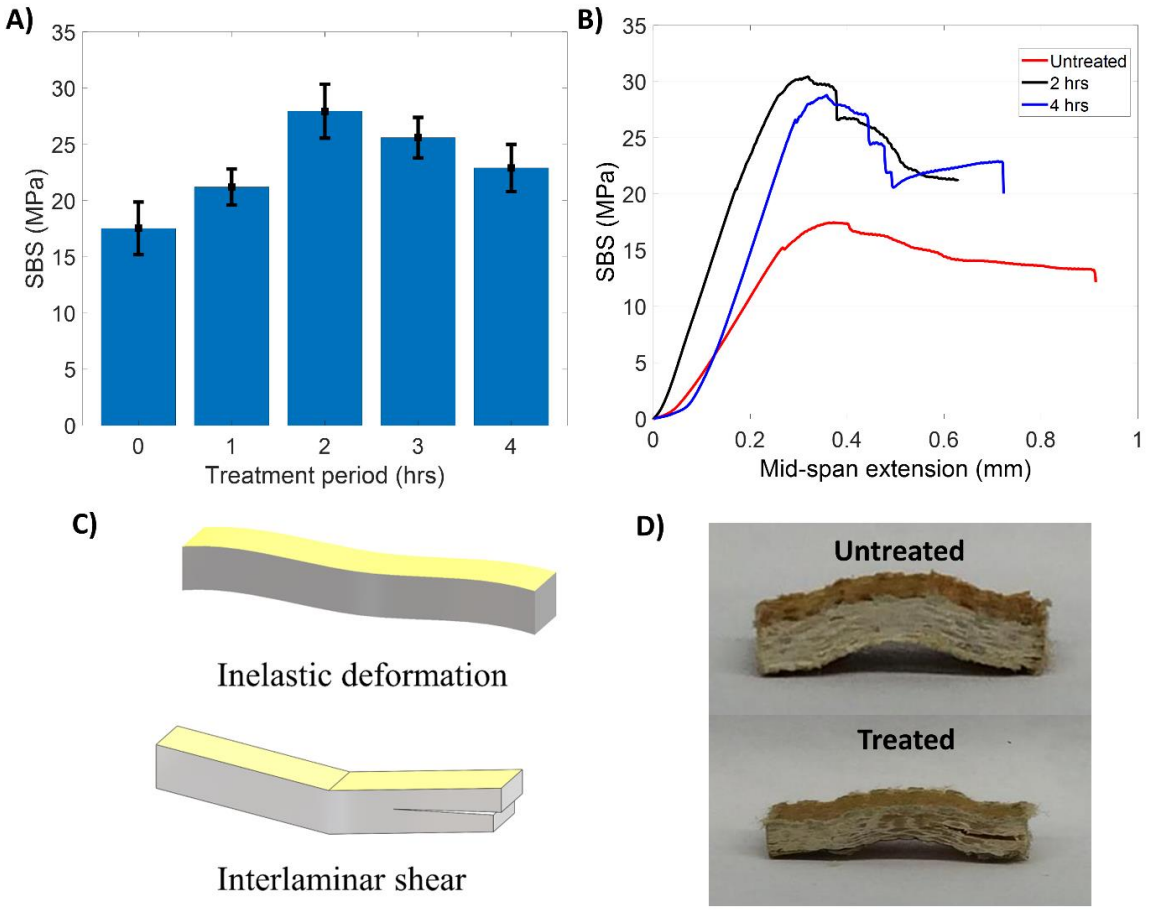

Figure 3.21. Interlaminar properties of untreated and fibrilized aramid composites. A) SBS of untreated and fibrilized aramid fiber reinforced composite specimens. B) SBS vs mid-span extension response. C) Failure modes in short beam specimens. D) Untreated and fibrilized aramid short beam specimens post-testing.

3.5. Chapter summary

In this chapter, the performance of aramid-based interphases as interfacial reinforcement in aramid and glass fiber reinforced composites are investigated for composites used in quasi-static structural applications. It is demonstrated through a simple dip-coating technique that ANFs can be phisisorbed and electrostatically adsorbed onto the surfaces of aramid and glass fibers, respectively, forming well-adhered and nanostructured interphases that present a more chemically reactive and rougher surface. The improved chemical interaction and mechanical interlocking mechanisms between the fiber and the matrix allow for up to 70.27% and 83% improvements in IFSS of single aramid and glass fiber composites, respectively, all while maintaining the tensile properties of the individual fibers. Furthermore, the interfacial reinforcements are demonstrated to

yield 25.6% and 35.3% improvements in the SBS of bulk aramid and glass composites, respectively. The benign ANF interphase design method presented here offers a rapid sizing process that can be applied in continuous fiber manufacturing, allowing for considerable improvements in as little as a three-minute treatment period. Therefore, such an ANF adsorption method has great potential to be integrated into the production processes of high-performance polymeric composites for several structural applications.

In addition, the dissolution and deprotonation process used to generate ANFs is demonstrated to be useful for the benign fibrilization of aramid fibers. Aramid fabric is treated in a DMSO/KOH solution for short periods of time in order to populate the aramid surface with nanofibrils and polar surface functional groups. The fibrilized aramid fibers are found to possess improved surface reactivity, along with surface attached nanofibrils that are capable of interlocking with the epoxy matrix. The fibrilized aramid fibers exhibit 128% and 62% increases to their interfacial and interlaminar properties under quasi-static loading conditions, without any signs of tensile strength degradation. The aramid fibrilization process presented here offers another rapid and low-cost technique that can be integrated in the large-scale production of high-performance aramid composites. In conclusion, these aramid-based nanostructured interphases are demonstrated to be capable of improving interfacial adhesion in aramid and glass fiber reinforced composites using scalable and fast techniques, while most importantly maintaining in-plane properties. In the next chapter, the effect of the developed fibrilization technique on the dynamic response of aramid fabric will be investigated. The changes to the fiber-fiber interactions within the fabric are investigated and studied through interyarn friction, ballistic limit, and dynamic stab testing. In addition, the dynamic response of high strength, yet brittle carbon and glass fiber composites will be assessed in the presence of ZnO interphases. The unique interfacial properties of the ZnO coated carbon and glass single fiber composites are examined using a novel experimental setup that accommodates high strain SFP testing, thus revealing the interfacial multifunctionality of the ceramic ZnO interphase.

CHAPTER 4. Development and Optimization of Nanostructured Interphases for Composites in Ballistic Applications

4.1. Chapter introduction

The following chapter focuses on the introduction of nanostructured interphases onto the fiber surfaces to optimally tailor their properties for soft and hard body ballistic applications. The absorption of impact energy is typically maximized when being carried by the tough fibers, as the matrix tends to fail in a brittle manner. This explains why tough polymer fabrics, such as aramids, have been heavily used to provide ballistic protection in soft-body armor applications. However, in the absence of a binding matrix, such protection lacks the structural integrity required for load bearing applications. While carbon and glass fiber reinforced polymer matrix composites possess the necessary strength and stiffness to support quasi-static structural loading, they tend to fracture easily when subject to dynamic impact. By allowing for easier fiber-matrix debonding, the fibers can absorb a greater amount of impact energy, thus improving the dynamic response of these composites. Yet such poor adhesion also deteriorates the load-bearing abilities of these composites, resulting in a trade-off between their structural and ballistic performance.

In the first part of this chapter, the dynamic response of fibrilized aramid fabric is investigated. It is demonstrated that the improved interyarn friction within the fabric due to fibrilization increases the ballistic limit and dynamic stab protection of aramid fabrics. The enhanced energy absorption mechanism of the fabric indicates the potential of the proposed surface fibrilization treatment as a fast and cost-effective technique to improve the ballistic and stab performance of aramid-based soft body armors. In the second part of the chapter, the performance of a zinc oxide (ZnO) interphase under dynamic loading conditions is investigated. Through variable strain rate single fiber pullout (SFP) testing, the grafting of a ZnO interphase is demonstrated to be a viable interphase design technique in order to tailor the interfacial properties of carbon and glass fiber composites for a simultaneously optimal behavior under quasi-static and dynamic loading conditions. The ZnO nanoparticles (NPs) and nanowires (NWs) are found to strengthen interfacial adhesion under quasi-static strain rates and weaken it under intermediate and high strain rates. The strain rate dependent interphase behavior is demonstrated to a result of the

brittle failure of the ceramic nanowires due to matrix stiffening effects at dynamic strain rates.

4.2. Review of dynamic interfacial testing techniques

The ballistic performance of woven fabrics is primarily assessed using projectile impact tests. These tests involve shooting projectiles of various geometries at the fixed fabric, and determining its ballistic limit, known as V_{50} [194]. The performance of these fabrics is heavily dependent on the interaction between neighboring yarns, given that yarn pullout is a common failure mechanism. Through tow pullout testing, the interyarn friction within a fabric can be studied and optimized to maximize the ballistic limit of the fabrics. The ballistic limit is considered as a reliable criterion for the quantification of impact response in woven fabrics, as it represents the speed limit up to which the target is impenetrable by a specific projectile. As for the stab resistance of such fabrics, this is typically assessed through drop tower testing coupled with a spike impactor [373]. These tests are universally accepted and are usually convenient for studying the performance of woven fabrics that are subjected to dynamic impacts.

Historically, the behavior of structural materials under dynamic loading conditions has been studied using a Split-Hopkinson pressure bar (SHPB) (Figure 4.1.) [374–376]. The SHPB achieves strain rates of up to 10^5 s^{-1} through a stress pulse traveling at the speed of sound inside an incident bar [377]. While, the SHPB technique may be useful for the characterization of the dynamic properties of a fiber reinforced composite, such as energy absorption and impact resistance, it is generally not suitable for characterizing interfacial behavior since the measured properties are typically that of the bulk, where the response from the fibers, matrix and interfaces are superimposed [378–382]. Interfacial testing that involves fiber bundles, as in the case of a composite laminate specimen, can lead to inaccurate measurements of the IFSS, due to what is known as the "matrix effects." The concomitant failure of the matrix surrounding the circumference of the fibers with that of the fiber-matrix interface in a composite laminate generates complex results, leading to data misinterpretation and misleading conclusions if not properly accounted for [357,365]. Other mechanical systems employing hydraulic [383] and pneumatic [380,384] actuators have also been developed, yet are similarly concerned with the measurement of bulk properties, while also being generally more focused on macroscale cementitious composites [380].

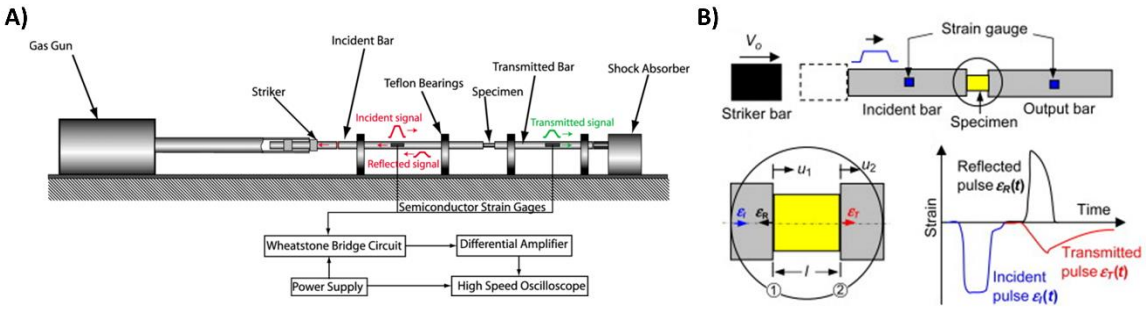

Figure 4.1. Split Hopkinson pressure bar for dynamic material testing. A) Schematic of the SHPB experimental setup. B) Enlarged view of specimen in SHPB and the measured wave across interfaces [385,386].

As previously mentioned, single fiber composite testing allows for accurate assessment of interfacial properties in isolation of the individual properties of the fiber and the matrix. However, most single fiber composite testing procedures and experimental setups have been designed for quasi-static loading [362]. While SFP testing at high strain rates has been reported, most deal with large diameter fibers [387], fiber bundles instead of single fibers [388], use a non-polymeric matrix [389], or are limited in terms of the maximum applied strain rate [382]. A new approach was recently developed by Hwang et al. that provides a method for the characterization of the interfacial shear strength (IFSS) at the filament level with strain rates reaching 10^4 s^{-1} [138]. The method uses a piezoelectric stack actuator along with a custom-built discharge circuit for actuation which enables the evaluation of interfacial properties of single fiber composite specimens at high dimensional accuracy. The pullout forces are generated by discharging the stack actuator, while controlling the strain rate through the choice of load resistance in the discharge circuit. The described technique allows the use of SFP to compare the performance of modified fiber-matrix interphase across loading conditions, ranging from quasi-static strain rates all the way to high ones.

4.3. Fibrilized aramid fabric

4.3.1. Review of fibrilization process

The effect of the previously discussed fibrilization process on the surface morphology of aramid fibers is confirmed through the SEM micrographs as shown in Figure 4.2. The deprotonation of the macroscale fibers inside the basic solution generates randomly oriented aramid fibrils with varying aspect ratios and diameters. As previously mentioned, shorter treatment

periods are found to reduce the breakage of inter-chain hydrogen bonds, allowing for a larger amount of the newly formed fibrils to remain attached to the macroscale fiber surface. The presence of these fibrils has been shown in the previous chapter to improve the mechanical interlocking capacity of aramid fabrics with polymers, such as epoxy, at the level of the fiber-matrix interface. High aspect ratio fibrils can be seen spanning across multiple fibers and at crossing points of tows in both weft and warp direction. These surface fibrils can help enhance the impact resistance of the aramid fabric against bowing by bridging between neighboring fibers and forming inter-fiber structures. These inter-fiber structures can also potentially increase interyarn friction within fabrics by inducing stronger mechanical interlocking between neighboring yarns. Moreover, the fibrilized aramid fabrics exhibit no increase in weight or decrease in flexibility, thus preserving important characteristics of aramid fibers for its ballistic performance in soft body armor applications.

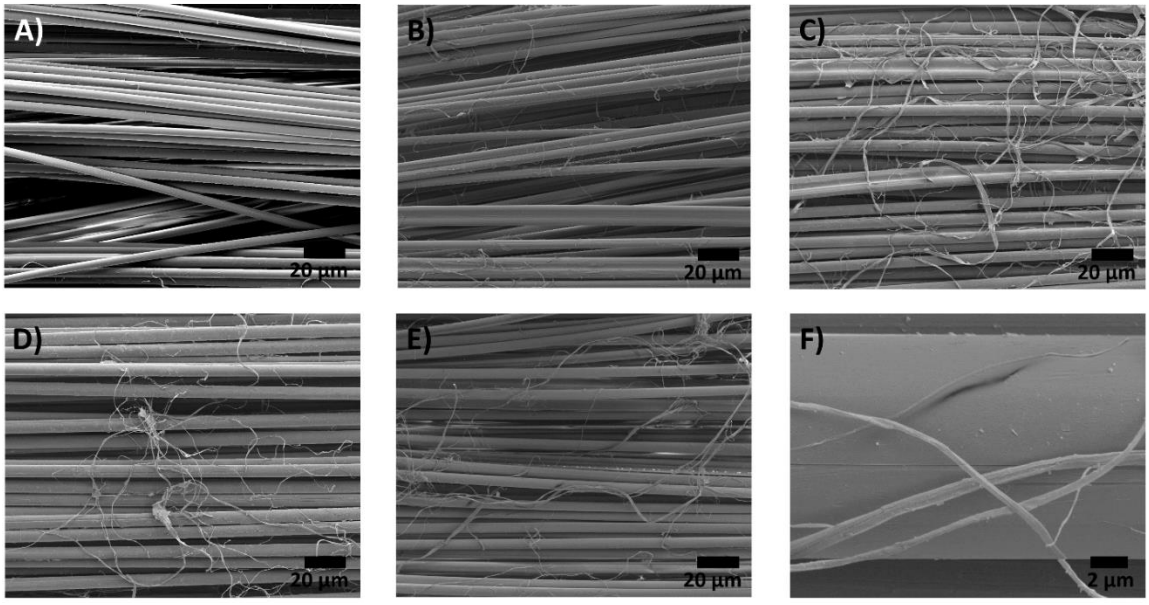

Figure 4.2. Scanning electron microscopy images of untreated and fibrilized aramid fibers. A) untreated fibers. B) Fibers after a 2-hours treatment. C) Fibers after a 5-hours treatment. F) Fibers after a 7-hours treatment. E) Fibers after a 10-hours treatment. F) Generated surface fibrils.

4.3.2. Measurement of fabric's tensile strength

The superior ballistic performance of aramid fabrics is partially attributed to their high tensile properties. Nilakantan et al. reported a direct correlation between the ballistic performance of the woven fabric and its corresponding yarn tensile strength, where a decrease in mean yarn

strength resulted in a reduction of fabric's V_{50} [390]. Therefore, any enhancement of the interyarn friction of aramid fabrics should not come at the expense of the tensile strength of the aramid fiber or fabric. To ensure no degradation of tensile properties in aramid fabrics occurs post-fibrilization, textile fabric and single fiber tensile testing of untreated and fibrilized samples is performed at quasi-static tensile loading. The elastic modulus and tensile strength of untreated and fibrilized single aramid fibers can be seen in Figures 4.3A & B. As previously shown, no significant statistical decrease in the tensile strength of fibrilized aramid fibers is observed until a minimum treatment period of 10 hours. The tensile strength and elastic modulus of aramid fibers treated for 10 hours are found to decrease by 8.9 % and 9.5 %, respectively. This trend is confirmed by the greater degradation of tensile properties of fibers treated for 24 hours, where a decrease of 12.6 % in the tensile strength is observed. The reduction in the aramid fibers' strength at longer treatment periods is due to the prolonged hydrolysis process occurring inside the basic treatment solution. The effect of fibrilization is further studied through the measurement of the tensile properties of both untreated and fibrilized aramid fabrics according to ASTM D5353 (Figures 4.3C & D). Similar to single fiber tensile testing, a 7.5% and 6.8 % decrease in the tensile strength and elastic modulus of 10 hours treated aramid fabric is observed, respectively. The expected decrease in the tensile properties of the fabric is due to weakened yarn and individual fiber strength, therefore indicating that prolonged treatment periods of longer than 10 hours can be expected to offer an inferior reinforcement performance to the impact response of the aramid fabric. It should be noted that the slight increase in tensile strength of 5 hours treated fabric is due to the potentially increased interyarn friction between the tows. It can be then concluded that the tensile strength of aramid fabrics is fully preserved post-fibrilization treatment periods of less than 10 hours, and its ballistic performance is not at risk of decreasing within that range.

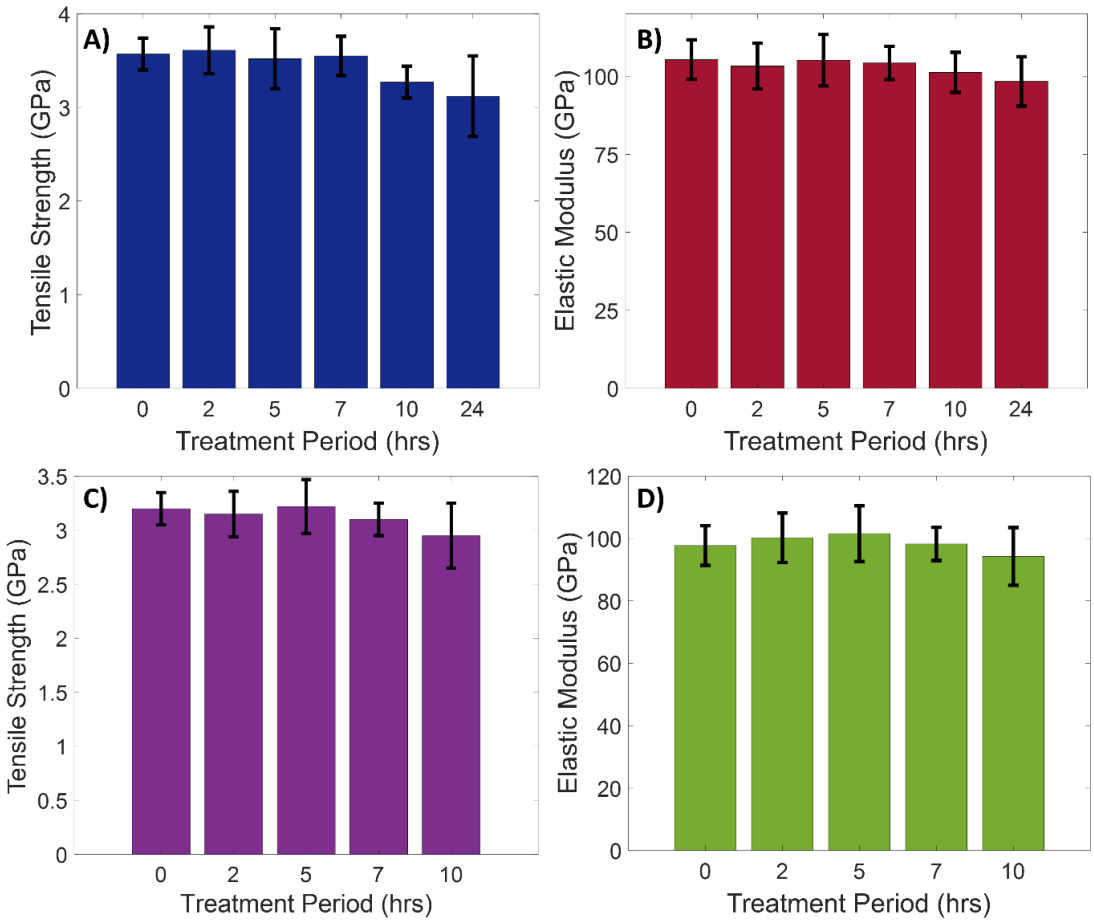

Figure 4.3. Tensile properties of untreated and fibrilized aramid fabric A) Tensile strength of untreated and treated single aramid fibers for various durations. B) Elastic modulus of untreated and fibrilized single aramid fibers for various durations. C) Tensile strength of untreated and fibrilized aramid fabric for various durations. D) Elastic modulus of untreated and fibrilized aramid fabric for various durations.

4.3.3. Effect of surface fibrilization on fabric's interyarn friction

To investigate the effect of the fibrilization treatment on the energy absorption capacity of the aramid fabrics, single tow pullout testing is performed under controlled transverse tension using the experimental setup shown in Figure 4.4**.** The shown setup is similar to that described by Hwang et al. and allows the clamping of the treated fabric between a fixed column and an adjustable link, where a lead screw can be used to adjust the clamping distance and thus apply lateral tension to the fabric [217]. The load-displacement curves are recorded at the same preload transverse tension of 100 N. The amount of energy absorbed during pullout, known as the pullout energy, is calculated through integration of the recorded load-displacement curves. By testing 7

tows per fabric, the uniformity of the fibrilization treatment and the repeatability of the tow pullout testing process are ensured. The averaged pullout energy of the untreated and fibrilized fabrics is listed in Table 4.1., and the peak loads along with the corresponding load-displacement curves are shown in Figure 4.5. Both pullout load and pullout energy are increased by more than 157 % and 194 %, respectively, after only 2 hours of fibrilization. A maximum increase in pullout properties is found in fibrilized aramid fabric with a treatment period of 5 hours, which shows an increase of 550 % and 665 % in peak load and pullout energy, respectively. By studying the recorded peak load-displacement curves, it can be seen that the loaded tow initially experiences static friction, highlighted by the first recorded peak. This is followed by a large drop in load, as the specimen undergoes kinetic friction when passing through the first transverse tow. The increase in static friction before un-crimping is attributed to the improved mechanical interlocking between fibrilized fibers and yarns, indicating increased interyarn friction. Further decrease in load along with certain local peaks are recorded as the loaded tow passes through all remaining transverse tows. Moreover, fibrilized aramid fabrics display slightly larger extensions before complete pullout, resulting in further enhancement of the pullout energy. The observed delay in pullout failure confirms larger resistance to yarn pullout stemming from the improved interaction between the neighboring and intersecting tows of the fibrilized aramid fabric. Such pullout behavior agrees well with that of other cases of aramid fabric treatment methods reported in previous studies, such as polymeric and ZnO nanoparticle coatings [218].

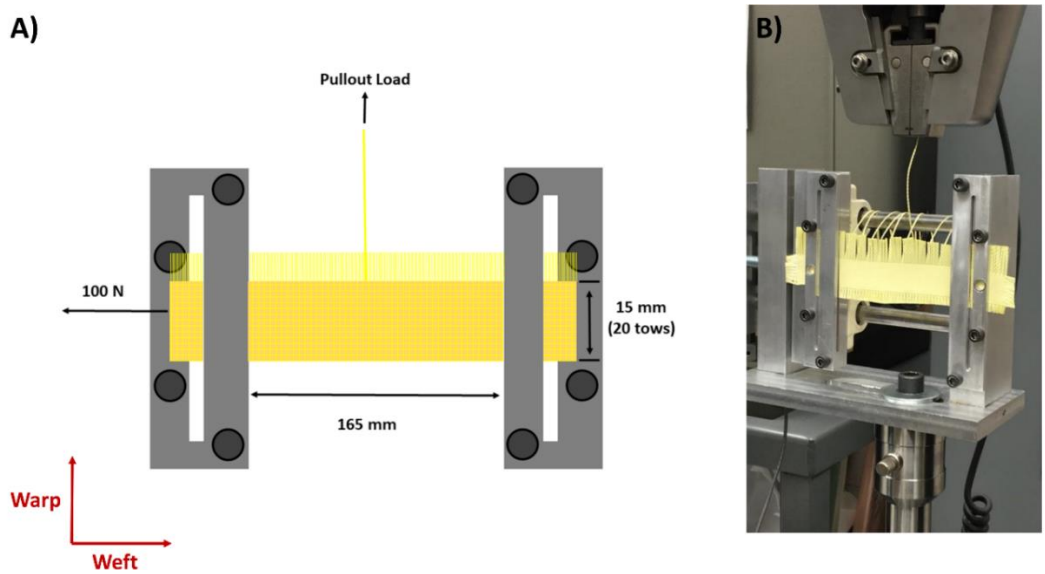

Figure 4.4. Tow pullout testing. A) Schematic of experimental setup for tow pullout test. B) Fibrilized aramid fabric sample for tow pullout.

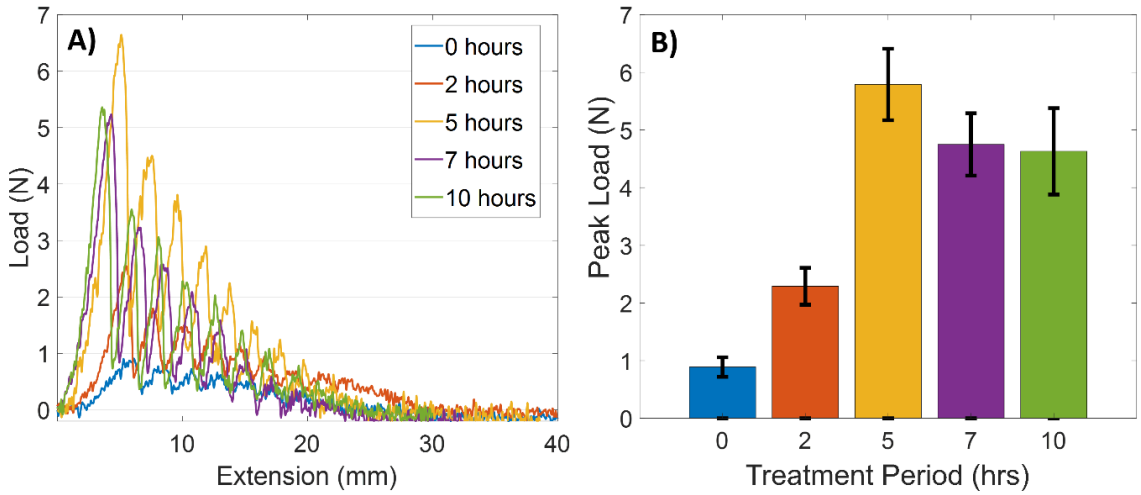

Figure 4.5. Interyarn friction of untreated and fibrilized aramid fabric. A) Load–displacement curve showing tow pullout behavior of different treatment periods. B) Comparison of average peak load values between fabric specimens of different treatment periods.

Table 4.1. Averaged pullout energy and peak load of untreated and fibrilized fabrics.

Treatment Period (hrs)	**0**	**2**	**5**	**7**	**10**
Pullout energy (mJ)	4.18	12.32	32.93	22.45	23.43
Standard deviation	0.91	1.39	3.29	2.01	1.87
% Improvement	-	194.4	665.3	437.3	460.2
Peak load (N)	0.89	2.29	5.79	4.75	4.63
Standard deviation	0.17	0.32	0.62	0.54	0.75
% Improvement	-	157.3	550.5	433.7	420.2

By performing an examination of tow pullout samples using SEM imaging following the completion of the test, dense bundles and layers of dispersed fibrils and fibrilized aramid fibers can be seen at the yarn-crossing points of 5 hours and 10 hours treated aramid fabrics, whereas untreated fabrics display no sign of excessive fibrilization (Figure 4.6). As expected, the degree of fibrilization in 5 hours treated fabric is considerably larger than that in 10 hours treated samples, further confirming the tow pullout results. The abrasive loading experienced during a tow pullout generates aramid surface fibrils in both the untreated and fibrilized case due to the breakage of the

hydrogen bonds responsible for holding individual polyamide macromolecules together; however, the deprotonation to which the aramid fabric is subjected prior to testing further weakens hydrogen bonding, promoting easier fibrilization of the treated aramid fiber surfaces under abrasive action. Therefore, the increased surface fibrils found in treated fabrics post-testing can be attributed to both the initial fibrilization treatment, and the breakage of hydrogen bonding during abrasive loading. The presence of these microstructures indicates an increase in interyarn friction by means of mechanical interlocking, explaining the observed improvement in initial peak load and pullout energy of the fabric. Thus, the preservation of tensile strength and the considerable enhancement in the interyarn friction of aramid fabrics after short treatment periods confirm the potential of fibrilization in yielding a higher fabric impact resistance, inducing a desirable and improved ballistic performance. It should also be noted that the improvements in interyarn friction saturate, as 7 and 10-hours treatments show a 20.4 % and 24.54 % decrease in pullout energy when compared to that of a 5-hours treatment, respectively. Regardless, these set of fibers still possess a minimum 437% higher pullout energy relative to that that of untreated fabrics. The reason for such a trend is the decrease in fibril density on the macroscale aramid fiber surfaces, since the fibrils generated at early treatment stages start to debond, therefore lowering the effectiveness of interyarn mechanical interlocking due to the fibrilization treatment. It should be noted that the observed trends are unique to the treatment conditions of this study, as the use of different bases and concentrations may alter the rate of the deprotonation process.

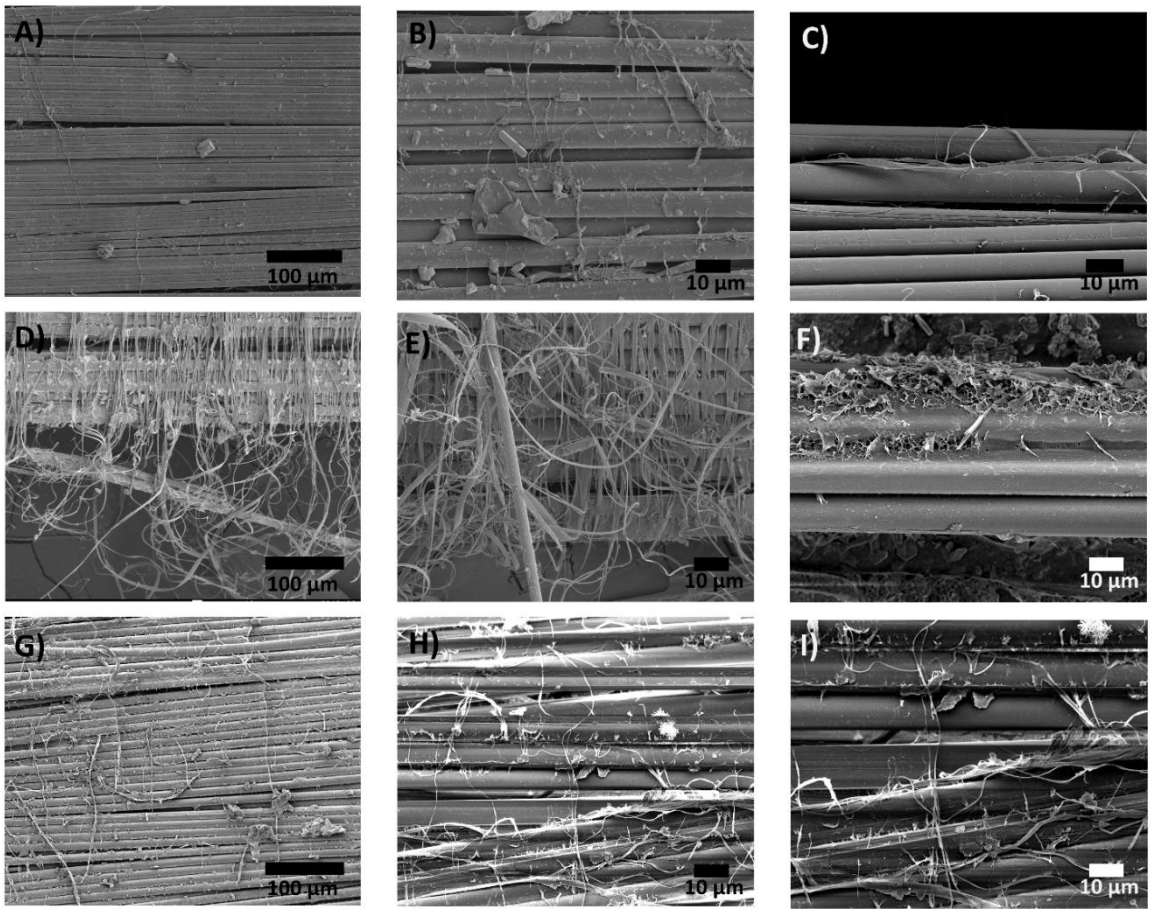

Figure 4.6**.** SEM images of aramid fabrics, both untreated and fibrilized, after pullout test at yarn-crossing points. A-C) Untreated. D-F) 5-hours treated fabric. G-I) 10-hours treated fabric.

4.3.4. A study of the ballistic limit of fibrilized aramid fabric

The ballistic performance of the fibrilized aramid fabric is further studied through ballistic impact tests performed using a custom designed gas gun setup as described in Stenzler et al. (Figure 4.7.) [26]. The compressed air driven ballistic setup is instrumented for accurate measurement of projectile's impact velocity. The velocity of the projectile is obtained by recording the time required for it to block the incident light by traveling between two photoresistors placed 19.05 mm (3/4 inch) apart at the end of the barrel (Figure 4.7C). A blunt 4130 alloy steel projectile (hemispherical face) with a mass of 29 g and a diameter of 11.4 mm is to be used to impact the fabric targets consisting of three cross-shaped aramid fabric plies with a square target area of 7.8 x 7.8 cm^2. The samples are clamped from all four sides using a steel plate with recessed bars as shown in Figures 4.7A & B. The applied torques to the steel plates and bars screws are controlled

using a torque-wrench to ensure uniform clamping and prevent any target slippage during impact. The impact of the projectile on the target surface are designed for zero degrees of obliquity, and a clay trap placed 2 inches behind the target is examined for penetration after each firing of a projectile. For each set of aramid fabric, 12 targets are shot and the ballistic limit (V_{50}) is obtained by taking the arithmetic mean of the three highest non-penetrating and the three lowest complete penetrating impact velocities into the clay trap.

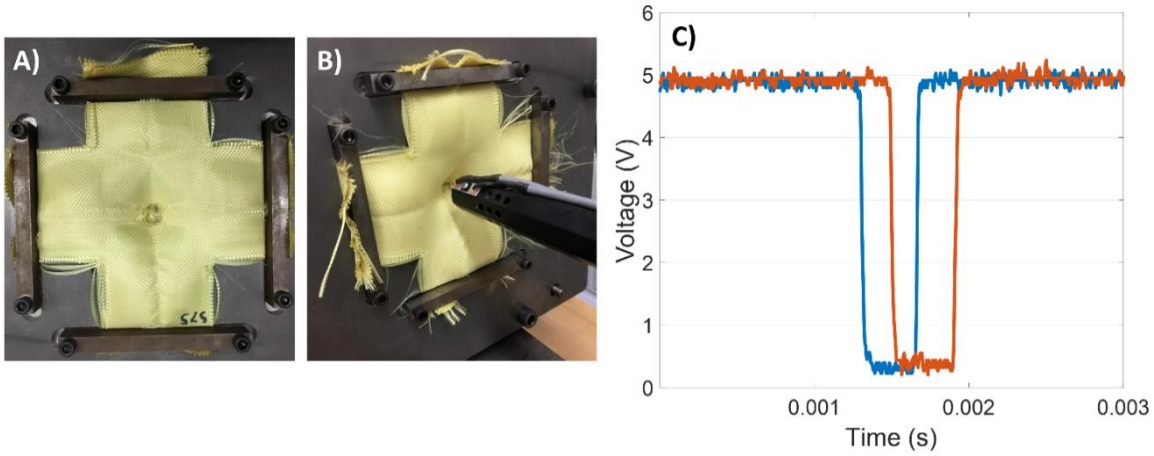

Figure 4.7. Impact testing. A) Cross-shaped, 4-sided clamped aramid fabrics. B) Experimental setup using 0.25-inch distance between barrel and target. C) Photogates recorded signal as projectile exits the barrel.

The influence of fibrilization on the impact resistance of aramid fabrics is evaluated by subjecting the treated fabrics to impact tests at velocities ranging from 75 m/s to 115 m/s. Given its optimized ability to maintain the tensile strength of the aramid fabric, while yielding maximum improvement in interyarn friction, a 5-hours treatment is chosen to be studied. The treated fabrics are tested over three different velocity zones before calculating the V_{50} speed. As previously mentioned, the V_{50} speed is considered a reliable criterion for quantification of the impact resistance of woven fabrics, as it represents the speed limit up to which the target is impenetrable by a specific projectile [391]. Proper clamping of the samples from all sides is necessary to avoid slippage, which can result in inaccurate impact responses. Penetration of the fabric is considered to be successful in the case where the projectile impacts the clay trap placed 2 inches behind the fabric target. The projectile's velocity for each performed test, along with the type of failure across all velocity zones are presented in Table 4.2. At speeds less than 88 m/s, both untreated and fibrilized aramid fabrics are able to stop the projectile, dissipating all its kinetic energy and

preventing it from penetrating and reaching the clay trap. However, as projectile's velocity is increased into the intermediate range of 88-98 m/s, the impactor is able to penetrate untreated aramid fabrics at certain speeds but not the fibrilized fabric. The higher impact resistance observed in the fibrilized aramid fabric is the result of an improved energy dissipation mechanism due to fibrilization. The increased interyarn friction of the fibrilized fabric limits the mobility between neighboring fibers and tows, which decreases the possibility of wedge-through projectile penetration due to bowing. Moreover, the fibrilized fabric visibly exhibits no more local or remote yarn failure than the untreated one, given both possess similar tensile strengths. As the velocity is further increased to over 97 m/s, complete projectile penetration starts to occur in fibrilized fabrics. At such speeds, the aramid fabric is unable to absorb all the projectile's kinetic energy, as penetration occurs, and the projectile's momentum is stopped by the clay trap. The calculated V_{50} of the fibrilized aramid fabric is found to be approximately 10 m/s higher than that of untreated fabric, indicating an improved impact response due to fibrilization. The observed 12% improvement in V_{50} speed of fibrilized aramid fabrics predictably agrees well with the previously discussed 550 % increase in yarn pullout force. The limited improvement in ballistic performance relative to that of interyarn friction is mainly due to the contribution of multiple failure mechanisms to the failure of the fabric under impact loading conditions. The high strain rate loading conditions of impact testing have been shown to excite *p*-phenylene terephthalamides (PPTA) bonds beyond their activation energy, resulting in primary bonds breakage and the promotion of brittle fracture [392]. The ability of aramid yarns to withstand rupture is independent of any interfacial properties, as it is primarily dictated by fiber and yarn's tensile properties. Therefore, the contribution of these other failure modes limits the effect of interfacial reinforcement on the impact resistance of aramid fabrics.

Table 4.2. Details of all the reported impact tests for untreated and fibrilized aramid fabrics.

Untreated		Fibrilized	
Impact speed (m/s)	**Failure**	**Impact speed (m/s)**	**Failure**
79.37	No Penetration	87.69	No Penetration
81.32	No Penetration	90.79	No Penetration
83.23	No Penetration	95.29	No Penetration
87.72	No Penetration	97.23	No Penetration
88.60	Penetration	98.25	Penetration
90.07	No Penetration	99.21	Penetration
92.96	Penetration	100.26	No Penetration
93.75	No Penetration	101.6	Penetration
95.25	Penetration	102.82	Penetration
97.60	Penetration	103.58	No Penetration
99.73	Penetration	104.09	No Penetration
102.97	Penetration	105.83	Penetration
112.34	Penetration	108.62	Penetration

Examining the failure modes of untreated and fibrilized aramid fabrics through post-testing imaging allows for accurate interpretation of the role of fibrilization treatment in the impact resistance reinforcement mechanism. At lower speeds, the projectile is unable to penetrate the target, yet still results in deformations to the fabric. In comparison to fibrilized fabric, the untreated fabric experiences larger deformations around the blast area due to bowing, along with further damage to the second and third ply, as the first ply absorbs less kinetic energy than in the case of fibrilized fabrics. The difference in bowing behavior correlates to the mobility of the tows and fibers within the fabric. As complete penetration starts to occur at higher projectile speeds, the failure mode of the aramid fabrics is modified. The ability of adjacent yarns and fibers in untreated fabric to easily slide results in traces of yarn pullout around the blast area, as well as a cross shaped yarn pullout (Figure 4.8.) due to the 4-sided clamping of the sample. Significantly less yarn pullout/sliding is observed in fibrilized fabrics due to the increased interyarn friction and decreased yarn mobility through the generated surface fibrils. Moreover, the blast hole left by the penetrating

projectile is significantly smaller in fibrilized fabrics than untreated ones, signaling a decrease in the ability of the projectile to wedge through the aramid yarns. It should be noted that both sets of fabric experience a high degree of remote and local yarn rupture which can be considered as the primary failure mechanism at such high speeds. SEM micrographs of the blast area of untreated and fibrilized fabric targets can be seen in Figure 4.9. Post-testing, untreated aramid fabrics are found to sustain substantial deformation around the blast area as the projectile velocity is increased. The deformation in untreated fabric is primarily in the form of yarn sliding and weave distortion, as no excessive signs of surface fibrillation are found. However, even at high projectile velocities, fibrilized fabrics display minimal yarn sliding and weave deformation, yet surface fibrillation is prominent. Moreover, both fabrics present structural failure in the form of the ruptured fibers. These observed differences in failure mechanisms agree well with the V_{50} metrics detailed in Table 4.2. Such results confirm the ability of the increased interyarn friction, achieved through fibrilization treatment, to contribute into an improved impact response of aramid woven fabrics.

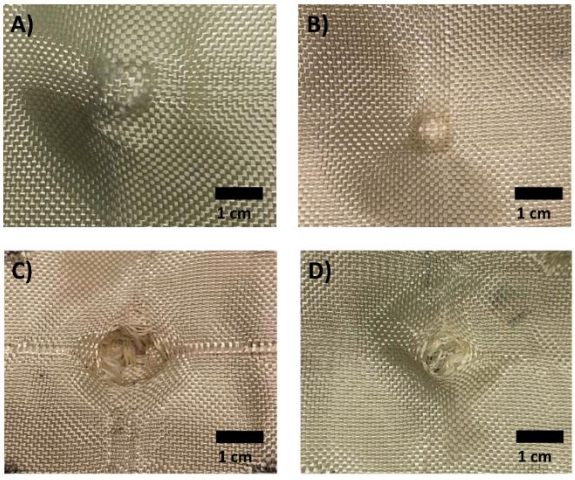

Figure 4.8. Comparison between untreated and fibrilized aramid fabrics (bottom row) after impact. A) Untreated aramid fabric after low velocity, non-penetrating impact (below 90 m/s). B) Fibrilized aramid fabric after low velocity, non-penetrating impact (below 90 m/s). C) Untreated aramid fabric after high velocity, fully penetrating impact (above 100 m/s). D) Fibrilized aramid fabric after high velocity, fully penetrating impact (above 100 m/s).

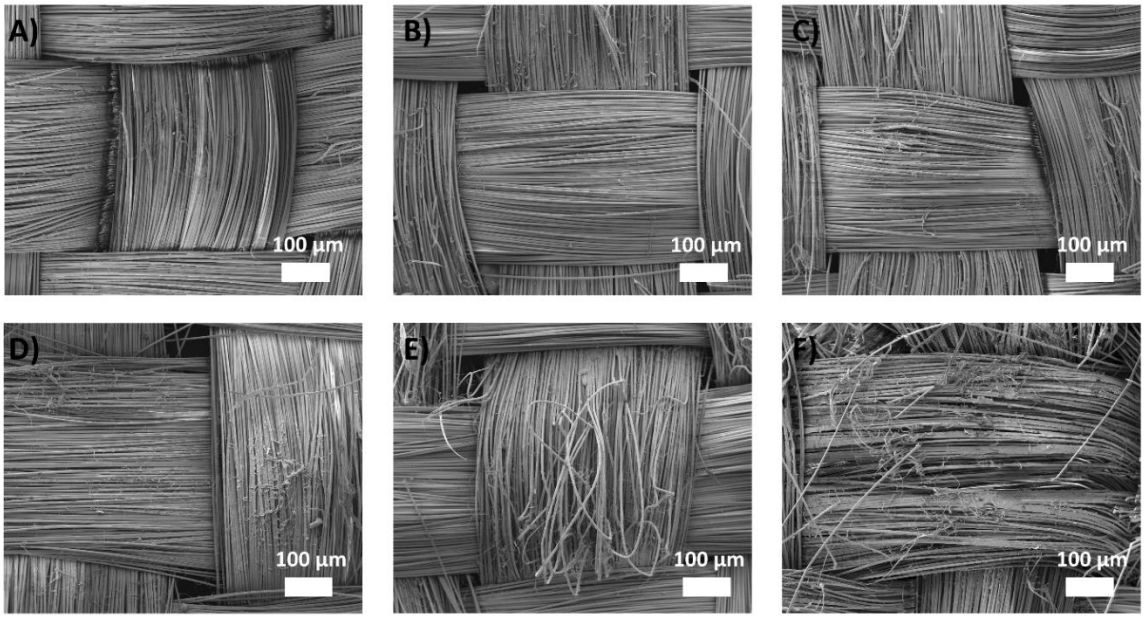

Figure 4.9. Micrographs of untreated and fibrilized aramid fabrics after impact testing. A) and B) Untreated and fibrilized aramid fabric tested at 87 m/s, respectively. C) And D) Untreated and fibrilized aramid fabric tested at 95 m/s, respectively. E) And F) Untreated and fibrilized aramid fabric tested at 102 m/s, respectively.

4.3.5. Investigation of the stab resistance of fibrilized aramid fabric

The capacity for fibrilized aramid fabric to improve stab protection against a spike is studied in this section by performing drop tower testing on aramid targets from a fixed height with varying drop masses (Figure 4.10.). Similar to ballistic testing, 8 aramid fabric plies are treated for 5 hours and used as impact targets. Again, the choice of a 5-hours treatment is due to its ideal effect on the tensile properties, interyarn friction and ballistic limit of the fabric. The fibrilization treatment has no considerable effect on the areal density, thickness, or flexibility of the aramid fabric, and therefore the same number of plies is used for both untreated and fibrilized fabric targets for adequate comparison. The drop height is fixed at 0.35 m, while the total drop mass can be varied between 1.407 kg, which is the mass of the carriage unloaded, and 1.907 kg. The use of witness papers to measure depth of penetration is chosen over other approaches due to ease of implementation, rapid assessment of penetration depth, and high resolution given the thickness of each witness paper (Figure 4.10B). Moreover, the witness paper approach avoids any inaccuracies while performing depth of penetration measurements, as it accounts for any possible spring-back of the impactor by recording the initial penetration depth. The depth of penetration, along with the

impact load for each drop mass can be seen in Table 4.3.

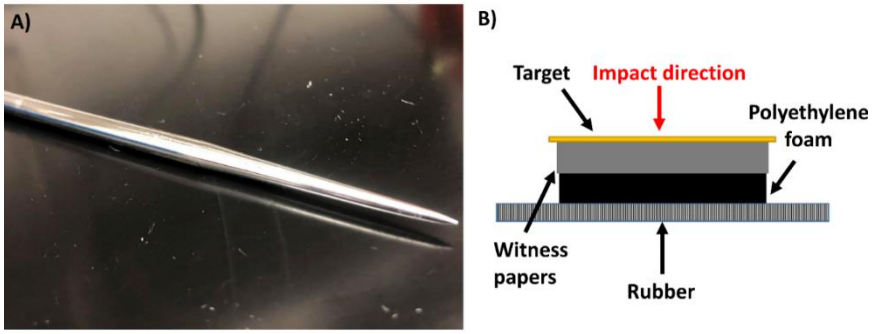

Figure 4.10. Fabric stab testing. A) Spike impactor. B) Drop tower and dynamic stabbing configuration.

Table 4.3. Conditions for drop tower stab testing.

Drop mass (kg)	Drop height (m)	Theoretical impact velocity (m/s)	Theoretical impact energy (J)
1.407	0.35	2.62	4.831
1.507	0.35	2.62	5.174
1.607	0.35	2.62	5.517
1.707	0.35	2.62	5.861
1.807	0.36	2.62	6.204
1.907	0.35	2.62	6.376

An increasing trend in depth of penetration and impact load is observed in both untreated and fibrilized fabrics with increasing drop mass (Figure 4.11.). However, fibrilized aramid fabrics display a significantly improved stab resistance compared to untreated aramid fabrics. For a drop mass of 1.407 kg, the fibrilized aramid fabric is able to prevent puncture, while untreated aramid fabric exhibits an approximately 1 mm deep penetration. As drop mass is increased, fibrilized aramid fabrics maintain their superior stab resistance, showing a maximum decrease of 230% in depth of penetration and a maximum increase of 110% in impact force. The decrease in penetration depth is expected to be accompanied by an increase in impact load, as a larger portion of the kinetic impact energy is damped and absorbed by the aramid target, thus reducing the distance traveled by the impactor into the backing material. It should be noted that the maximum allowable depth of penetration without the likelihood of an injury is considered to be at 7 mm [212].

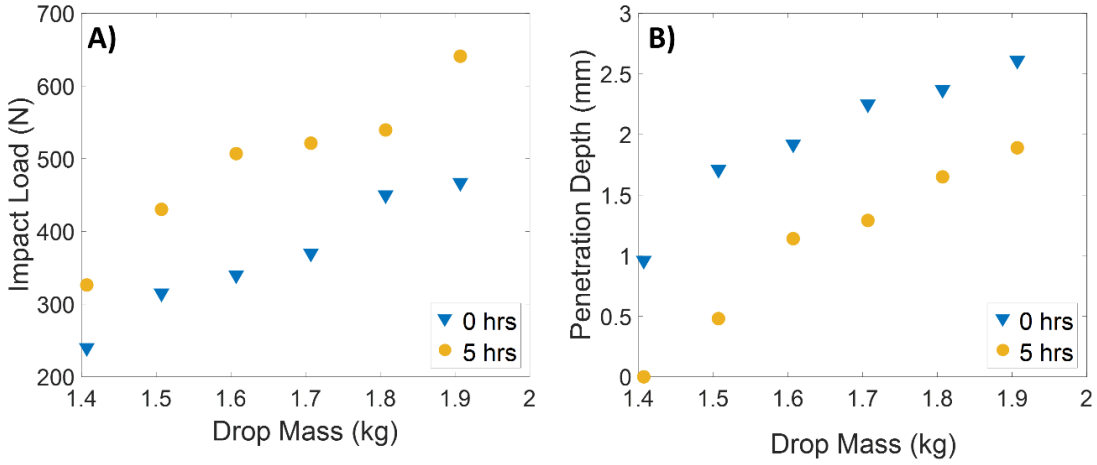

Figure 4.11. Dynamic stab testing. A) Penetration depths of untreated and fibrilized aramid fabric targets against spike impactor for different drop masses. B) Impact loads of untreated and fibrilized aramid fabric targets against spike impactor for different drop masses.

An inspection of the failure modes in both untreated and treated aramid fabrics post-stabbing provides greater understanding of the role of the fibrilization treatment in the stab resistance reinforcement mechanism (Figure 4.12.). For the same drop mass and height, untreated aramid targets display considerably more significant puncture damage than fibrilized ones. Generally, spike impactors are able to penetrate aramid fabrics through intra- and interyarn slippage, resulting in little to no fiber tensile failure. The restricted mobility of neighboring fibers and tows in treated fabrics due to the improved interyarn friction provides higher resistance against stabbing by preventing the spike from sliding between the filaments and penetrating. These results are further supported by quasi-static stab testing, where similar aramid targets were used. Figure 4.13. shows an 80% increase in supported stabbing load over a 15 mm penetration depth in fibrilized aramid fabrics compared to that in untreated fabrics. While both fabrics are completely penetrated by the spike impactor, treated fabrics displayed a delay in complete target rupture and a significantly reduced stabbing compliance. This improvement in stab resistance at low loading rates is another indicator of the role of reduced yarn and fibers mobility in improving the stab resistance performance of aramid fibers. In conclusion, these results indicate the possibility of the fibrilization treatment providing significant stab protection without any increase in weight or decrease in flexibility of the aramid fabric. While this section detailed the potential of fibrilization in improving the performance of soft body armor, the following section will detail the ability of

ceramic ZnO interphases in proving hard body composite armors with a multifunctional structural performance.

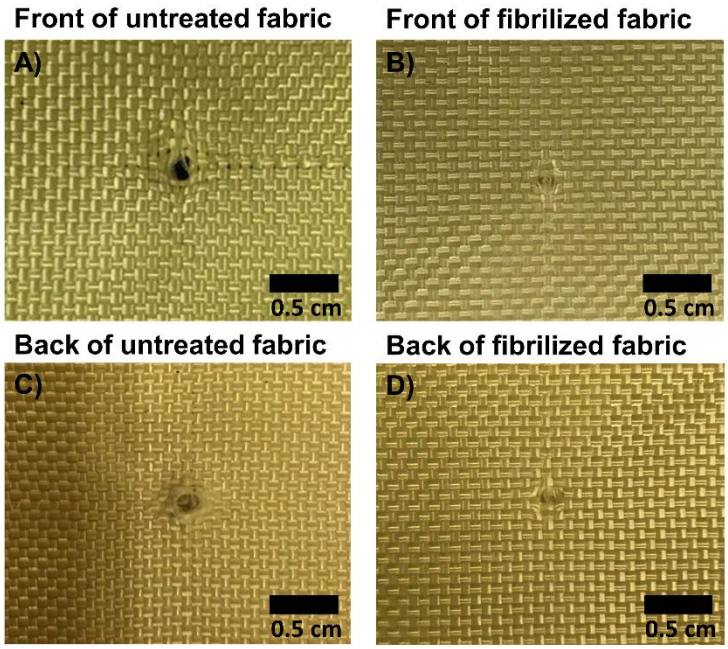

Figure 4.12. Comparison between untreated and fibrilized aramid fabrics after testing against spike impactor. A) and B) Damage to the front of aramid targets at a drop mass of 1.807 kg, respectively. C) and D) Damage to the back of aramid targets at a drop mass of 1.807 kg, respectively.

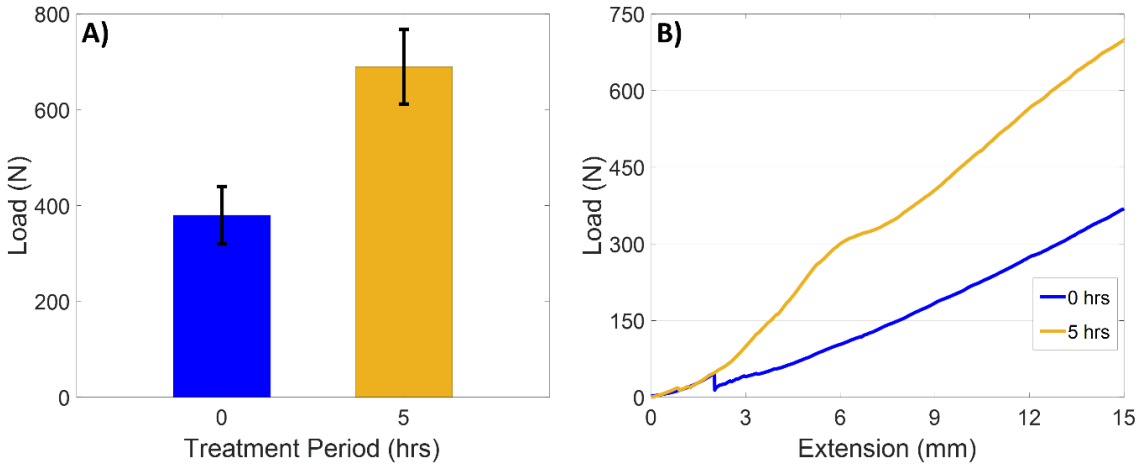

Figure 4.13. Quasi-static stab testing. A) Maximum supported load by untreated and fibrilized aramid fabric targets against spike impactor. B) Load-displacement curves for of untreated and fibrilized aramid fabric targets against spike impactor.

4.4. Ceramic fiber reinforced composites

4.4.1. Surface functionalization and ZnO synthesis

The benign growth of ZnO interphases on the surface of fibers can be typically achieved using a hydrothermal reaction (Figure 4.14.). Here, AS-4 carbon fibers (Hexcel) are sonicated in acetone and ethanol successively, and functionalized through an oxidative technique in order to increase the oxygen surface functional groups [344]. Nitric acid oxidation is then performed through first refluxing AS-4 carbon fiber tows in 100 ml of 70 % nitric acid (70%, ACS certified: Fisher Scientific) for 4 hours. This is followed by soxhlet extraction for 8 hours in order to wash the fibers with deionized water, before further ultra-sonication for 15 minutes and drying at 100 °C overnight. E-glass fiber tows are also cleaned through successive sonication in acetone (≥ 99.5%, ACS reagent: MilliporeSigma) and ethanol (≥ 99.5%, ACS reagent: Fisher Scientific) in order to eliminate any surface sizing or organic contaminants. The fibers are then functionalized using an oxidizing piranha solution treatment in order to increase the surface oxygen content and thus the binding between the fibers and ZnO coating. The oxidation process is performed for 10 minutes inside a 20 ml solution with a 3:1 volumetric mixture of sulfuric acid (95.0-98%, ACS reagent, Sigma Aldrich) and hydrogen peroxide acid (30%, ACS reagent, Sigma Aldrich), respectively. The pH of the fiber surfaces is then neutralized by washing with ammonium hydroxide (28-30% ACROS Organics) and water, successively. The washing process is to be repeated until a slightly basic PH is achieved.

A ZnO NPs seeding solution can be prepared using a multiple steps synthesis process. First, a 0.02 M solution of sodium hydroxide (NaOH) (ACS certified: Fisher Scientific) in ethanol and a 0.0125 M solution of zinc acetate dihydrate ($Zn(CH_3CO_2)_2 \cdot 2H_2O$) (Alfa Aesar) in ethanol are prepared and vigorously stirred at 60 °C and 50 °C, respectively. Once both solutions are dissolved completely, 32 mL of the sodium hydroxide solution is diluted in 80 mL of ethanol, while 32 mL of the zinc acetate solution is diluted in 256 mL of ethanol and both solutions are heated up to 55 °C. The sodium hydroxide solution is then added dropwise to the zinc acetate solution, before vigorously stirring for 45 min in a sealed glass jar to yield 516 mL of seeding suspension. Finally, the suspension is quenched in an ice bath to interrupt the growth of the ZnO NPs. In order to grow ZnO NWs on the fiber's surface, individual carbon fibers are laid across nylon frames and successively sonicated in acetone and ethanol for 10 minutes. Once clean, the frames are dipped in the seeding solution to deposit ZnO NPs on the fiber's surface, before annealing them in a

convection oven for 10 minutes at 150 °C. The same process is repeated two more times, while allowing for a cooling down period of 5 minutes between cycles. Next, the frame is placed inside an aqueous growth solution of equal molar concentrations of hexamethylenetetramine ($C_6H_{12}N_4$) (Alfa Aesar) and Zinc nitrate hexahydrate ($Zn(NO_3)_2 \cdot 6H_2O$) (Alfa Aesar) at 150 °C for 150 minutes. After removal from the growth solution, ultrapure water and methanol washings are performed on the ZnO NW coated fibers, respectively, and the fibers are dried at 100 °C overnight. It should be noted that ZnO NP coated carbon fibers are prepared using a similar seeding process, while omitting the final growth process.

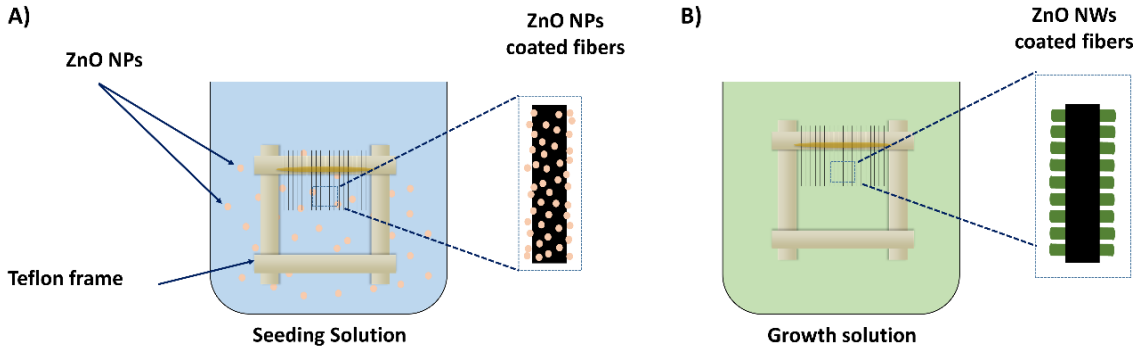

Figure 4.14. ZnO NWs synthesis process. A) Coating of carbon or glass fiber surface with ZnO NPs inside seeding solution. B) Whiskerization of carbon or glass fiber surface with ZnO NWs inside the growth solution.

4.4.2. ZnO interphase morphology

Surface morphology of fibers following seeding and growth is characterized through SEM imaging (Figure 4.15). To accurately evaluate the mechanical performance of a ZnO interphase using pullout testing, it is important that the embedded lengths of tested fibers are sufficiently and uniformly coated with ZnO NPs and NWs. Figures 4.15A, B & I show a side view of the roughened carbon and glass fiber surface after nanoparticle deposition, respectively. The deposited nanoparticles form a uniform and tightly packed thin film, of which the bonding strength relies on the uniformity of the crystal sizes and structure. The dip-coated fibers provide functional sites for the suspended ZnO NPs inside the ethanol solution to self-assemble on its surface. The diameters of these nanoparticles are measured to vary between 10 and 15 nm and the thickness of the surface coating can be easily increased by increasing the number of dip-coating cycles inside the seeding solution. While the interfacial behavior of the ZnO NP interphase will be studied, it can also serve

a seed layer for the radial growth of ZnO NWs on the fiber surfaces (Figures 4.15C-G and J-L). As demonstrated by Lin et al. [180], the seed layer nucleates into arrays of vertically aligned ceramic ZnO NWs on the surface of the fibers when placed inside a growth solution. This observed nanowire geometry is attributed to the discrepancy in the growth rate between the [0001] polar face and the lateral faces [335]. Following growth, gentle washing of the fibers eliminates any ZnO crystalline prism precipitation deposited on the surface. This is a necessary step to ensure a defect-free and uniform fiber surface morphology, thus reducing errors and inaccuracies in IFSS measurements using pullout testing. As seen in Figures 4.15C-G &J-L, the dense ZnO NWs interphase uniformly covers carbon and glass fiber surfaces, respectively, providing a considerable increase in the surface area of the fibers and their capacity to mechanically interlock with the matrix. The interfacial reinforcing performance of the grown interphase is proven to be reliant on the morphology of the nanowires, which can be tuned through a number of parameters such as growth period, addition of inhibitors [182]. The ZnO NWs used in this study are typically grown to possess an aspect ratio of 10, having a diameter of ~100 nm and a length of ~1 μm. Previous studies reported greater improvement in IFSS of carbon fiber composites under quasi-static loading conditions when increasing nanowire diameter and length [182]. It should be noted that the neutralization of the glass fiber surface with ammonium hydroxide and water post-functionalization is necessary for obtaining a high quality ZnO NWs interphase. Given the basic nature of the growth environment, an acidic fiber surface can disturb the aqueous solution's pH and result in inconsistent ZnO NW growth (Figure 4.15L). Nonetheless, the absence of any visible defects or signs of etching indicates that the employed functionalization techniques oxidize the fiber surface, all while maintaining the integrity of the fiber. The benign nature of the functionalization and its effect on the mechanical properties of the fibers are further confirmed and discussed in the following section.

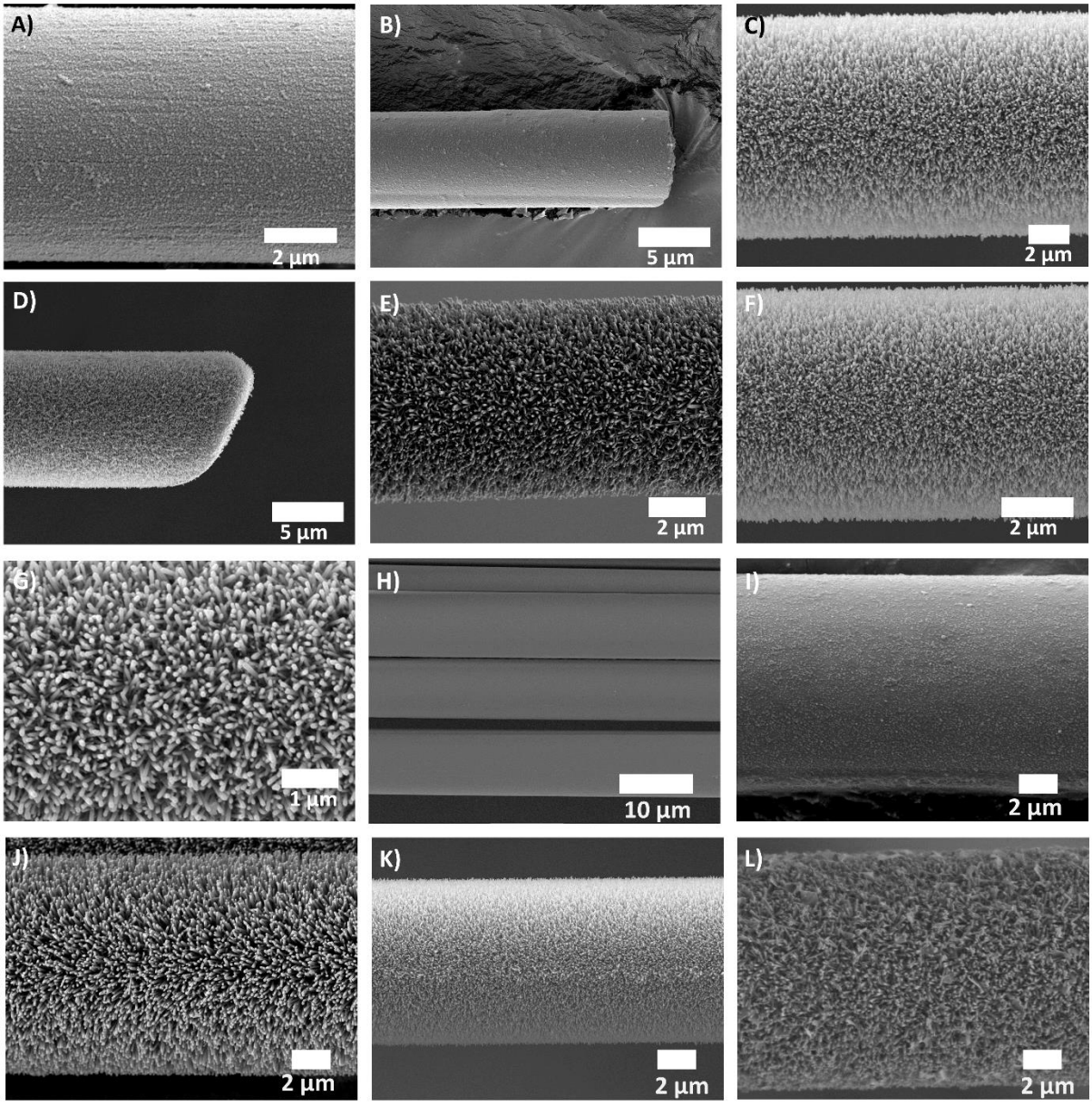

Figure 4.15. Zinc oxide-coated fibers. A, B) ZnO NPs coated carbon fibers. C- G) ZnO NW coated carbon fibers. H) Functionalized glass fiber I) Zinc NP coated glass fiber. J, K) Zinc oxide NW coated glass fiber. L) Poor ZnO interphase morphology when glass fiber surface neutralization process is omitted.

4.4.3. Single fiber dynamic testing experimental setup

When quasi-statically loaded, a well bonded and adhered fiber-matrix interface contributes to a reinforcement effect inside the composite, as it bridges the discontinuities found in such heterogeneous materials and allows for improved load transfer from the compliant matrix to the

tough fibers. However, a different fiber-matrix behavior is required under dynamic loading conditions. At high loading rates, the composite interface is typically designed with weak adhesion such that the tough fibers separate from the matrix, allowing them to absorb the impact. As the fiber releases from the matrix, there is significant energy absorption due to the friction between both components. Such different fiber-matrix properties can be simultaneously satisfied by the grafting of a ZnO interphase on the surface of carbon and glass fibers. To prove this, the IFSS of ZnO coated fibers/epoxy matrix systems is quantified using SFP at low, intermediate, and high strain rate loading conditions. The SFP at intermediate and high strain rates are performed using the experimental setup described first by Hwang et al. [138] The experimental procedure, explained in Figure 4.16A, uses a piezoelectric actuator coupled with a discharge circuit that allows up to 10^4 s^{-1} in strain rate and 100 µm in displacement. The resulting strain rate is dependent on the speed of discharge, which can be controlled by adjusting the circuit's bias resistor (Figure 4.16B). While the experimental setup is capable of simulating a wide range of strain rates, rates of 470 s^{-1} and 2200 s^{-1} are used to dynamically load the fiber-matrix interface. The selected strain rates mimic typical intermediate and high strain rates dynamic conditions to which composites used in ballistic applications are usually subjected. Moreover, these strain rates are several orders of magnitude larger than that used for quasi-static loading of 0.0016 s^{-1}, thus accurately replicating dynamic conditions relative to quasi-static IFSS testing.

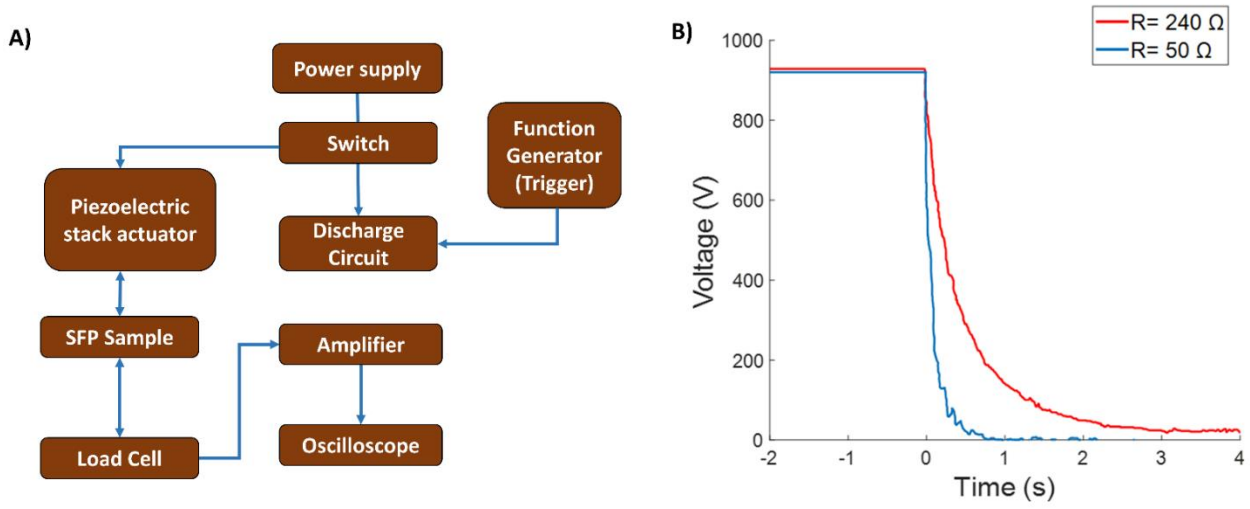

Figure 4.16. Dynamic SFP experimental design. A) Block diagram of the experimental setup's main components. B) Voltage vs. time plot of a PZT piezoelectric actuator, showing the resistance-controlled discharge times for the cases where R = 240 Ω, R = 50 Ω, and C = 1.33 µF.

The embedded lengths of the specimens are controlled to be smaller than 60 μm using an optical microscope, so that it satisfies the displacement limitations of the actuator. The previously described molds in chapter 2 ensure that the embedded lengths of specimens remain unchanged post-curing, immobilizing the fibers inside the molds' slits. When choosing the embedded fiber length for dynamic SFP testing, it is mandatory for it to satisfy multiple distinct criteria. First, it should ensure that interfacial failure happens before tensile failure by accounting for the maximum applied pullout load. Second, the embedded fiber length should result in a catastrophic failure of the interface, and therefore a linear elastic stress-strain behavior throughout the pullout test. This is primarily important in order to avoid initiating interfacial failure through crack propagation, thus leading to inaccurate IFSS calculation due to effect of frictional forces [365]. As discussed later, this is also necessary to maintain consistency in testing procedures for both static and dynamic loading conditions, as the piezoelectric actuator may be unable to ensure complete fiber pullout, while the dynamic load cell is incapable of accurately recording frictional effects. Finally, the embedded length is designed to be considerably larger than the fiber diameter in order to satisfy the assumption of a cylindrical embedded fiber geometry and avoid cross-sectional effects. Therefore, choosing an embedded length that is ranging between 20 μm and 60 μm eliminates any considerations with regards to Poisson shrinkage effects [393]. The fiber's free length is another parameter that requires proper design to ensure successful pullout across all strain rates, since the free length will strain, and if not accounted for, can absorb the 100 μm stack displacement. For a clean fiber pullout from the matrix, the fiber's free length is required to store sufficient energy to ensure the embedded length's pullout. Meanwhile, the elastic deformation of the fiber's free length should also be designed to be smaller than the fiber's embedded length, a feature that is proportionally dependent on the fiber's free length [393]. The proximity of the embedded lengths to the actuator's maximum displacement requires for a perfect vertical alignment when setting up specimens for testing (Figure 4.17A), which can be maintained using a high-speed camera (Figures 4.17B & C) and the application of a minimal pre-load of ~ 0.0178 N to the fiber. The pre-load of the fiber is kept consistent across all samples, as it is controlled using the fine precision controller of the testing frame and monitored through a static load cell. Once discharge is initiated, The IFSS is calculated using the voltage-time response recorded through a piezoelectric shock load cell. Unlike the load-displacement curves generated under quasi-static loading (Figure 4.17D), here, the pullout process results in an instantaneous voltage signal inside the piezoelectric dynamic load

cell whose period is dependent on the applied strain rate (Figure 4.17E). Any trailing oscillations caused by post-pullout vibrations of the grip are transient and can be isolated from the detected pullout load signal that precedes it. Using such load measurement technique, frictional effects during pullout are difficult to accurately capture, further justifying the adopted design approach for SFP specimens. The discharge time is inversely proportional to the applied strain rate and is represented through the duration of the response. Finally, the piezoelectric actuator's displacement is kept at 90 µm for all tested specimens.

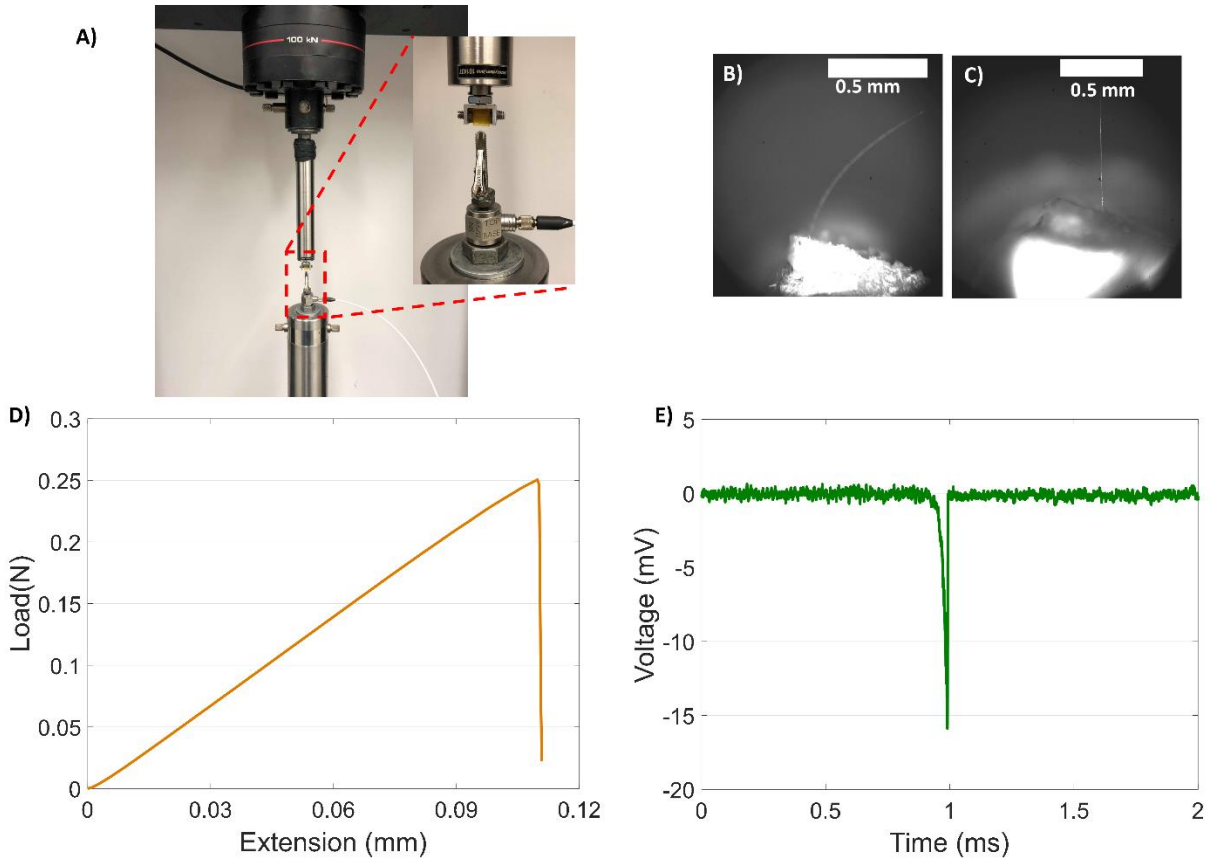

Figure 4.17. Dynamic SFP testing. A) experimental setup for intermediate and high strain rate single fiber pullout testing. B, C) High speed camera image of the initial fiber position and vertically aligned and re-strained carbon fiber ready for testing. D) Load-extension response of SFP specimen at quasi-static loading rate. E) Voltage-time response of SFP specimen at dynamic loading rate.

4.4.4. Dynamic SFP and tensile testing

Irrespective of the applied loading rate, the IFSS of functionalized carbon fibers shows no significant statistical change, remaining relatively constant at approximately 53 MPa (Figure

4.18A). Similarly, the IFSS of functionalized glass fibers is also found to be unchanged across strain rates, at approximately 61 MPa (Figure 4.18B). The loading rate independency of IFSS in conventional fiber-matrix interfaces is expected in the case of ceramic fibers. The quality of a conventional fiber-matrix interface is dictated by two rate independent parameters: the chemical interaction and mechanical interlocking between both components. Given that the reinforcement mechanism due to functionalization is strictly chemical, average IFSS is expected to remain relatively unchanged with increasing strain rate. Moreover, by designing pullout testing for catastrophic interfacial failure, frictional and additional shearing effects between the fiber and the matrix are eliminated. Nonetheless, improvement in surface chemistry due to functionalization can increase interfacial properties of fibers at a given strain rate. At a pullout rate of 0.0016 s^{-1}, the IFSS of piranha solution functionalized glass fibers is found to increase by 14.8 %, in comparison to that of untreated glass fibers. Given that surface morphology remains relatively smooth post-functionalization (Figure 4.15H), the observed increase in IFSS can be attributed to the enrichment of the glass fiber surface with oxygen functional groups, leading to improved chemical interaction between the fiber surface and the epoxy matrix. Similar behavior is obtained at intermediate and high strain rates of 470 s^{-1} and 2200 s^{-1}, as the average IFSS of functionalized glass fibers improved by 11.3% and 15.1% relative to untreated ones, respectively. Once a ZnO interphase is introduced, the IFFS of ZnO coated carbon and glass fibers is found to become dependent on loading conditions. At a quasi-static loading rate of 0.0016 s^{-1}, a maximum IFSS of 85.6 MPa is observed for ZnO NW coated carbon fibers, showing approximately a 75.7% increase when compared to an IFSS of 48.7 MPa for the untreated fibers. However, as loading rate is increased to 470 s^{-1} and 2200 s^{-1}, the IFSS of ZnO NW coated carbon fibers is decreased to 32 and 23 MPa, respectively. Similarly, when compared to untreated carbon fibers, ZnO NP coated carbon fibers display a 39% increase in IFSS when quasi-statically loaded, and a 23% and 38% decrease in IFSS when loaded at intermediate and high strain rates, respectively, all relative to untreated fibers at similar strain rates. The IFSS of ZnO carbon coated fibers thus display a decreasing trend with increasing strain rate, with either higher or lower IFSS than that of untreated fibers under identical loading conditions. Moreover, Figure 4.18A shows that a ZnO NW interphase transitions from a higher IFSS relative to that of a ZnO NP interphase at a quasi-static loading rate, to a lower one at intermediate and high strain rates, as the IFSS of ZnO NW coated fibers goes from being 19.1% higher IFSS than ZnO NP coated fibers at 0.0016 s^{-1}, to 16% and 28% lower IFSS at 470 s^{-1} and

2200 s^{-1}, respectively. In the case of glass fibers, Once the interface is mechanically reinforced using a ZnO interphase, IFSS sensitivity to the applied loading conditions is also observed. At 0.0016 s^{-1}, the ZnO NW the ZnO NP interphase display an IFSS of 106 MPa and 78 MPa, respectively, equivalent to 83% and 44% improvement in IFSS relative to untreated glass fibers. Once strain rate is increased to 470 s^{-1}, a 34% and 25% decrease in IFSS is observed for ZnO NP and ZnO NW coated glass fibers, respectively, in comparison to untreated glass fibers at a similar strain rate. Further decrease in average IFSS by 45 % is found in the case of ZnO NW coated glass fibers at 2200 s^{-1}, while ZnO NP coated fibers displayed saturation. These results highlight the influence of interphase geometry, especially its aspect ratio, on its performance across strain rates, causing nanowires and nanoparticles to exhibit different failure modes when the fiber-matrix interface is dynamically loaded. The observed decrease in IFSS indicates weaker fiber-matrix interfaces, a desirable interfacial property for dynamic loading conditions. Such results offer insight into the reversal of the role of a ZnO interphase inside a composite when loading rate is increased. At a quasi-static loading rate, the rigid ceramic nanowires penetrate into the matrix, providing localized reinforcement by increasing the bonding area and improving load transfer. The functionally graded interface bridges the typically discrete boundaries of the fiber-matrix interface, reducing stress concentrations and improving the IFSS of the composite. However, the observed decrease in IFSS of ZnO NP and NW coated fibers with increasing strain rates demonstrates the ability of a ZnO interphase to allow easier interfacial debonding under dynamic loading conditions. Therefore, the effectiveness of the functional gradient provided by the ZnO interphase is decreased at intermediate and high strain rates, as the fiber-matrix interface exhibits premature failure. It should be noted that improvements in IFSS at quasi-static loading condition are maximized by the piranha functionalization in the case of glass fiber composites, which improves chemical adhesion between the ZnO nanomaterials and the glass fiber surface (Figure 4.18C). Previous studies have also shown the impact of nitric acid functionalization on adhesion between ZnO and carbon fiber surfaces, and subsequently the IFSS of carbon fiber composites [344]. Therefore, the ZnO interphase is found to be capable of tailoring interfacial properties in ceramic fiber reinforced composites for optimal response under quasi-static and dynamic loading conditions.

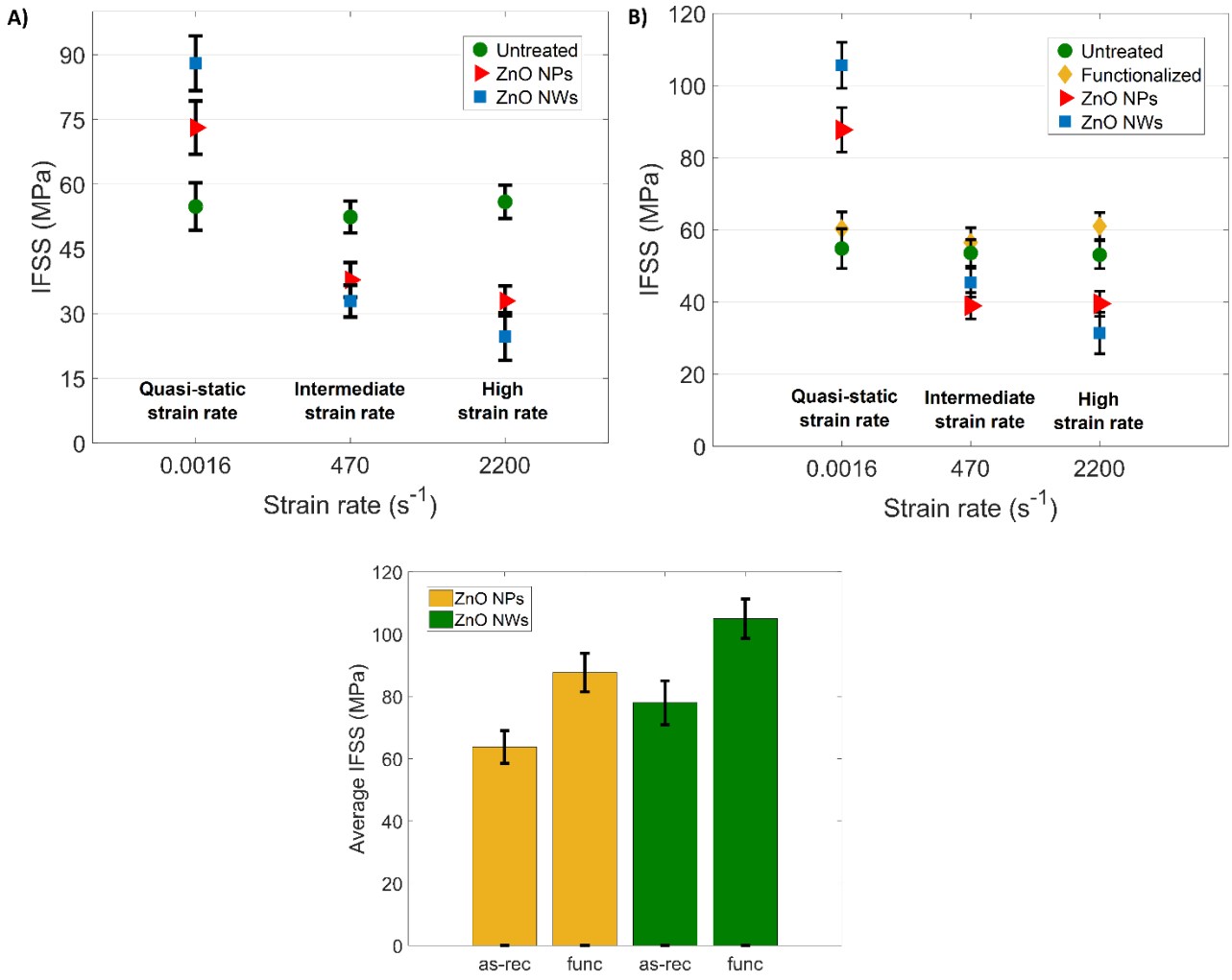

Figure 4.18. Interfacial shear strength of untreated and ZnO coated fibers across various strain rates: 0.0016, 470, and 2200 s^{-1}. A) Carbon fiber. B) Glass fiber. C) IFSS of as-received (as-rec) and functionalized (func) ZnO coated glass fiber at a loading rate of 0.0016 s^{-1}.

Given that the ballistic and structural performance of composite laminates are both dependent on in-plane properties, it is important to maintain the strength of the fiber post-treatment. In addition to strength limitations due to manufacturing defects, many surface modification treatments further etch the fiber and weaken it, sacrificing the tensile strength of the fiber, and thus the in-plane composite properties at the expense of interfacial gains. In this study, the effect of the proposed surface functionalization and ZnO interphase on the tensile properties of the carbon and glass fibers is assessed using tensile testing of single filaments at low, intermediate, and high strain rates, as described in ASTM C1557-03. A gauge length of 5 mm is

chosen based on the fiber's strain to failure and the piezoelectric stack actuator's maximum stroke of 100 μm, thus ensuring tensile failure of the fiber. The same gauge length is also adopted at quasi-static loading for consistency when comparing fiber strength across strain rates. Figure 4.19 shows that, at a quasi-static loading rate, a statistically invariant tensile strength is observed when comparing that of untreated fibers to ZnO NP coated fibers. The same behavior is also observed when the ZnO NP coated fibers are loaded at intermediate and high strain rates. In contrast, the tensile strength of ZnO NW coated fibers is found to be increased across all strain rates, relative to untreated ones. The tensile strength of ZnO NW coated carbon fibers is found to increase by 10.2 %, 8.4% and 14.5% at 0.0016 s^{-1}, 470, and 2200 s^{-1}, respectively (Figure 4.19A). Meanwhile, the tensile strength of ZnO NW coated glass fibers is found to display a slight increase in strength by 8.91%, 9.15%, and 10.83% at 0.0016 s^{-1}, 470 s^{-1} and 2200 s^{-1}, relative to that of untreated glass fibers at the corresponding strain rates, respectively (Figure 4.19B). These results are in agreement with other studies in literature reporting an increase in single fiber tensile strength when whiskerized with ZnO [216,218]. In addition, the tensile strength of both untreated and ZnO coated fibers is found to be unchanged when compared across strain rates. Unlike polymer fibers, the ceramic carbon and glass fibers do not evoke a viscoelastic response that is dependent on the applied strain rate [394]. Furthermore, these results indicate the fact that both nitric acid and piranha solution functionalization are benign to carbon and glass fibers, respectively, and preserve their tensile strength. Drawing from these results, the employed functionalization treatments in this work allow for sufficient oxidization of the fiber surfaces while avoiding surface etching. Therefore, the tensile strength of these ceramic fibers is found to be maintained post-functionalization and interphase growth, preserving the in-plane properties of carbon and glass fiber composites under both static and dynamic loading conditions.

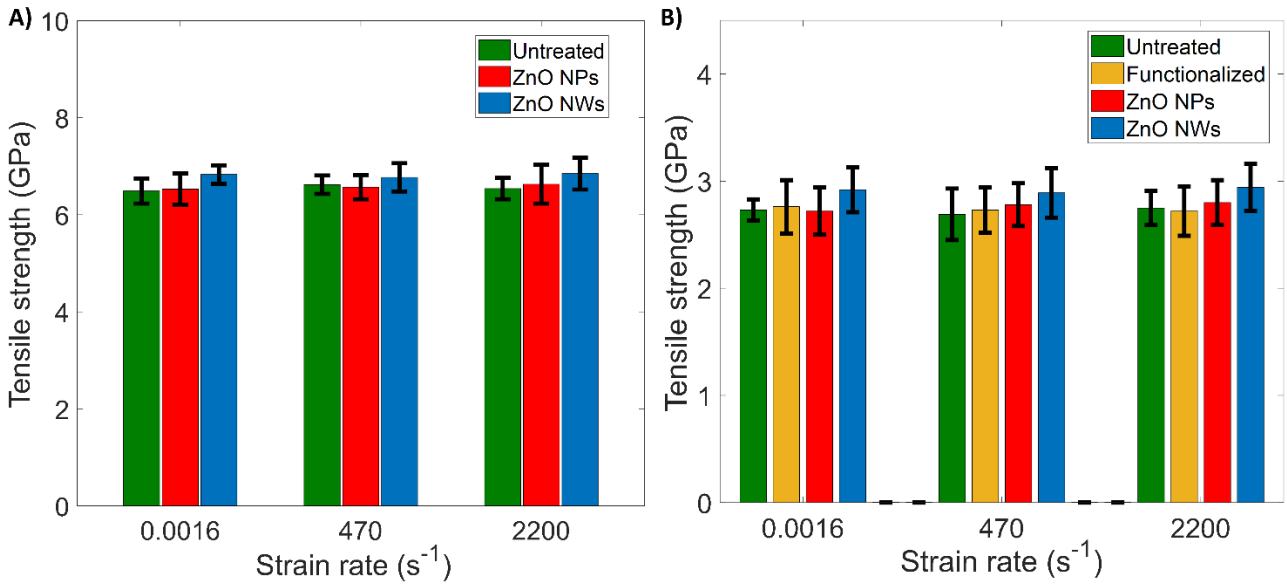

Figure 4.19. Tensile strength of untreated and ZnO coated fibers across various strain rates: 0.0016, 470, and 2200 s^{-1}. A) Carbon fiber. B) Glass fiber.

4.4.5. Study of dynamic interfacial failure mechanism

The rate dependency of IFSS in the presence of a ZnO interphase can be further explained by examining the polymer matrix behavior with increasing strain rate (Figure 4.20). The EPON 862 polymer matrix used during pullout testing is expected to display a rate dependent viscoelastic behavior. Stiffness measurements of the EPON 862 matrix are performed using the same setup described for static and dynamic tensile testing. At a strain rate of 2200 s^{-1}, a matrix elastic modulus of 9.2 GPa is observed, showing approximately a 187.5% increase from an elastic modulus of 3.24 GPa at 0.0016 s^{-1} (Figure 4.20D). Such measurements are in agreement with other reported studies in literature discussing the viscoelastic behavior of polymers across strain rates [395,396]. This considerable increase in matrix stiffness changes the load transfer mechanism between the fiber and the matrix due to a ZnO interphase. Malakooti et al. experimentally studied the effect of a whiskerized interphase on strain distribution at the interface region [137]. He reported that the higher stiffness of the nanocomposite interphase leads to a reduction of shear strain and pushes it to the softer matrix. Based on the shear lag theory, the shear stress at the matrix would be lower due to its greater distance from the fiber in the presence of the nanowires [139]. In addition, the nanowires create a functional gradient that smoothens the transition of shear strains between the elastically mismatched interfacial constituents (Figure 4.20B). The following mechanism

eliminates local strain concentrations in the vicinity of the interfacial region and moves it away a considerable distance, and into the relatively tougher and more crack resistive epoxy matrix (Figure 4.20A). Such findings also explain how a nanostructured gradient can result in large interfacial shear strengths that exceed that of the matrix [397], thus avoiding matrix shear failure before interfacial debonding. Under such conditions, fiber pullout occurs when the ZnO nanowires/fiber interface fails which is dependent on the chemical interaction between the ZnO interphase and the fiber surface. However, as loading conditions are changed and strain rate is increased, the matrix surrounding the interphase stiffens, thus weakening its functional gradient and re-introducing interfacial shear strain concentrations. This results in an unusual and sudden shear loading of the ZnO interphase which would cause brittle failure (Figure 4.20C). Moreover, ZnO NWs and NPs are ceramic nanomaterials of wurtzite structure, that when loaded at room temperatures, tend to fail in a brittle manner along the (0001) cleavage plane [337–339]. With that, the interfacial failure mode is modified, as the ZnO interphase experiences brittle failure before debonding from the fiber surface, leading to disconnections in the functionally graded interface and allowing for easier debonding between the fiber and the matrix.

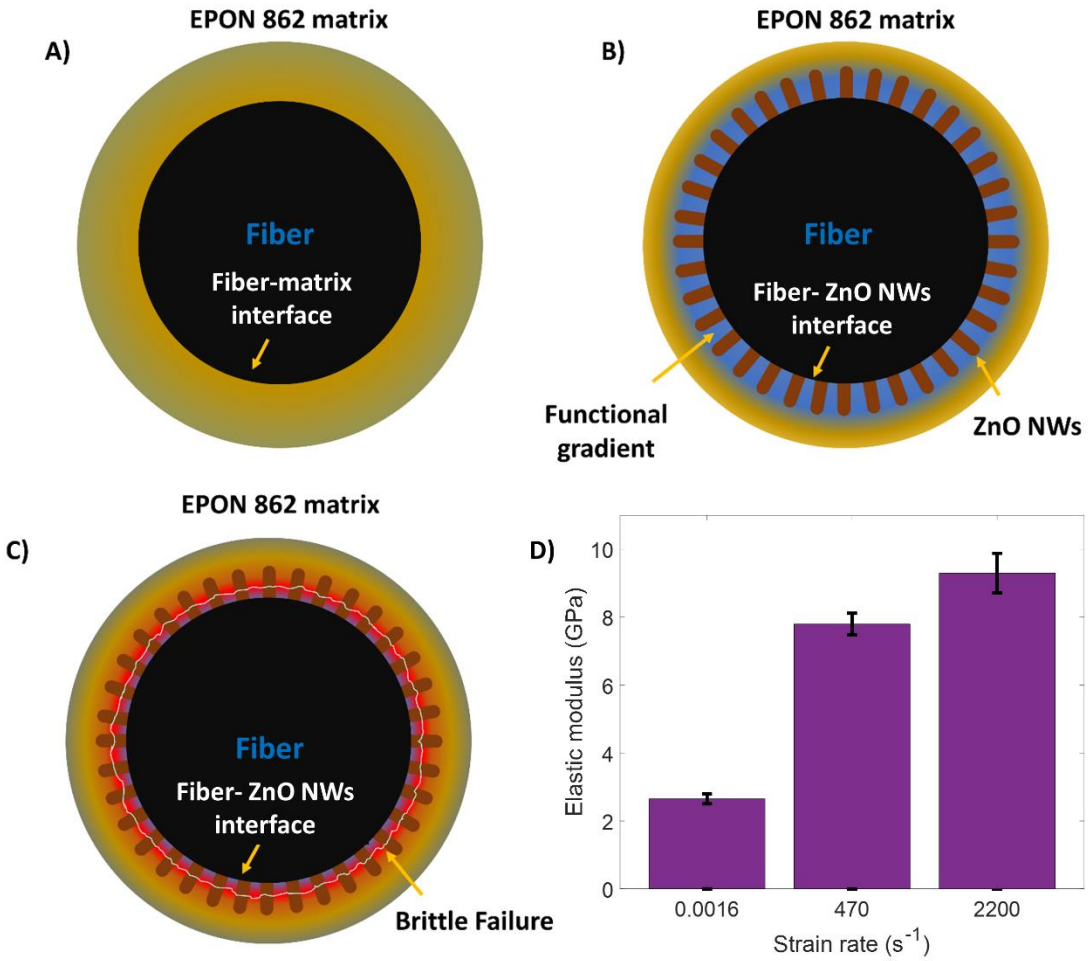

Figure 4.20. Failure mechanism of a ZnO interphase under varying loading rates. A) Elastic modulus of neat EPON 862 epoxy across various strain rates: 0.0016, 470, and 2200 s^{-1}. B) Traditional fiber-matrix interface subjected to shear strain. C) Functional gradient effect of a ZnO interphase under static loading conditions, smoothening interfacial shear strain transition, and reducing stress concentrations (blue region). D) Brittle failure of the ZnO interphase under dynamic loading conditions due to stiffening of matrix and interphase.

Further insight into the interfacial failure mechanism is obtained through examining the embedded portion of the fibers post-testing using SEM imaging. The embedded section of quasi-statically loaded ZnO NW coated carbon and glass fibers are shown in Figures 4.21A-C & 4.22A-C, displaying clean, nanowires-free surfaces. The ZnO NWs are initially strongly bonded to the fiber surfaces through oxygen functional groups, as well to the matrix through an embedded, stiff and large bonding area, providing two interfaces that are stronger than the traditional fiber-epoxy interface [180]. Under quasi-static loading, the ZnO NWs detach from the surface of the fibers and remain interlocked inside the matrix. This is due to the interaction area between the matrix-

nanowires interface being considerably larger than that of the fiber surface-nanowire interface, resulting in the initiation of interfacial failure at the level of the latter. Moreover, the absence of any resin residue on the fiber surface indicates that the matrix does not exhibit failure in the presence of a ZnO interphase, even at high IFSS of ~90-100 MPa. In comparison, the surface of untreated embedded carbon fiber lengths is also found to be relatively smooth due to the brittle nature of EPON 862 (Figures 4.21D & E). However, unlike the case of ZnO NWs coated fibers, the surfaces of untreated fibers still display residual matrix material in a number of spots. Similar surface morphology is expected in the case of untreated embedded glass fiber embedded length. The interfacial shear testing methodology of SFP used in this work does not allow for examining of the ZnO NWs-epoxy interface, nor the matrix itself, yet the observed ZnO NWs-free embedded lengths surfaces confirm that the nanowires remain anchored inside the matrix. Under dynamic loading of 2200 s^{-1}, the interfacial failure mode is changed, as debonding of the ZnO interphase is preceded by a brittle failure of the ZnO interphase due to the stiffening of the surrounding matrix. Figures 4.21F-G & 4.22D-F show bundles of broken ZnO NWs that remain attached the carbon and glass fiber surfaces post-pullout. However, it is difficult to assess these fractured nanowires, as the surrounding and embedding matrix impedes proper assessment of their lengths. These SEM images support the failure mechanism in Figure 4.20, as the ZnO interphase is expected to fail before complete debonding of the nanowires from the fibers' surface. The resulting brittle failure of the ZnO interphase reduces the IFSS of the single fiber composites specimens with increasing loading rate up to where a ZnO interphase is weaker than a traditional carbon fiber-matrix interface. With that, easier debonding of the fibers from the matrix is achieved, allowing them to carry the load in the cases of impact or ballistic events. Finally, it should be noted that the geometry and aspect ratio of the ZnO interphase plays an important role during failure. The vertically aligned nanowires are firmly embedded inside the epoxy matrix, whereas the spherical ZnO NPs roughen the fiber surface. Therefore, ZnO NWs offer a higher degree of mechanical interlocking and superior reinforcement performance under quasi-static loading. However, when dynamically loaded, the embedded nanowires are highly constrained when epoxy matrix stiffens, increasing the possibility of brittle interphase failure, and leading to a lower IFSS through a ZnO NWs interphase in comparison with that of a ZnO NPs interphase. It can be then concluded that under dynamic loading conditions, brittle failure of the ZnO interphase, especially nanowires, allows for easier release of the fibers from the matrix, and an improved performance of carbon and glass fiber

reinforced composites in ballistics and impact applications, while maintaining its reinforcement role in quasi-static loading applications through the introduction of a functionally graded interface.

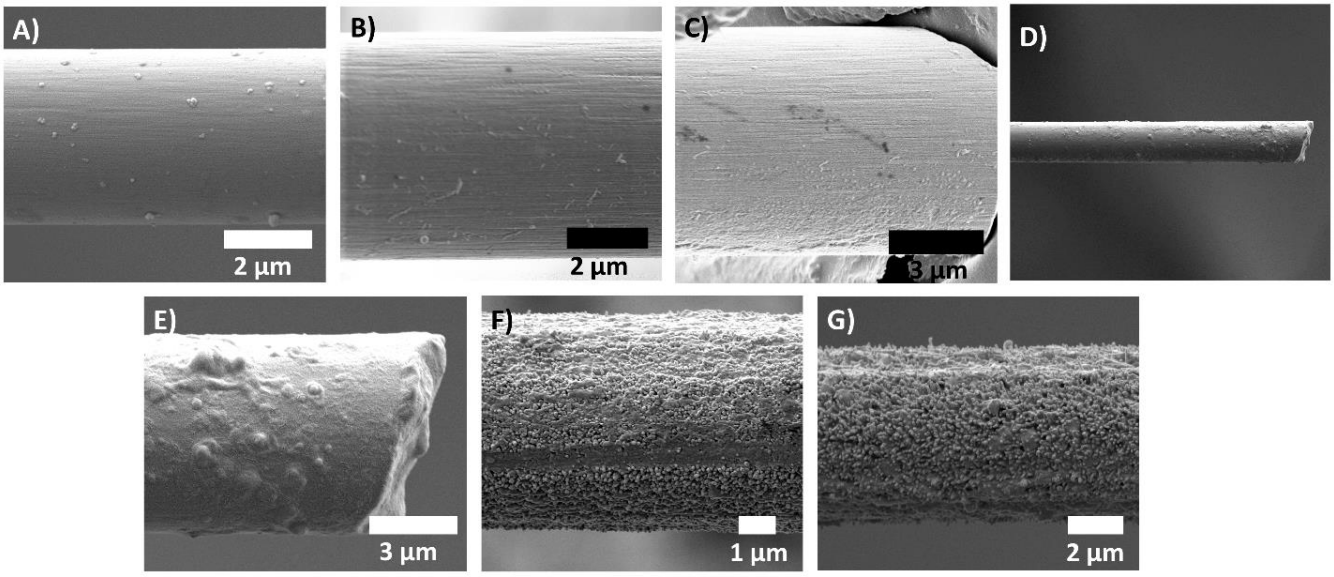

Figure 4.21. SEM images of the carbon fiber embedded length following pullout. A-C) ZnO NWs coated carbon fibers at quasi-static loading rate. D, E) Untreated carbon fibers at quasi-static loading rate. F, G) ZnO NWs coated carbon fibers at 2200 s^{-1}.

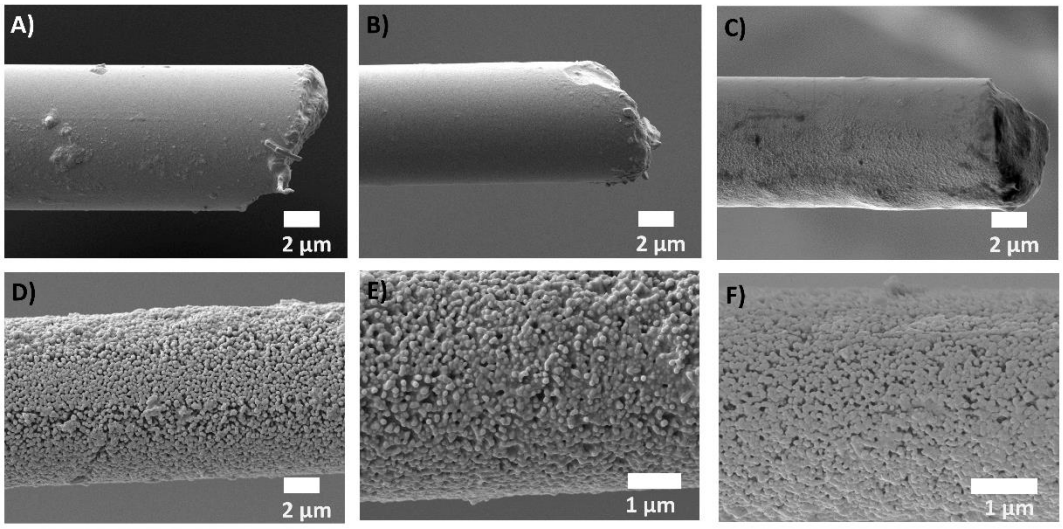

Figure 4.22. SEM images of glass fiber embedded length following pullout. A-C) ZnO NWs coated glass fibers at quasi-static loading rate. D-F) ZnO NWs coated glass fibers at 2200 s^{-1}.

4.5. Chapter summary

In this chapter, nanostructured interphases are demonstrated to tailor an improved the impact response of woven fabric and fiber reinforced composites under dynamic loading conditions. Through a simple fibrilization method, it is demonstrated that the interyarn friction in woven aramid fabric can be improved by up to 500%. The enhanced yarn pullout energy is the result of increased mechanical interlocking between aramid yarns due to the generated fibrils. The enhanced fiber-fiber interactions also translate into 10% and 230% improvement in the ballistic limit and stab resistance of the aramid fabric. Given the preservation of the strength, light weight, and flexibility of the aramid fabric post-treatment, the described rapid and low-cost fibrilization method possesses great potential to be integrated into the production of high-performance soft body armors.

In addition, it is shown that ZnO interphases can be used to tailor the interfacial properties of fiber reinforced composites for a multifunctional performance and optimal response under both static and dynamic loading conditions. As expected, the ceramic interphases are shown to improve the IFSS of carbon and glass fiber composites under quasi-static loading conditions through a combination of mechanical interlocking and increased surface area. Under dynamic loading conditions, brittle failure of the ZnO interphases is found to decrease the IFSS of these fiber reinforced composites, allowing for an enhanced ballistic performance. The ZnO NP coated fibers displayed a maximum decrease in IFSS of 34% and 38% at intermediate and high loading strain rates of 470 s^{-1} and 2200 s^{-1}, respectively, relative to untreated fibers at similar loading rates. Similarly, ZnO NW coated fibers are shown to display a maximum decrease in IFSS of 34% and 56%, relative to untreated fibers at similar loading rates. The reduced IFSS under dynamic loading conditions is found to be due to the stiffening of the polymer matrix at higher strain rates, limiting the effectiveness of the interphase's functional gradient, and leading to its brittle failure. This work is the first to report such a unique interfacial performance in composites, as it allows for the tough fibers to absorb the ballistic impact energy in the event of dynamic loading, while preserving their structural properties. Thus, ZnO interphases enable the design of multifunctional carbon and glass fiber reinforced composites, with optimal performance under both static and dynamic loading conditions, giving way towards the integration of lightweight and flexible ballistic protection into structural components.

CHAPTER 5. Development and Optimization of Nanostructured Interlayers for Composite Toughening

5.1. Chapter introduction

While the previous two chapters have discussed the potential of nanostructured interphases to improve interfacial adhesion, delamination remains the "Achilles heel" of laminated composites [238,398]. Due to out-of-plane loading, such as compression and bending, or cyclic loading, interlaminar stresses form between adjacent plies within a composite, ultimately leading to the formation and propagation of cracks within its interlaminar region and resulting in catastrophic failure [239]. Typically, delamination can be characterized as either mode I (peel), mode II (shear), mode III (tearing) or a combination of them. With delamination being a large concern when designing and adopting fiber reinforced composites in structural and ballistic applications, it is necessary to develop viable interlaminar reinforcement techniques that toughen composites. While early approaches relied on modifying fabric architecture or the use of large reinforcement agents such as z-pins, recent efforts have aimed to use microscale interlayers to improve the fracture toughness of fiber reinforced composites. Yet many of these techniques sacrifice the in-plane properties of the composites due to either the harsh treatment conditions, or the excessive interlayer thickness. In this chapter, nanostructured interlayers are introduced on the surface of aramid and carbon fiber reinforced composites for improved interlaminar properties, while maintaining its tensile strength.

In the first part of the following chapter, ANFs are deposited on the surface of carbon fabric using a simple and benign spray coating technique that avoids agglomeration issues, and that is easily scalable to industrial levels. The nanoscale and low areal density ANF interlayer is found able to improve chemical and mechanical interaction between the fiber and the matrix. Through short beam shear and Mode I testing, the ANF interlayered carbon fiber composites are found to exhibit higher resistance to crack initiation and propagation, as highlighted by their improved fractured toughness, along with maintaining their tensile properties. In the second part of this chapter, laser induced graphene (LIG) is used to introduce multifunctional interlayers of various morphologies into both aramid and carbon fiber reinforced composites in a simple and benign

manner. The conductive and fuzzy LIG morphologies are obtained on aramid fabric and carbon fiber prepregs through direct laser writing and transfer printing, respectively. The modified surface morphology provides great potential for improving mechanical interlocking with the matrix when integrated into composites. The mechanical properties of the LIG interlayered aramid and carbon fiber composites are investigated through a series of mechanical testing such as short beam shear, Mode I and Mode II fracture testing, dynamic mechanical analysis (DMA), and tensile testing. Both aramid and carbon fiber composites are demonstrated to exhibit a tougher response, and preserved elastic and viscoelastic properties.

5.2. ANF interlayer in carbon fiber composites

5.2.1. Deposition of ANF interlayer on carbon fiber surface

Previous work that discusses the use of ANFs in carbon fiber composites relies on energy intensive techniques such as electrophoretic deposition to coat the carbon fabric [134]. Moreover, ANF resin mixing has been shown to potentially suffer from agglomeration issues at higher weight fractions [136]. Therefore, here, in order to deposit an ANF interlayer onto the surface of the carbon fabric, a simple and rapid spray-coating process is employed (Figure 5.1A). Initially, the ANFs are negatively charged and stably dispersed in a mildly basic dimethyl sulfoxide (DMSO)/potassium hydroxide (KOH) solution. Given the high boiling point of DMSO and the presence of KOH, this solution is not ideal for the spray-coating process employed in this work. Thus, the ANFs are thoroughly washed and neutralized before re-dispersing them in a new solvent. For the purpose of this study, acetone is chosen since it is a polar aprotic solvent similar to DMSO, thus allowing for the formation of a new, uniform and stable dispersion of ANFs post-washing. Moreover, the low boiling point of acetone (> 50 °C) is suitable for a multi-layer spray coating process, as the solvent can be easily and quickly evaporated off the surface before depositing another layer. It should be noted that this approach deviates from what was reported in Lin et al., as the ANFs are not completely dried into powder and re-dispersed, hence considerably reducing the required ANF processing period [110]. The air pressure and distance between the spraying nozzle and the substrate is kept consistent throughout the spray process. Multiple layers of ANFs are successively deposited on one side of the carbon fabric surface, while allowing for the solvent to evaporate between layers. The evaporation of the solvent is achieved through the heating of the substrate to a temperature of 50 °C for 5 minutes, before spraying a new ANF layer. Once all layers

are deposited, the carbon fabric is dried under vacuum in an oven for 12 hours prior to VARTM fabrication. The dimensions and morphology of the ANFs in the acetone solution are found to be similar to those of the ANFs originally dispersed in the DMSO/KOH solution, with diameters and lengths ranging between 5-10 nm and 2-10 μm as measured using AFM, respectively (Figure 5.1B). These AFM measurements also indicate that de-swelling did not occur, as the ANFs were never completely dried throughout the washing and re-dispersion process [110]. The amount of ANFs sprayed on the carbon fiber surface can be quantified using the following linear relationship:

$$A = fN \qquad (5.1.)$$

Where A is the total areal density of the ANF interlayer, N is the number of ANF layers spray coated, and f is a fitting parameter that approximates the areal density of a single ANF layer (4.0389 x 10^{-6} g/cm^2/layer). Given that it is hard to measure the areal density of a single sprayed ANF layer, at least 15 ANF layers are used to obtain areal densities before fitting a linear relationship to obtain the fitting parameter (Figure 5.1C). To ensure consistency between ANF layers, each layer is sprayed under near-identical conditions, while also allowing proper time for the solvent to evaporate between successive sprays. It should be noted that the previously obtained relationship does not hold if parameters such as spraying air pressure or ANF solution concentration are modified, and a new linear relationship must be determined. Therefore, the ANF interlayer can be quantified through its areal density, providing a calibration tool that can be used to optimize their mechanical performance in carbon fiber reinforced composites.

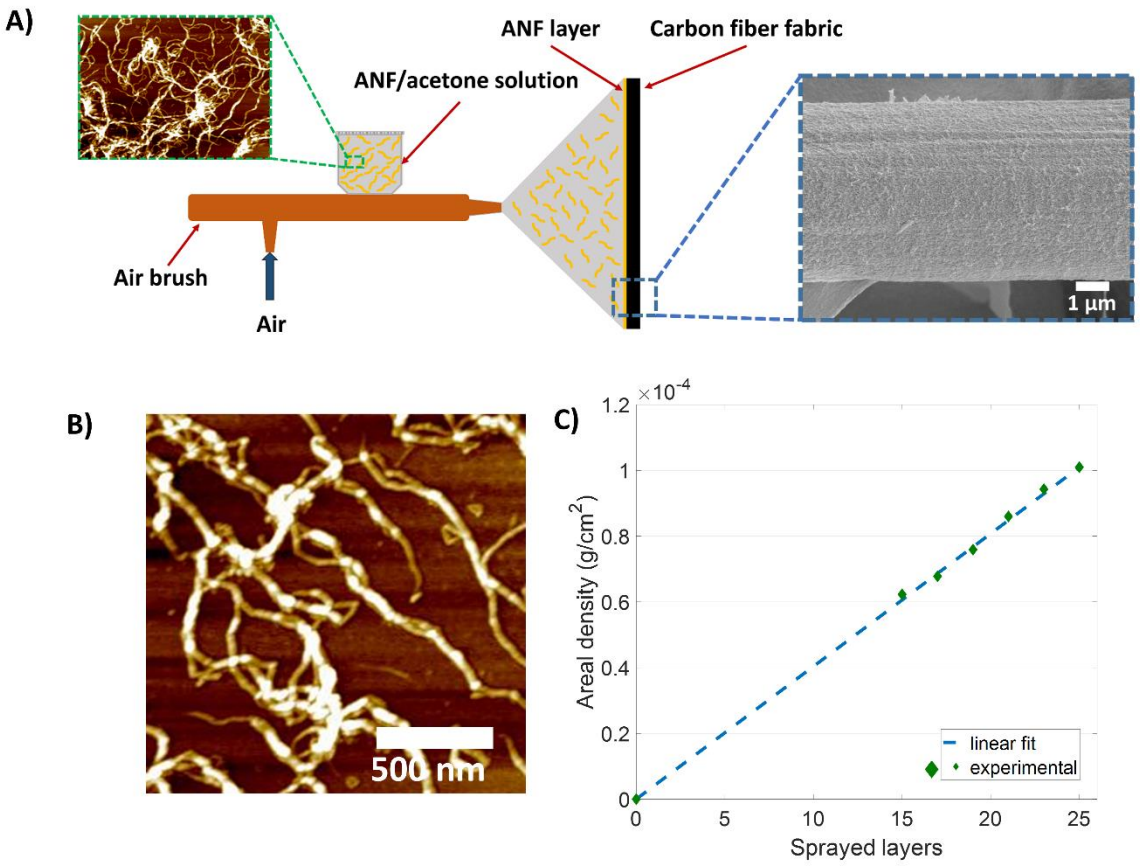

Figure 5.1. Spray-coating of ANFs onto carbon fabric A) Schematic of spray-coating process. B) AFM imaging of ANFs spin-coated on silicon wafer substrate. C) Areal density of carbon fabric for various number of spray-coated ANF layers and linear fit.

5.2.2. Characterization of surface morphology and chemistry

The various surface morphologies resulting from the ANF spray-coating process are investigated using SEM imaging (Figure 5.2). For optimal mechanical performance, it is necessary to deposit a considerable amount of ANFs in order to form a consistent and uniform polymeric interlayer across the carbon fiber fabric. However, excessive ANF coating can negatively affect the interlaminar properties of carbon fiber composites, as it impedes the infusion of the resin through the micro-channels of the fabric and results in defects and voids in composites. The primary advantage of spray-coating over other electro-chemical approaches that have been used to coat ANF on fabric surfaces, such as dip-coating or electrophoretic deposition [134], is that it provides superior control over the density and uniformity of the ANF interlayer. By ensuring an equal amount of ANFs are deposited across the entirety of the fabric area, the effect of the ANF

interlayer on the mechanical performance of the composites is both repeatable and spatially consistent throughout the composite. As seen in Figures 5.2C-E, only a negligible amount of ANFs are introduced on the fabric surface when 1 to 3 layers are sprayed, resulting in a relatively unchanged fabric morphology in comparison to that of untreated fabric (Figures 5.2A & B). When 5 to 10 layers are sprayed on the surface, uniform ANF coatings are found to form across the carbon fiber surface. These coatings are comprised of entangled and randomly aligned ANFs which form networked structures of larger scale than that of the individual nanofibers (Figures 5.3F - I). Nonetheless, the thickness of the ANF coatings remains at a nanoscale level, due to them being simply the outcome of the agglomeration of a few nanofibers. This relatively rough and coarse fabric morphology is desirable due to its ability to improve mechanical interlocking between the fabric and matrix. Moreover, negligible changes to the diameter of the carbon fibers is detected post-spray coating, therefore confirming the nanoscale nature of the thickness of the coating. Such observations agree with other reported research in the literature that have studied ANF coatings [108,282]. The nanoscale thickness of the ANF interlayer is important for the preservation of in-plane properties, as micrometer thick interlayers are found to degrade the tensile strength of carbon fiber composites despite the improvements to interlaminar properties[276]. Furthermore, porous ANF web-like structures are observed between adjacent fibers, thus providing the ANF interlayer with the ability to be firmly anchored in the infused matrix (Figure 5.2J). However, the porosity of these inter-fiber structures is completely lost when 11 to 18 layers are sprayed on the carbon fabric surface, as Figures 5.3K and L show continuous ANF films covering the carbon fiber surface. Such surface morphology can prove to be problematic when trying to fabricate carbon fiber composites using VARTM due to difficult resin infusion, leading to the formation of a poor and defective interlaminar region. This indicates the importance of optimizing the areal density of the ANF interlayer in order to maximize its interlaminar performance in carbon fiber composites.

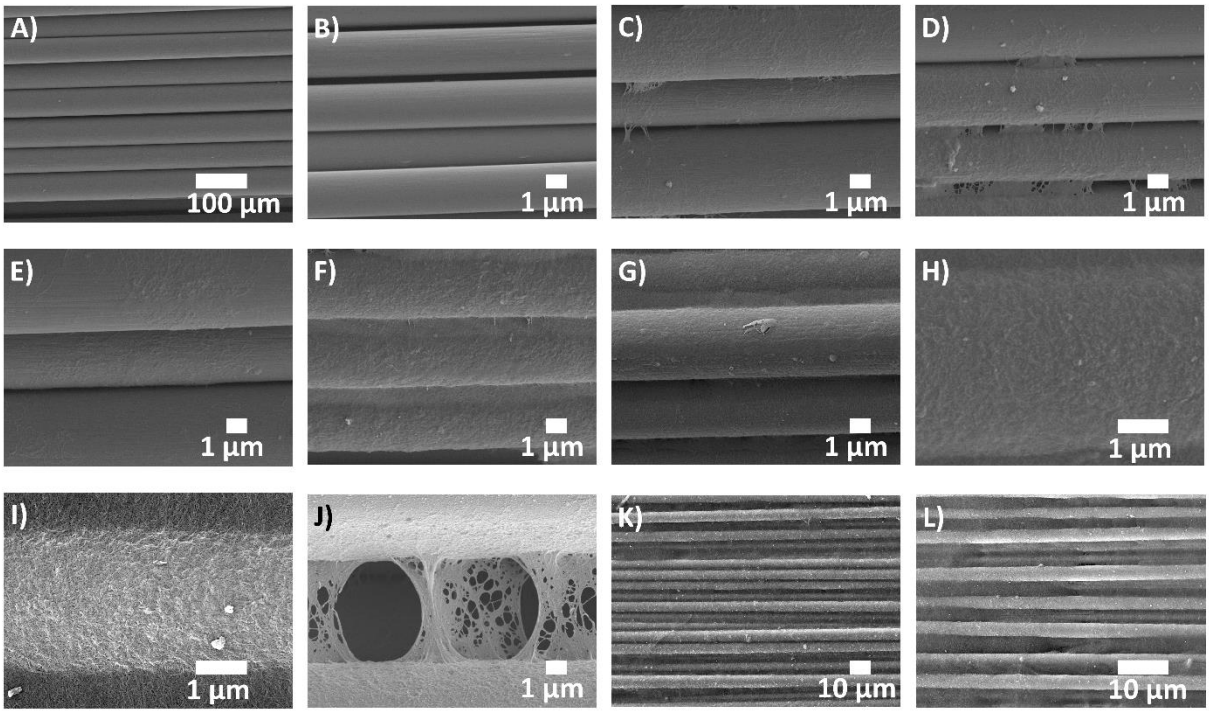

Figure 5.2. SEM imaging of carbon fabric surface post-ANFs spray coating. A) & B) Untreated. C) 1 ANF layer. D) 2 ANF layers. E) 3 ANF layers. F & G) 5 ANF layers. H-J) 8 ANF layers. K) 11 ANF layers. L) 16 ANF layers.

The introduced ANF interlayer results in considerable changes to the chemical structure of the carbon fabric. Figure 5.3A shows a typical FTIR spectrum of untreated carbon fiber fabric. The higher absorbance at low wavenumbers relative to higher wavenumbers arises from the fact that the penetration depth of the electric field in the conductive fabric during FTIR is inversely proportional to the wavenumber [399]. When ANFs are deposited on the surface, characteristic bands of ANFs such as C=O stretching (1649 cm^{-1}), N-H deformation and C-N stretching (1545 cm^{-1}), C=C stretching (1516 cm^{-1}), and Ph-N vibrations (1319 cm^{-1}) can be clearly detected in the collected fabric spectra. Similar results can be confirmed using Raman spectroscopy, where the ANF coated fabric displays the characteristic PPTA peaks of C=C ring stretching (1183 cm^{-1}, 1279 cm^{-1}, 1331 cm^{-1}), amide I (1569 cm^{-1}) and amide II radial vibrational mode (1647 cm^{-1}) (Figure 5.3B) [400]. Due to the overlapping G and D peaks of carbon fiber, the C=C ring axial mode peak (1569 cm^{-1}) is difficult to detect. These polar functional groups that are introduced due the ANF coating have been shown to be highly compatible with epoxy functional groups, therefore providing greater opportunities for chemical bonding between the surface of the fabric and the

matrix [110]. Such improved chemical interaction is desirable due to its potential to improve the interlaminar performance of carbon fiber composites. It should also be noted that the thermal stability of ANFs is important for their integration in fiber reinforced polymeric composites. Previously discussed TGA analysis of the ANFs show that they maintain good thermal stability up to 500 °C, before thermal degradation is initiated, thus making them suitable for VARTM fabrication and high temperature composite applications.

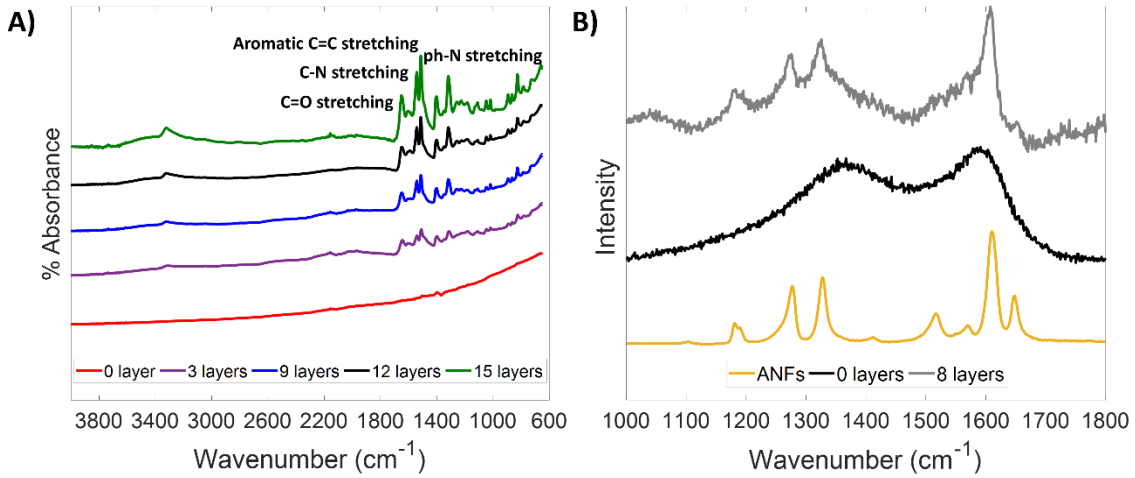

Figure 5.3. Chemical characterization of ANF coated carbon fabric. A) FTIR of untreated and ANF coated carbon fabric. B) Raman spectra of ANFs, untreated carbon fabric, and ANF coated carbon fabric.

5.2.3. Examination of interlaminar properties

The interlaminar performance of ANF interlayered carbon fiber composites is first characterized by investigating short beam strength (SBS). It should be noted that SBS measurements are generally highly sensitive to specimen thickness and the testing span to thickness ratio [401]. Given the nanoscale size of the ANF layers, the spray-coating process does not considerably increase the thickness of the carbon laminates. Figure 5.4A shows a statistically unchanged short beam specimen thickness across all data sets, therefore allowing for direct comparison between the untreated samples and those containing ANF interlayers. As seen in Figure 5.4B, both carbon fiber composites with 1 and 3 layers of ANF coating display negligible improvement in SBS relative to that of the untreated ones (52.1 MPa). While such treatment would be ideal with regards to processing time, SEM imaging previously indicated that the resulting ANF coating after only 3 layers is not dense enough to strengthen the interlaminar region of the

composites. As more ANF layers are sprayed onto the carbon fabric surface, a greater increase in the SBS of carbon fiber composites is observed, reaching a maximum improvement of 69.7 MPa with 8 layers of ANF coating when compared to untreated ones, and resulting in a maximum improvement of 33.7%. Therefore, it can be concluded that the ANFs are able to increase the resistance of carbon fiber reinforced composites to mid-plane delamination by improving interlocking between the fiber and the matrix. This mechanism reduces interfacial stress concentrations and allows for the tougher matrix to support a larger portion of the induced shear stresses. Moreover, ANFs have been proven to improve the fracture toughness of epoxy, therefore locally reinforcing the matrix in the vicinity of the interfacial region and improving its resistance to cracking [110]. These results highlight the ability of the ANF interlayer to improve the interlaminar properties of such composites, as the ANF interlayer provides better adhesion between the adjacent carbon fiber plies, while also toughening the matrix. Further increasing the areal density of the ANF interlayer resulted in a degradation of short beam performance, as the spraying of 9, 11, and 16 layers of ANFs is found to reduce SBS by 2.3%, 9.26%, and 18.52%, relative to untreated composites, respectively. The thick and continuous ANF coating impedes the resin from infusing the fabric during VARTM, leading to the formation of defects and voids in the composite. By observing the stress-displacement curves in Figure 5.4C, it can be clearly observed that the specimen stiffness follows a similar trend to SBS, while mid-span deformations at failure are unchanged irrespective of treatment. Finally, the addition of ANF interlayers is observed to transition short beam failure from spontaneous delamination due to interlaminar shear at the mid-plane, into a more constant failure behavior that is capable of withstanding residual loads. With ANFs being derived from aramids, which are well-known for their high fracture toughness and energy absorption abilities, such changes to the short beam response are expected. Nonetheless, the predominant failure mode remains interlaminar shear. Therefore, the following changes to the short beam responses further confirm the ability of ANFs to toughen the interlaminar region and absorb larger loading energy.

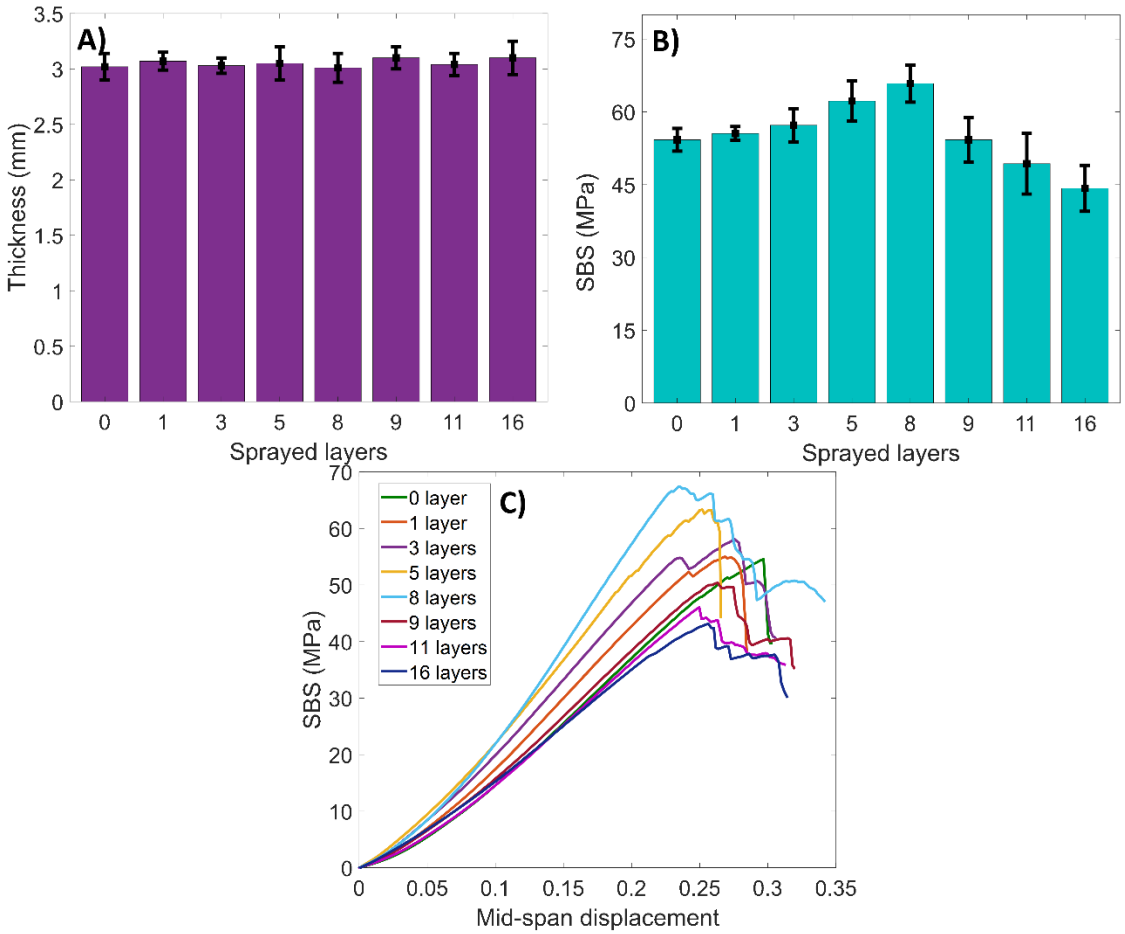

Figure 5.4. Short beam shear testing of ANF coated carbon fiber reinforced composites. A) Thickness of untreated and ANF coated carbon fiber short beam specimens. B) short beam strength (SBS) of untreated and ANF coated carbon fiber reinforced composites. C) Corresponding stress-mid-span displacement curves.

Another approach to assess the interlaminar properties of carbon fiber composites is Mode I fracture toughness testing. Here, delamination is concretely manifested through the initiation and propagation of a crack in the interlaminar region of double cantilever beams (DCBs) through a combination of tensile and shear stresses (Figure 5.5A). The VARTM fabricated composite plates consist of 16 plies of carbon fiber fabric and a 20 um thick Teflon sheet that creates an initial 50 mm crack between the 8^{th} and ANF treated 9^{th} plies. It should be noted that ANF interlayers are also introduced between the 7^{th} and 8^{th}, and 9^{th} and 10^{th} plies to ensure similar behavior in neighboring interlaminar regions during testing. As per standard, the Teflon insert used to generate pre-cracking is approximately 63 mm long. This corresponds to an initial delamination length of

50 mm, in addition to the extra length required to bond the hinges or load blocks. The resulting 4 mm thick panels are cut into six, 140 mm long by 23 mm wide DCBs. The edges of the DBCs were coated with white paint to allow for easier detection and monitoring of crack initiation and propagation. The specimens are then loaded through 11.2 mm long piano hinges that were attached to both sides using high shear strength epoxy (Loctite® 9430™ Hysol). DCB loading is performed at a crosshead speed of 2 mm/min up until a 35 mm crack is propagated into them. The specimens are initially loaded until the crack is slightly advanced from the insert and stable delamination growth is ensured, before unloading the sample and reloading it again. This is necessary in order to obtain stable crack growth and avoid overestimating the initiation Mode I fracture toughness (G_{IC}) by eliminating the effects of resin pocket formed at the end of the insert. These cracks are expected to propagate exclusively at the mid-plane of DCBs due to the help of the generated pre-crack generated. G_{IC} can be calculated according to the modified beam theory:

$$G_{IC} = \frac{3P\delta}{b(a + |\Delta|)} \tag{5.2.}$$

where P and δ are the load and load point displacement, respectively, a is the crack delamination length, b is the width of the DCB specimens, and Δ is a correction delamination length obtained from the linear regression analysis of the relationship between the cubic root of the compliance ($C^{1/3}$) and a. As per ASTM D5528, the recorded load-displacement curves were used to generate the corresponding delamination resistance (R) curves. The R-curves in Figure 5.5B clearly show that, up to a certain ANF interlayer areal density, both the initiation and propagation G_{IC} are improved. As expected, untreated DCBs exhibit an initial and steady increase in G_{IC} at short crack lengths before starting to saturate. When 4 to 9 ANF layers are included, the G_{IC} of the DCBs continue to increase as the crack propagates, transitioning saturation to a crack length greater than 85 mm. This is the result of extensive fiber bridging induced by the reinforcing interlayer which provides greater resistance in the path of the propagating crack. When a greater number of layers are sprayed, the initiation G_{IC} is reduced and continues to decrease as the crack propagates, signaling a weaker interlaminar region. Using the 5%-Max criterion, a maximum increase in initiation G_{IC} of 692 J/m^2 is observed using 8 ANF layers relative to untreated DCB specimens (381 J/m^2), resulting in an improvement of 81.6% (Figure 5.5C). This indicates that the ANF interlayer is able to improve inter-ply adhesion and resist the initiation of cracks in carbon fiber composites. The ANFs enlarge the interlaminar interaction surface area, interlocking the matrix

with the fabric surface, while also chemically bonding to it. Denser ANF interlayers resulted in a maximum decrease in initiation G_{IC} to 410 J/m^2 when 18 layers are used, which is a 40.75 % decrease relative to when 8 layers are used. The excessive ANF coating restricts the resin from properly wetting the carbon fiber surface, weakening the interlaminar region and enabling easier delamination. Moreover, the decrease in G_{IC} with increasing crack length observed in the R-curves indicates that the crack propagates in an undesirable weak resistance path, possibly along the interfacial region. In conclusion, the optimized ANF interlayer morphology toughens the interlaminar region of carbon fiber reinforced composites and inhibits delamination by delaying the initiation and propagation of cracks.

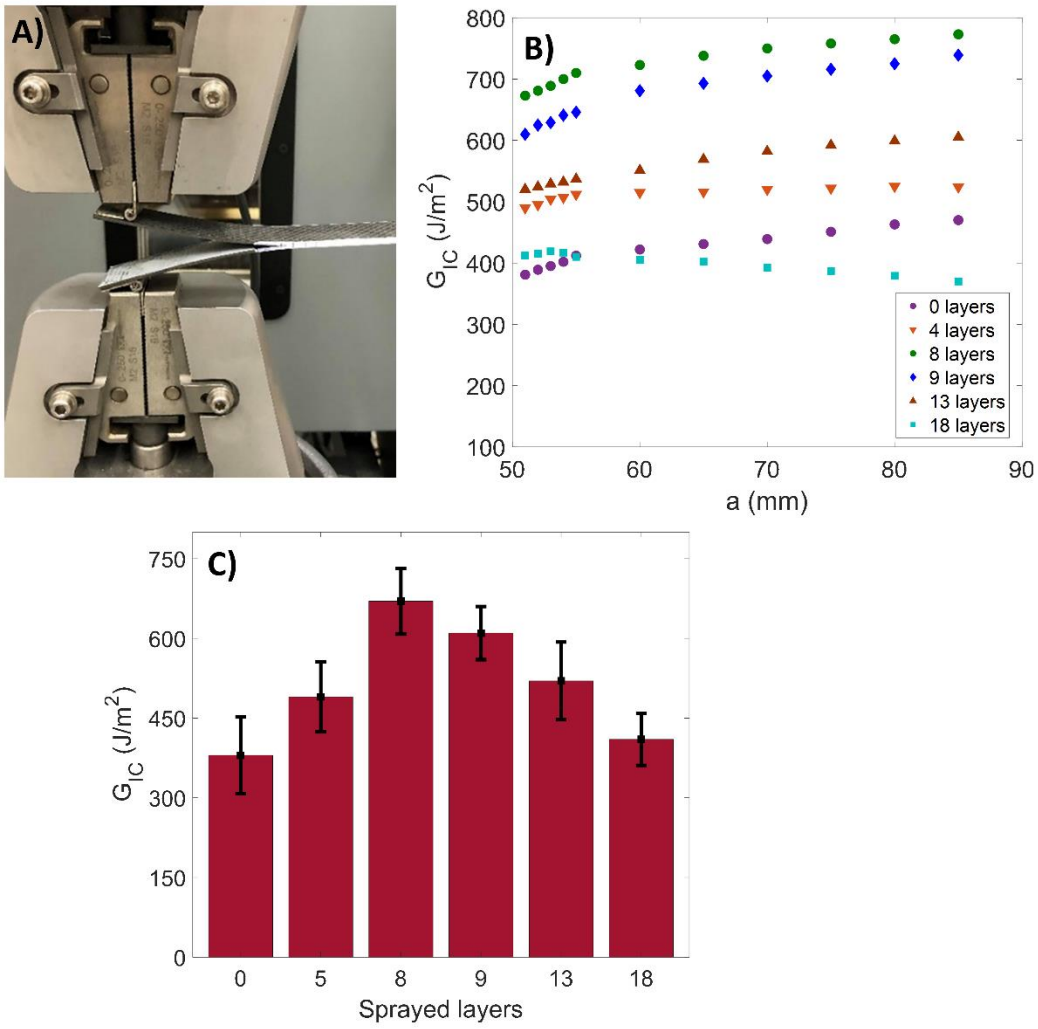

Figure 5.5. Mode I fracture toughness of ANF coated carbon fiber composites. A) Loaded DCB specimen. B) Delamination resistance curves for untreated and ANF coated DCB specimens. C) Initiation Mode I fracture toughness for untreated and ANF coated DCB specimens based on the 5%-Max criterion.

The toughening of the interlaminar region due to the ANF interlayer can be further understood through SEM imaging of the fractured DCB surfaces (Figure 5.6.). Untreated specimens display the typical signs of adhesive failure expected in brittle carbon fiber reinforced polymer matrix composites, where clean interfacial debonding uncovers the carbon fiber surface and leaves minimal traces of matrix material (Figures 5.6A-D). This is the result of the crack traveling along the weak fiber-matrix interfacial region which provides minimal resistance. The broken fibers on the DCBs surface are the result of fiber bridging as delamination ensues. Once ANFs are introduced, the DCB surface is uniformly covered with patterned matrix material, indicative of a more cohesive failure mode (Figures 5.6E & F). Under such conditions, the crack is forced away from the weak fiber-matrix interface and into the tougher matrix, thus absorbing higher fracture energy during the process. Furthermore, ANF residues can be clearly seen on the surface of both sides of the DCBs, despite being only introduced on one of them (Figures 5.6G & H). This shows that the ANF interlayer induces a nano-bridging effect that provides greater resistance against the propagating crack, relative to untreated carbon DCBs. These energy absorption mechanisms help deflect and lengthen the crack path and transition it away from the boundaries of the interlaminar region. It should be noted that similar fracture surfaces are also observed in carbon fiber composites fabricated using fabric coated with 13 ANF layers, despite exhibiting a weaker interlaminar performance in comparison to 8 layers (Figures 5.6I-L). Therefore, the ANF interlayer produces a more cohesive interlaminar failure mode, along with signs of nano-bridging, enhancing the overall resistance of carbon fiber composites to delamination.

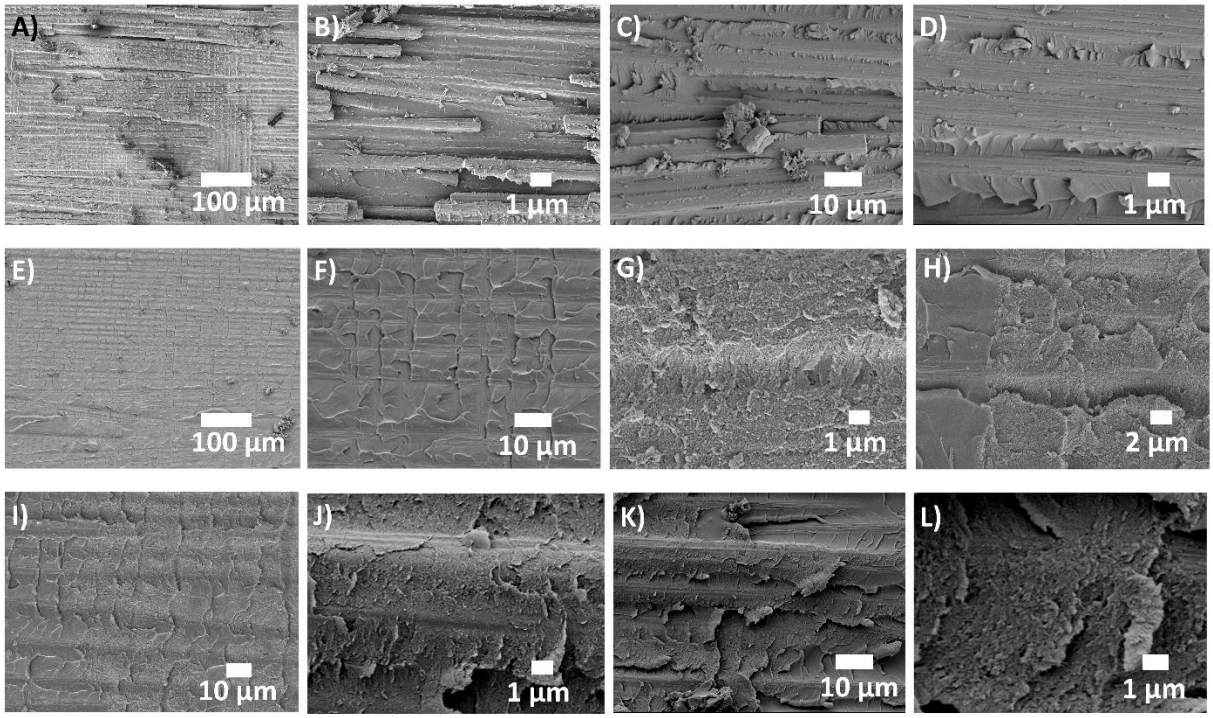

Figure 5.6. SEM micrographs of the fracture surface of untreated and ANF coated DCB specimens. A - D) untreated. E – H) 8 ANF layers. I – L) 13 ANF layers.

5.2.4. Tensile properties and other aramid-based interleaving techniques

Finally, to ensure that the introduction of an ANF interlayer does not reduce the in-plane properties of carbon fiber composites, five specimens of each data set are subjected to tensile testing per ASTM standard D3039. As clearly seen in Figure 5.7., the tensile properties of carbon fiber reinforced composites are statistically unchanged when 5, 8, and 9 ANFs layers are sprayed. Nonetheless, when 13 layers are used, the tensile strength and elastic modulus are found to be decreased by 5.5% and 6.43% relative to untreated carbon fiber composites, respectively. This can be attributed to the high areal density of the ANF interlayer, and the resulting poor resin infiltration. Given that the optimal interlaminar performance of the ANF interlayer coincides with the preservation of tensile properties, the spray-coating technique discussed in this study can be used to toughen carbon fiber composites, while maintaining in-plane strength.

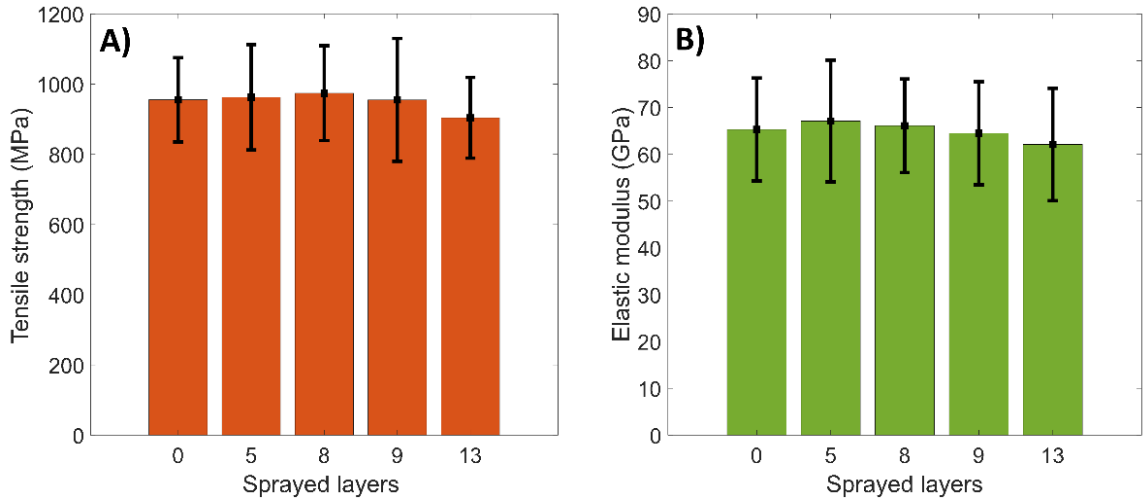

Figure 5.7. Tensile properties of ANF coated carbon fiber reinforced composites. A) Tensile strength. B) Elastic modulus.

To understand the advantages of the proposed ANF interlayer over other previously reported aramid-based approaches, it is necessary to compare their performance and characteristics. Many studies have focused on using aramid materials to improve the out-of-plane properties of carbon fiber composites due to their exceptional toughness and energy absorption properties. Early work suggested the manual spread of chopped aramid fibers across the surface of carbon fabric to act as an interlaminar reinforcement layer [402]. The 30-100 μm thick interlayers consisted of 5-15 mm long chopped, macroscale aramid fibers, and possessed areal densities that ranged between 17 and 27 g/m^2. The observed improvement in G_{IIC} of the composites was attributed to the ability of the chopped aramid fibers to improve fiber bridging mechanisms. However, such thick interlayers reduce the fiber volume fraction within the composite, thus decreasing its in-plane strength [403]. Moreover, the manual approach used to introduce these chopped fibers gives little control over the uniformity of the interlayer thickness. Yasaee et al. were also able to considerably improve the Mode II fracture toughness (G_{IIC}) of carbon fiber composites through 90-270 μm thick chopped aramid fiber intrleaves, an at an areal density of 67 g/m^2 [404]. However, despite their ability to improve fracture toughness and impact response, these thick and dense interlayers are unlikely to be adopted in large scale composite industries due to their effect on the tensile strength of the composites [403]. In an effort to scale down the size of these interlayer, recent studies focused on the use of aramid pulp (AP) in order to improve the flexural propereties of fiber reinforced composites [405,406]. Using an in-house prepreg fabrication

process, AP interlayers of less than 20 μm in thickness and 10 g/m^2 in areal density can be achieved. While up to 30% and 100% increase in the longitidunal and transverse flexural loads of carbon fiber composites are obtained using such intrlayers, its effect on the tensile strength of the composites remains undetermined. Moreover, this technique relies on mixing the AP in the resin prior to prepreg fabrication. As shown by Lin et al., APs tend to poorly disperse in epoxy resin due to their tendency to entangle and their poor chemical interaction with the matrix [110]. This limits their ability to mechanically reinforce the matrix and induces a more brittle behavior, resulting in the epoxy polymer failing at lower strains. In contrast, ANFs are found to be considerably easier to disperse in epoxy resin due to their more reactive surfaces. Moreover, unlike APs, ANF reinforced epoxy exhibits a simoultaneous improvement in both strength and toughness, a usually difficult feature to realize in polymer nanocomposites. The spray-coating technique used here to fabricate low areal density, ultra-thin ANF interlayers is capable of considerably toughnening carbon fiber composites.The thickness of these ANF interlayers is within the range of the ANFs diameters, thus of a nanoscale nature. Yang et al. previously reported that the thickness of individual ANFs layers fabricated through dip-coating are approximately 1.6 nm [108]. Furthermore, the areal density of these spray-coated interlayers does not exceed 1 g/m^2. Such features give ANF interlayers distinct advantages over chopped aramid fibers and AP, especially with regards to maintaining in-plane strength of the carbon fiber composites. Finally, while ANFs might not possess the ideal length for fiber bridging mechanisms [404], their ability to create web-like networked structures of much larger scale than individual nanofibers across the carbon allows the interlayer to introduce a toughening mechanism within the interlaminar region of composites. Therefore, the ANF interlayer is capable of providing interlaminar reinforcement in carbon fiber composites comparable to that of chopped aramid fibers and AP, yet at significantly lower interlayer thickness and areal density, and using a technique that is easily scalable to industrial level composite fabrication processes. Nonetheless, other alternatives can potentially provide a similar toughening effect in fiber reinforced composites, while introducing additional multifunctionality that ANFs lack. In the following section, the introduction of a piezoresistive LIG interlayer into aramid and carbon fiber reinforced composites will be detailed and discussed.

5.3. LIG interlayer in aramid and carbon fiber reinforced composites

5.3.1. Synthesis and transfer of LIG interlayer

As discussed in chapter 2, LIG can be introduced on aramid surfaces using a direct laser writing process. Kevlar® KM2+ unidirectional tape (style 790 scoured, CS-800) is cleaned through soaking in boiling acetone and ethanol before rinsing with deionized water and drying at 100 °C overnight under vacuum. The carbonization of the aramid fabric can be achieved through a 40 W CO_2 laser of a universal laser system (Epilog Zing 16) operating in raster Mode (Figure 5.8A). Using the built-in software, the output power of the laser is varied between 8% and 20% in order to generate various surface morphologies, while the impulse per unit area and the laser raster speed is kept constant at 400 dots per inches (DPI) and 1 $cm^2.s^{-1}$, respectively. Two LIG configurations are adopted, the first with LIG only on one side of the fabric, and a second where LIG is formed on both sides of the fabric, thus eliminating any interlaminar aramid region when infused with a resin matrix.

Given that such a technique is not suitable for carbon fabric, a transfer printing technique is employed to introduce LIG onto the surface carbon fiber prepregs (Figure 5.8B). First, vertically aligned arrays of laser induced graphene are generated on polyimide (Kapton) substrates using the same laser system. The LIG morphology is varied by controlling the pulsing density of the induction process between 100 and 400 dots per inches (DPI), while keeping raster powering and speed constant at 16% and 1 $cm^2 \cdot s^{-1}$, respectively. The LIG forests are then mechanically transferred onto unidirectional carbon fiber prepregs (HexTow® IM7/HexPly® 8552) through the process described in Figure 5.8B. The carbon fiber prepreg is rolled across an 80 °C pre-heated polyimide surface while applying manual pressure, thus bonding the LIG to the prepreg and subsequently transferring the LIG to the prepreg after peeling the polyimide and prepreg apart. It should be noted that the LIG transfer process is unsuccessful if performed on an unheated substrate, as the heat-induced reduction in resin viscosity is necessary for adequate adhesion between the prepreg and the substrate, ensuring a uniform transfer of the LIG array to the prepreg.

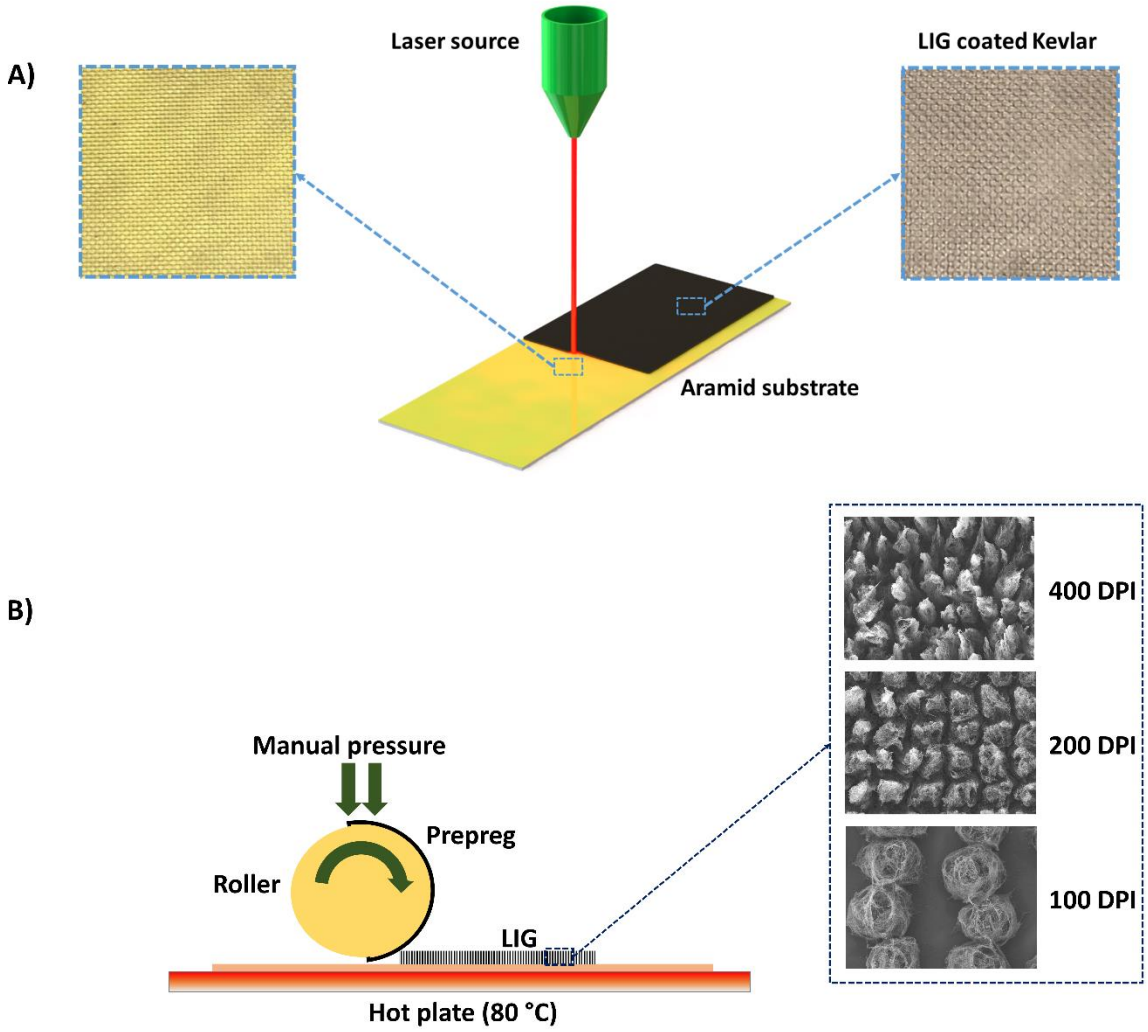

Figure 5.8. LIG on aramid and carbon surfaces. A) Schematic of graphene laser induction process on aramid fabric. B) Schematic of LIG transfer from polyimide substrate to carbon fiber prepreg ply.

The modified aramid surface morphology due to the laser induction process is investigated using SEM imaging (Figure 5.9.). Figures 5.9A & B show the original aramid fabric surface consisting of smooth aramid fibers. Unlike carbon fibers, aramid fibers lack the striations and surface roughness that can help induce mechanical interlocking between the fiber and the matrix resin, which combined with their inert chemical structure, result in weak fiber-matrix interfaces. By subjecting the aramid substrate to laser induction, the surface morphology is considerably modified while being dependent on the output power of the process. Unlike the initially reported LIG fabrication method on polyimide films, the replication of this process on aramid substrates is

achieved at considerably lower fluences than the reported critical value of 5.5 J.cm^2 on polyimide substrates[304]. As previously discussed, the conversion of high temperature polymers, such as Kevlar, into amorphous carbon is possible at lower fluences through the defocusing of the laser's focal length, thus protecting the fiber from ablation and thermal damage, which would otherwise diminish its performance [308]. An impulse density of 400 DPI is chosen in order to generate forests of individual and distinct LIG micro-fibers instead of continuous micro-sheets[304]. As shown in Figures 5.9C and D, at low output powers of 8% and 10%, the graphene induction process can be initiated but does not result in hierarchical surface morphology. At such low fluences, the induction process is limited to the top surface of the aramid fabric, limiting the formation of 3D micro-structures that are potentially capable of reinforcing the interlaminar region. Moreover, given the woven surface of aramid fabric, the resulting morphology is non-uniform as the amount of fluence varies at different locations on the substrate. Interestingly, at 12% output power, the aramid fibers are found to be coated with a uniform sizing (Figure 5.9E), as 3D structures appear in the form of stiff, striated grooves and ridges (Figures 5.9E & F). These morphological changes considerably increase the aramid fiber surface roughness and allow for a greater degree of interlocking between the fiber and matrix. In addition, the wettability of the fabric is also increased due to the fact that the aramid fabric is further embedded inside the matrix, thus significantly strengthening the interlaminar region. As the output power is increased to 16%, LIG forests begin to sporadically appear across the aramid substrate without any microstructure uniformity (Figures 5.9H and I). Further increasing the output power to 20% results in a 3D LIG forest that uniformly coats the aramid fiber (Figures 5.9J and K). The generated LIG micro-fibers possess aspect ratios ranging between 20 and 40, with lengths between 200 and 400 μm, and diameters between 10 and 15 μm. These LIG forests give the aramid fabric a surface morphology that is able to be firmly embedded and interlocked in the matrix, while also increasing interfacial interaction surface area, thus reinforcing the interlaminar region using a microstructure of great mechanical properties. Moreover, the porous nature of these micro-fibers, as seen in Figure 5.9L, allows for facile resin wetting and infusion, eliminating the possibility of wicking and preserving the reinforcing capacity of the LIG. It can thus be seen that the laser induction process on aramid substrates can result in LIG surface morphologies capable of strengthening the interlaminar region of aramid composites.

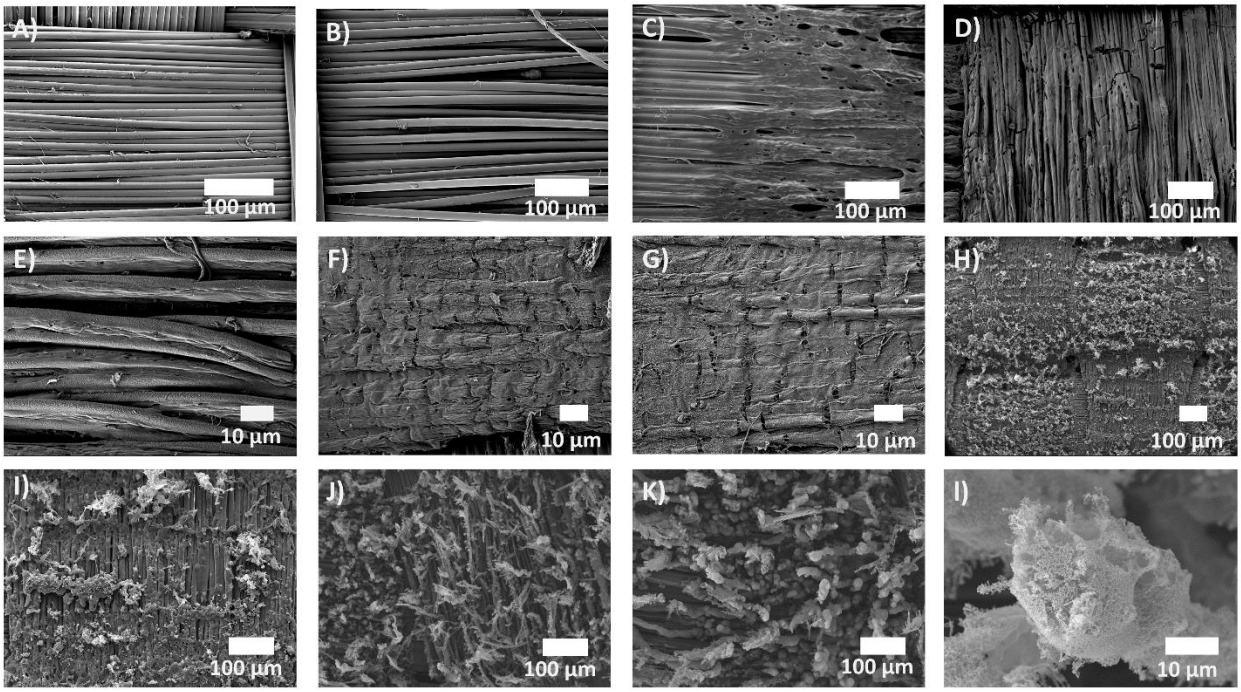

Figure 5.9. Surface morphology of LIG on aramid fabric surface at various power outputs. A, B) 0%. C) 8%. D) 10%. E-G) 12%. H, I) 16%. J-L) 20%.

The LIG morphology on carbon fiber prepreg is also investigated through SEM imaging. As previously mentioned, the LIG forests are mechanically transferred onto the tacky carbon fiber prepreg through pressure, resulting in uniform coating which is crucial for the performance of the reinforced composites (Figure 5.10A). The morphology and spatial density of the LIG fibers can be readily controlled through the pulsing density of the induction process. The laser is rastered across the polyimide substrate at 400 DPI which results in pillars with sharp, pin like ends (Figure 5.10B), while performing the laser induction at 200 DPI generates pillars with blunter ends (Figure 5.10C). It should be noted that increasing the pulsing density results in a continuous micro-sheet structure that is difficult to adequately transfer [304], whereas decreasing the pulsing density will result in low-aspect ratio LIG micro-fibers bundled into micro-hemispheres with minimal vertical alignment **(**Figure 5.8B). The 40W CO2 laser system used here is equipped with a 50.8 mm inch focal length lens that yields a laser beam spot size ranging between 101.6 µm and 152.4 µm when focused. The pillars generated at 400 DPI range between 180-260 µm in length and 8-15 µm in width. Each individual pillar is a porous bundle of intertwined and networked LIG fibers of less than 1 µm in diameter. As the pulsing density is decreased to 200 DPI, the overlap between

successive laser pulses is decreased, resulting in blunter and wider pillars. Moreover, the decrease in pulsing density is accompanied with a decrease in fluence, resulting in shorter LIG pillars. The porous LIG forests generated at 200 DPI are found to range between 120-180 μm in length, and 40-85 μm in width. At 100 DPI, the resulting LIG consists of porous LIG micro-hemispheres, each representing an individual laser pulse. As expected, the width of these micro-hemisphere is similar to the laser spot size, varying between 105 μm and 150 μm in width, while being only 25-40 μm high. Therefore, the generated LIG forests are wider and shorter with decreasing pulsing density. Therefore, the decrease in pulsing density is expected to also result in a decrease in fluence intensity during LIG generation, yielding wider, yet shorter LIG pillars. Each of the displayed LIG morphologies can potentially provide a unique interlaminar reinforcing performance, as their distinct arrangement and interaction area are expected to behave differently when sandwiched between two carbon fiber plies. The complete detachment of the LIG off the substrate during the transfer process is confirmed in Fig. 5.9D, where no residues of LIG fibers are observed on the substrate and the next polyimide layer is clearly uncovered, illustrating the uniformity and consistency of the transfer printing method. Despite the fact that the proposed direct transfer printing technique avoids typical agglomeration problems observed in other studies that use CNTs, it is necessary that the LIG preserves its spatial density and vertical alignment in order to eliminate the introduction of discontinuities and defects to the interlaminar region of the composite. As seen in Figures 5.10E-G, the LIG forests maintain their original pattern, density, and vertical alignment during the transfer process. This shows that the LIG forests can survive the performed mechanical transfer under a uniform-pressure process. This process is aided by the heating of the substrate which increases prepreg tackiness and improves adhesion between the prepreg and the LIG. This allows for easier LIG detachment off the substrate and stronger bonding to the carbon fiber plies. The ability of the LIG to maintain its vertical alignment on individually cured carbon fiber plies following transfer can also be confirmed through SEM imaging. As observed in Figures 5.10H & I, the 400 DPI LIG fiber bundles are completely wetted and embedded inside the cured epoxy matrix while substantially maintaining their vertical alignment. Similarly, the 200 DPI bundles are also found to be completely embedded within the matrix, considerably roughening the prepreg surface (Figure 5.10J). The conservation of the LIG array's alignment is partially due their porous nature, which allows for the pre-impregnated resin to easily wet and impregnate the transferred microstructure while minimizing the possibility of wicking and LIG misalignment. Nonetheless,

the LIG interlayer is expected to be considerably thinner inside carbon fiber composites due to the applied pressure of 100 psi during the VARTM fabrication process. Given its fuzzy nature, the LIG interlayer is not at risk of being damaged or fractured during such process, yet alignment within the interlaminar region can be potentially reduced. Once embedded in the composite, the LIG interlayer provides a considerable increase to the interaction area between adjacent plies, while also improving mechanical interlocking within the interlaminar region. Moreover, various graphene derived nanomaterials have been shown to improve both in- and out-of-plane properties of epoxy-based nanocomposites by increasing their tensile strength, fracture toughness and flexural modulus [407–410]. Such enhancement of the mechanical properties of the matrix is highly desirable, as the interlaminar behavior of carbon fiber composites is heavily dependent on the toughness of the matrix.

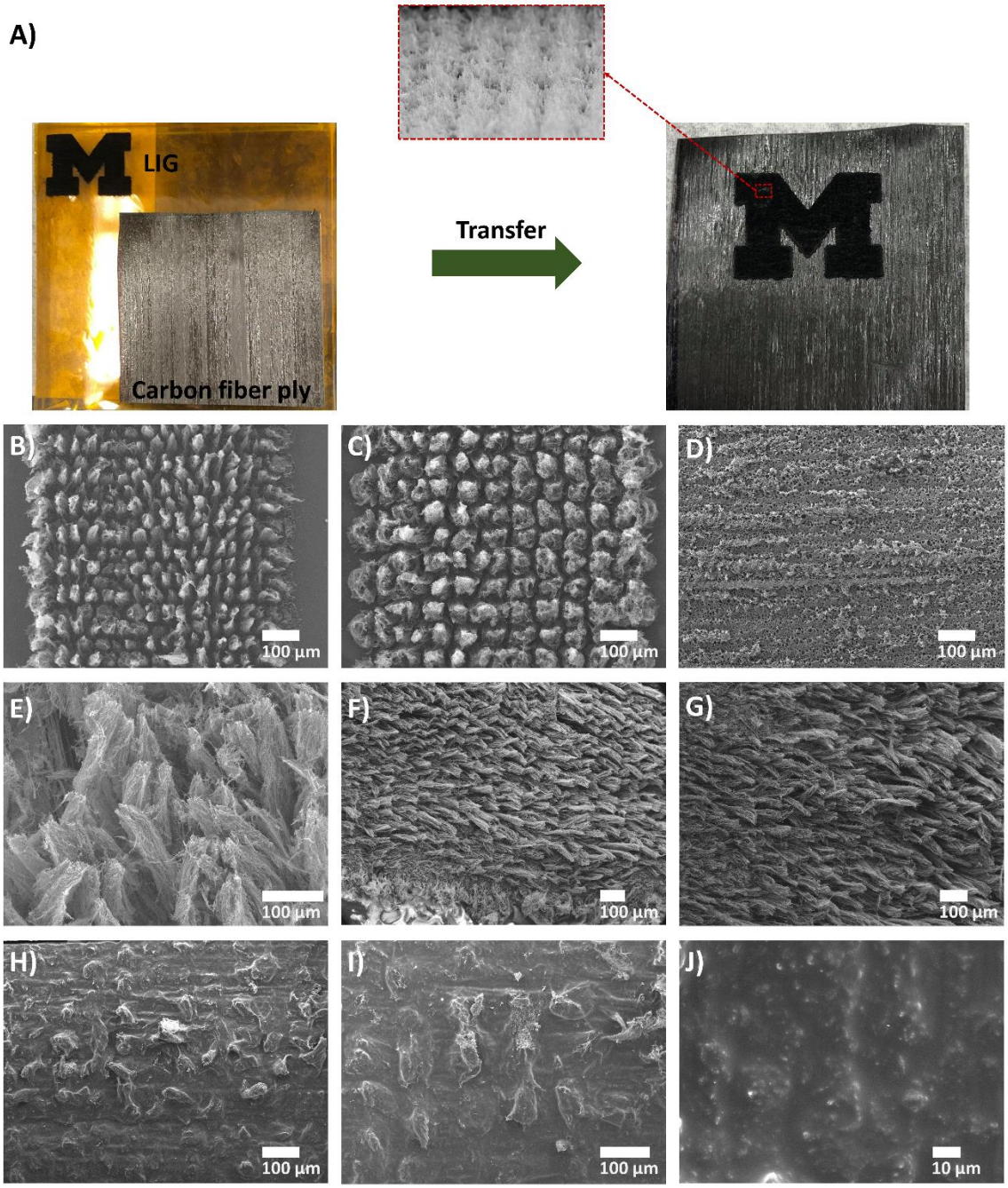

Figure 5.10. Transfer printed LIG on carbon fiber prepregs. A) Transfer of patterned LIG forest from substrate to LIG while maintaining alignment. B) LIG forests generated at 400 DPI on a polyimide substrate. C) LIG generated at 200 DPI on a polyimide substrate. D) Polyimide substrate surface post-transfer of the LIG. E-G) LIG forests maintaining a large degree of their alignment post-transfer to the carbon fiber prepreg. H, I) Cured 400 DPI LIG coated single carbon fabric prepreg ply. J) Cured 200 DPI LIG single coated carbon fabric prepreg ply.

5.3.2. Examination of interlaminar properties

The merit of introducing LIG onto aramid and carbon fiber composites can be assessed using various forms of mechanical testing. First, the effect of LIG on the interlaminar shear response of these composites is to be quantified using short beam shear testing according to ASTM D2344. Along with matrix toughness, interlaminar adhesion is a critical factor in short beam failure modes, therefore allowing for such testing approach to reveal any interlaminar reinforcement gains due to the LIG. The aramid short beam specimens are fabricated in two distinct configurations, both shown in Figure 5.11A. In the one-sided configuration, the LIG is generated solely on one side of the aramid fabric, resulting in inter-ply regions of thickness t with LIG-aramid interfaces. Using the double-sided configuration (D), an intermediate LIG-LIG interface is added inside the interlaminar region, due to the LIG coating on both sides of the aramid fabric. In this case, three interfacial regions are created, with two of them being LIG-aramid interfacial regions, and the third region containing the graphitic interface at the intersection of both LIG layers. As for carbon fiber composites, the resin rich interlaminar region in this study is interleaved with LIG fibers forests generated at 200 DPI, acting as a thin interlayer that mechanically joins the adjacent plies of the carbon fiber composites. Given that LIG can be only transferred on one side of a prepreg due to the backing on its other side, only the one-sided configuration is adopted. The interlaminar behavior of the fabricated composites is expected to be dependent on the modified chemical interactions and mechanical interlocking between the fabric and the matrix due to the introduced LIG. The presence of the LIG inside aramid composites is confirmed using an optical microscope (Figures 5.11C & E), which shows uniform and continuous LIG coated interlaminar regions. This is further characterized using SEM imaging, which shows thin interlaminar regions of less than 15 μm for aramid composites reinforced with LIG in the double-sided configuration (Figures 5.11D & F). The thin nature of the interlayer reinforcement is important to preserve the desired composite properties by reducing the number of polymer-rich regions that are devoid from any in-plane reinforcement. Such images are difficult to capture in carbon fiber composites given the lack of color contrast or conductivity between the LIG and the carbon fiber material. It should be noted that along with its potential mechanical advantages, LIG has been shown to possess excellent electrical properties, particularly piezoresistivity, allowing for the introduction of conductive pathways into traditionally insulating aramid fiber reinforced composites. The resistivity across the top of the LIG coated short beam specimens at 12% induction power and in the one-sided

configuration is found to range between and 0.291 Ω m and 0.449 Ω m, while that of the double-sided configuration varies between 0.162 Ω m and 0.291 Ω m. Once induction power is increased to 20%, the resistivity of the specimens considerably drops to range between and 0.0331 Ω m and 0.0645 Ω m for the one-sided configuration, and between 0.0155 Ω m and 0.031 Ω m for the double sided one. Moreover, the double-sided configuration is also found to be conductive through the thickness of the sample. As for the originally carbon fiber composites, the introduced LIG is found to yield a slight increase in conductivity. These findings unlock great potential for the embedding of numerous unprecedented functions into aramid composites such as strain sensing, damage detection, and joule heating. The introduced multifunctionality will potentially help reduce the weight and complexity of aramid fiber reinforced composites by eliminating the need for certain external sensors and actuators.

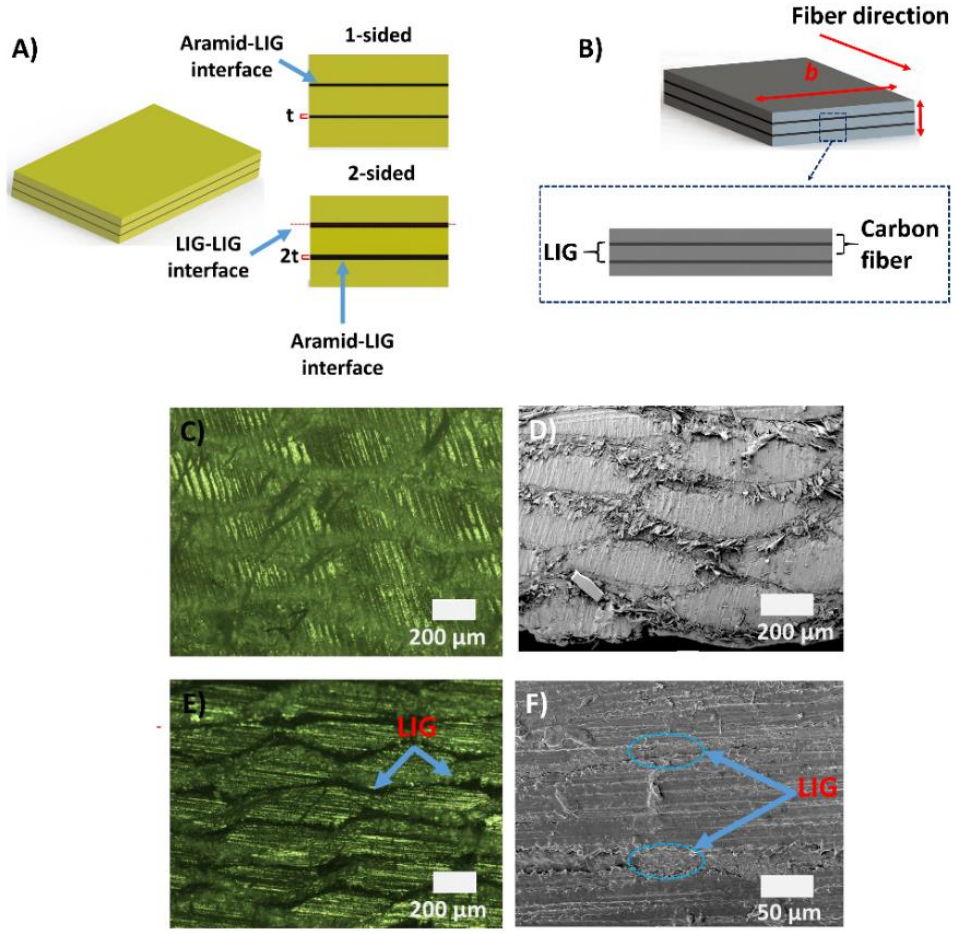

Figure 5.11. LIG interlayered aramid and carbon composites configurations. A) Short beam aramid fiber reinforced composite specimens in both the one-sided and double-sided configuration. Each LIG layer is of thickness t. B) Short beam carbon fiber reinforced composite specimens in the one-sided configuration. C) Optical microscope image of the cross-section of untreated aramid fiber

reinforced composites. D) Corresponding SEM images. E) Optical microscope image of the cross-section of LIG coated aramid fiber reinforced composites. F) Corresponding SEM images.

As seen in Figure 5.12A & B, the SBS of LIG coated aramid fiber reinforced composites is found to be increased independent of induction power and LIG configuration (one-sided or double-sided), relative to that of untreated aramid composites. A maximum improvement of 70% in SBS is observed at an induction power of 12% in the one-sided configuration relative to the untreated fabric, whereas LIG induced at 20% in the same configuration results in only 55% improvement. This indicates that the morphology of the grooves and ridges at 12% leads to a slightly higher degree of interlaminar reinforcement than the LIG micro-fibers at 20%. This can be attributed to the stiffer nature of the former in comparison to the fuzzy structure of the latter. Nonetheless, both sets of LIG microstructures enhance the resistance of the composites to shear stress and allow for a higher ability to withstand induced deformation. The observed improvement is derived from an enhanced adhesion between the fiber and the resin, as the LIG becomes anchored inside the epoxy matrix. The addition of the LIG creates hierarchical composites where interlaminar discontinuities are bridged, thus allowing for improved load transfer between the fiber and matrix, therefore limiting interlaminar failure. Moreover, graphene has been shown to improve mechanical properties, such as fracture toughness and flexural modulus, of epoxy polymer matrices when in the form of nanocomposites [407–410]. By toughening the matrix, the LIG further reinforces the interlaminar region and increases the shear strength of aramid composites. Although the double-sided configuration at both induction powers results in up to 53% increase in SBS relative to untreated aramid composites, its performance is found to be 11.3% and 8.8% inferior to that of the one-sided configuration at 12% and 20%, respectively. This slight decrease in reinforcement capability can be explained by the possible weak interlocking at the LIG-LIG interface, causing a slightly more discontinuous and defective interlaminar region relative to that obtained in the one-sided configuration. As for the SBS of the LIG coated carbon fiber composites, it is found to be statistically unchanged relative to the untreated short beam specimens, indicating that 400 and 200 DPI LIG interlayers did not strengthen nor weaken the interlaminar region under such loading conditions (Figure 5.12C). Nonetheless, when examining the stress response of both data sets, considerable differences can be observed (Figure 5.12D). Notably, before reaching peak stress, the introduced LIG interlayer does not cause significant changes to the stress-extension

response, as both short beam strength and stiffness are maintained. The measured high short beam strength and stiffness are characteristics of unidirectional carbon fiber prepreg composites. Yet these advantages are usually coupled with a brittle response, which is manifested through a sharp drop in the stress at low mid-span extensions, highlighting the low toughness of carbon fiber composites. The mutual exclusivity of strength and toughness is problematic in carbon fiber composites, especially when used in structural applications. Typically, the inability to absorb interlaminar shear stress results in the susceptibility of these composites to catastrophic failure in the form of delamination or matrix fracture. However, as can be seen in Figure 5.12D, the LIG interlaminar reinforcement allows for the specimens to smoothly transition from the peak short beam stress down to a residual stress that is greater than 100 MPa, while also supporting up to 175% larger mid-span deformations, relative to that of untreated specimens. These changes to the stress-displacement response render short beam testing unsuitable for comparing the shear resistance of untreated and LIG coated carbon fiber composites [401]. However, the LIG interlayer clearly increases the ductility and resistance to failure of these carbon composites, therefore improving their ability to absorb out-of-plane loads and resist cracks and delamination. While the fracture energy of carbon fiber composites in various loading modes will be assessed in later sections, the LIG interlayer results in up to 300% increase in the short beam energy, relative to that of untreated ones (Figure 5.12E). Although short beam energy is non-indicative of any specific mechanical properties and is hard to interpret, this observation points to the ability of the LIG interlayer to reduce stress concentrations within the interlaminar region and improve load transfer between adjacent plies, thus delaying catastrophic interlaminar shear failure under such loading conditions. It should be noted that the interlayer morphology at 100 DPI is not suitable for maintaining the interlaminar properties of carbon fiber composites as it considerably weakens short beam strength, despite an increase in toughness. Therefore, only 200 and 400 DPI LIG interlayers can hybridize the response of carbon fiber reinforced composites to introduce high toughness characteristics, while also maintaining their unique high strength and stiffness properties

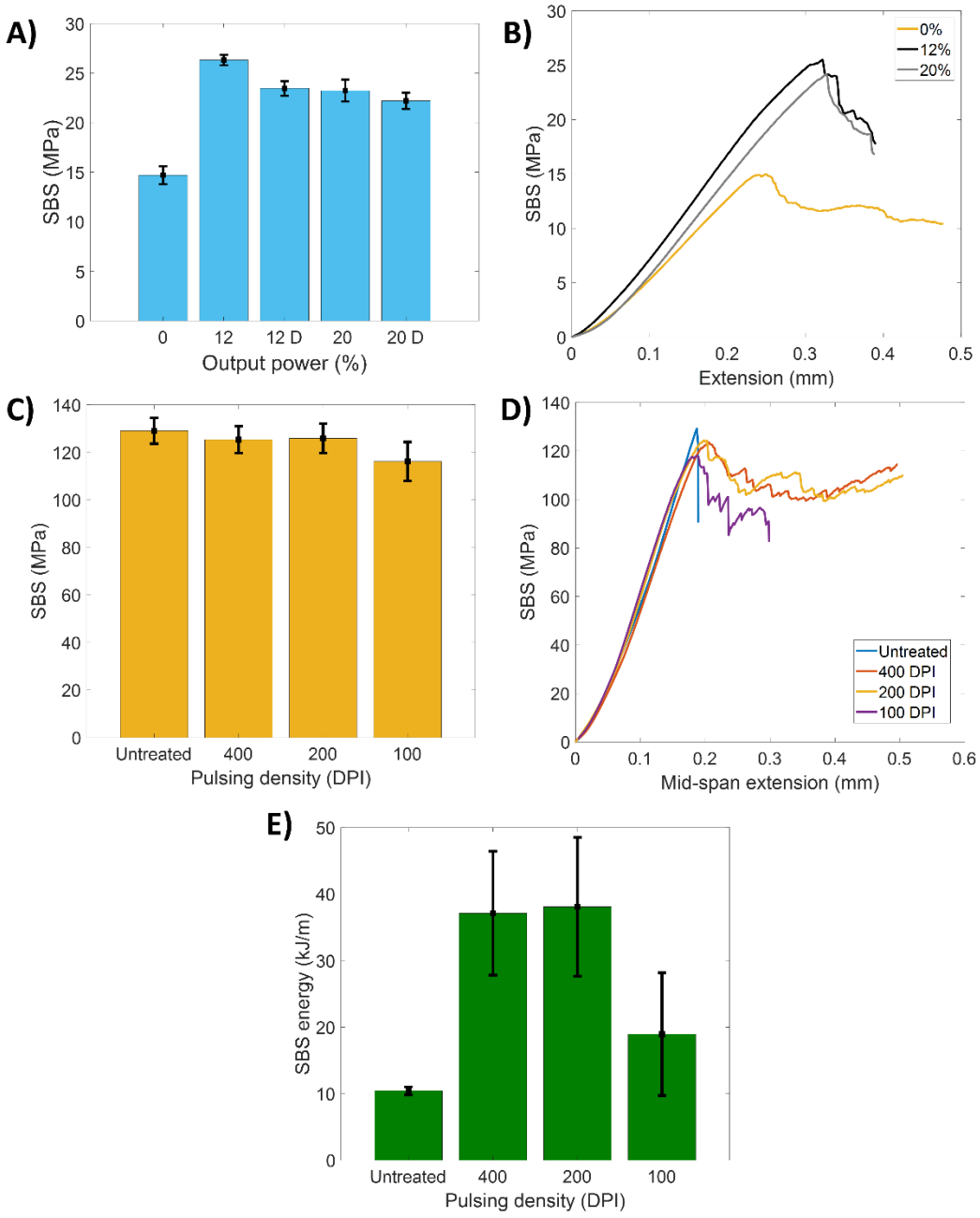

Figure 5.12. Short beam shear testing of LIG coated specimens. A) SBS of LIG coated aramid fiber reinforced composites at various induction power and configurations. B) Corresponding stress-extension curves of loaded short beam specimens. C) SBS of untreated and LIG coated carbon fiber reinforced composites. D) Corresponding stress-mid-span extension curves. E) short beam energy calculated from the SBS-extension curves.

In practice, composites are often subjected to more complex loading conditions which combine various forms of stresses such as axial, compressive, and shear. Therefore, a

reinforcement of the interlaminar region of fiber reinforced composites is expected to be reflected through an improvement of its mechanical response to combinations of these stresses. A critical property of fiber reinforced composites is their ability to delay damage initiation and propagation under structural loading. It is therefore desired from the introduction of an interlaminar interlayer to improve the resistance of composite structures to delamination. Mode I DCB testing is the most used technique to simulate these complex loading conditions and quantify the resistance of fiber reinforced composites to delamination (Figure 5.13.). By initiating delamination in the DCB specimens using a Teflon insert, a mid-plane crack propagates purely in the interlaminar region of the DCBs, and Mode I fracture toughness can be measured. Following ASTM D5528, the crack is propagated from the mid-plane of the composite for a total crack length of 35 mm from the end of the Teflon insert, while recording both load and load point displacement. G_{IC} is then calculated according to the modified beam theory discuss in section 5.2 of this chapter.

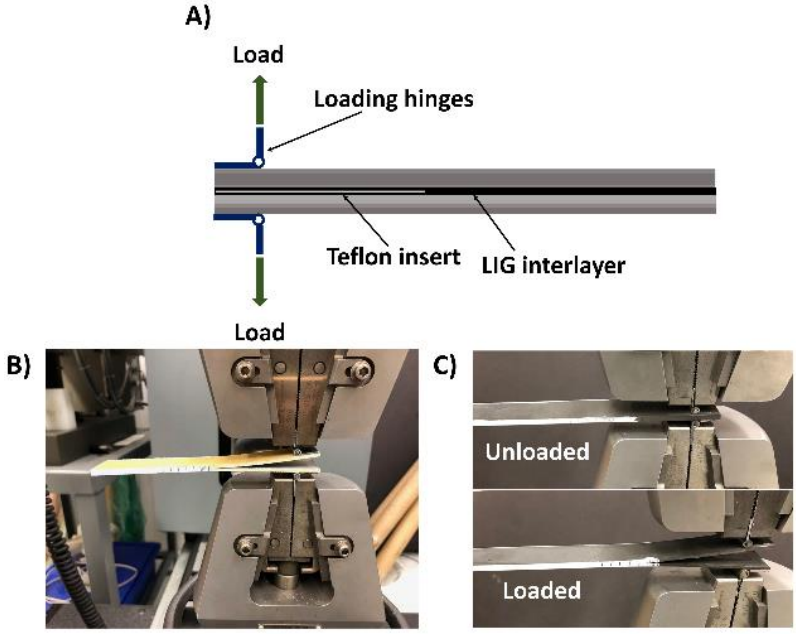

Figure 5.13. Mode I fracture toughness (G_{IC}) testing experimental setup. A) Schematic of double cantilever beam (DCB) specimen for G_{IC} measurement. B) LIG coated aramid DCB during Mode I loading. C) LIG coated carbon DCB during loading and unloading.

As seen in Figure 5.14A, a maximum increase in G_{IC} of 540 J/m^2 is observed in aramid DCBs coated with LIG generated at 20% induction power and in the one-sided configuration, resulting in a 20% improvement when compared to untreated aramid composites (462 J/m^2). The statistical significance of the improvement is further confirmed using one-way ANOVA analysis

at a p-value of <0.01. The increase in fracture toughness of LIG coated aramid composites is the result of the enhanced interlaminar bonding between the aramid surface and the matrix. However, unlike short beam testing, the LIG induced micro-fiber morphology generated at 20% output power shows better Mode I fracture resistance than LIG induced at 12%. This is attributed to the 3D structure of the LIG micro-fibers, which effectively bridges between adjacent plies during crack propagation, potentially acting as "nanostitches" [275,411–413]. Other carbon-based nanostructures of similar morphology, such as CNTs, have been shown to suppress delamination in fiber reinforced composites using comparable mechanisms. Furthermore, the double-sided configuration is observed to results in weaker fracture toughness relative to the one-sided configuration at a similar induction power. This observation confirms that the LIG-LIG interface presented in the double-sided configuration reduces the effectiveness of the reinforcement due to weakened mechanical interlocking and the formation of agglomerations inside the matrix. As for LIG coated carbon DCBs, a tougher interlaminar behavior is also observed. When inspecting the obtained resistance (R) curves, considerable improvements in both the initiation and propagation G_{IC} of LIG coated DCBs can be seen, relative to that of untreated ones. The R-curves of all data sets display similar trends of increased initiation G_{IC}, before exhibiting a plateau that signals a steady crack propagation within the interlaminar region (Figure 5.14B). It should be noted that the absence of a saturation region in the R-curve of the 200 DPI LIG coated DCBs indicates that steady state crack propagation is not reached within the studied crack length range, but is expected to be eventually attained at crack lengths greater than 85 mm. This delay in reaching steady state is possibly the result of extensive fiber bridging induced by the toughening of the interlaminar region using such a LIG interlayer morphology. Based on the 5%-Max criterion, a maximum increase in initiation G_{IC} of 425 J/m^2 is observed when using a LIG generated at 200 DPI when compared to untreated DCB specimens (292 J/m^2), resulting in an improvement of 41% (Figure 5.14C). The LIG interlayer is thus capable of toughening the interlaminar region of the DCBs by providing out-of-plane reinforcement, increasing the resistance to crack initiation, and hindering its propagation within the interlaminar region. The role of the LIG morphology is illustrated by the dependence of interlaminar strength on raster pulsing density. The maximum improvement achieved using a 200 DPI LIG can be attributed to the larger interlayer surface area created using such morphology, as the blunt LIG bundles (Figure 5.10C) provide a larger interaction zone between the interlayer and the subsequent plies, relative to the sharp bundles generated at 400 DPI (Figure 5.10B). Moreover,

the shorter LIG at 200 DPI can provide better interaction with the matrix within the interlaminar region, avoiding significant agglomeration and reducing the potential of defect site formation. Further decreasing the pulsing density down to 100 DPI causes a 20% decrease in G_{IC}, therefore considerably weakening the interlaminar region. The low aspect ratio and excessive bundle spacing of this LIG morphology results in a defective LIG interlayer that promotes crack initiation and propagation. Therefore, the introduction of an optimized LIG interlayer morphology into aramid and carbon fiber reinforced composites toughens the interlaminar region and suppresses delamination by delaying the initiation and propagation of cracks.

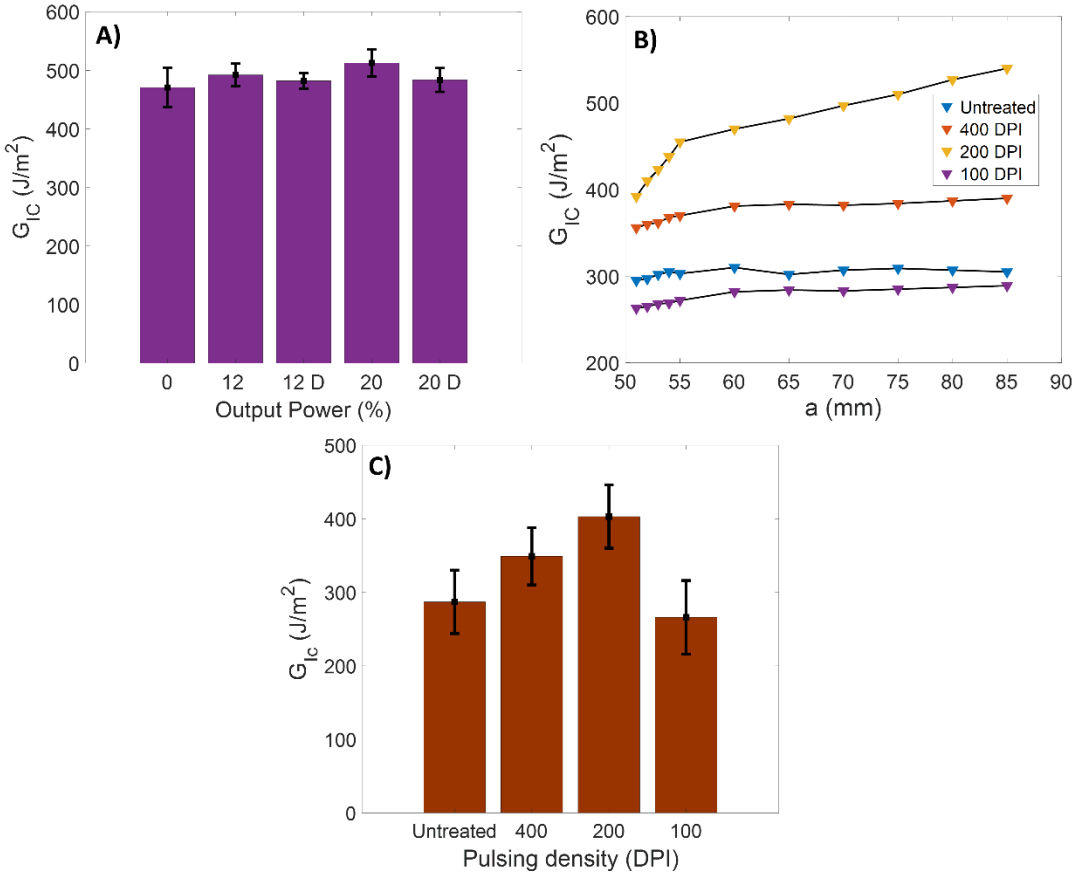

Figure 5.14. Mode I fracture toughness of aramid and carbon fiber reinforced composites. A) Initiation G_{IC} for untreated and LIG coated aramid DCB specimens based on the 5%-Max criterion. B) Delamination resistance curves for untreated and LIG coated DCB specimens. C) Initiation G_{IC} for untreated and LIG coated carbon DCB specimens based on the 5%-Max criterion.

Greater understanding of the observed interlaminar behavior of aramid and carbon DCBs can be obtained by inspecting the resulting fracture surfaces. First, the difference in the optimal

LIG morphology in aramid fiber reinforced composites during short beam and Mode I testing can be attributed to the difference in failure modes between the two tests. During short beam testing, the LIG coated specimens fail primarily due to inelastic deformation without any signs of delamination. Such failure mode favors the rougher LIG morphology generated at 12%, as its superior mechanical interlocking performance allows for a higher resistance to shear stresses. However, during Mode I testing, the propagating crack causes clear delamination within the composite. Under such conditions, the LIG micro-fibers generated at 20% can hinder the initiation and propagation of the crack, necessitating a larger fracture energy to achieve delamination. Visual inspection of the fracture surface of DCBs show that only those containing a 20 % LIG in the one-sided configuration present LIG residues on both surfaces, despite being introduced on only one of the plies (Figures 5.15A-C). This confirms that the following LIG morphology is capable of suppressing the propagation of cracks and delamination through a bridging mechanism, that can be only exploited during Mode I testing. In addition, post-testing micrographs of delaminated aramid DCB surfaces can be seen in Figures 5.15D-I. Due to the weak interlaminar strength and bonding in untreated aramid composites, delamination occurs in an easy and clean manner as displayed by the smooth aramid fiber surfaces in Figure 5.15D. Given the weak adhesion between the untreated aramid fiber and the matrix, interfacial debonding is the primary cause of failure in untreated Mode I specimens. In contrast, LIG coated specimens show a considerable amount of epoxy resin residue in the form of plates on the fractured aramid surface (Figures 5.15E & F). Moreover, the fractured aramid surface is found to be considerably coarser than that of untreated fibers, as layers of resin remains adhered to the surface (Figure 5.15G). By transitioning interlaminar failure from an adhesive mode to a cohesive one, the fiber-matrix interface of the aramid fiber reinforced composites can withstand higher loads as cracks propagate inside the bulk resin. This is further supported by the revealed LIG on the fractured surfaces, seen in Figure 5.15H and I, which suggests strong adhesion between the resin and the LIG. The following agrees with the conclusion drawn from the simple visual inspection of the aramid fracture surfaces. The limited increase in fracture toughness is possibly due to the inability of current fracture toughness testing methods to account for reinforcing effects which prohibit or reduce intralaminar failure. However, such a claim requires further verification and investigation using techniques such as micro-computed tomography (CT) scan imagery. Thus, the following failure behavior highlights the ability of the LIG to reinforce the aramid fiber-matrix interface, resulting in stronger interlaminar

regions that fail in a cohesive manner under Mode I loading.

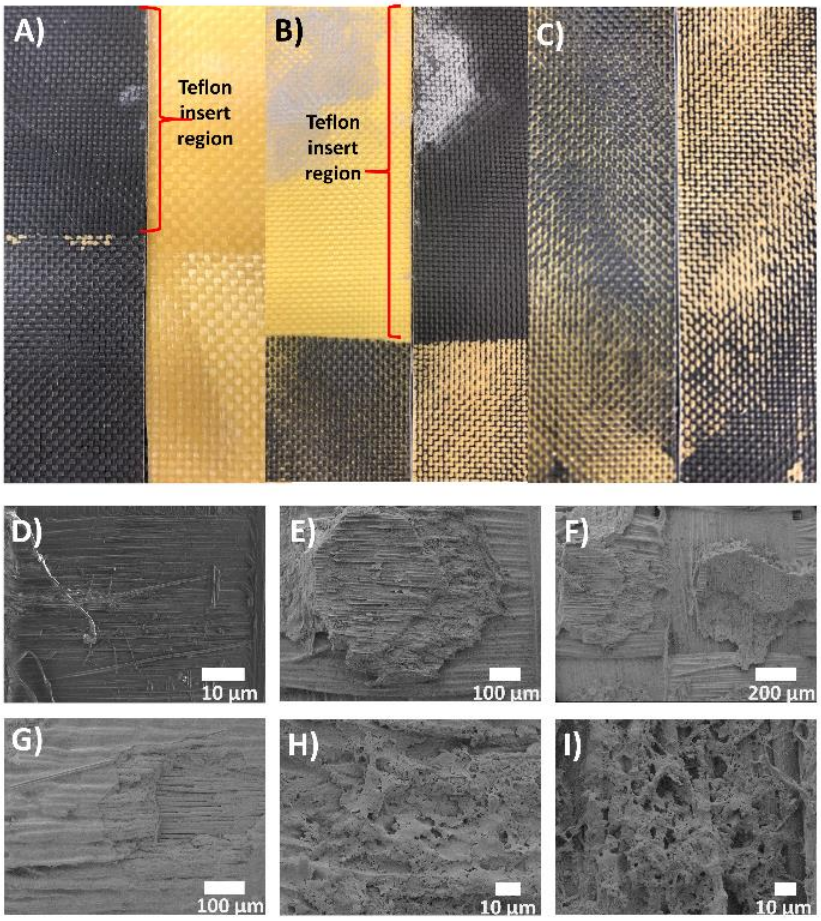

Figure 5.15. Micrographs of the fracture surface of untreated and LIG coated aramid DCB specimens. A-C) Fractured surfaces of LIG coated aramid double cantilever beams at various power outputs. A) 12 %. B), C) 20%. D-I) SEM imaging of untreated and LIG coated aramid fiber reinforced composites fracture surfaces following Mode I testing. D) Untreated. E-I) 20%.

Figure 5.16 displays the optical microscope-imaged crack pathways in carbon DCBs and their corresponding SEM-imaged fractured surfaces. In untreated DCBs, the crack propagates along a minimal resistance, straight path, with no signs of any deviation or deflection in its trajectory. This is common for brittle carbon fiber composites, whose weak interfacial adhesion allows cracks to easily propagate along the easiest path in the interlaminar region, typically existing along the fiber-matrix interface. On the other hand, crack propagation in 200 DPI LIG coated DCBs does not follow a straight path, as it oscillates and "zigzags" with increasing crack length. The LIG interlayer helps deflect the path of the crack, therefore creating a larger fracture

surface area and providing higher resistance to crack propagation. These observations are consistent with other reported studies that use a nanostructured interlayer, such as CNTs, to reinforce the interlaminar region [41,44,52]. SEM imaging of the fractured DCB surfaces reveals that the crack propagates partially within the LIG interlayer instead of exclusively along the fiber matrix interface. The untreated DCB fracture surface shown in Figure 5.16B-D displays typical adhesive failure; as minimal matrix material residue can be found. In addition to the brittle interfacial behavior, the considerable amount of broken fibers along the fracture surface is indicative of significant fiber bridging. While similar fracture surface morphology can also be observed in the presence of a 200 DPI LIG interlayer, the surface is found to be mostly covered with matrix material that is well bonded to the carbon fiber surface, suggesting cohesive failure of the interlaminar region (Figures 5.16E & F). Such a failure mode insinuates that interfacial adhesion is stronger in LIG coated DCB specimens due to the interlayer absorbing more fracture energy. By inducing stronger adhesion between adjacent plies, cracks are forced to grow away from the boundaries of the interlaminar region, and into the strong and crack resistive interlayer. This allows the LIG forests to introduce higher energy absorption mechanisms, such as crack nano-bridging and pull-out. These mechanisms are confirmed in Figures 5.16G-I, where LIG fibers and bundles are found partially embedded on both sides of the fractured DCB specimen at similar spots despite the LIG being primarily coated on only one of the laminas. In conclusion, the LIG interlayer toughens DCB specimens by deflecting cracks away from the weak interfacial region and into the strengthened interlaminar region, resulting in a hybrid cohesive/adhesive failure mode capable of absorbing a larger amounts of fracture energy.

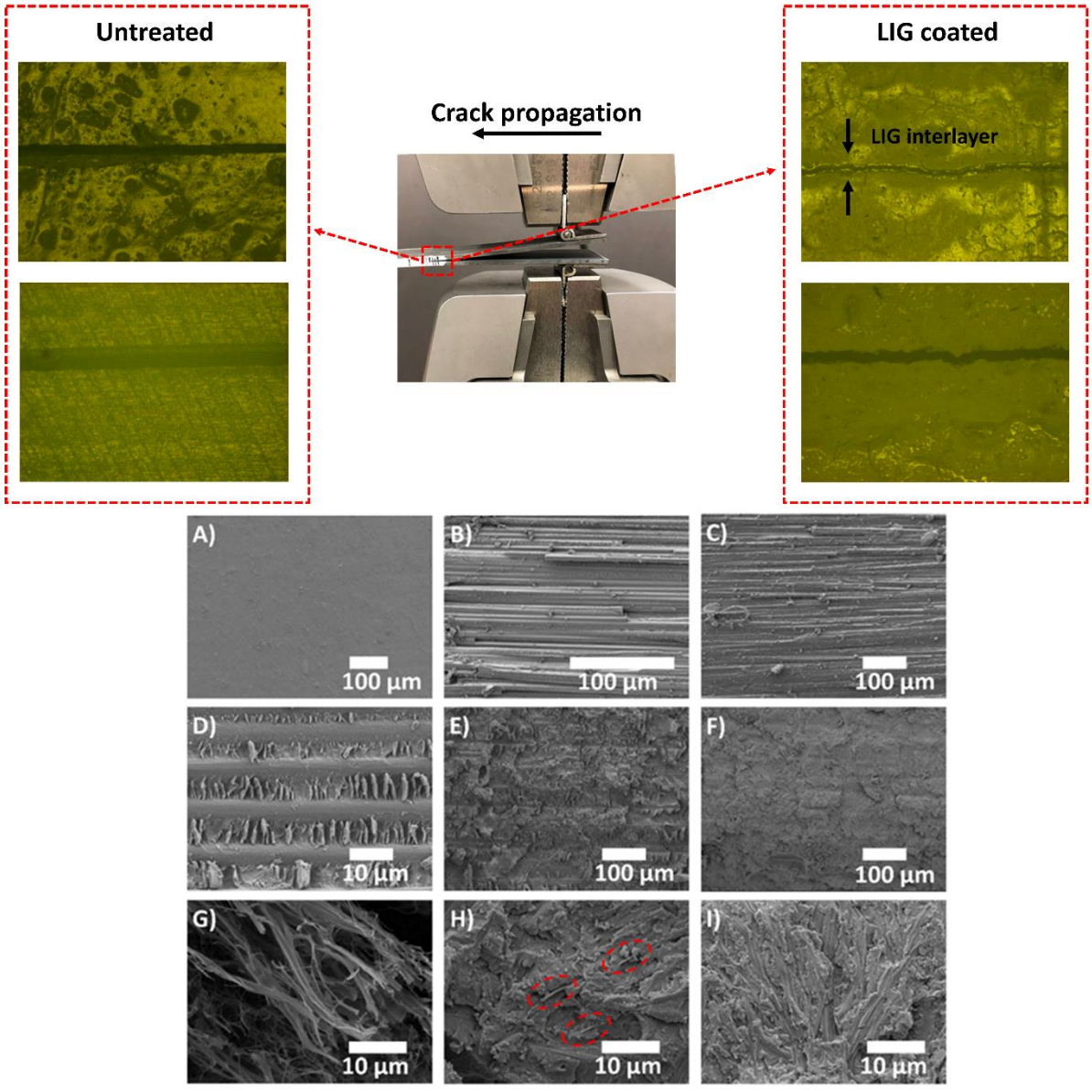

Figure 5.16. SEM micrographs of the fracture surface of untreated and 200 DPI LIG coated carbon DCBs. A) Pre-crack DCB region. B-D) Fracture surface of untreated DCB specimens showing adhesive failure. E), F) Fracture surface of LIG coated DCB specimens showing adhesive failure. G) LIG bundle image at high magnification. H), I) LIG interlayer at the fracture surface of LIG coated DCB specimens. LIG nanofiber pullout is indicated using the dashed red circles.

Delamination under pure shear loading is another concern and major failure mode of fiber reinforced composites. The response of composite materials under such loading conditions can be evaluated using Mode II interlaminar fracture toughness (G_{IIC}) testing. Here, the crack is also propagated with the help of a Teflon insert placed at the mid-plane of end notch flexure (ENF)

specimens, but in a 3-point bend loading configuration similar to that used for short beam testing. However, given the tendency of aramid composites to inelastically deform when loaded in such a configuration, as shown in chapter 3, G_{IIC} can only be assessed in carbon fiber ENF specimens using the approach detailed in ASTM D7905. During Mode II testing, aramid ENFs tend to absorb large mid-span deformations, causing unstable crack propagation and inaccurate results. Carbon ENF specimens are cut from 30 plies unidirectional carbon laminates with a 76.2 mm long Teflon spacer midway through its thickness (Figure 5.17A). The samples are then loaded at a crosshead speed of 0.5 mm/min on a 5982 Instron loading frame series using a 100 kN load cell and a 3-point bending fixture. The Mode II fracture toughness is obtained according to the compliance calibration (CC) method described in ASTM D7905, such as:

$$G_{IIC} = \frac{3mP_{max}{}^2a^2}{2B} \tag{5.3.}$$

where P_{max} is the maximum force recorded during the fracture test, B is the width of the ENF specimen, a is the crack delamination length, and m is a calibration compliance constant obtained from the linear regression analysis of the relationship between the ENF compliance (C) and a^3. The described relationship is established through data reduction of information obtained during two initial load-unload CC cycles, followed by a load until fracture-unload cycle. Two initiation G_{IIC} are usually obtained during Mode II testing: the first one through the Teflon insert, and a second one through the subsequently generated pre-crack [414]. These G_{IIC} values are referred to as Teflon insert or non-pre-cracked (NPC) G_{IIC}, and pre-cracked (PC) G_{IIC}, respectively. The same procedure was used to calculate both NPC and PC G_{IIC} using their corresponding load-unload cycles. It should be noted that the crack length a used to calculate NPC and PC G_{IIC} is taken to be the longest between that measured through visual inspection and the one calculated using the fitted C vs a^3 relationship, as per ASTM D7905. The response of each specimen under 3-point bend loading is typically linear up until maximum loading is reached, where a sharp drop in the load measurement indicates unstable crack initiation in the ENFs (Figure 5.17B). This instability is usually due to the resin rich region formed at the end of the Teflon insert, causing an initiation NPC G_{IIC} that overestimates the actual fracture toughness. Once each ENF specimen is pre-cracked, more accurate and reliable measurement of the G_{IIC} can be obtained. Figure 5.17C indicates that both the NPC and PC G_{IIC} display similar trends when an LIG interlayer is introduced. As previously mentioned, less focus is warranted to the NPC G_{IIC}, given the effect of

the Teflon insert on the measurements. In addition, due to the poor performance under Mode I testing conditions, the 100 DPI LIG interlayer was not studied in this case. Both 400 and 200 DPI LIG coated ENFs specimens result in 31 % and 69 % improvement in PC G_{IIC}, relative to that of untreated specimens, respectively. The agreement in optimal LIG morphology (200 DPI) for both Mode I and II testing is a desirable feature for a multifunctional LIG interlayer performance. These results prove that the previously discussed tougher short beam response in the presence of an LIG interlayer is indicative of a higher resistance to delamination and crack propagation in carbon fiber composites when subjected to shear loading. The discrepancy between the improvement in SBS vs G_{IIC} implies that the LIG is more sensitive to interlaminar crack propagation induced under Mode II testing conditions. This confirms that the LIG role in carbon fiber composites is heavily centered around toughening rather than strengthening the composite structure.

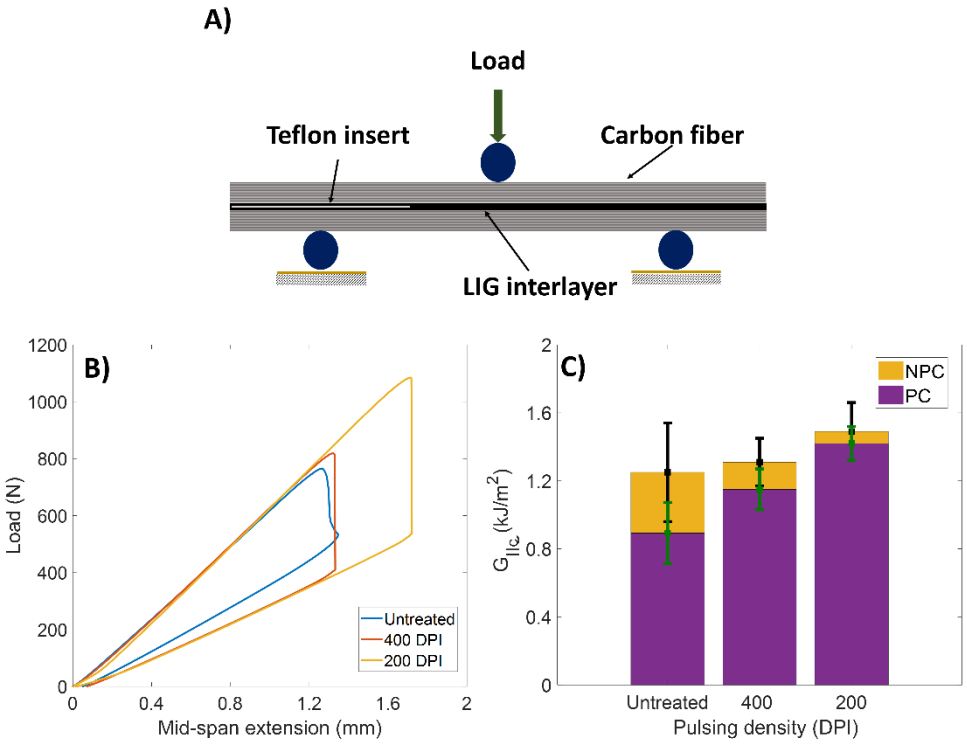

Figure 5.17. Mode II fracture toughness (G_{IIC}) testing. A) Schematic of end notch flexure (ENF) specimen for G_{IIC} measurement. B) NPC load-displacement curves for typical carbon fiber ENF specimens. C) NPC and PC G_{IIC} of untreated and LIG coated carbon fiber ENF specimens.

Further insight into the reinforcement mechanism of the LIG interlayer under such loading conditions can be obtained through SEM imaging of the fractured ENF surfaces. The untreated ENF specimens display a clean fracture surface with minimal residue of polymer matrix material,

due to adhesive interfacial failure (Figures 5.18A-C). This failure mode is typical of carbon fiber composites, as cracks tend to propagate in a straight line, along the minimum path of resistance which occurs in many cases along the fiber-matrix interface. In contrast, the LIG coated ENF specimens display increased cohesive failure, as the imaged surfaces are found to be covered with epoxy resin residue (Figures 5.18D-F). By forcing the crack to propagate both in the interlayer and along its boundaries, the fracture area is considerably enlarged, and higher fracture energy is necessitated to propagate the crack in the composite. Therefore, the induced cohesive failure of the interlaminar region indicates that the crack is propagated along a more crack-resistive path. Signs of nano-bridging can also be observed, as fragments of the damaged LIG interlayer is observed on both sides of the ENF specimens (Figures 5.18G-I). The LIG microstructure is thus capable of mechanically joining adjacent lamina, bridging the initiation and propagation of cracks, and ultimately resulting in a toughening of the interlaminar region. While these toughening mechanisms are highly desirable to help overcome delamination in carbon fiber composites, their effect on the in-plane and viscoelastic properties of the composites remains unknown and requires further investigation.

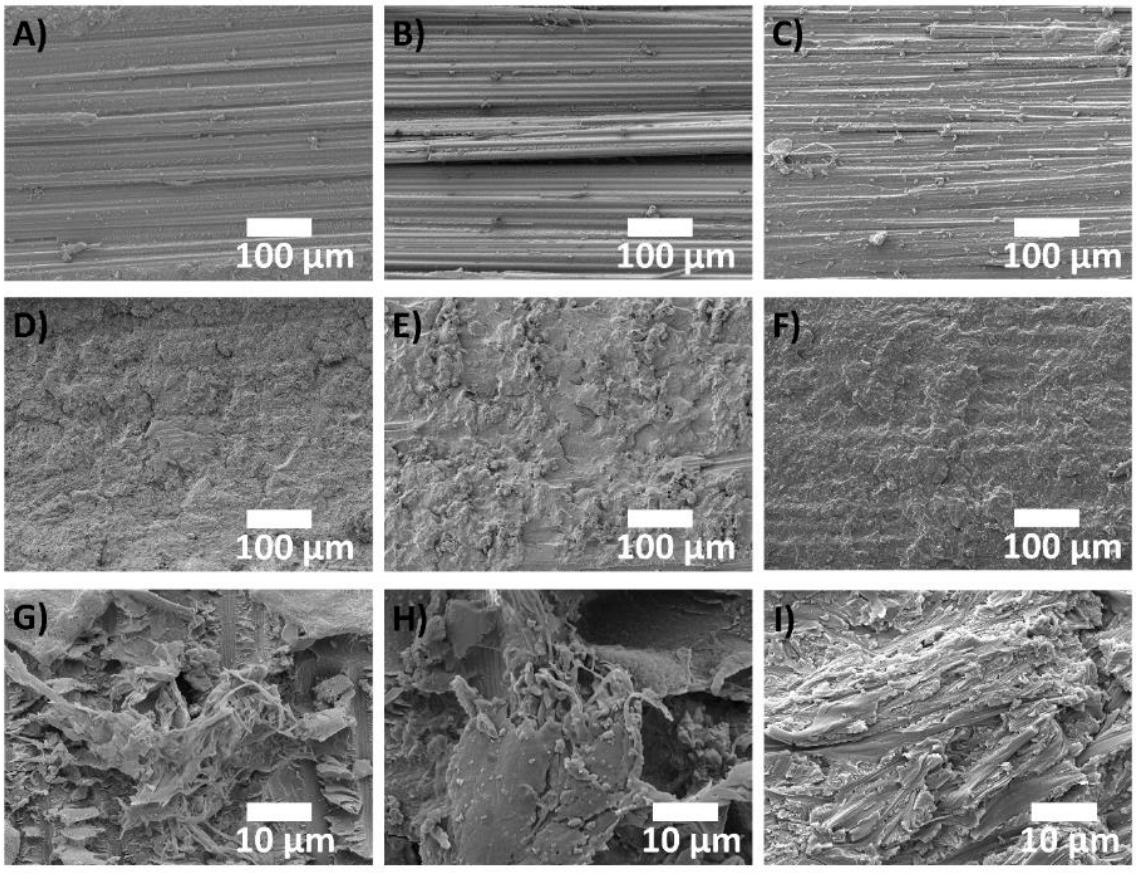

Figure 5.18. SEM micrographs of the fracture surface of untreated and LIG coated carbon ENF. A) Pre-crack DCB region. B), C) Fracture surface of untreated ENFs showing adhesive failure. D-F) Fracture surface of LIG coated ENFs showing cohesive failure. G-I) LIG interlayer at fracture surface of LIG coated ENFs.

5.3.3. Measurement of composite tensile and viscoelastic properties

While we have shown that a LIG can improve out-of-plane properties, it remains critical that any interlaminar reinforcement approach does not reduce the in-plane properties of the composite. The tensile strength of composites depends primarily on the properties of the fiber or fabric which provide in-plane reinforcement inside composites. As previously pointed out, many techniques for growing nanomaterials onto fiber surfaces have been shown to result in etching and defect formation, thus failing to maintain the tensile properties of the fiber [167,415]. This is caused by the harsh synthesis conditions, such as high temperatures or the use of catalysts, thus leading to research focusing on the development of more benign grafting techniques, namely hydrothermal reactions [184,217,416]. In the case of aramid fabric, the LIG in this work is synthesized using a photo-thermal conversion process by means of pulsed laser irradiation, whose effects can be investigated using fabric tensile testing. When compared to the tensile strength of untreated aramid fabric (3.22 GPa), the tensile strength of LIG coated aramid fabric is observed to decrease with increasing induction power, yielding up to 16.4% decrease in strength at 20% output power in the double side configuration (2.71 GPa) (Figure 5.19A). Moreover, at constant induction powers of 12% and 20%, the double-sided configuration is further weakened relative to fabric coated only on one side, showing 2% and 7% further decrease in tensile strength, respectively. By generating LIG on the aramid surface, in-plane reinforcement is reduced at the expense of out-of-plane reinforcement, as aramid fibers are irradiated into graphitic microstructure with normal orientation relative to the substrate. The amount of aramid fibers inside the fabric along both the weft and warp directions is therefore decreased, reducing its ability to support tensile and compressive loads. This is undesirable for composite applications, as it yields aramid fiber reinforced composites with weaker structural and ballistic performance. However, the induction process also results in a decrease in the weight of the aramid fabric; Figure 5.19B shows maximum reduction in the areal density of the fabric of up to 17% when induction power reaches 20%. Similarly, the double-sided configuration further lowers the areal density, relative to the one-sided configuration, independent of induction power. These changes to the areal density are obtained by

measuring the weight of a constant aramid fabric area before and after the induction of the LIG. Given that the induction process has been quantified through weight yields in previous studies, a weight approach is chosen over a volumetric one to describe the changes to the composition of the fabric [303,308]. The considerably low yield of the laser induction process insinuates that the measured weight is primarily that of the aramid fabric. The decrease in weight with increasing output power is an expected outcome, as a thicker layer of aramid is transformed into LIG when exposed to a stronger irradiation process. This confirms that the decrease in tensile properties is not due to diminishing individual fiber strength during the treatment, but rather to the conversion of PPTA into LIG and gaseous products, as the induction process uses the surface of aramid fibers as reactants, thus decreasing the overall weight of the fabric [352]. Therefore, as seen in Figure 5.19C, none of the LIG coated fabrics display any statistical decrease in specific strength when compared to untreated fibers, leading to the conclusion that the LIG coating results in out of plane reinforcement while maintaining the original specific strength of the fibers. Furthermore, the effect of LIG on the elastic properties of carbon fiber laminate composites is examined using also tensile testing according to ASTM standard D3039, where both tensile strength and stiffness are found to be statistically unchanged following the introduction of a 200 DPI LIG interlayer. In the case of carbon fiber composites, weight considerations are irrelevant, given the lightweight LIG is transfer printed onto the prepregs and not generated through using them as precursors, such as in aramids. Only the tensile properties of 200 DPI LIG coated specimens are studied and compared to that of untreated ones, given its optimal interlaminar performance, as determined using Mode I and II testing. The preserved elastic properties observed in Figures 5.19D & E indicate that the LIG does not accelerate tensile failure in carbon fiber composites and does not act as defects or micro-stress concentration sites in the interlaminar region. It is then possible to fabricate lightweight LIG coated fiber reinforced composite structures with preserved in-plane properties and an improved out-of-plane performance.

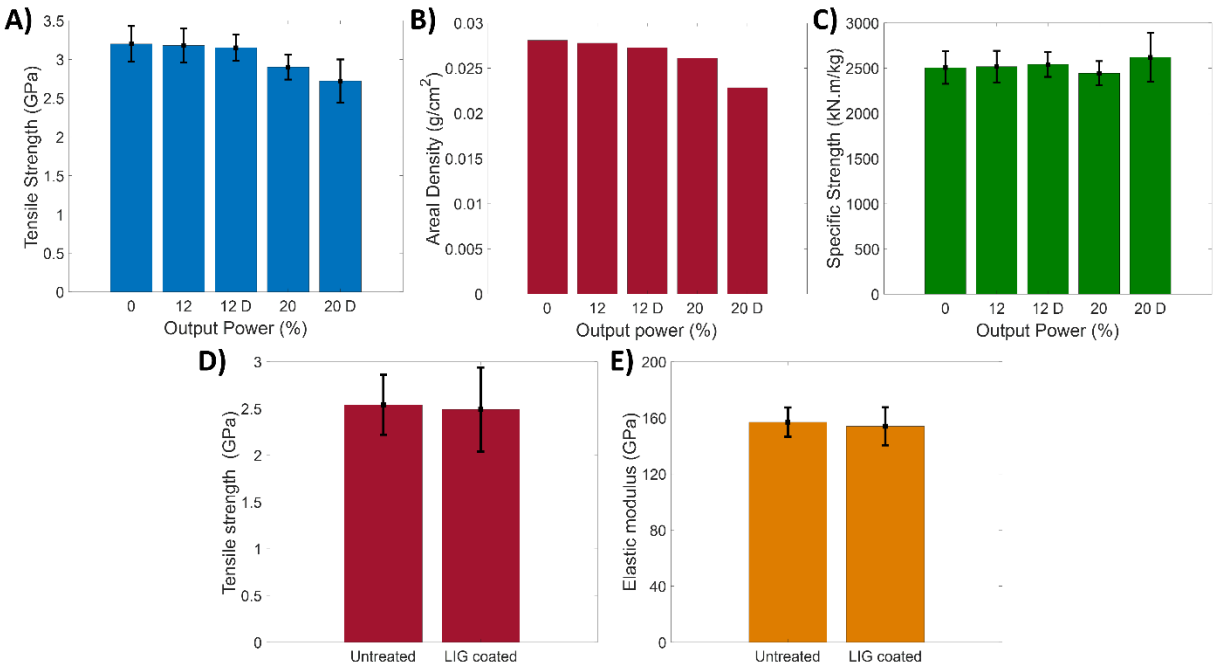

Figure 5.19. Tensile properties of untreated and LIG coated aramid and carbon fiber reinforced composites. A-C) Aramid fiber reinforced composites: A) Tensile strength. B) Areal density. C) Specific tensile strength. D-E) Carbon fiber reinforced composites: D) Tensile strength. E) Elastic modulus.

In addition to the preservation of in-plane properties, the introduction of the LIG is found to not interfere with the viscoelastic and damping behavior of both aramid and carbon fiber reinforced composite. Aramid composites are highly used in dynamic loading applications, such as in hard body armor and blast protection, due to their excellent energy absorption abilities [19]. Therefore, improvements to their structural performance are ideally desired to be coupled with a good dynamic response. Although viscoelastic properties are heavily dominated by the matrix, modification to the interlaminar and interfacial regions can alter the dynamic response of the composite[417,418]. The effect of these interlaminar modifications are studied through dynamic mechanical thermal analysis (DMTA) performed in the three-point bending configuration. The specific storage modulus (E') and loss modulus (E'') are obtained through a normalization similar to the one reported in the previous section. This allows for more accurate assessment of the LIG influence on the response of the composite by accounting for the decrease in weight of the in-plane reinforcement. Figure 5.20. shows unchanged specific viscoelastic properties when LIG aramid composite specimens are compared to untreated ones. The unaffected specific storage and loss

modulus insinuates a preservation of the flexural rigidity and energy dissipation performance of the composite, respectively (Figures 5.20A & B). Given that the loss tangent is the ratio of E'' to E', the damping behavior of the aramid composite is expected to be conserved as seen in Figure 5.20C. This indicates that the damping properties of the aramid fiber reinforced composites are preserved, while maintaining their elastic and viscous response. It should be noted that similar trends are found irrespective of the LIG morphology, induction power, or configuration, thus only the case of laser induction at 20% and in the double-sided configuration is reported due to it having the largest effect on the fabric's weight, and thus potentially its dynamic response. Furthermore, the viscoelastic behavior of carbon fiber composites in the presence of the LIG interlayer is also examined using DMTA. As previously mentioned, the dynamic response of fiber reinforced composites is heavily reflective of its viscoelastic properties and damping capacity. As seen in Figures 5.20D & E, both storage and loss modulus are unaffected by the introduction of the 200 DPI LIG interlayer, signaling a conservation of flexural rigidity and energy dissipation capacity of the composite. Given that the loss tangent is the ratio of the loss modulus to the storage modulus, unchanged damping behavior is also expected (Figure 5.20F). With both the elastic and viscous responses being unchanged in the presence of the LIG interlayer, the tougher carbon fiber composites can preserve their damping properties by maintaining both their dynamic stability and load-bearing ability. It should be noted that the morphology of the LIG interlayer could be optimized to improve the damping properties of these composites, yet achieving it in concurrence with optimal interlaminar reinforcement performance cannot be guaranteed. Finally, the glass transition temperature (T_g) is shown to exhibit a 6.6 °C increase, going from 230.7 °C for untreated specimens up to 237.1 °C for LIG coated ones. Such increase in the T_g allows for carbon fiber composites to be operated at slightly higher temperatures. In conclusion, the LIG interlayer is capable of improve the toughness of aramid and carbon fiber reinforced composites under various loading conditions, all while maintaining both their elastic and viscoelastic properties.

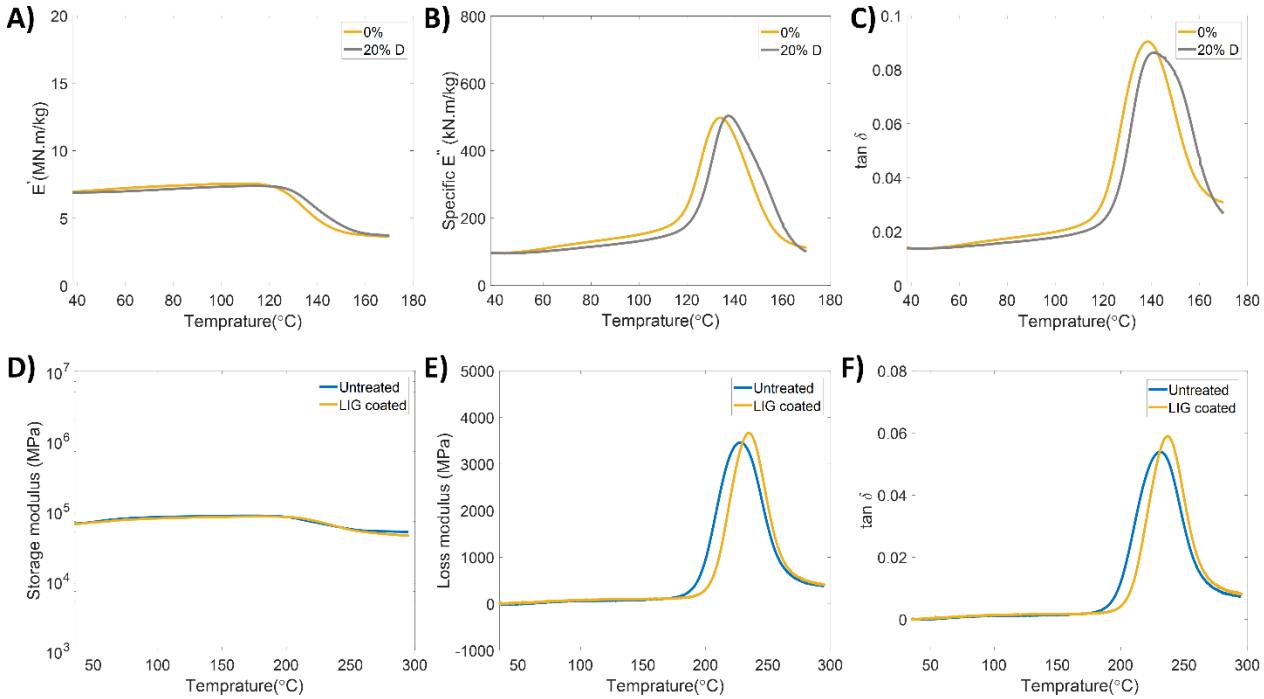

Figure 5.20. Dynamic mechanical thermal analysis of untreated and LIG coated aramid and carbon fiber reinforced composites. A-C) Aramid fiber reinforced composites: A) Specific storage modulus. B) Specific loss modulus. C) Loss tangent. D-F) Carbon fiber reinforced composites: D) Storage modulus. E) Loss modulus. F) Loss tangent.

5.4. Chapter summary

In this chapter, nanostructured interlayers are demonstrated to toughen aramid and carbon fiber reinforced composites and improve their resistance to delamination under a variety of loading conditions. Using a simple spray-coating technique, it is demonstrated that an optimized ANF interlayer is capable of improving short beam strength and initiation Mode I fracture toughness of carbon fiber reinforced composites by 33.7% and 81.6%, respectively. The improved resistance to crack initiation and propagation is the result of the transition from an adhesive to a cohesive interlaminar failure mode in the presence of ANF reinforcement. Moreover, in comparison to other aramid interleaving techniques, the ANF interlayer presented advantages of nanoscale thickness, low areal density, and preserved composite tensile strength, Therefore, this work presents a simple, fast, and cost-effective technique that can be scaled up to industrial production levels for the fabrication of high toughness carbon fiber reinforced composite structures.

Furthermore, it is shown that LIG can be also used as an interlayer that improves the interlaminar properties of aramid and carbon fiber reinforced composites. It is demonstrated that

the piezoresistive LIG is easily introduced on the surfaces of aramid fabric and carbon fiber prepregs through direct laser writing or transfer printing, respectively. The LIG interlayer is found to result in 70% and 20% improvement in short beam strength and Mode I fracture toughness of aramid fiber reinforced composites, respectively. Similarly, the LIG interlayer is capable of yielding a 41% and 69% increase in both initiation Mode I and pre-cracked Mode II fracture toughness of carbon fiber prepreg composites, respectively. The LIG is found to increase resistance to crack initiation and propagation, and thus delamination, by inducing a more cohesive interlaminar failure mode and nano-bridging. The improved interlaminar performance is demonstrated to be obtained while maintaining the tensile and viscoelastic properties of the resulting aramid and carbon composites. Such results demonstrate that LIG can act as multifunctional and nanoscale building block in aramid and carbon fiber reinforced composites in order to provide a fast and cost-effective reinforcement to the mechanical and multifunctional performance of their composite structures.

CHAPTER 6. Conclusions

Fiber reinforced polymer matrix composites have attracted great attention over the last century due to their unique specific mechanical properties. Compared to traditional and homogenous materials, such as metals and ceramics, fiber reinforced composites can provide superior specific strength and stiffness, while also being lightweight and tailorable for particular application requirements. With these advantages, the field of composites is continuously growing in a number of large-scale industries, such as aerospace, energy, automotive, and infrastructure. The mechanical performance of fiber reinforced composites typically depends on the properties of the reinforcement, the matrix, and the quality of their interface. A primary concern in composite applications is the weakly adhered fiber-matrix interface, which causes premature failure and limits them from realizing their theoretical potential. The poor interfacial adhesion is the result of large mismatch in stiffness between the fiber and the matrix, along with the lack of sufficient chemical interaction and mechanical interlocking between them. Research efforts aimed to improve these interfacial interactions through the development of chemical surface treatments and filler additive approaches. Yet the application of such techniques is typically hindered by the damage they induce to the fiber surface when being applied, or the encountered agglomeration issues when incorporating the fillers. With the continuous innovation of the nanomaterials field, efforts shifted to exploiting interphase design techniques to strengthen the fiber-matrix interface. However, currently developed methods are either detrimental to the fiber properties, too energy intensive, or non-scalable to industrial levels. In this dissertation, multifunctional and hierarchical fiber reinforced composites with improved interfacial adhesion were developed through the introduction of nanostructured interphases and interlayers. It is shown that these nanomaterials-based reinforcements can be introduced in benign, cost-effective, and scalable manners that maintain in-plane properties of the composites. Specifically, ANF, ZnO, and LIG nanomaterials are incorporated into aramid, glass, and carbon fiber composites to achieve a variety of interfacial, interlaminar functionalities.

Given the importance of fiber/interphase adhesion, the role of chemical interactions between the introduced nanomaterials and the fiber surfaces was initially studied, characterized,

and optimized. First, in order to achieve a well-adhered nanostructured ANF interphase on aramid fiber surfaces, the potential of amide-amide hydrogen bonding between ANFs and polyamide molecules was demonstrated through chemical and mechanical characterization, highlighting the potential of ANFs assembly on aramid fiber surfaces through physisorption. In the absence of such interactions, the use of a high charge density cationic polymer coating was considered as an alternative approach to electrostatically adsorb negatively charged ANFs on the surface of glass fibers. In addition, an aramid fibrilized interphase is developed to improve the aramid surface morphology and chemistry for an improved performance in composite materials. Functionalization techniques were also developed to benignly oxidize the surfaces of carbon and glass fibers and improve their adhesion with ZnO NWs and NPs. Through XPS analysis, the employed functionalization techniques were demonstrated to increase surface oxygen content in carbon and glass fibers by 5.05% and 14%, respectively. Finally, it is demonstrated that graphene nanomaterials (LIG) can be directly induced on the surfaces of aramid fibers or transferable to the surface of carbon fiber prepregs. The resulting LIG interlayer is well adhered to the fiber surfaces through inherent chemical and mechanical interactions. In addition, the LIG coated surface chemistry was studied and characterized in order to understand the potential of such a graphitic interlayer in fiber reinforced composites. Therefore, chemical interactions between nanomaterials and fiber surfaces were investigated and optimized through experimental approaches prior to the application in fiber reinforced composites.

The potential of aramid-based nanostructured interphases in improving interfacial properties of aramid and glass fiber composites under quasi-static loading conditions was then investigated. The ANF interphases were grafted on the fiber surfaces using a simple and fast dip-coating process. SEM and AFM imaging showed that the introduction of ANF interphases greatly improves surface roughness, while FTIR and XPS analysis demonstrated an increase in polar surface functional groups. The improved chemical interaction and mechanical interlocking between the fiber and the matrix resulted in 70.27% and 83% increase in quasi-static IFSS of aramid and glass fiber composites after 3-minute treatments, respectively. The enhanced interfacial adhesion also resulted in 25% and 35% improvements in SBS of aramid and glass fiber composites, respectively. The obtained interfacial gains were achieved while maintaining the tensile strength of the fibers. The aramid fiber fibrilization treatment was also investigated. The fibrilized aramid fibers were demonstrated to present nanofibrils across their surfaces, along with an increase in

oxygen surface functional groups. When incorporated into aramid fiber reinforced composites, the fibrilization treatment was found to yield 128% and 62% improvements in IFSS and SBS, respectively, along with maintained tensile properties. Thus, aramid-based nanostructured interphases are capable of improving interfacial adhesion, and thus quasi-static load bearing abilities in fiber reinforced composites.

In contrast, composite materials used in ballistic applications require a different set of properties. First, the simple and fast fibrilization treatment was shown to be capable of increasing interyarn friction in aramid fabric by up to 500%. The improved fiber-fiber interactions were demonstrated to yield 10% and 230% improvement in the fabric's ballistic limit and dynamic stab resistance, respectively. The fibrilization treatment was optimized in order to obtain these improvements in the fabric's ballistic performance, while maintaining its strength. In the case of fiber reinforced composites, ceramic ZnO interphases were shown to tailor interfacial properties of carbon and glass fiber composites for a simultaneously optimal performance under both quasi-static and dynamic loading conditions. The ZnO nanomaterials were grown on the fiber surfaces using a hydrothermal process that preserves the fiber's strength. IFSS of ZnO coated single-fiber carbon and glass fiber composites were quasi-statically and dynamically measured using a novel experimental setup. The ZnO interphase was demonstrated to improve interfacial adhesion under quasi-static loading rates, resulting in a minimum increase in IFSS of 87%, while weakening it under dynamic loading rates, as highlighted by the minimum decrease of 34% in IFSS, all relative to a conventional fiber-matrix interface at similar strain rates. Through the inspection of embedded fiber lengths post-pullout, it was found that the cause of such strain rate dependent behavior is the brittle fracture of the ceramic ZnO interphase at high strain rates due to matrix stiffening effects. The described behavior allows for a reduction in weight through the integration of ballistic functionality into carbon and glass fiber composites, in addition to improving its original structural functionality.

After investigating interfacial modification techniques, the merits of nanostructured interlayers for toughening and suppressing delamination in fiber reinforced composites were studied. It was shown that an ANF interlayer can be deposited on carbon fiber surfaces using a simple and fast spray-coating technique. The areal density and morphology of the interlayer were optimized to result in 34% and 82% improvements in the SBS and G_{IC} of carbon fiber reinforced composites, respectively. The ANF interlayered composites exhibited a more cohesive

interlaminar failure mode, as confirmed through SEM imaging. Elsewhere, an LIG multifunctional interlayer was demonstrated to toughen aramid and carbon fiber reinforced composites. The thin carbon-based interlayer was directly induced through laser irradiation on aramid fabric, and was later transfer printed on carbon fiber prepregs. The LIG interlayered aramid composites were demonstrated to experience 70% and 20% improvements in SBS and initiation G_{IC}, respectively; while carbon fiber ones exhibited 41% and 69% increase in both initiation G_{IC}, and pre-cracked G_{IIC}, respectively. The toughening of the interlaminar region of these composites was achieved while maintaining their elastic and viscoelastic properties. The thin LIG interlayer is therefore capable of toughening aramid and carbon fiber composites, while potentially introducing unprecedented functionality to aramid composites in the form of improved electrical and thermal properties. The hierarchical fiber reinforced composites developed in this dissertation can ease their integration into industrial scale processes and expand their use in structural and ballistic applications.

6.1. Contributions

This dissertation investigated the fiber-matrix interfacial properties of fiber reinforced polymer matrix composites and developed a number of novel interphase design methods to improve their out-of-plane performance, while maintaining in-plane one. This work has provided cost-effective and scalable solutions to address weak interfacial adhesion and delamination in fiber reinforced composites and has made numerous contributions detailed in the following section.

The first contribution of this work is developing a simple and cost-effective technique to adsorb ANFs onto aramid surfaces. By studying the potential of amide-amide hydrogen bonding between a nanofiller and a matrix, well-adhered and nanostructured ANF interphases are formed on the surfaces of macroscale aramid fibers in less than 5 minutes through a simple phisisorption process. The introduced nanoscale aramid interphase does not degrade the individual fiber strength, and yields improved interfacial adhesion, as reflected through the improved IFSS and SBS composite performances. The benign nature of the adsorption process makes this technique practical and easy to integrate in a variety of structural aramid composite applications.

The second contribution of this dissertation is the development of an electrostatic-based approach to adsorb ANFs onto glass fiber surfaces. By applying a positively charged PDDA coating to the glass surface, electrostatic adsorption of negatively charged ANFs onto the glass

fiber surfaces is achieved in less than 5 minutes. Similar to the case of aramid fibers, the nanostructured ANF interphase considerably roughens the glass surface and populates it with polar functional groups, improving interfacial adhesion and enhancing IFSS and SBS of glass fiber composites. The described process can prove to be an alternative to current fiberglass sizing techniques, as it can be applied at a later time post-fiber extrusion, and at room temperature.

Another contribution of this work is the development of a benign aramid fabric fibrilization technique. The method is unique as it takes advantage of the dissolution and deprotonation process developed to yield ANFs in order to generate nanofibrils across the aramid surface and increase surface oxygen content. In fiber matrix reinforced composites, the fibrilization treatment contributes to improved IFSS and SBS performances. When applied to aramid fabric, the fibrilization process yields a large increase in interyarn friction, which translates into improved ballistic limit and stab resistance properties. The simple, benign, and fast nature of this process will make this technique a popular choice to strengthen adhesion in aramid fiber polymer matrix composites or improve the ballistic performance of aramid fabric.

In addition, the revealing of the ability of ZnO interphases to tailor the interfacial properties of carbon and glass fiber composites for a simultaneously optimal interfacial adhesion under quasi-static and dynamic loading rates is another contribution of this work. The hydrothermally grown ceramic interphases are confirmed to reinforce the fiber-matrix interface under quasi-static loading conditions. A novel piranha solution functionalization treatment was developed for glass fiber surfaces in order to improve adhesion between the ZnO interphase and the fiber. Using a novel and in-house developed dynamic single fiber pullout experimental setup, the performance of the ZnO interphase is found to be reversed under dynamic loading rates, yielding weaker fiber-matrix interfaces. Such multifunctional interfacial behavior can eliminate the need for multi-component ballistic protection that is currently added to composite structures, thus reducing system weight and increasing its flexibility.

On an interlaminar level, the introduction of an ultra-thin ANF interlayer into carbon fiber composites using a simple and scalable spray-coating technique is also a contribution of this dissertation. The spray-coating process avoids ANF agglomeration issues and allows for easy control over the morphology and areal density of the nanoscale interlayer. The ANF interlayered carbon fiber composites displayed a tougher behavior, as highlighted by its more cohesive interlaminar failure mechanism. In addition, the in-plane properties of these composites were

determined to be maintained, highlighting the superiority of such a quick and scalable interleaving technique over currently proposed or used ones in the composite industry to address delamination.

The final contribution of this work is introducing LIG interlayers into aramid and carbon fiber reinforced composites for a tougher and multifunctional behavior. This recently discovered piezoresistive nanomaterials have been used in the fabrication of a number of sensors and devices but are yet to be exploited for mechanical functionalities. The LIG is generated directly on the aramid surfaces, while a transfer printing technique that maintains their alignment is used to graft them on carbon fiber prepregs. The LIG interlayered aramid and carbon fiber composites are demonstrated to exhibit a tougher response under various loading conditions, as their ability to resist crack initiation and propagation, and thus delamination, is improved. This is achieved while maintaining the elastic and viscoelastic properties of the composites and integrating unprecedented electrical conductivity into aramid fiber composites. These findings highlight the potential of overcoming delamination in fiber reinforced composites using a multifunctional and easily synthesized laser induced graphene interlayer.

6.2. Recommendations for future work

This dissertation performed fundamental research on improving interfacial adhesion in fiber reinforced polymer matrix composites. The results demonstrated a number of nanostructured interphases and interlayers that can be introduced in fiber reinforced composites using benign, fast, and scalable approaches in order to improve interfacial adhesion and toughen these composites. Different aspects of this research have led to interesting scientific contributions that can be used to advance the field of composite materials through the integration of nanomaterials into such structures. Nonetheless, the work presented here is not complete and can be complemented with further studies that expand the potential of the presented efforts. A number of experimental and theoretical or analytical studies can be built on the detailed findings in this dissertation.

Here, the ANF interphases and interlayers were realized in a simple manner across the aramid and glass fiber surfaces, while controlling treatment periods. However, the morphology of the interphase can also be studied through controlling the aspect ratio of the ANFs. By varying certain parameters of the dissolution and deprotonation process, the ANFs geometry and aspect ratio can be modified and their effects on the adsorption process and on interfacial properties of a composite can be studied. The concentration or type of base used to generate the ANF suspension

can be varied to yield ANFs of considerably larger aspect ratio, potentially resulting in an improved interphase performance. Furthermore, large aspect ratio nano-reinforcement has been shown to yield a better interleaving performance due to improving fiber bridging toughening mechanism. Therefore, the performance of a large aspect ratio ANF interlayer spray-coated in carbon fiber composites is an interesting topic to investigate.

In addition, any numerical studies that involve ANF reinforcement lack accurate data pertaining to their strength, stiffness, and elongation. While it is assumed that the ANFs maintain similar mechanical properties to that of their macroscale version, this remains an unproven hypothesis. Moreover, many research studies of nanoscale materials, such as CNTs, show that they considerably outperform their macroscale counterparts due to a considerable decrease in defects. Therefore, for accurate modeling of ANF performance either as a nanofiller, an interphase, or an interlayer, it is necessary to assess the mechanical properties of a single ANF. Through nano-manipulation lift-off, individual ANF can be placed on push-to-pull devices in order to perform mechanical testing inside a transmission electron microscope (TEM). Such an experiment allows for obtaining the exact mechanical properties of ANFs, thus improving the accuracy of micro-mechanic models, and helping bridge the gap between theoretical and experimental studies.

Elsewhere, the multifunctional performance of the ZnO interphase requires further investigation to fully understand its behavior under dynamic loading conditions. Its observed brittle fracture can be further understood by a mapping of the strain distribution at the level of the interphase during high strain rate SFP testing. This can be achieved through in-situ SFP testing inside a SEM, coupled with digital imaging correlation (DIC). Another important parameter to study when it comes to the performance of such an interphase is its morphology. Given the demonstrated dependence of IFSS on ZnO geometry, a better understanding of this relationship can be obtained by controlling the length and diameter of the ZnO nanostructure and assessing its effect on IFSS of single-fiber composite under dynamic loading conditions.

One of the last aspects of this dissertation was the development of a multifunctional LIG interlayer for aramid and carbon fiber reinforced composites. While the LIG was used to primarily toughen these composites, its piezoresistive multifunctionality remain unexploited for applications such as structural health monitoring, joule heating, and out-of-autoclave curing. A comprehensive study that addresses these other functionalities can maximize the performance of LIG in aramid fiber reinforced composites, and further justify its integration into these composites. As for carbon

fiber composites, The LIG morphology can potentially be optimized by controlling induction fluence to simultaneously toughen these composites, while improving their viscoelastic performance. Future work therefore should focus on identifying new structural and non-structural functionalities of the LIG in aramid, carbon and potentially glass fiber reinforced polymer matrix composites.

REFERENCES

[1] Chawla KK. Composite materials : science and engineering. Springer; 2012. doi:10.1007/978-0-387-74365-3.

[2] Mangalgiri PD. Composite materials for aerospace applications. Bull Mater Sci 1999;22:657–64. doi:10.1007/BF02749982.

[3] Baker AA, Scott ML. Composite Materials for Aircraft Structures, Third Edition. Washington, DC: American Institute of Aeronautics and Astronautics, Inc.; 2016. doi:10.2514/4.103261.

[4] Gay D, Hoa S, Tsai S. Composite Materials. CRC Press; 2002. doi:10.1201/9781420031683.

[5] Balasubramanian M. Composite materials and processing. CRC Press; 2017.

[6] Witten E, Mathes V, Sauer M, Kuhnel M. Composites Market Report 2018. 2018.

[7] Marsh G. Reclaiming value from post-use carbon composite. Reinf Plast 2008;52:36–9. doi:10.1016/S0034-3617(08)70242-X.

[8] Kim J-K, Mai YW. Engineered interfaces in fiber reinforced composites. Elsevier Sciences; 1998.

[9] Fratzl P, Weinkamer R. Nature's hierarchical materials. Prog Mater Sci 2007;52:1263–334. doi:10.1016/j.pmatsci.2007.06.001.

[10] Wegst UGK, Bai H, Saiz E, Tomsia AP, Ritchie RO. Bioinspired structural materials. Nat Mater 2015;14:23–36. doi:10.1038/nmat4089.

[11] Imbeni V, Kruzic JJ, Marshall GW, Marshall SJ, Ritchie RO. The dentin-enamel junction and the fracture of human teeth. Nat Mater 2005;4:229–32. doi:10.1038/nmat1323.

[12] Palucka T, Bensaude-Vincent B. History of composites - overview. 2002.

[13] Stahl GA. A Short History of Polymer Science, 1981, p. 25–44. doi:10.1021/bk-1981-0175.ch003.

[14] Daniel IM, Ishai O. Engineering mechanics of composite materials. Oxford University Press; 2006.

[15] Kim YJ. Advanced composites in bridge construction and repair. Woodhead Publishing; 2014.

[16] Kabir SMF, Mathur K, Seyam AFM. A critical review on 3D printed continuous fiber-reinforced composites: History, mechanism, materials and properties. Compos Struct 2020;232:111476. doi:10.1016/j.compstruct.2019.111476.

[17] Ramesan MT, Suhailath K. Role of nanoparticles on polymer composites. Micro Nano Fibrillar Compos. (MFCs NFCs) from Polym. Blends, Elsevier Inc.; 2017, p. 301–26. doi:10.1016/B978-0-

08-101991-7.00013-3.

[18] Bhatnagar A, Tan CBC. Ballistic fabric laminates. US684675B2, 2002.

[19] Bhatnagar A. Lightweight Ballistic Composites. Elsevier; 2016. doi:10.1016/C2014-0-03657-X.

[20] Cheeseman BA, Bogetti TA. Ballistic impact into fabric and compliant composite laminates. Compos Struct 2003;61:161–73. doi:10.1016/S0263-8223(03)00029-1.

[21] Jacobs MJN, Van Dingenen JLJ. Ballistic protection mechanisms in personal armour. J Mater Sci 2001;36:3137–42. doi:10.1023/A:1017922000090.

[22] Nikbakt S, Kamarian S, Shakeri M. A review on optimization of composite structures Part I: Laminated composites. Compos Struct 2018;195:158–85. doi:10.1016/j.compstruct.2018.03.063.

[23] Bandaru AK, Sachan Y, Ahmad S, Alagirusamy R, Bhatnagar N. On the mechanical response of 2D plain woven and 3D angle-interlock fabrics. Compos Part B Eng 2017;118:135–48. doi:10.1016/J.COMPOSITESB.2017.03.011.

[24] Grujicic M, Pandurangan B, Koudela KL, Cheeseman BA. A computational analysis of the ballistic performance of light-weight hybrid composite armors. Appl Surf Sci 2006;253:730–45. doi:10.1016/J.APSUSC.2006.01.016.

[25] Chung DDL. A review of multifunctional polymer-matrix structural composites. Compos Part B Eng 2019;160:644–60. doi:10.1016/j.compositesb.2018.12.117.

[26] Stenzler JS. Impact Mechanics of PMMA/PC Multi-Laminates with Soft Polymer Interlayers. Virginia Tech, 2009.

[27] Sahay R, Reddy VJ, Ramakrishna S. Synthesis and applications of multifunctional composite nanomaterials. Int J Mech Mater Eng 2014;9:1–13. doi:10.1186/s40712-014-0025-4.

[28] Liu W, Ullah B, Kuo C-C, Cai X. Two-Dimensional Nanomaterials-Based Polymer Composites: Fabrication and Energy Storage Applications 2019. doi:10.1155/2019/4294306.

[29] Sodano HA, Park G, Inman DJ. Estimation of Electric Charge Output for Piezoelectric Energy Harvesting. Strain 2004;40:49–58. doi:10.1111/j.1475-1305.2004.00120.x.

[30] Sodano HA, Inman DJ, Park G. Generation and Storage of Electricity from Power Harvesting Devices. J Intell Mater Syst Struct 2005;16:67–75. doi:10.1177/1045389X05047210.

[31] Anton SR, Sodano HA. A review of power harvesting using piezoelectric materials (2003–2006). Smart Mater Struct 2007;16:R1. doi:10.1088/0964-1726/16/3/R01.

[32] Kang I, Schulz MJ, Kim JH, Shanov V, Shi D. A carbon nanotube strain sensor for structural health monitoring. Smart Mater Struct 2006;15:737–48. doi:10.1088/0964-1726/15/3/009.

[33] Zou Y, Tong L, Steven GP. Vibration-based model-dependent damage (delamination) identification and health monitoring for composite structures — a review. J Sound Vib 2000;230:357–78. doi:10.1006/JSVI.1999.2624.

[34] Diamanti K, Soutis C. Structural health monitoring techniques for aircraft composite structures. Prog Aerosp Sci 2010;46:342–52. doi:10.1016/J.PAEROSCI.2010.05.001.

[35] Staszewski WJ, Mahzan S, Traynor R. Health monitoring of aerospace composite structures – Active and passive approach. Compos Sci Technol 2009;69:1678–85. doi:10.1016/J.COMPSCITECH.2008.09.034.

[36] Li C, Thostenson ET, Chou T-W. Sensors and actuators based on carbon nanotubes and their composites: A review. Compos Sci Technol 2008;68:1227–49. doi:10.1016/J.COMPSCITECH.2008.01.006.

[37] Kang H-K, Kang D-H, Bang H-J, Hong C-S, Kim C-G. Cure monitoring of composite laminates using fiber optic sensors. Smart Mater Struct 2002;11:279–87. doi:10.1088/0964-1726/11/2/311.

[38] Wang S, Chung DDL. Self-sensing of flexural strain and damage in carbon fiber polymer-matrix composite by electrical resistance measurement. Carbon N Y 2006;44:2739–51. doi:10.1016/J.CARBON.2006.03.034.

[39] Zhang L, Tian X, Malakooti MH, Sodano HA. Novel self-healing CFRP composites with high glass transition temperatures. Compos Sci Technol 2018;168:96–103. doi:10.1016/J.COMPSCITECH.2018.09.008.

[40] Das R, Melchior C, Karumbaiah KM. Self-healing composites for aerospace applications. Adv Compos Mater Aerosp Eng 2016:333–64. doi:10.1016/B978-0-08-100037-3.00011-0.

[41] Marshiya K, Zhang W. A self-healing thermosetting composite material. Compos Part A Appl Sci Manuf 2007;38:1116–20. doi:10.1016/J.COMPOSITESA.2006.06.008.

[42] Hayes S., Zhang W, Branthwaite M, Jones F. Self-healing of damage in fibre-reinforced polymer-matrix composites. J R Soc Interface 2007;4:381–7. doi:10.1098/rsif.2006.0209.

[43] Liu M, Younes H, Hong H, Peterson GP. Polymer nanocomposites with improved mechanical and thermal properties by magnetically aligned carbon nanotubes. Polymer (Guildf) 2019;166:81–7. doi:10.1016/j.polymer.2019.01.031.

[44] Jin F-L, Park S-J. A review of the preparation and properties of carbon nanotubes-reinforced polymer compositess. Carbon Lett 2011;12:57–69. doi:10.5714/cl.2011.12.2.057.

[45] Micheli D, Vricella A, Pastore R, Delfini A, Giusti A, Albano M, et al. Ballistic and electromagnetic shielding behaviour of multifunctional Kevlar fiber reinforced epoxy composites modified by carbon nanotubes. Carbon N Y 2016;104:141–56. doi:10.1016/J.CARBON.2016.03.059.

[46] Gómez EF, Michel FC. Biodegradability of conventional and bio-based plastics and natural fiber composites during composting, anaerobic digestion and long-term soil incubation. Polym Degrad Stab 2013;98:2583–91. doi:10.1016/j.polymdegradstab.2013.09.018.

[47] Wagner PA, Little BJ, Hart KR, Ray RI. Biodegradation of composite materials. Int Biodeterior Biodegrad 1996;38:125–32. doi:10.1016/S0964-8305(96)00036-4.

[48] Thomas JP, Qidwai MA. Mechanical design and performance of composite multifunctional materials. Acta Mater 2004;52:2155–64. doi:10.1016/j.actamat.2004.01.007.

[49] Thomas JP, Qidwai MA. The design and application of multifunctional structure-battery materials systems. JOM 2005;57:18–24. doi:10.1007/s11837-005-0228-5.

[50] Qian H, Kucernak AR, Greenhalgh ES, Bismarck A, Shaffer MSP. Multifunctional structural supercapacitor composites based on carbon aerogel modified high performance carbon fiber fabric. ACS Appl Mater Interfaces 2013;5:6113–22. doi:10.1021/am400947j.

[51] Lin Y, Sodano HA. Concept and model of a piezoelectric structural fiber for multifunctional composites. Compos Sci Technol 2008;68:1911–8. doi:10.1016/j.compscitech.2007.12.017.

[52] Lin Y, Sodano HA. Characterization of multifunctional structural capacitors for embedded energy storage. J Appl Phys 2009;106:114108. doi:10.1063/1.3267482.

[53] Malakooti MH, Patterson BA, Hwang H-S, Sodano HA. ZnO nanowire interfaces for high strength multifunctional composites with embedded energy harvesting. Energy Environ Sci 2016;9:634–43. doi:10.1039/C5EE03181H.

[54] Chapuis B. Introduction to Structural Health Monitoring, Springer, Cham; 2018, p. 1–11. doi:10.1007/978-3-319-69233-3_1.

[55] Thostenson ET, Chou T-W. Carbon Nanotube Networks: Sensing of Distributed Strain and Damage for Life Prediction and Self Healing. Adv Mater 2006;18:2837–41. doi:10.1002/adma.200600977.

[56] Sharma S, Dhakate SR, Majumdar A, Singh BP. Improved static and dynamic mechanical properties of multiscale bucky paper interleaved Kevlar fiber composites. Carbon N Y 2019. doi:10.1016/J.CARBON.2019.06.055.

[57] Groo LA, Nasser J, Inman D, Sodano H. Laser induced graphene for in situ damage sensing in aramid fiber reinforced composites. Compos Sci Technol 2021;201:108541. doi:10.1016/j.compscitech.2020.108541.

[58] Groo LA, Nasser J, Zhang L, Steinke K, Inman D, Sodano H. Laser induced graphene in fiberglass-reinforced composites for strain and damage sensing. Compos Sci Technol 2020;199:108367. doi:10.1016/j.compscitech.2020.108367.

[59] Abliz D, Duan Y, Steuernagel L, Xie L, Li D, Ziegmann G. Curing methods for advanced polymer composites -A review. Polym Polym Compos 2013;21:341–8. doi:10.1177/096739111302100602.

[60] Lee J, Ni X, Daso F, Xiao X, King D, Gómez JS, et al. Advanced carbon fiber composite out-of-autoclave laminate manufacture via nanostructured out-of-oven conductive curing. Compos Sci Technol 2018;166:150–9. doi:10.1016/j.compscitech.2018.02.031.

[61] Raji A-RO, Varadhachary T, Nan K, Wang T, Lin J, Ji Y, et al. Composites of Graphene Nanoribbon Stacks and Epoxy for Joule Heating and Deicing of Surfaces. ACS Appl Mater Interfaces 2016;8:3551–6. doi:10.1021/acsami.5b11131.

[62] Aouraghe MA, Xu F, Liu X, Qiu Y. Flexible, quickly responsive and highly efficient E-heating carbon nanotube film. Compos Sci Technol 2019:107824.

doi:10.1016/J.COMPSCITECH.2019.107824.

[63] Groo L, Inman DJ, Sodano HA. In Situ Damage Detection for Fiber-Reinforced Composites Using Integrated Zinc Oxide Nanowires. Adv Funct Mater 2018;28:1802846. doi:10.1002/adfm.201802846.

[64] Park JM, Kong JW, Kim DS, Yoon DJ. Nondestructive damage detection and interfacial evaluation of single-fibers/epoxy composites using PZT, PVDF and P(VDF-TrFE) copolymer sensors. Compos Sci Technol 2005;65:241–56. doi:10.1016/j.compscitech.2004.07.006.

[65] Brei D, Cannon BJ. Piezoceramic hollow fiber active composites. Compos Sci Technol 2004;64:245–61. doi:10.1016/S0266-3538(03)00259-8.

[66] Blaiszik BJ, Kramer SLB, Olugebefola SC, Moore JS, Sottos NR, White SR. Self-Healing Polymers and Composites. Annu Rev Mater Res 2010;40:179–211. doi:10.1146/annurev-matsci-070909-104532.

[67] Wool RP. A material fix. Nature 2001;409:773–4. doi:10.1038/35057412.

[68] Toohey KS, Sottos NR, White SR. Characterization of microvascular-based self-healing coatings. Exp Mech 2009;49:707–17. doi:10.1007/s11340-008-9176-7.

[69] Toohey KS, Sottos NR, Lewis JA, Moore JS, White SR. Self-healing materials with microvascular networks. Nat Mater 2007;6:581–5. doi:10.1038/nmat1934.

[70] Heo Y, Malakooti MH, Sodano HA. Self-healing polymers and composites for extreme environments. J Mater Chem A 2016;4:17403–11. doi:10.1039/c6ta06213j.

[71] Liu YL, Chuo TW. Self-healing polymers based on thermally reversible Diels-Alder chemistry. Polym Chem 2013;4:2194–205. doi:10.1039/c2py20957h.

[72] Zhang L, Julé F, Sodano HA. High service temperature, self-mendable thermosets networked by isocyanurate rings. Polymer (Guildf) 2017;114:249–56. doi:10.1016/j.polymer.2017.03.008.

[73] Zhang L, Lin J, Sodano HA. Isocyanurate transformation induced healing of isocyanurate–oxazolidone polymers. J Appl Polym Sci 2020;137:48698. doi:10.1002/app.48698.

[74] Crosby AJ, Lee J. Polymer Nanocomposites: The “Nano” Effect on Mechanical Properties. Polym Rev 2007;47:217–29. doi:10.1080/15583720701271278.

[75] Chow WS, Mohd Ishak ZA. Polyamide blend-based nanocomposites: A review. Express Polym Lett 2015;9:211–32. doi:10.3144/expresspolymlett.2015.22.

[76] Tjong SC, Mai YW. Physical properties and applications of polymer nanocomposites. Woodhead Pub; 2010.

[77] Tjong SC, Xu SA, Kwok-Yiu Li R, Mai YW. Short glass fiber-reinforced polyamide 6,6 composites toughened with maleated SEBS. Compos Sci Technol 2002;62:2017–27. doi:10.1016/S0266-3538(02)00140-9.

[78] Zhao G, Hussainova I, Antonov M, Wang Q, Wang T. Friction and wear of fiber reinforced polyimide composites. Wear 2013;301:122–9. doi:10.1016/j.wear.2012.12.019.

[79] Karsli NG, Aytac A. Tensile and thermomechanical properties of short carbon fiber reinforced polyamide 6 composites. Compos Part B Eng 2013;51:270–5. doi:10.1016/j.compositesb.2013.03.023.

[80] Torlon® 4000TF | Solvay. 2019.

[81] Chavarria F, Paul DR. Morphology and properties of thermoplastic polyurethane nanocomposites: Effect of organoclay structure. Polymer (Guildf) 2006;47:7760–73. doi:10.1016/j.polymer.2006.08.067.

[82] Lan T, Pinnavaia TJ. Clay-Reinforced Epoxy Nanocomposites. Chem Mater 1994;6:2216–9. doi:10.1021/cm00048a006.

[83] Islam ME, Mahdi TH, Hosur M V., Tcherbi-Narteh A, Jeelani S. Low velocity impact characterization of nanoclay and MWCNTS binary nanoparticles modified carbon/epoxy composites subjected to marine environmental conditioning. ASME Int. Mech. Eng. Congr. Expo. Proc., vol. 14, American Society of Mechanical Engineers (ASME); 2014. doi:10.1115/IMECE2014-36173.

[84] Wang K, Chen L, Wu J, Toh ML, He C, Yee AF. Epoxy nanocomposites with highly exfoliated clay: Mechanical properties and fracture mechanisms. Macromolecules 2005;38:788–800. doi:10.1021/ma048465n.

[85] Kelnar I, Khunová V, Kotek J, Kaprálková L. Effect of clay treatment on structure and mechanical behavior of elastomer-containing polyamide 6 nanocomposite. Polymer (Guildf) 2007;48:5332–9. doi:10.1016/j.polymer.2007.06.062.

[86] Almeida F De, Correia A, Silva ECE, Lopes IC, Silva FJG. Compatibilization effect of organophilic clays in PA6/PP polymer blend. Procedia Manuf 2018;17:1154–61. doi:10.1016/j.promfg.2018.10.016.

[87] Hegde RR, Bhat GS, Spruiell JE, Benson R. Structure and properties of polypropylene-nanoclay composites. J Polym Res 2013;20. doi:10.1007/s10965-013-0323-1.

[88] Mallick S, Kar P, Khatua BB. Morphology and properties of nylon 6 and high density polyethylene blends in presence of nanoclay and PE-g-MA. J Appl Polym Sci 2012;123:1801–11. doi:10.1002/app.34648.

[89] Mallakpour S, Naghdi M. Polymer/SiO2 nanocomposites: Production and applications. Prog Mater Sci 2018;97:409–47. doi:10.1016/j.pmatsci.2018.04.002.

[90] Al-Turaif HA. Effect of nano TiO2 particle size on mechanical properties of cured epoxy resin. Prog Org Coatings 2010;69:241–6. doi:10.1016/j.porgcoat.2010.05.011.

[91] Choi EY, Kim K, Kim CK, Kang E. Reinforcement of nylon 6,6/nylon 6,6 grafted nanodiamond composites by in situ reactive extrusion. Sci Rep 2016;6. doi:10.1038/srep37010.

[92] Popov VN. Carbon nanotubes: properties and application. Mater Sci Eng R Reports 2004;43:61–102. doi:10.1016/J.MSER.2003.10.001.

[93] Gao J, Itkis ME, Yu A, Bekyarova E, Zhao B, Haddon RC. Continuous spinning of a single-walled carbon nanotube-nylon composite fiber. J Am Chem Soc 2005;127:3847–54. doi:10.1021/ja0446193.

[94] De Zhang W, Shen L, Phang IY, Liu T. Carbon Nanotubes Reinforced Nylon-6 Composite Prepared by Simple Melt-Compounding. Macromolecules 2004;37:256–9. doi:10.1021/ma035594f.

[95] Yoonessi M, Lebroín-Coloín M, Scheiman D, Meador MA. Carbon nanotube epoxy nanocomposites: The effects of interfacial modifications on the dynamic mechanical properties of the nanocomposites. ACS Appl Mater Interfaces 2014;6:16621–30. doi:10.1021/am5056849.

[96] Manchado MAL, Valentini L, Biagiotti J, Kenny JM. Thermal and mechanical properties of single-walled carbon nanotubes-polypropylene composites prepared by melt processing. Carbon N Y 2005;43:1499–505. doi:10.1016/j.carbon.2005.01.031.

[97] Ruan SL, Gao P, Yang XG, Yu TX. Toughening high performance ultrahigh molecular weight polyethylene using multiwalled carbon nanotubes. Polymer (Guildf) 2003;44:5643–54. doi:10.1016/S0032-3861(03)00628-1.

[98] Singh S, Pei Y, Miller R, Sundararajan PR. Long-Range, Entangled Carbon Nanotube Networks in Polycarbonate. Adv Funct Mater 2003;13:868–72. doi:10.1002/adfm.200304411.

[99] Safadi B, Andrews R, Grulke EA. Multiwalled carbon nanotube polymer composites: Synthesis and characterization of thin films. J Appl Polym Sci 2002;84:2660–9. doi:10.1002/app.10436.

[100] Guan Y, Li W, Zhang Y, Shi Z, Tan J, Wang F, et al. Aramid nanofibers and poly (vinyl alcohol) nanocomposites for ideal combination of strength and toughness via hydrogen bonding interactions. Compos Sci Technol 2017;144:193–201. doi:10.1016/j.compscitech.2017.03.010.

[101] Ryan KP, Cadek M, Nicolosi V, Blond D, Ruether M, Armstrong G, et al. Carbon nanotubes for reinforcement of plastics? A case study with poly(vinyl alcohol). Compos Sci Technol 2007;67:1640–9. doi:10.1016/j.compscitech.2006.07.006.

[102] Weidt D, Figiel Ł. Effect of CNT waviness and van der Waals interaction on the nonlinear compressive behaviour of epoxy/CNT nanocomposites. Compos Sci Technol 2015;115:52–9. doi:10.1016/j.compscitech.2015.04.018.

[103] Bin Y, Kitanaka M, Zhu D, Matsuo M. Development of highly oriented polyethylene filled with aligned carbon nanotubes by gelation/crystallization from solutions. Macromolecules 2003;36:6213–9. doi:10.1021/ma0301956.

[104] Meincke O, Kaempfer D, Weickmann H, Friedrich C, Vathauer M, Warth H. Mechanical properties and electrical conductivity of carbon-nanotube filled polyamide-6 and its blends with acrylonitrile/butadiene/styrene. Polymer (Guildf) 2004;45:739–48. doi:10.1016/j.polymer.2003.12.013.

[105] Siochi EJ, Working DC, Park C, Lillehei PT, Rouse JH, Topping CC, et al. Melt processing of SWCNT-polyimide nanocomposite fibers. Compos Part B Eng 2004;35:439–46.

doi:10.1016/j.compositesb.2003.09.007.

[106] Ma P-C, Mo S-Y, Tang B-Z, Kim J-K. Dispersion, interfacial interaction and re-agglomeration of functionalized carbon nanotubes in epoxy composites. Carbon N Y 2010;48:1824–34. doi:10.1016/J.CARBON.2010.01.028.

[107] Shen Z, Bateman S, Wu DY, McMahon P, Dell'Olio M, Gotama J. The effects of carbon nanotubes on mechanical and thermal properties of woven glass fibre reinforced polyamide-6 nanocomposites. Compos Sci Technol 2009;69:239–44. doi:10.1016/j.compscitech.2008.10.017.

[108] Yang M, Cao K, Sui L, Qi Y, Zhu J, Waas A, et al. Dispersions of Aramid Nanofibers: A New Nanoscale Building Block. ACS Nano 2011;5:6945–54. doi:10.1021/nn2014003.

[109] Xu L, Zhao X, Xu C, Kotov NA. Water-Rich Biomimetic Composites with Abiotic Self-Organizing Nanofiber Network. Adv Mater 2018;30:1703343. doi:10.1002/adma.201703343.

[110] Lin J, Bang SH, Malakooti MH, Sodano HA. Isolation of Aramid Nanofibers for High Strength and Toughness Polymer Nanocomposites. ACS Appl Mater Interfaces 2017;9:11167–75. doi:10.1021/acsami.7b01488.

[111] Kwon SR, Harris J, Zhou T, Loufakis D, Boyd JG, Lutkenhaus JL. Mechanically Strong Graphene/Aramid Nanofiber Composite Electrodes for Structural Energy and Power. ACS Nano 2017;11:6682–90. doi:10.1021/acsnano.7b00790.

[112] Zhu J, Cao W, Yue M, Hou Y, Han J, Yang M. Strong and stiff aramid nanofiber/carbon nanotube nanocomposites. ACS Nano 2015;9:2489–501. doi:10.1021/nn504927e.

[113] Cheng M, Chen W, Weerasooriya T. Mechanical Properties of Kevlar® KM2 Single Fiber. J Eng Mater Technol 2005;127:197. doi:10.1115/1.1857937.

[114] Singh TJ, Samanta S. Characterization of Kevlar Fiber and Its Composites: A Review. Mater Today Proc 2015;2:1381–7. doi:10.1016/J.MATPR.2015.07.057.

[115] Thostenson ET, Ren Z, Chou T-W. Advances in the science and technology of carbon nanotubes and their composites: a review. Compos Sci Technol 2001;61:1899–912. doi:10.1016/S0266-3538(01)00094-X.

[116] Godara A, Mezzo L, Luizi F, Warrier A, Lomov SV, van Vuure AW, et al. Influence of carbon nanotube reinforcement on the processing and the mechanical behaviour of carbon fiber/epoxy composites. Carbon N Y 2009;47:2914–23. doi:10.1016/J.CARBON.2009.06.039.

[117] Borowski E, Soliman E, Kandil U, Taha M. Interlaminar Fracture Toughness of CFRP Laminates Incorporating Multi-Walled Carbon Nanotubes. Polymers (Basel) 2015;7:1020–45. doi:10.3390/polym7061020.

[118] Subadra SP, Yousef S, Griskevicius P, Makarevicius V. High-performance fiberglass/epoxy reinforced by functionalized CNTs for vehicle applications with less fuel consumption and greenhouse gas emissions. Polym Test 2020;86:106480. doi:10.1016/j.polymertesting.2020.106480.

[119] Dalina WADW, Tan SH, Mariatti M. Properties of Fiberglass/MWCNT Buckypaper/Epoxy Laminated Composites. Procedia Chem 2016;19:935–42. doi:10.1016/j.proche.2016.03.138.

[120] Kwon DJ, Shin PS, Kim JH, Baek YM, Park HS, DeVries KL, et al. Interfacial properties and thermal aging of glass fiber/epoxy composites reinforced with SiC and SiO2 nanoparticles. Compos Part B Eng 2017;130:46–53. doi:10.1016/j.compositesb.2017.07.045.

[121] Halder S, Ahemad S, Das S, Wang J. Epoxy/Glass Fiber Laminated Composites Integrated with Amino Functionalized ZrO2 for Advanced Structural Applications. ACS Appl Mater Interfaces 2016;8:1695–706. doi:10.1021/acsami.5b09149.

[122] Prusty RK, Ghosh SK, Rathore DK, Ray BC. Reinforcement effect of graphene oxide in glass fibre/epoxy composites at in-situ elevated temperature environments: An emphasis on graphene oxide content. Compos Part A Appl Sci Manuf 2017;95:40–53. doi:10.1016/j.compositesa.2017.01.001.

[123] Wang F, Drzal LT, Qin Y, Huang Z. Size effect of graphene nanoplatelets on the morphology and mechanical behavior of glass fiber/epoxy composites. J Mater Sci 2016;51:3337–48. doi:10.1007/s10853-015-9649-x.

[124] Karippal JJ, Narasimha Murthy HN, Rai KS, Sreejith M, Krishna M. Study of mechanical properties of epoxy/glass/nanoclay hybrid composites. J Compos Mater 2011;45:1893–9. doi:10.1177/0021998310389087.

[125] Pol MH, Liaghat G, Hajiarazi F. Effect of nanoclay on ballistic behavior of woven fabric composites: Experimental investigation. J Compos Mater 2013;47:1563–73. doi:10.1177/0021998312449768.

[126] Laurenzi S, Pastore R, Giannini G, Marchetti M. Experimental study of impact resistance in multi-walled carbon nanotube reinforced epoxy. Compos Struct 2013;99:62–8. doi:10.1016/j.compstruct.2012.12.002.

[127] Rahman M, Hosur M, Zainuddin S, Vaidya U, Tauhid A, Kumar A, et al. Effects of amino-functionalized MWCNTs on ballistic impact performance of E-glass/epoxy composites using a spherical projectile. Int J Impact Eng 2013;57:108–18. doi:10.1016/j.ijimpeng.2013.01.011.

[128] Domun N, Kaboglu C, Paton KR, Dear JP, Liu J, Blackman BRK, et al. Ballistic impact behaviour of glass fibre reinforced polymer composite with 1D/2D nanomodified epoxy matrices. Compos Part B Eng 2019;167:497–506. doi:10.1016/j.compositesb.2019.03.024.

[129] Ozdemir NG, Zhang T, Aspin I, Scarpa F, Hadavinia H, Song Y. Toughening of carbon fibre reinforced polymer composites with rubber nanoparticles for advanced industrial applications. Express Polym Lett 2016;10:394–407. doi:10.3144/expresspolymlett.2016.37.

[130] Uddin MF, Sun CT. Strength of unidirectional glass/epoxy composite with silica nanoparticle-enhanced matrix. Compos Sci Technol 2008;68:1637–43. doi:10.1016/j.compscitech.2008.02.026.

[131] Juntaro J, Pommet M, Mantalaris A, Shaffer M, Bismarck A. Nanocellulose enhanced interfaces in truly green unidirectional fibre reinforced composites. Compos Interfaces 2007;14:753–62. doi:10.1163/156855407782106573.

[132] Lee K-Y, Aitomäki Y, Berglund LA, Oksman K, Bismarck A. On the use of nanocellulose as reinforcement in polymer matrix composites. Compos Sci Technol 2014;105:15–27. doi:10.1016/j.compscitech.2014.08.032.

[133] Jang J, Bae J, Lee K. Synthesis and characterization of polyaniline nanorods as curing agent and nanofiller for epoxy matrix composite. Polymer (Guildf) 2005;46:3677–84. doi:10.1016/j.polymer.2005.03.030.

[134] Lee JU, Park B, Kim B-S, Bae D-R, Lee W. Electrophoretic deposition of aramid nanofibers on carbon fibers for highly enhanced interfacial adhesion at low content. Compos Part A Appl Sci Manuf 2016;84:482–9. doi:10.1016/J.COMPOSITESA.2016.02.029.

[135] Park B, Lee W, Lee E, Min SH, Kim B-S. Highly Tunable Interfacial Adhesion of Glass Fiber by Hybrid Multilayers of Graphene Oxide and Aramid Nanofiber. ACS Appl Mater Interfaces 2015;7:3329–34. doi:10.1021/am5082364.

[136] Patterson BA, Malakooti MH, Lin J, Okorom A, Sodano HA. Aramid nanofibers for multiscale fiber reinforcement of polymer composites. Compos Sci Technol 2018;161:92–9. doi:10.1016/J.COMPSCITECH.2018.04.005.

[137] Malakooti MH, Zhou Z, Spears JH, Shankwitz TJ, Sodano HA. Biomimetic Nanostructured Interfaces for Hierarchical Composites. Adv Mater Interfaces 2016;3:1500404. doi:10.1002/admi.201500404.

[138] Hwang HS, Nasser J, Sodano HA. Piezoelectric Stack Actuator for Measurement of Interfacial Shear Strength at High Strain Rates. Exp Mech 2019:1–12. doi:10.1007/s11340-019-00502-6.

[139] Clyne TW. A simple development of the shear lag theory appropriate for composites with a relatively small modulus mismatch. Mater Sci Eng A 1989;122:183–92. doi:10.1016/0921-5093(89)90629-1.

[140] Fukuda H, Chou T-W. An Advanced Shear-Lag Model Applicable to Discontinuous Fiber Composites. J Compos Mater 1981;15:79–91. doi:10.1177/002199838101500107.

[141] Chen Z, Yan W. A shear-lag model with a cohesive fibre-matrix interface for analysis of fibre pull-out. Mech Mater 2015;91:119–35. doi:10.1016/j.mechmat.2015.07.007.

[142] Li G, Zhang C, Wang Y, Li P, Yu Y, Jia X, et al. Interface correlation and toughness matching of phosphoric acid functionalized Kevlar fiber and epoxy matrix for filament winding composites. Compos Sci Technol 2008;68:3208–14. doi:10.1016/j.compscitech.2008.08.006.

[143] Dong H, Wu J, Wang G, Chen Z, Zhang G. The ultrasound-based interfacial treatment of aramid fiber/epoxy composites. J Appl Polym Sci 2009;113:1816–21. doi:10.1002/app.30055.

[144] Ehlert GJ, Lin Y, Sodano HA. Carboxyl functionalization of carbon fibers through a grafting reaction that preserves fiber tensile strength. Carbon N Y 2011;49:4246–55. doi:10.1016/j.carbon.2011.05.057.

[145] Deng T, Zhang G, Dai F, Zhang F. Mild surface modification of *para* -aramid fiber by dilute sulfuric acid under microwave irradiation. Text Res J 2017;87:799–806. doi:10.1177/0040517516639831.

[146] Tarantili PA, Andreopoulos AG. Mechanical properties of epoxies reinforced with chloride-treated aramid fibers. J Appl Polym Sci 1997;65:267–76. doi:10.1002/(SICI)1097-4628(19970711)65:2<267::AID-APP7>3.0.CO;2-M.

[147] Yue CY, Padmanabhan K. Interfacial studies on surface modified Kevlar fibre/epoxy matrix composites. Compos Part B Eng 1999;30:205–17. doi:10.1016/S1359-8368(98)00053-5.

[148] Lu, Qiu, Lu, Wang, Xiao, Zheng, et al. Enhancing the Interfacial Strength of Carbon Fiber/Poly(ether ether ketone) Hybrid Composites by Plasma Treatments. Polymers (Basel) 2019;11:753. doi:10.3390/polym11050753.

[149] Li Z-F, Netravali AN. Surface modification of UHSPE fibers through allylamine plasma deposition. II. Effect on fiber and fiber/epoxy interface. J Appl Polym Sci 1992;44:333–46. doi:10.1002/app.1992.070440217.

[150] Han SH, Oh HJ, Kim SS. Evaluation of fiber surface treatment on the interfacial behavior of carbon fiber-reinforced polypropylene composites. Compos Part B Eng 2014;60:98–105. doi:10.1016/j.compositesb.2013.12.069.

[151] Benrashid R, Tesoro GC. Effect of Surface-Limited Reactions on the Properties of Kevlar® Fibers. Text Res J 1990;60:334–44. doi:10.1177/004051759006000604.

[152] Wang TWH, Blum FD, Dharani LR. Effect of interfacial mobility on flexural strength and fracture toughness of glass/epoxy laminates. J Mater Sci 1999;34:4873–82. doi:10.1023/A:1004676214290.

[153] Frenzel H, Bunzel U, Häßler R, Pompe G. Influence of different glass fiber sizings on selected mechanical properties of PET/glass composites. J Adhes Sci Technol 2000;14:651–60. doi:10.1163/156856100742906.

[154] Iglesias JG, González-Benito J, Aznar AJ, Bravo J, Baselga J. Effect of Glass Fiber Surface Treatments on Mechanical Strength of Epoxy Based Composite Materials. J Colloid Interface Sci 2002;250:251–60. doi:10.1006/JCIS.2002.8332.

[155] Feih S, Wei J, Kingshott P, Sørensen BF. The influence of fibre sizing on the strength and fracture toughness of glass fibre composites. Compos Part A Appl Sci Manuf 2005;36:245–55. doi:10.1016/J.COMPOSITESA.2004.06.019.

[156] Gao S., Mäder E, Abdkader A, Offermann P. Environmental resistance and mechanical performance of alkali-resistant glass fibers with surface sizings. J Non Cryst Solids 2003;325:230–41. doi:10.1016/S0022-3093(03)00330-2.

[157] Xie Y, Hill CAS, Xiao Z, Militz H, Mai C. Silane coupling agents used for natural fiber/polymer composites: A review. Compos Part A Appl Sci Manuf 2010;41:806–19. doi:10.1016/J.COMPOSITESA.2010.03.005.

[158] Korjakin A, Rikards R, Buchholz F-G, Wang H, Bledzki AK, Kessler A. Comparative study of interlaminar fracture toughness of GFRP with different fiber surface treatments. Polym Compos 1998;19:793–806. doi:10.1002/pc.10154.

[159] Gao X, Jensen RE, McKnight SH, Gillespie JW. Effect of colloidal silica on the strength and energy absorption of glass fiber/epoxy interphases. Compos Part A Appl Sci Manuf 2011;42:1738–47. doi:10.1016/j.compositesa.2011.07.029.

[160] Cross WM, Cross WM, Kjerengtroen L, Kellar JJ. Interphase variation in silane-treated glass-fiber-reinforced epoxy composites. J Adhes Sci Technol 2005;19:279–90. doi:10.1163/1568561054352649.

[161] Jensen RE, Palmese GR, McKnight SH. Viscoelastic properties of alkoxy silane-epoxy interpenetrating networks. Int J Adhes Adhes 2006;26:103–15. doi:10.1016/J.IJADHADH.2005.03.004.

[162] Patterson BA, Sodano HA. Enhanced Interfacial Strength and UV Shielding of Aramid Fiber Composites through ZnO Nanoparticle Sizing. ACS Appl Mater Interfaces 2016;8:33963–71. doi:10.1021/acsami.6b07555.

[163] Wang B, Duan Y, Zhang J. Titanium dioxide nanoparticles-coated aramid fiber showing enhanced interfacial strength and UV resistance properties. Mater Des 2016;103:330–8. doi:10.1016/j.matdes.2016.04.085.

[164] Qiangang F, Hejun L, Xiaohong S, Kezhi L, Zhibiao H, Jian W. Microstructure and growth mechanism of SiC whiskers on carbon/carbon composites prepared by CVD. Mater Lett 2005;59:2593–7. doi:10.1016/J.MATLET.2005.02.088.

[165] Anthony DB, Qian H, Clancy AJ, Greenhalgh ES, Bismarck A, Shaffer MSP. Applying a potential difference to minimise damage to carbon fibres during carbon nanotube grafting by chemical vapour deposition. Nanotechnology 2017;28:305602. doi:10.1088/1361-6528/aa783f.

[166] Tzeng SS, Hung KH, Ko TH. Growth of carbon nanofibers on activated carbon fiber fabrics. Carbon N Y 2006;44:859–65. doi:10.1016/j.carbon.2005.10.033.

[167] Qian H, Bismarck A, Greenhalgh ES, Shaffer MSP. Carbon nanotube grafted silica fibres: Characterising the interface at the single fibre level. Compos Sci Technol 2010;70:393–9. doi:10.1016/j.compscitech.2009.11.014.

[168] Downs WB, Baker RTK. Modification of the surface properties of carbon fibers via the catalytic growth of carbon nanofibers. J Mater Res 1995;10:625–33. doi:10.1557/JMR.1995.0625.

[169] An Q, Rider AN, Thostenson ET. Hierarchical Composite Structures Prepared by Electrophoretic Deposition of Carbon Nanotubes onto Glass Fibers. ACS Appl Mater Interfaces 2013;5:2022–32. doi:10.1021/am3028734.

[170] Godara A, Gorbatikh L, Kalinka G, Warrier A, Rochez O, Mezzo L, et al. Interfacial shear strength of a glass fiber/epoxy bonding in composites modified with carbon nanotubes. Compos Sci Technol 2010;70:1346–52. doi:10.1016/J.COMPSCITECH.2010.04.010.

[171] An Q, Tamrakar S, Gillespie JW, Rider AN, Thostenson ET. Tailored glass fiber interphases via electrophoretic deposition of carbon nanotubes: Fiber and interphase characterization. Compos Sci Technol 2018;166:131–9. doi:10.1016/j.compscitech.2018.01.003.

[172] An Q, Rider AN, Thostenson ET. Electrophoretic deposition of carbon nanotubes onto carbon-fiber fabric for production of carbon/epoxy composites with improved mechanical properties. Carbon N Y 2012;50:4130–43. doi:10.1016/J.CARBON.2012.04.061.

[173] Cho BG, Joshi SR, Lee J, Park Y Bin, Kim GH. Direct growth of thermally reduced graphene oxide on carbon fiber for enhanced mechanical strength. Compos Part B Eng 2020;193:108010. doi:10.1016/j.compositesb.2020.108010.

[174] Gangineni PK, Yandrapu S, Ghosh SK, Anand A, Prusty RK, Ray BC. Mechanical behavior of Graphene decorated carbon fiber reinforced polymer composites: An assessment of the influence of functional groups. Compos Part A Appl Sci Manuf 2019;122:36–44. doi:10.1016/j.compositesa.2019.04.017.

[175] Srivastava AK, Gupta V, Yerramalli CS, Singh A. Flexural strength enhancement in carbon-fiber epoxy composites through graphene nano-platelets coating on fibers. Compos Part B Eng 2019;179:107539. doi:10.1016/j.compositesb.2019.107539.

[176] Qin W, Vautard F, Drzal LT, Yu J. Mechanical and electrical properties of carbon fiber composites with incorporation of graphene nanoplatelets at the fiber-matrix interphase. Compos Part B Eng 2015;69:335–41. doi:10.1016/j.compositesb.2014.10.014.

[177] Ma L, Zhu Y, Feng P, Song G, Huang Y, Liu H, et al. Reinforcing carbon fiber epoxy composites with triazine derivatives functionalized graphene oxide modified sizing agent. Compos Part B Eng 2019;176:107078. doi:10.1016/j.compositesb.2019.107078.

[178] Gao B, Zhang R, He M, Sun L, Wang C, Liu L, et al. Effect of a multiscale reinforcement by carbon fiber surface treatment with graphene oxide/carbon nanotubes on the mechanical properties of reinforced carbon/carbon composites. Compos Part A Appl Sci Manuf 2016;90:433–40. doi:10.1016/j.compositesa.2016.08.012.

[179] Bhanuprakash L, Parasuram S, Varghese S. Experimental investigation on graphene oxides coated carbon fibre/epoxy hybrid composites: Mechanical and electrical properties. Compos Sci Technol 2019;179:134–44. doi:10.1016/j.compscitech.2019.04.034.

[180] Lin Y, Ehlert G, Sodano HA. Increased Interface Strength in Carbon Fiber Composites through a ZnO Nanowire Interphase. Adv Funct Mater 2009;19:2654–60. doi:10.1002/adfm.200900011.

[181] Patterson BA, Sodano HA. Effect of zinc oxide nanowire length on interfacial strength of carbon fiber composites. ASME Int. Mech. Eng. Congr. Expo. Proc., vol. 9, American Society of Mechanical Engineers (ASME); 2013. doi:10.1115/IMECE2013-66509.

[182] Galan U, Lin Y, Ehlert GJ, Sodano HA. Effect of ZnO nanowire morphology on the interfacial strength of nanowire coated carbon fibers. Compos Sci Technol 2011;71:946–54. doi:10.1016/j.compscitech.2011.02.010.

[183] Swaminathan G, Palanisamy C, Chidambaram G, Henri G, Udayagiri C. Enhancing the interfacial strength of glass/epoxy composites using ZnO nanowires. Compos Interfaces 2018;25:151–68. doi:10.1080/09276440.2017.1341790.

[184] Ehlert GJ, Sodano HA. Zinc Oxide Nanowire Interphase for Enhanced Interfacial Strength in Lightweight Polymer Fiber Composites. ACS Appl Mater Interfaces 2009;1:1827–33. doi:10.1021/am900376t.

[185] Tanner D, Fitzgerald JA, Phillips BR. The Kevlar Story-an Advanced Materials Case Study. Angew Chemie Int Ed English 1989;28:649–54. doi:10.1002/anie.198906491.

[186] Tashiro K, Kobayashi M, Tadokoro H. Elastic Moduli and Molecular Structures of Several Crystalline Polymers, Including Aromatic Polyamides. Macromolecules 1977;10:413–20.

doi:10.1021/ma60056a033.

[187] Rabb RJ, Fahrenthold EP. Evaluation of shear-thickening-fluid Kevlar for large-fragment-containment applications. J Aircr 2011;48:230–4. doi:10.2514/1.C031081.

[188] Lee YS, Wetzel ED, Wagner NJ. The ballistic impact characteristics of Kevlar® woven fabrics impregnated with a colloidal shear thickening fluid. J Mater Sci 2003;38:2825–33. doi:10.1023/A:1024424200221.

[189] Naik NK, Shrirao P. Composite structures under ballistic impact. Compos Struct 2004;66:579–90. doi:10.1016/J.COMPSTRUCT.2004.05.006.

[190] Zheng JQ, Walsh SM. 14 – Materials, manufacturing, and enablers for future soldier protection. Light. Ballist. Compos., 2016, p. 393–437. doi:10.1016/B978-0-08-100406-7.00014-3.

[191] Knudsen PJT, Heigaard Sørensen O. The destabilizing effect of body armour on military rifle bullets. Int J Legal Med 1997;110:82–7. doi:10.1007/s004140050036.

[192] Hogg PJ. Composites in armor. Science (80-) 2006;314:1100–1. doi:10.1126/science.1131118.

[193] Tabiei A, Nilakantan G. Ballistic Impact of Dry Woven Fabric Composites: A Review. Appl Mech Rev 2008;61:010801. doi:10.1115/1.2821711.

[194] Roylance D, Wilde A, Tocci G. Ballistic Impact of Textile Structures. Text Res J 1973;43:34–41. doi:10.1177/004051757304300105.

[195] Improved Barriers to Turbine Engine Fragments: Interim Report II. 1999.

[196] Chitrangad. Hybrid ballistic fabric. US5187003A, 1993.

[197] Lim C., Tan VB., Cheong C. Perforation of high-strength double-ply fabric system by varying shaped projectiles. Int J Impact Eng 2002;27:577–91. doi:10.1016/S0734-743X(02)00004-0.

[198] Cunniff PM. An Analysis of the System Effects in Woven Fabrics under Ballistic Impact. Text Res J 1992;62:495–509. doi:10.1177/004051759206200902.

[199] Rao Y, Farris RJ. A modeling and experimental study of the influence of twist on the mechanical properties of high-performance fiber yarns. J Appl Polym Sci 2000;77:1938–49. doi:10.1002/1097-4628(20000829)77:9<1938::AID-APP9>3.0.CO;2-D.

[200] Pereira JM, D. RG, Revilock DM. J. Elevated Temperature Ballistic Impact Testing of PBO and Kevlar Fabrics for Application in Supersonic Jet Engine Fan Containment Systems 1997.

[201] Pandya K, Kumar CVS, Nair N, Patil P, Naik N. Analytical and experimental studies on ballistic impact behavior of 2D woven fabric composites. Int J Damage Mech 2015;24:471–511. doi:10.1177/1056789514531440.

[202] Carr DJ. Failure Mechanisms of Yarns Subjected to Ballistic Impact. J Mater Sci Lett 1999;18:585–8. doi:10.1023/A:1006655301587.

[203] Briscoe BJ, Motamedi F. The ballistic impact characteristics of aramid fabrics: The influence of interface friction. Wear 1992;158:229–47. doi:10.1016/0043-1648(92)90041-6.

[204] Briscoe BJ, Motamedi F. Role of Interfacial Friction and Lubrication in Yarn and Fabric Mechanics. Text Res J 1990;60:697–708. doi:10.1177/004051759006001201.

[205] Gorowara RL, Kosik WE, McKnight SH, McCullough RL. Molecular characterization of glass fiber surface coatings for thermosetting polymer matrix/glass fiber composites. Compos Part A Appl Sci Manuf 2001;32:323–9. doi:10.1016/S1359-835X(00)00112-3.

[206] LaBarre ED, Calderon-Colon X, Morris M, Tiffany J, Wetzel E, Merkle A, et al. Effect of a carbon nanotube coating on friction and impact performance of Kevlar. J Mater Sci 2015;50:5431–42. doi:10.1007/s10853-015-9088-8.

[207] Lee W, Lee JU, Byun J-H. Catecholamine polymers as surface modifiers for enhancing interfacial strength of fiber-reinforced composites. Compos Sci Technol 2015;110:53–61. doi:10.1016/J.COMPSCITECH.2015.01.021.

[208] Dischler L. Bullet resistant fabric and method of manufacture. US5225241A, 1993.

[209] Chitrangad JMR-P. Fluorinated finishes for aramids. EP0623180B1, 1996.

[210] Bazhenov S. Dissipation of energy by bulletproof aramid fabric. J Mater Sci 1997;32:4167–73. doi:10.1023/A:1018674528993.

[211] Rebouillat S. Surface treated aramid fibers and a process for making them. US5443896A, 1995.

[212] Egres RG, Decker MJ, Halbach CJ, Lee YS, Kirkwood JE, Kirkwood KM, et al. Stab Resistance of Shear Thickening Fluid (stf)-Kevlar Composites for Body Armor Applications. Transform. Sci. Technol. Curr. Futur. Force, world scientific; 2006, p. 264–71. doi:10.1142/9789812772572_0034.

[213] Gawandi A, Thostenson ET, Gilllespie JW. Tow pullout behavior of polymer-coated Kevlar fabric. J Mater Sci 2011;46:77–89. doi:10.1007/s10853-010-4819-3.

[214] Obradović V, Stojanović DB, Jančić - Heinemann R, Živković I, Radojević V, Uskoković PS, et al. Ballistic Properties of Hybrid Thermoplastic Composites with Silica Nanoparticles. J Eng Fiber Fabr 2014;9:155892501400900. doi:10.1177/155892501400900412.

[215] Malakooti MH, Hwang H-S, Sodano HA. Morphology-Controlled ZnO Nanowire Arrays for Tailored Hybrid Composites with High Damping. ACS Appl Mater Interfaces 2015;7:332–9. doi:10.1021/am506272c.

[216] Hwang H-S, Malakooti MH, Sodano HA. Tailored interyarn friction in aramid fabrics through morphology control of surface grown ZnO nanowires. Compos Part A Appl Sci Manuf 2015;76:326–33. doi:10.1016/j.compositesa.2015.06.012.

[217] Hwang H-S, Malakooti MH, Patterson BA, Sodano HA. Increased interyarn friction through ZnO nanowire arrays grown on aramid fabric. Compos Sci Technol 2015;107:75–81. doi:10.1016/J.COMPSCITECH.2014.12.001.

[218] Malakooti MH, Hwang H-S, Goulbourne NC, Sodano HA. Role of ZnO nanowire arrays on the impact response of aramid fabrics. Compos Part B Eng 2017;127:222–31. doi:10.1016/J.COMPOSITESB.2017.05.084.

[219] Ehlert GJ, Lin Y, Galan U, Sodano HA. Interaction of ZnO Nanowires with Carbon Fibers for Hierarchical Composites with High Interfacial Strength. J Solid Mech Mater Eng 2010;4:1687–98. doi:10.1299/jmmp.4.1687.

[220] Fink BK. Performance Metrics for Composite Integral Armor. J Thermoplast Compos Mater 2000;13:417–31. doi:10.1106/FR0L-T33W-JPD0-VFH3.

[221] Mcgrane RA, Loos AC, Batra RC, Gurdal Z. Vacuum Assisted Resin Transfer Molding of Foam Sandwich Composite Materials: Process Development and Model Verification. Virginia Polytechnic Institute and State University , 2001.

[222] Morgan AC. Rifle Rated Ballistic Helmet. US20110203024A1, 2010.

[223] Tan L Bin, Tse KM, Lee HP, Tan VBC, Lim SP. Performance of an advanced combat helmet with different interior cushioning systems in ballistic impact: Experiments and finite element simulations. Int J Impact Eng 2012;50:99–112. doi:10.1016/J.IJIMPENG.2012.06.003.

[224] Norris RG. Military helmet extension and military helmet including the extension. US7797764B2, 2010.

[225] Harach DJ, Vecchio KS. Microstructure evolution in metal-intermetallic laminate (MIL) composites synthesized by reactive foil sintering in air. Metall Mater Trans A 2001;32:1493–505. doi:10.1007/s11661-001-0237-0.

[226] Vecchio KS. Synthetic multifunctional metallic-intermetallic laminate composites. JOM 2005;57:25–31. doi:10.1007/s11837-005-0229-4.

[227] Vieille B, Casado VM, Bouvet C. Comparative study on the impact behavior and damage tolerance of woven carbon fiber reinforced thermoplastic-and thermosetting-composites. 15th Eur. Conf. Compos. Mater., Venice: 2012.

[228] Tanoglu M, McKnight S., Palmese G., Gillespie Jr J. The effects of glass-fiber sizings on the strength and energy absorption of the fiber/matrix interphase under high loading rates. Compos Sci Technol 2001;61:205–20. doi:10.1016/S0266-3538(00)00195-0.

[229] Ansari MM, Chakrabarti A. Ballistic Performance of Unidirectional Glass Fiber Laminated Composite Plate under Normal and Oblique Impact. Procedia Eng 2017;173:161–8. doi:10.1016/J.PROENG.2016.12.053.

[230] Goldsmith W, Dharan CKH, Chang H. Quasi-static and ballistic perforation of carbon fiber laminates. Int J Solids Struct 1995;32:89–103. doi:10.1016/0020-7683(94)00109-A.

[231] Chawla KK. Composite materials science and engineering. Composites 2003;20:286. doi:10.1016/0010-4361(89)90346-7.

[232] Lee BL, Walsh TF, Won ST, Patts HM, Song JW, Mayer AH. Penetration Failure Mechanisms of Armor-Grade Fiber Composites under Impact. J Compos Mater 2001;35. doi:10.1106/YRBH-JGT9-

U6PT-L555.

[233] Dai Z, Shi F, Zhang B, Li M, Zhang Z. Effect of sizing on carbon fiber surface properties and fibers/epoxy interfacial adhesion. Appl Surf Sci 2011;257:6980–5. doi:10.1016/J.APSUSC.2011.03.047.

[234] Gao B, Zhang R, Gao F, He M, Wang C, Liu L, et al. Interfacial Microstructure and Enhanced Mechanical Properties of Carbon Fiber Composites Caused by Growing Generation 1–4 Dendritic Poly(amidoamine) on a Fiber Surface. Langmuir 2016;32:8339–49. doi:10.1021/acs.langmuir.6b01485.

[235] Latif R, Wakeel S, Zaman Khan N, Noor Siddiquee A, Lal Verma S, Akhtar Khan Z. Surface treatments of plant fibers and their effects on mechanical properties of fiber-reinforced composites: A review. J Reinf Plast Compos 2019;38:15–30. doi:10.1177/0731684418802022.

[236] Sharma SP, Lakkad SC. Impact behavior and fractographic study of carbon nanotubes grafted carbon fiber-reinforced epoxy matrix multi-scale hybrid composites. Compos Part A Appl Sci Manuf 2015;69:124–31. doi:10.1016/J.COMPOSITESA.2014.11.005.

[237] Groo L, Steinke K, Inman DJ, Sodano HA. Vibration Damping Mechanism of Fiber-Reinforced Composites with Integrated Piezoelectric Nanowires. ACS Appl Mater Interfaces 2019;11:47373–81. doi:10.1021/acsami.9b17029.

[238] Ye L. Characterization of delamination resistance in composite laminates. Composites 1989;20:275–81. doi:10.1016/0010-4361(89)90343-1.

[239] Wisnom MR. The role of delamination in failure of fibre-reinforced composites. Philos Trans R Soc A Math Phys Eng Sci 2012;370:1850–70. doi:10.1098/rsta.2011.0441.

[240] Tong L, Mouritz AP, Bannister MK. 3D fibre reinforced polymer composites. Elsevier; 2002.

[241] Turner P, Liu T, Zeng X. Collapse of 3D orthogonal woven carbon fibre composites under in-plane tension/compression and out-of-plane bending. Compos Struct 2016;142:286–97. doi:10.1016/J.COMPSTRUCT.2016.01.100.

[242] Mouritz AP, Bannister MK, Falzon PJ, Leong KH. Review of applications for advanced three-dimensional fibre textile composites. Compos Part A Appl Sci Manuf 1999;30:1445–61. doi:10.1016/S1359-835X(99)00034-2.

[243] Xu F, Huang D, Du X. Improving the delamination resistance of carbon fiber/epoxy composites by brushing and abrading of the woven fabrics. Constr Build Mater 2018;158:257–63. doi:10.1016/J.CONBUILDMAT.2017.10.015.

[244] Deconinck P, Capelle J, Bouchart V, Chevrier P, Ravailler F. Delamination propagation analysis in tufted carbon fibre-reinforced plastic composites subjected to high-velocity impact. J Reinf Plast Compos 2014;33:1353–63. doi:10.1177/0731684414533017.

[245] Mouritz AP. Review of z-pinned composite laminates. Compos Part A Appl Sci Manuf 2007;38:2383–97. doi:10.1016/j.compositesa.2007.08.016.

[246] Koh TM, Isa MD, Feih S, Mouritz AP. Experimental assessment of the damage tolerance of z-pinned T-stiffened composite panels. Compos Part B Eng 2013;44:620–7. doi:10.1016/J.COMPOSITESB.2012.02.017.

[247] De Baere I, Jacques S, Van Paepegem W, Degrieck J. Study of the Mode I and Mode II interlaminar behaviour of a carbon fabric reinforced thermoplastic. Polym Test 2012;31:322–32. doi:10.1016/J.POLYMERTESTING.2011.12.009.

[248] Vieille B, Chabchoub M, Gautrelet C. Influence of matrix ductility and toughness on strain energy release rate and failure behavior of woven-ply reinforced thermoplastic structures at high temperature. Compos Part B Eng 2018;132:125–40. doi:10.1016/J.COMPOSITESB.2017.08.011.

[249] Bhudolia SK, Perrotey P, Joshi SC. Mode I fracture toughness and fractographic investigation of carbon fibre composites with liquid Methylmethacrylate thermoplastic matrix. Compos Part B Eng 2018;134:246–53. doi:10.1016/j.compositesb.2017.09.057.

[250] Friedrich K, Gogeva T, Fakirov S. Thermoplastic impregnated fiber bundles: Manufacturing of laminates and fracture mechanics characterization. Compos Sci Technol 1988;33:97–120. doi:10.1016/0266-3538(88)90013-9.

[251] Sihn S, Kim RY, Huh W, Lee K-H, Roy AK. Improvement of damage resistance in laminated composites with electrospun nano-interlayers. Compos Sci Technol 2008;68:673–83. doi:10.1016/J.COMPSCITECH.2007.09.015.

[252] Shivakumar K, Lingaiah S, Chen H, Akangah P, Swaminathan G, Russell L. Polymer Nanofabric Interleaved Composite Laminates. AIAA J 2009;47:1723–9. doi:10.2514/1.41791.

[253] Daelemans L, van der Heijden S, De Baere I, Rahier H, Van Paepegem W, De Clerck K. Nanofibre bridging as a toughening mechanism in carbon/epoxy composite laminates interleaved with electrospun polyamide nanofibrous veils. Compos Sci Technol 2015;117:244–56. doi:10.1016/J.COMPSCITECH.2015.06.021.

[254] Daelemans L, van der Heijden S, De Baere I, Rahier H, Van Paepegem W, De Clerck K. Using aligned nanofibres for identifying the toughening micromechanisms in nanofibre interleaved laminates. Compos Sci Technol 2016;124:17–26. doi:10.1016/J.COMPSCITECH.2015.11.021.

[255] Huang Z-M, Zhang Y-Z, Kotaki M, Ramakrishna S. A review on polymer nanofibers by electrospinning and their applications in nanocomposites. Compos Sci Technol 2003;63:2223–53. doi:10.1016/S0266-3538(03)00178-7.

[256] Zhang J, Lin T, Wang X. Electrospun nanofibre toughened carbon/epoxy composites: Effects of polyetherketone cardo (PEK-C) nanofibre diameter and interlayer thickness. Compos Sci Technol 2010;70:1660–6. doi:10.1016/J.COMPSCITECH.2010.06.019.

[257] Hamer S, Leibovich H, Green A, Intrater R, Avrahami R, Zussman E, et al. Mode I interlaminar fracture toughness of Nylon 66 nanofibrilmat interleaved carbon/epoxy laminates. Polym Compos 2011;32:1781–9. doi:10.1002/pc.21210.

[258] Magniez K, Chaffraix T, Fox B. Toughening of a Carbon-Fibre Composite Using Electrospun Poly(Hydroxyether of Bisphenol A) Nanofibrous Membranes Through Inverse Phase Separation

and Inter-Domain Etherification. Materials (Basel) 2011;4:1967–84. doi:10.3390/ma4111967.

[259] Li G, Li P, Zhang C, Yu Y, Liu H, Zhang S, et al. Inhomogeneous toughening of carbon fiber/epoxy composite using electrospun polysulfone nanofibrous membranes by in situ phase separation. Compos Sci Technol 2008;68:987–94. doi:10.1016/J.COMPSCITECH.2007.07.010.

[260] van der Heijden S, Daelemans L, De Schoenmaker B, De Baere I, Rahier H, Van Paepegem W, et al. Interlaminar toughening of resin transfer moulded glass fibre epoxy laminates by polycaprolactone electrospun nanofibres. Compos Sci Technol 2014;104:66–73. doi:10.1016/J.COMPSCITECH.2014.09.005.

[261] Dzenis YA, Reneker DH. Delamination resistant composites prepared by small diameter fiber reinforcement at ply interfaces. US6265333B1, 1998.

[262] Zhang H, Liu Y, Kuwata M, Bilotti E, Peijs T. Improved fracture toughness and integrated damage sensing capability by spray coated CNTs on carbon fibre prepreg. Compos Part A Appl Sci Manuf 2015;70:102–10. doi:10.1016/J.COMPOSITESA.2014.11.029.

[263] Shan FL, Gu YZ, Li M, Liu YN, Zhang ZG. Effect of deposited carbon nanotubes on interlaminar properties of carbon fiber-reinforced epoxy composites using a developed spraying processing. Polym Compos 2013;34:41–50. doi:10.1002/pc.22375.

[264] Abot JL, Song Y, Schulz MJ, Shanov VN. Novel carbon nanotube array-reinforced laminated composite materials with higher interlaminar elastic properties. Compos Sci Technol 2008;68:2755–60. doi:10.1016/j.compscitech.2008.05.023.

[265] Khan SU, Kim J-K. Improved interlaminar shear properties of multiscale carbon fiber composites with bucky paper interleaves made from carbon nanofibers. Carbon N Y 2012;50:5265–77. doi:10.1016/j.carbon.2012.07.011.

[266] Lee S-H, Kim H, Hang S, Cheong S-K. Interlaminar fracture toughness of composite laminates with CNT-enhanced nonwoven carbon tissue interleave. Compos Sci Technol 2012;73:1–8. doi:10.1016/j.compscitech.2012.09.011.

[267] Nistal A, Falzon BG, Hawkins SC, Chitwan R, García-Diego C, Rubio F. Enhancing the fracture toughness of hierarchical composites through amino–functionalised carbon nanotube webs. Compos Part B Eng 2019;165:537–44. doi:10.1016/J.COMPOSITESB.2019.02.001.

[268] Ou Y, González C, Vilatela JJ. Interlaminar toughening in structural carbon fiber/epoxy composites interleaved with carbon nanotube veils. Compos Part A Appl Sci Manuf 2019;124:105477. doi:10.1016/j.compositesa.2019.105477.

[269] Zhao X, Chen W, Han X, Zhao Y, Du S. Enhancement of interlaminar fracture toughness in textile-reinforced epoxy composites with polyamide 6/graphene oxide interlaminar toughening tackifier. Compos Sci Technol 2020;191:108094. doi:10.1016/j.compscitech.2020.108094.

[270] Du X, Zhou H, Sun W, Liu HY, Zhou G, Zhou H, et al. Graphene/epoxy interleaves for delamination toughening and monitoring of crack damage in carbon fibre/epoxy composite laminates. Compos Sci Technol 2017;140:123–33. doi:10.1016/j.compscitech.2016.12.028.

[271] Ning H, Li J, Hu N, Yan C, Liu Y, Wu L, et al. Interlaminar mechanical properties of carbon fiber reinforced plastic laminates modified with graphene oxide interleaf. Carbon N Y 2015;91:224–33. doi:10.1016/j.carbon.2015.04.054.

[272] Liu B, Cao S, Gao N, Cheng L, Liu Y, Zhang Y, et al. Thermosetting CFRP interlaminar toughening with multi-layers graphene and MWCNTs under mode I fracture. Compos Sci Technol 2019;183:107829. doi:10.1016/j.compscitech.2019.107829.

[273] Liu B, Gao N, Cao S, Ye F, Liu Y, Zhang Y, et al. Interlaminar toughening of unidirectional CFRP with multilayers graphene and MWCNTs for Mode II fracture. Compos Struct 2020;236:111888. doi:10.1016/j.compstruct.2020.111888.

[274] Jia J, Du X, Chen C, Sun X, Mai YW, Kim JK. 3D network graphene interlayer for excellent interlaminar toughness and strength in fiber reinforced composites. Carbon N Y 2015;95:978–86. doi:10.1016/j.carbon.2015.09.001.

[275] Garcia EJ, Wardle BL, John Hart A. Joining prepreg composite interfaces with aligned carbon nanotubes. Compos Part A Appl Sci Manuf 2008;39:1065–70. doi:10.1016/J.COMPOSITESA.2008.03.011.

[276] Lewis D, Wardle BL. Interlaminar shear strength investigation of aligned carbon nanotube-reinforced prepreg composite interfaces. 56th AIAA/ASCE/AHS/ASC Struct. Struct. Dyn. Mater. Conf., American Institute of Aeronautics and Astronautics Inc.; 2015. doi:10.2514/6.2015-0127.

[277] Ni X, Wardle BL. Experimental investigation of interlaminar fracture micro-mechanisms of aligned carbon nanotube-reinforced aerospace laminated composites. AIAA Scitech 2019 Forum, American Institute of Aeronautics and Astronautics Inc, AIAA; 2019. doi:10.2514/6.2019-1201.

[278] Yang B, Wang L, Zhang M, Luo J, Lu Z, Ding X. Fabrication, Applications, and Prospects of Aramid Nanofiber. Adv Funct Mater 2020:2000186. doi:10.1002/adfm.202000186.

[279] Fan J, Wang J, Shi Z, Yu S, Yin J. Kevlar nanofiber-functionalized multiwalled carbon nanotubes for polymer reinforcement. Mater Chem Phys 2013;141:861–8. doi:10.1016/j.matchemphys.2013.06.015.

[280] Lyu J, Wang X, Liu L, Kim Y, Tanyi EK, Chi H, et al. High Strength Conductive Composites with Plasmonic Nanoparticles Aligned on Aramid Nanofibers. Adv Funct Mater 2016;26:8435–45. doi:10.1002/adfm.201603230.

[281] Wang F, Wu Y, Huang Y, Liu L. Strong, transparent and flexible aramid nanofiber/POSS hybrid organic/inorganic nanocomposite membranes. Compos Sci Technol 2018;156:269–75. doi:10.1016/j.compscitech.2018.01.016.

[282] Cao K, Siepermann CP, Yang M, Waas AM, Kotov NA, Thouless MD, et al. Reactive Aramid Nanostructures as High-Performance Polymeric Building Blocks for Advanced Composites. Adv Funct Mater 2013;23:2072–80. doi:10.1002/adfm.201202466.

[283] Tung S on, Fisher SL, Kotov NA, Thompson LT. Nanoporous aramid nanofibre separators for nonaqueous redox flow batteries. Nat Commun 2018;9:4193. doi:10.1038/s41467-018-05752-x.

[284] Xie F, Jia F, Zhuo L, Lu Z, Si L, Huang J, et al. Ultrathin MXene/aramid nanofiber composite paper with excellent mechanical properties for efficient electromagnetic interference shielding. Nanoscale 2019;11:23382–91. doi:10.1039/c9nr07331k.

[285] Liu Z, Lyu J, Fang D, Zhang X. Nanofibrous Kevlar Aerogel Threads for Thermal Insulation in Harsh Environments. ACS Nano 2019;13:5703–11. doi:10.1021/acsnano.9b01094.

[286] Lyu J, Liu Z, Wu X, Li G, Fang D, Zhang X. Nanofibrous Kevlar aerogel films and their phase-change composites for highly efficient infrared stealth. ACS Nano 2019;13:2236–45. doi:10.1021/acsnano.8b08913.

[287] Yang B, Wang L, Zhang M, Luo J, Ding X. Timesaving, High-Efficiency Approaches to Fabricate Aramid Nanofibers. ACS Nano 2019;13:7886–97. doi:10.1021/acsnano.9b02258.

[288] Cui J. Zinc oxide nanowires. Mater Charact 2012;64:43–52. doi:10.1016/J.MATCHAR.2011.11.017.

[289] Bagga S, Akhtar J, Mishra S. Synthesis and applications of ZnO nanowire: A review. AIP Conf. Proc., vol. 1989, AIP Publishing LLC ; 2018, p. 020004. doi:10.1063/1.5047680.

[290] Malakooti MH, Patterson BA, Hwang H-S, Sodano HA. Development of multifunctional fiber reinforced polymer composites through ZnO nanowire arrays. In: Goulbourne NC, editor. vol. 9800, International Society for Optics and Photonics; 2016, p. 98000L. doi:10.1117/12.2222050.

[291] Yu J, Yu X. Hydrothermal Synthesis and Photocatalytic Activity of Zinc Oxide Hollow Spheres. Environ Sci Technol 2008;42:4902–7. doi:10.1021/es800036n.

[292] Kuo SY, Lin HI. Field emission characteristics of zinc oxide nanowires synthesized by vapor-solid process. Nanoscale Res Lett 2014;9:1–5. doi:10.1186/1556-276X-9-70.

[293] Khokhra R, Bharti B, Lee HN, Kumar R. Visible and UV photo-detection in ZnO nanostructured thin films via simple tuning of solution method . Sci Rep 2017;7:1–14. doi:10.1038/s41598-017-15125-x.

[294] Li X, Zhao C, Liu X. A paper-based microfluidic biosensor integrating zinc oxide nanowires for electrochemical glucose detection. Microsystems Nanoeng 2015;1:1–7. doi:10.1038/micronano.2015.14.

[295] Syrrokostas G, Govatsi K, Leftheriotis G, Yannopoulos SN. Platinum decorated zinc oxide nanowires as an efficient counter electrode for dye sensitized solar cells. J Electroanal Chem 2019;835:86–95. doi:10.1016/j.jelechem.2019.01.013.

[296] Chang PC, Fan Z, Wang D, Tseng WY, Chiou WA, Hong J, et al. ZnO nanowires synthesized by vapor trapping CVD method. Chem Mater 2004;16:5133–7. doi:10.1021/cm049182c.

[297] Greene LE, Yuhas BD, Law M, Zitoun D, Yang P. Solution-grown zinc oxide nanowires. Inorg Chem 2006;45:7535–43. doi:10.1021/ic0601900.

[298] Siqueira JR, Oliveira ON. Carbon-based nanomaterials. Nanostructures, Elsevier Inc.; 2017, p. 233–49. doi:10.1016/B978-0-323-49782-4.00009-7.

[299] Novoselov KS, Fal9ko VI, Colombo L, Gellert PR, Schwab MG, Kim & K. A roadmap for graphene. Nature 2012;490. doi:10.1038/nature11458.

[300] Liu J, Tang J, Gooding JJ. Strategies for chemical modification of graphene and applications of chemically modified graphene. J Mater Chem 2012;22:12435. doi:10.1039/c2jm31218b.

[301] Araújo MP, Soares OSGP, Fernandes AJS, Pereira MFR, Freire C. Tuning the surface chemistry of graphene flakes: new strategies for selective oxidation. RSC Adv 2017;7:14290–301. doi:10.1039/c6ra28868e.

[302] Ahmad H, Fan M, Hui D. Graphene oxide incorporated functional materials: A review. Compos Part B Eng 2018;145:270–80. doi:10.1016/j.compositesb.2018.02.006.

[303] Lin J, Peng Z, Liu Y, Ruiz-Zepeda F, Ye R, Samuel ELG, et al. Laser-induced porous graphene films from commercial polymers. Nat Commun 2014;5:5714. doi:10.1038/ncomms6714.

[304] Duy LX, Peng Z, Li Y, Zhang J, Ji Y, Tour JM. Laser-induced graphene fibers. Carbon N Y 2018;126:472–9. doi:10.1016/J.CARBON.2017.10.036.

[305] Luong DX, Yang K, Yoon J, Singh SP, Wang T, Arnusch CJ, et al. Laser-Induced Graphene Composites as Multifunctional Surfaces. ACS Nano 2019:acsnano.8b09626. doi:10.1021/acsnano.8b09626.

[306] Ye R, James DK, Tour JM. Laser-Induced Graphene: From Discovery to Translation. Adv Mater 2019;31:1803621. doi:10.1002/adma.201803621.

[307] Nasser J, Lin J, Zhang L, Sodano HA. Laser induced graphene printing of spatially controlled super-hydrophobic/hydrophilic surfaces. Carbon N Y 2020;162:570–8. doi:10.1016/j.carbon.2020.03.002.

[308] Chyan Y, Ye R, Li Y, Pratap Singh S, Arnusch CJ, Tour JM. Laser-Induced Graphene by Multiple Lasing: Toward Electronics on Cloth, Paper, and Food Article. ACS Nano 2018;12. doi:10.1021/acsnano.7b08539.

[309] Frenking G, Shaik S. The Chemical Bond. vol. 9783527333158. Weinheim, Germany: Wiley-VCH Verlag GmbH & Co. KGaA; 2014. doi:10.1002/9783527664658.

[310] Nilsson A, Pettersson LGM, Nørskov JK. Chemical Bonding at Surfaces and Interfaces. Elsevier; 2008. doi:10.1016/B978-0-444-52837-7.X5001-1.

[311] Jeffrey GA. An introduction to hydrogen bonding. Oxford University Press; 1997.

[312] Cangelosi F, Shaw MT. A Review of hydrogen bonding in solid polymers: Structural relationships, analysis, and importance. Polym Plast Technol Eng 1983;21:13–98. doi:10.1080/03602558308070020.

[313] Marcus Y. The effectiveness of solvents as hydrogen bond donors. J Solution Chem 1991;20:929–44. doi:10.1007/BF01074953.

[314] Hubbard RE, Kamran Haider M. Hydrogen Bonds in Proteins: Role and Strength. Encycl. Life Sci., Chichester, UK: John Wiley & Sons, Ltd; 2010. doi:10.1002/9780470015902.a0003011.pub2.

[315] Šponer J, Leszczynski J, Hobza P. Hydrogen bonding and stacking of dna bases: A review of quantum-chemical ab initio studies. J Biomol Struct Dyn 1996;14:117–35. doi:10.1080/07391102.1996.10508935.

[316] Geim AK, Grigorieva I V. Van der Waals heterostructures. Nature 2013;499:419–25. doi:10.1038/nature12385.

[317] Berland K, Cooper VR, Lee K, Schröder E, Thonhauser T, Hyldgaard P, et al. van der Waals forces in density functional theory: a review of the vdW-DF method. Reports Prog Phys 2015;78:066501. doi:10.1088/0034-4885/78/6/066501.

[318] Karger-Kocsis J, Mahmood H, Pegoretti A. Recent advances in fiber/matrix interphase engineering for polymer composites. Prog Mater Sci 2015;73:1–43. doi:10.1016/j.pmatsci.2015.02.003.

[319] Yan H, Li J, Tian W, He L, Tuo X, Qiu T. A new approach to the preparation of poly(p-phenylene terephthalamide) nanofibers. RSC Adv 2016;6:26599–605. doi:10.1039/c6ra01602b.

[320] Yao J, Jin J, Lepore E, Pugno NM, Bastiaansen CWM, Peijs T. Electrospinning of p-Aramid Fibers. Macromol Mater Eng 2015;300:1238–45. doi:10.1002/mame.201500130.

[321] Ifuku S, Maeta H, Izawa H, Morimoto M, Saimoto H. Facile preparation of aramid nanofibers from Twaron fibers by a downsizing process. RSC Adv 2014;4:40377–80. doi:10.1039/c4ra06924b.

[322] Yang B, Zhang M, Lu Z, Luo J, Song S, Zhang Q. From Poly(p-phenylene terephthalamide) Broken Paper: High-Performance Aramid Nanofibers and Their Application in Electrical Insulating Nanomaterials with Enhanced Properties. ACS Sustain Chem Eng 2018;6:8954–63. doi:10.1021/acssuschemeng.8b01311.

[323] Yang B, Zhang M, Lu Z, Tan J, Luo JJ, Song S, et al. Comparative study of aramid nanofiber (ANF) and cellulose nanofiber (CNF). Carbohydr Polym 2019;208:372–81. doi:10.1016/j.carbpol.2018.12.086.

[324] Jung J, Sodano HA. High strength epoxy nanocomposites reinforced by epoxy functionalized aramid nanofibers. Polymer (Guildf) 2020;195:122438. doi:10.1016/j.polymer.2020.122438.

[325] Nafari A. Flexible Piezoelectric Nanocomposite Energy Harvester for Extreme Temperature Applications. University of Michigan, 2019.

[326] Han L, Zhang K, Ishida H, Froimowicz P. Study of the Effects of Intramolecular and Intermolecular Hydrogen-Bonding Systems on the Polymerization of Amide-Containing Benzoxazines. Macromol Chem Phys 2017;218:1600562. doi:10.1002/macp.201600562.

[327] Fagnani DE, Meese MJ, Abboud KA, Castellano RK. Homochiral [2.2]Paracyclophane Self-Assembly Promoted by Transannular Hydrogen Bonding. Angew Chemie Int Ed 2016;55:10726–31. doi:10.1002/anie.201605286.

[328] Chenon B, Sandorfy C. Hydrogen bonding in the amide hydrohalides: I. general aspects. Can J Chem 1958;36:1181–206. doi:10.1139/v58-173.

[329] ASTM. AS for T and M. Designation: D638-14 Standard test Method for Tensile Properties of Plastics. ASTM Int 2014;82:1–15. doi:10.1520/D0638-14.

[330] Marcelo G, Tarazona MP, Saiz E. Solution properties of poly(diallyldimethylammonium chloride) (PDDA). Polymer (Guildf) 2005;46:2584–94. doi:10.1016/j.polymer.2005.01.078.

[331] Yang B, Lu Z, Zhang M, Liu Y, Liu G. A ductile and highly fibrillating PPTA-pulp and its reinforcement and filling effects of PPTA-pulp on properties of paper-based materials. J Appl Polym Sci 2016;133:n/a-n/a. doi:10.1002/app.43209.

[332] Wang ZL. ZnO nanowire and nanobelt platform for nanotechnology. Mater Sci Eng R Reports 2009;64:33–71. doi:10.1016/j.mser.2009.02.001.

[333] Xu S, Lin Wang Z. One-Dimensional ZnO Nanostructures: Solution Growth and Functional Properties. Nano Res 2011;4:1013–98. doi:10.1007/s12274-011-0160-7.

[334] Feng ZC. Zinc Oxide and Materials. CRC Press; 2012.

[335] Ehlert GJ. Development of a Zinc Oxide Nanowire Interphase for Enhanced Structural Composites. University of Florida, 2012.

[336] Wang ZL. Zinc oxide nanostructures: growth, properties and applications. J Phys Condens Matter 2004;16:R829–58. doi:10.1088/0953-8984/16/25/R01.

[337] Agrawal R, Peng B, Espinosa HD. Experimental-Computational Investigation of ZnO nanowires Strength and Fracture. Nano Lett 2009;9:4177–83. doi:10.1021/nl9023885.

[338] Desai AV, Haque MA. Mechanical properties of ZnO nanowires. Sensors Actuators A Phys 2007;134:169–76. doi:10.1016/J.SNA.2006.04.046.

[339] Hoffmann S, Östlund F, Michler J, Fan HJ, Zacharias M, Christiansen SH, et al. Fracture strength and Young's modulus of ZnO nanowires. Nanotechnology 2007;18:205503. doi:10.1088/0957-4484/18/20/205503.

[340] Lee WJ, Chang JG, Ju SP, Weng MH, Lee CH. Structure-dependent mechanical properties of ultrathin zinc oxide nanowires. Nanoscale Res Lett 2011;6:1–8. doi:10.1186/1556-276X-6-352.

[341] Manoharan MP, Desai A V, Neely G, Haque MA. Synthesis and Elastic Characterization of Zinc Oxide Nanowires. J Nanomater 2008;849745. doi:10.1155/2008/849745.

[342] Zeng J, Wang X, G. J. Colloidal Hybrid Nanocrystals: Synthesis, Properties, and Perspectives. Nanocrystal, InTech; 2011. doi:10.5772/16418.

[343] Das S, Dutta K, Pramanik A. Morphology control of ZnO with citrate: A time and concentration dependent mechanistic insight. CrystEngComm 2013;15:6349–58. doi:10.1039/c3ce40822a.

[344] Ehlert GJ, Galan U, Sodano HA. Role of Surface Chemistry in Adhesion between ZnO Nanowires and Carbon Fibers in Hybrid Composites. ACS Appl Mater Interfaces 2013;5:635–45. doi:10.1021/am302060v.

[345] Seu KJ, Pandey AP, Haque F, Proctor EA, Ribbe AE, Hovis JS. Effect of surface treatment on diffusion and domain formation in supported lipid bilayers. Biophys J 2007;92:2445–50. doi:10.1529/biophysj.106.099721.

[346] González-Benito J. The nature of the structural gradient in epoxy curing at a glass fiber/epoxy matrix interface using FTIR imaging. J Colloid Interface Sci 2003;267:326–32. doi:10.1016/S0021-9797(03)00550-2.

[347] Shokri B, Abbasi-Firouzjah M, Iman Hosseini S. FTIR analysis of silicon dioxide thin film deposited by Metal organic-based PECVD. 19th Int. Symp. plasma Chem. Soc., Bochum: 2009.

[348] Geim AK, Novoselov KS. The rise of graphene. Nat Mater 2007;6:183–91. doi:10.1038/nmat1849.

[349] Ferrari AC, Meyer JC, Scardaci V, Casiraghi C, Lazzeri M, Mauri F, et al. Raman spectrum of graphene and graphene layers. Phys Rev Lett 2006;97. doi:10.1103/PhysRevLett.97.187401.

[350] Sun Z, Raji ARO, Zhu Y, Xiang C, Yan Z, Kittrell C, et al. Large-area Bernal-stacked bi-, tri-, and tetralayer graphene. ACS Nano 2012;6:9790–6. doi:10.1021/nn303328e.

[351] Li Y, Luong DX, Zhang J, Tarkunde YR, Kittrell C, Sargunaraj F, et al. Laser-Induced Graphene in Controlled Atmospheres: From Superhydrophilic to Superhydrophobic Surfaces. Adv Mater 2017;29:1700496. doi:10.1002/adma.201700496.

[352] Wang H, Wang H, Wang Y, Su X, Wang C, Zhang M, et al. Laser Writing of Janus Graphene/Kevlar Textile for Intelligent Protective Clothing. ACS Nano 2020;14:3219–26. doi:10.1021/acsnano.9b08638.

[353] Kerans RJ, Parthasarathy TA. Theoretical Analysis of the Fiber Pullout and Pushout Tests. J Am Ceram Soc 1991;74:1585–96. doi:10.1111/j.1151-2916.1991.tb07144.x.

[354] Hodzic A., Stachurski Z.H., kim J.K. An analysis of microdroplet test: Effects of specimen geometry, matrix type, fibre treatment and water ageing. Polym Polym Compos 2001;9:499–508.

[355] Hodzic A, Kalyanasundaram S, Lowe A, Stachurski ZH. The microdroplet test: experimental and finite element analysis of the dependance of failure mode on droplet shape. Compos Interfaces 1998;6:375–89. doi:10.1163/156855498X00379.

[356] Kang S-K, Lee D-B, Choi N-S. Fiber/epoxy interfacial shear strength measured by the microdroplet test. Compos Sci Technol 2009;69:245–51. doi:10.1016/J.COMPSCITECH.2008.10.016.

[357] Piggott MR. Why interface testing by single-fibre methods can be misleading. Compos Sci Technol 1997;57:965–74. doi:10.1016/S0266-3538(97)00036-5.

[358] ten Busschen A, Selvadurai APS. Mechanics of the Segmentation of an Embedded Fiber, Part I: Experimental Investigations. J Appl Mech 1995;62:87. doi:10.1115/1.2895888.

[359] Gong XJ, Arthur JA, Penn LS. Strain rate effect in the single-fiber-fragmentation test. Polym Compos 2001;22:349–60. doi:10.1002/pc.10543.

[360] Li Z, Bi X, Lambros J, Geubelle PH. Dynamic fiber debonding and frictional push-out in mode composite systems: Experimental observations. Exp Mech 2002;42:417–25.

doi:10.1007/BF02412147.

[361] Rao V, Herrera-Franco P, Ozzello AD, Drzal LT. A Direct Comparison of the Fragmentation Test and the Microbond Pull-out Test for Determining the Interfacial Shear Strength. J Adhes 1991;34:65–77. doi:10.1080/00218469108026506.

[362] DiFrancia C, Ward TC, Claus RO. The single-fibre pull-out test. 1: Review and interpretation. Compos Part A Appl Sci Manuf 1996;27:597–612. doi:10.1016/1359-835X(95)00069-E.

[363] Piggott MR. Composite Interfaces The single-fibre pull-out method: its advantages, interpretation and experimental realization. Compos Interfaces 2012;1:211–23. doi:10.1163/156855493X00086.

[364] Kelly A, Tyson WR. Tensile properties of fibre-reinforced metals: Copper/tungsten and copper/molybdenum. J Mech Phys Solids 1965;13:329–50. doi:10.1016/0022-5096(65)90035-9.

[365] Herrera-Franco PJ, Drzal LT. Comparison of methods for the measurement of fibre/matrix adhesion in composites. Composites 1992;23:2–27. doi:10.1016/0010-4361(92)90282-Y.

[366] Sørensen BF, Lilholt H. Fiber pull-out test and single fiber fragmentation test - analysis and modelling. IOP Conf Ser Mater Sci Eng 2016;139:012009. doi:10.1088/1757-899X/139/1/012009.

[367] Gibson RF. Principles of composite material mechanics. 4th ed. Boca Raton: CRC Press; 2016.

[368] Chawla KK. Glass Fibers. Ref. Modul. Mater. Sci. Mater. Eng., Elsevier; 2016. doi:10.1016/B978-0-12-803581-8.02325-0.

[369] Kang S, Hong S Il, Choe CR, Park M, Rim S, Kim J. Preparation and characterization of epoxy composites filled with functionalized nanosilica particles obtained via sol–gel process. Polymer (Guildf) 2001;42:879–87. doi:10.1016/S0032-3861(00)00392-X.

[370] Zhu J, Wei S, Ryu J, Budhathoki M, Liang G, Guo Z. In situ stabilized carbon nanofiber (CNF) reinforced epoxy nanocomposites. J Mater Chem 2010;20:4937. doi:10.1039/c0jm00063a.

[371] Short SR. Characterization of interlaminar shear failures of graphite/epoxy composite materials. Composites 1995;26:431–49. doi:10.1016/0010-4361(95)90916-N.

[372] Alsaadi M, Ugla AA, Erklig A. A comparative study on the interlaminar shear strength of carbon, glass, and Kevlar fabric/epoxy laminates filled with SiC particles. J Compos Mater 2017;51:2835–44. doi:10.1177/0021998317701559.

[373] Qin J, Zhang G, Zhou L, Li J, Shi X. Dynamic/quasi-static stab-resistance and mechanical properties of soft body armour composites constructed from Kevlar fabrics and shear thickening fluids. RSC Adv 2017;7:39803–13. doi:10.1039/C7RA07549A.

[374] Kolsky H, H. An Investigation of the Mechanical Properties of Materials at very High Rates of Loading. Proc Phys Soc Sect B 1949;62:676–700. doi:10.1088/0370-1301/62/11/302.

[375] Owens AT. Development of a Split Hopkinson Tension Bar for Testing Stress-Strain Response of Particulate Composites under High Rates of Loading. Auburn University, 2007.

[376] Kaiser MA, Wilson L, Saunders W. Advancements in the Split Hopkinson Bar Test. Virginia Polytechnic Institute and State University, 1998.

[377] Chen WW, Song B. Split Hopkinson (Kolsky) bar : design, testing and applications. Springer; 2011.

[378] Hao Y, Hao H. Dynamic compressive behaviour of spiral steel fibre reinforced concrete in split Hopkinson pressure bar tests. Constr Build Mater 2013;48:521–32. doi:10.1016/J.CONBUILDMAT.2013.07.022.

[379] Hosur M., Alexander J, Vaidya U., Jeelani S. High strain rate compression response of carbon/epoxy laminate composites. Compos Struct 2001;52:405–17. doi:10.1016/S0263-8223(01)00031-9.

[380] Caverzan A, Cadoni E, di Prisco M. Tensile behaviour of high performance fibre-reinforced cementitious composites at high strain rates. Int J Impact Eng 2012;45:28–38. doi:10.1016/J.IJIMPENG.2012.01.006.

[381] Zhu D, Mobasher B, Erni J, Bansal S, Rajan SD. Strain rate and gage length effects on tensile behavior of Kevlar 49 single yarn. Compos Part A Appl Sci Manuf 2012;43:2021–9. doi:10.1016/J.COMPOSITESA.2012.06.007.

[382] Kim D joo, El-Tawil S, Naaman AE. Rate-dependent tensile behavior of high performance fiber reinforced cementitious composites. Mater Struct 2009;42:399–414. doi:10.1617/s11527-008-9390-x.

[383] Mahmoud MA, Elafandy TH, Okail HO, Abdelrahman AA. Interfacial shear behavior of composite flanged concrete beams. HBRC J 2014;10:206–14. doi:10.1016/J.HBRCJ.2013.11.001.

[384] Kolitawong C. High strain rate behavior of steel cord rubber composite for pneumatic tyre. 12th Japanese-European Symp Compos Mater n.d.

[385] Wong E-H, Mai YW. Robust design of microelectronics assemblies against mechanical shock, temperature and moisture. Woodhead Publishing; 2015.

[386] Yuan F, Prakash V, Tullis T. Origin of pulverized rocks during earthquake fault rupture. J Geophys Res 2011;116:B06309. doi:10.1029/2010JB007721.

[387] Shannag MJ, Brincker R, Hansen W. Pullout behavior of steel fibers from cement-based composites. Cem Concr Res 1997;27:925–36. doi:10.1016/S0008-8846(97)00061-6.

[388] Davies IJ, Ogasawara T, Ishikawa T. Distribution of fibre pullout length and interface shear strength within a single fibre bundle for an orthogonal 3-D woven Si-Ti-C-O fibre/Si-Ti-C-O matrix composite tested at 1100 • C in air. J Eur Ceram Soc 2005;25:599–604. doi:10.1016/j.jeurceramsoc.2004.03.022.

[389] Pompo A, Stupak PR, Nicolais L, Marchese B. Analysis of steel fibre pull-out from a cement matrix using video photography. Cem Concr Compos 1996;18:3–8. doi:10.1016/0958-9465(95)00034-8.

[390] Nilakantan G, Keefe M, Wetzel ED, Bogetti TA, Gillespie JW. Effect of statistical yarn tensile strength on the probabilistic impact response of woven fabrics. Compos Sci Technol 2012;72:320–9. doi:10.1016/J.COMPSCITECH.2011.11.021.

[391] Gibson J, McKee J, Freihofer G, Raghavan S, Gou J. Enhancement in ballistic performance of composite hard armor through carbon nanotubes. Int J Smart Nano Mater 2013;4:212–28. doi:10.1080/19475411.2013.870938.

[392] Seymour RB. High Modulus Polymers. Appl. Polym., Boston, MA: Springer US; 1988, p. 15–15. doi:10.1007/978-1-4684-5448-2_3.

[393] Chua PS, Piggott MR. The glass fibre—polymer interface: I—theoretical consideration for single fibre pull-out tests. Compos Sci Technol 1985;22:33–42. doi:10.1016/0266-3538(85)90089-2.

[394] Giannopoulos IP, Burgoyne CJ. Viscoelasticity of Kevlar 49 fibres. 16th Natl. Conf. Concr. Struct., 2009.

[395] Goldberg RK, Roberts GD. Strain Rate Sensitivity of Epoxy Resin in Tensile and Shear Loading. 2005.

[396] Siviour CR, Jordan JL. High Strain Rate Mechanics of Polymers: A Review. J Dyn Behav Mater 2016;2:15–32. doi:10.1007/s40870-016-0052-8.

[397] Klimek-McDonald DR, King JA, Miskioglu I, Pineda EJ, Odegard GM. Determination and Modeling of Mechanical Properties for Graphene Nanoplatelet/Epoxy Composites. Polym Compos 2018;39:1845–51. doi:10.1002/pc.24137.

[398] Delamination-dominated failures in polymer composites. Fail Anal Fractography Polym Compos 2009:164–237. doi:10.1533/9781845696818.164.

[399] Sellitti C, Koenig JL, Ishida H. Surface characterization of graphitized carbon fibers by attenuated total reflection fourier transform infrared spectroscopy. Carbon N Y 1990;28:221–8. doi:10.1016/0008-6223(90)90116-G.

[400] Washer G, Brooks T, Saulsberry R. Characterization of Kevlar Using Raman Spectroscopy. J Mater Civ Eng 2009;21:226–34. doi:10.1061/(ASCE)0899-1561(2009)21:5(226).

[401] Cui W, Wisnom MR, Jones M. Effect of specimen size on interlaminar shear strength of unidirectional carbon fibre-epoxy. Compos Eng 1994;4:299–307. doi:10.1016/0961-9526(94)90080-9.

[402] Sohn MS, Hu XZ. Mode II delamination toughness of carbon-fibre/epoxy composites with chopped Kevlar fibre reinforcement. Compos Sci Technol 1994;52:439–48. doi:10.1016/0266-3538(94)90179-1.

[403] García-Rodríguez SM, Costa J, Rankin KE, Boardman RP, Singery V, Mayugo JA. Interleaving light veils to minimise the trade-off between mode-I interlaminar fracture toughness and in-plane properties. Compos Part A Appl Sci Manuf 2020;128:105659. doi:10.1016/j.compositesa.2019.105659.

[404] Yasaee M, Bond IP, Trask RS, Greenhalgh ES. Mode II interfacial toughening through discontinuous interleaves for damage suppression and control. Compos Part A Appl Sci Manuf 2012;43:121–8. doi:10.1016/j.compositesa.2011.09.026.

[405] Hu Y, Cheng F, Ji Y, Yuan B, Hu X. Effect of aramid pulp on low temperature flexural properties of carbon fibre reinforced plastics. Compos Sci Technol 2020;192. doi:10.1016/j.compscitech.2020.108095.

[406] Cheng F, Hu Y, Yuan B, Hu X, Huang Z. Transverse and longitudinal flexural properties of unidirectional carbon fiber composites interleaved with hierarchical Aramid pulp micro/nano-fibers. Compos Part B Eng 2020;188. doi:10.1016/j.compositesb.2020.107897.

[407] Naebe M, Wang J, Amini A, Khayyam H, Hameed N, Li LH, et al. Mechanical Property and Structure of Covalent Functionalised Graphene/Epoxy Nanocomposites. Sci Rep 2015;4:4375. doi:10.1038/srep04375.

[408] Al-Shiblawi KA, Pershin VF, Jarcev VP, Pasko T V. Modification of epoxy resin using graphene. AIP Conf. Proc., vol. 2041, AIP Publishing LLC ; 2018, p. 020015. doi:10.1063/1.5079346.

[409] Abdullah SI, Ansari MNM. Mechanical properties of graphene oxide (GO)/epoxy composites. HBRC J 2015;11:151–6. doi:10.1016/j.hbrcj.2014.06.001.

[410] Tang L-C, Wan Y-J, Yan D, Pei Y-B, Zhao L, Li Y-B, et al. The effect of graphene dispersion on the mechanical properties of graphene/epoxy composites. Carbon N Y 2013;60:16–27. doi:10.1016/J.CARBON.2013.03.050.

[411] Blanco J, García EJ, Guzmán de Villoria R, Wardle BL. Limiting Mechanisms of Mode I Interlaminar Toughening of Composites Reinforced with Aligned Carbon Nanotubes. J Compos Mater 2009;43:825–41. doi:10.1177/0021998309102398.

[412] Bilisik K, Erdogan G, Sapanci E. Interlaminar shear properties of nanostitched/nanoprepreg aramid/phenolic composites by short beam method. J Compos Mater 2018:002199831881152. doi:10.1177/0021998318811523.

[413] Hosur MV, Vaidya UK, Ulven C, Jeelani S. Performance of stitched/unstitched woven carbon/epoxy composites under high velocity impact loading. Compos Struct 2004;64:455–66. doi:10.1016/J.COMPSTRUCT.2003.09.046.

[414] Kevin O'brien T, Johnston WM, Toland GJ. Mode II Interlaminar Fracture Toughness and Fatigue Characterization of a Graphite Epoxy Composite Material. Hampton: 2010.

[415] Zhang Q, Liu J, Sager R, Dai L, Baur J. Hierarchical composites of carbon nanotubes on carbon fiber: Influence of growth condition on fiber tensile properties. Compos Sci Technol 2009;69:594–601. doi:10.1016/J.COMPSCITECH.2008.12.002.

[416] Gogotsi Y, Libera JA, Yoshimura M. Hydrothermal synthesis of multiwall carbon nanotubes. J Mater Res 2000;15:2591–4. doi:10.1557/JMR.2000.0370.

[417] Chua PS. Dynamic mechanical analysis studies of the interphase. Polym Compos 1987;8:308–13. doi:10.1002/pc.750080505.

[418] Mohanty S, Verma SK, Nayak SK. Dynamic mechanical and thermal properties of MAPE treated jute/HDPE composites. Compos Sci Technol 2006;66:538–47.

doi:10.1016/J.COMPSCITECH.2005.06.014.